Universidade do Vale do Paraíba
Programa de Pós-Graduação em Física e Astronomia

Impact of CIR/HSS-Driven Geomagnetic Storm and HILDCAAs* Events on Brazilian Equatorial and Low Latitude Ionosphere

Impacto de Tempestade Geomagnética Impulsionada por CIR/HSS e de Eventos HILDCAAs* na Ionosfera Brasileira Equatorial e de Baixas Latitudes.

Samuel Abaidoo

São Jose dos Campos, SP
2025

Samuel Abaidoo

IMPACT OF CIR/HSS-DRIVEN GEOMAGNETIC STORM AND HILDCAAs* EVENTS ON BRAZILIAN EQUATORIAL AND LOW LATITUDE IONOSPHERE

Doctorate Dissertation submitted to the Institute of Research and Development of the University of Vale do Paraíba, as a final requirement for the Doctorate degree in Physics and Astronomy

Supervised by: Dr. Virginia Klausner and Dr. Claudia M N Candido.

São José dos Campos, SP

2025

TERMO DE AUTORIZAÇÃO DE DIVULGAÇÃO DA OBRA

Ficha catalográfica

Abaidoo, Samuel
Impact of CIR/HSS-Driven Geomagnetic Storm and HILDCAAs* Events on Brazilian Equatorial and Low Latitude Ionosphere = Impacto de Tempestade Geomagnetica Impulsionada por CIR/HSS e de Eventos HILDCAAs* na Ionosfera Brasileira Equatorial e de Baixas Latitudes / Samuel Abaidoo; orientadora, Virginia Klausner de Oliveira; co-orientadora Claudia Maria Nicoli Candido. - São José dos Campos, SP, 2025.
276 p.

Tese (Doutorado) - Universidade do Vale do Paraíba, São José dos Campos. Programa de Pós-Graduação em Física e Astronomia.

Inclui referências

1. Física e Astronomia. 2. Ionosfera. 3. Ondas eletromagnéticas. 4. Ionossonda. I. Oliveira, Virginia Klausner de , orient. II. Candido, Claudia Maria Nicoli, co-orient. III. Universidade do Vale do Paraíba. Programa de Pós-Graduação em Física e Astronomia. IV. Título.

I, Samuel Abaidoo, author of the referenced work above:

Authorize the total or partial dissemination of the work in print, digital, or fixed on any other type of media, as well as its total or partial reproduction, provided that the user of the reproduction attributes credit to the author of the work, citing the source.

I declare, for all legal purposes and effects, that the Work was prepared in compliance with the principles of morality and ethics and did not violate any intellectual property rights, under penalty of being held civilly, criminally, ethically, and professionally responsible for my actions.

São José dos Campos, 20 de outubro de 2025.

Autor(a) da Obra

UniVap
Universidade do Vale do Paraíba

P&D
Instituto de Pesquisa
e Desenvolvimento

SAMUEL ABAIDOO

"IMPACT OF CIR/HSS-DRIVEN GEOMAGNETIC STORM AND HILDCAAs* EVENTS ON THE BRAZILIAN EQUATORIAL AND LOW LATITUDE IONOSPHERE."

Tese aprovada como requisito parcial à obtenção do grau de Doutor, do Programa de Pós-Graduação em Física e Astronomia, do Instituto de Pesquisa e Desenvolvimento da Universidade do Vale do Paraíba, São José dos Campos, SP, pela seguinte banca examinadora:

Prof. Dr. Valdir Gil Pillat	Valdir Gil Pillat
Prof.ª Dr.ª Virginia Klausner de Oliveira	Virginia Klausner de Oliveira
Prof.ª Dr.ª Cláudia Maria Nicoli Cândido	Cláudia Maria Nicoli Cândido
Prof. Dr. Alan Prestes	Alan Prestes
Prof. Dr. Giorgio Arlan da Silva Picanço	Giorgio Alan da Silva Picanço
Prof. Dr. Ezequiel Echer - INPE	Ezequiel Echer
Prof. Dr. Marlos Rockenbach da Silva - INPE	Marlos Rockenbach da Silva
Prof. Dr. Patrick Essien - UCC	Patrick Essien

Prof.ª Dr.ª Juliana Ferreira Strixino
Diretora do IP&D – Univap
São José dos Campos, 21 de agosto de 2025.

Acknowledgement

I extend my heartfelt gratitude to Almighty God for His guiding hand; without His divine support, reaching this milestone would not have been possible.

I am deeply grateful to my esteemed principal advisor, Dr. Virginia Klausner, for her unwavering support throughout this research journey, particularly during challenging moments. Her guidance, training, and expertise, even within a short period, led to a profound transformation in my academic and professional development. Her dedication was essential to the direction and success of this project. I also extend special thanks to the Instituto de Pesquisa e Desenvolvimento (IP&D), its researchers, and staff for their support.

I sincerely appreciate Dr. Claudia M. N. Candido's support when I first arrived at INPE in 2019. Her invaluable guidance during my Master's program, as well as her continued contributions to my PhD research, have been truly instrumental.

I am grateful to Universidade do Vale do Paraiba (UNIVAP) and CAPES for their generous support and conducive environment. The financial assistance from CAPES was vital in facilitating our experiments, data collection, and the dissemination of results, ultimately ensuring the successful completion of this research. I am especially grateful for the opportunity to work under their guidance and for the grant provided.

Furthermore, I express my heartfelt appreciation to my parents, as well as to Prof. Nana Ama Browne Klutse, a Senior Lecturer at the University of Ghana and Chief Executive of the Environmental Protection Authority–Ghana, and Dr. Patrick Essien, a Lecturer at the University of Cape Coast, who were instrumental in initiating my journey. They were among the first to introduce me to the significance of this field during my time as a teaching assistant at the University of Ghana, Michael Obiri Yeboah, Kayoko Tochigi Yeboah, and Michael Tochigi for their wisdom and steadfast support, particularly during difficult times. I also wish to thank David Pareja Quispe, my colleagues for their constant encouragement. Finally, I dedicate this work to the entire Abaidoo's family, my beloved mother Eunice Eshun, my future wife and children.

Abstract

This research investigates the impact of CIRs/HSS-driven geomagnetic storms and High-Intensity, Long-Duration Continuous Auroral Electrojet Activity (HILDCAA) events on the Brazilian equatorial and low-latitude ionosphere during the early descending phase of solar cycle 23, with a focus on the geomagnetic disturbance from October 12–23, 2003. Ionospheric variability was analyzed using Digisonde data from São Luís and Cachoeira Paulista, representing the equatorial region and the southern crest of the Equatorial Ionization Anomaly (EIA), respectively, along with GNSS-derived Total Electron Content (TEC) data from a latitudinal chain of stations spanning Fortaleza to Uruguaiana, Brazil. To assess ionospheric perturbations, disturbed-day values were compared with a five quiet-day (5QD) average, serving as a baseline for normal conditions. Plasma drift disturbances were examined using the Fejer-Scherliess empirical model, employing the auroral electrojet index (AE) as a key parameter. The CIR/HSS events were characterized by prolonged geomagnetic forcing, with solar wind speeds reaching $\approx$ 619 km/s and IMF-Bz components facilitating enhanced magnetosphere-ionosphere coupling. These storms exhibited an intense main phase (Sym-H $\approx$ -100 nT) and a notably extended recovery phase ($\approx$ 8 days), during which disturbance dynamo electric fields (DDEFs) played a crucial role in ionospheric restructuring. Results indicate a strong coupling between the auroral and equatorial ionospheres, with equatorward propagating disturbance winds driving F-region uplifts and nighttime spread-F occurrences. TEC variations exhibited distinct temporal and latitudinal patterns, with enhancements predominantly observed during daytime and post-sunset hours, influenced by the interplay of penetration electric fields (PPEFs), DDEFs, and auroral-driven disturbance winds. Notably, TEC increases were prominent at the Equatorial Ionization Anomaly (EIA) crest during equinoctial months, particularly in March–April, whereas winter months exhibited minima. Analysis of thermospheric O/N_2 ratios confirmed that neutral composition changes were not the primary driver of TEC variability during HILDCAA events, whereas they played a significant role during CIR/HSS-driven geomagnetic storms. Additionally, large-scale ionospheric irregularities, examined through the Rate of TEC Index (ROTI), were most pronounced from nighttime to post-midnight, peaking at the equator during equinoxes and shifting toward lower latitudes from May to August. Empirical modeling validated that disturbance-induced vertical plasma drifts modulate F-region dynamics, with significant uplifts in h'F and hmF2, alongside foF2 reductions. Comparative statistical analysis of geomagnetic, solar wind, and ionospheric parameters demonstrated that CIR/HSS-driven

HILDCAA events induce persistent ionospheric perturbations, comparable to intense ICME-driven storms. These findings underscore the prolonged influence of CIR/HSS-induced geomagnetic activity on equatorial and low-latitude ionospheric behavior, contributing to a deeper understanding of space weather impacts on radio propagation and other technological systems in the near-Earth environment.

keywords: Ionospheric response. Digisonde. Declining phase. Coronal Mass Ejection, (CMEs). Corotating Interaction Regions, (CIRs). High-Intensity Long-Duration Continuous Auroral Electrojet Activity, (HILDCAA)

Resumo

Esta pesquisa investiga o impacto de tempestades geomagnéticas induzidas por CIRs/HSS e de eventos de Atividade Contínua do Eletrojato Auroral de Longa Duração e Alta Intensidade (HILDCAA) sobre a ionosfera equatorial e de baixas latitudes brasileiras, durante a fase inicial descendente do ciclo solar 23, com foco na perturbação geomagnética de 12 a 23 de outubro de 2003. A variabilidade ionosférica foi analisada utilizando dados de Digissonda de São Luís e Cachoeira Paulista, representando, respectivamente, a região equatorial e o bordo sul da Anomalia de Ionização Equatorial (EIA), juntamente com dados de Conteúdo Total de Elétrons (TEC) derivados de GNSS, obtidos de uma cadeia latitudinal de estações que se estende de Fortaleza a Uruguaiana, Brasil. Para avaliar as perturbações ionosféricas, os valores dos dias perturbados foram comparados com a média de cinco dias calmos (5QD), servindo como referência de condições normais. As perturbações no arrasto do plasma foram examinadas por meio do modelo empírico de Fejer-Scherliess, empregando o índice do eletrojato auroral (AE) como parâmetro chave. Os eventos de CIR/HSS foram caracterizados por um forçamento geomagnético prolongado, com velocidades do vento solar atingindo $\approx$ 619 km/s e componentes IMF-Bz favorecendo um acoplamento intensificado entre a magnetosfera e a ionosfera. Essas tempestades apresentaram uma fase principal intensa (Sym-H $\approx$ -100 nT) e uma fase de recuperação notavelmente prolongada ($\approx$ 8 dias), durante a qual os campos elétricos do dínamo de perturbação (DDEFs) desempenharam papel crucial na reestruturação ionosférica. Os resultados indicam um forte acoplamento entre as ionosferas auroral e equatorial, com ventos de perturbação propagando-se em direção ao equador, impulsionando elevações da região F e ocorrências de espalhamento-F noturno. As variações do TEC apresentaram padrões temporais e latitudinais distintos, com intensificações predominantemente observadas durante o dia e nas horas pós-pôr do sol, influenciadas pela interação de campos elétricos de penetração (PPEFs), DDEFs e ventos de perturbação impulsionados pela atividade auroral. Notadamente, os aumentos de TEC foram proeminentes no bordo da Anomalia de Ionização Equatorial (EIA) durante os meses equinociais, particularmente em março–abril, enquanto os meses de inverno exibiram valores mínimos. A análise das razões O/N_2 na termosfera confirmou que as mudanças na composição neutra não foram o principal fator das variações de TEC durante os eventos HILDCAA, embora tenham desempenhado papel significativo durante as tempestades geomagnéticas induzidas por CIR/HSS. Além disso, irregularidades ionosféricas de grande escala, examinadas por meio do Índice de Taxa do TEC (ROTI), foram mais pronunciadas do período noturno ao pós-meia-noite, atingindo seu pico no equador durante os equinócios e deslocando-se em direção a latitudes mais baixas de maio a agosto. A modelagem empírica validou que os arrastos verticais do plasma induzidos por perturbações modulam a dinâmica da região F, com elevações significativas em h'F e hmF2, acompanhadas por reduções em foF2. A análise estatística comparativa dos parâmetros geomagnéticos, do vento solar e da ionosfera demonstrou que os eventos HILDCAA associados a CIR/HSS induzem perturbações ionosféricas persistentes, comparáveis às tempestades intensas induzidas por ICMEs. Esses resultados destacam a influência prolongada da atividade geomagnética induzida por CIR/HSS sobre o comportamento ionosférico equatorial e de baixas latitudes, contribuindo para um entendimento mais profundo dos impactos do clima espacial na propagação de rádio e em outros sistemas tecnológicos no ambiente próximo à Terra.

Palavras-chave: Resposta ionosférica. Digissonda. Fase descendente. Ejeção de Massa Coronal (CMEs). Regiões de Interação em Corotação (CIRs). Atividade Contínua do Eletrojato Auroral de Longa Duração e Alta Intensidade (HILDCAA).

List of Figures

List of Tables

List of Symbols

γ	Growth rate of the instability
$\varepsilon_\circ$	Electrical permittivity in a vacuum
Å	Anstrong
ω	Angular frequency of electromagnetic wave
B	terrestrial magnetic induction field
E	zonal electric field
e	charge of the electron
f	frequency of the electromagnetic wave
F_n	frequency of the plasma
g	gravitational acceleration
$\overline{\sigma_H}$	Hall conductivty
Ω_i	ion gyro-frequency
V_{in}	ion-neutral collision frequency
J	Current
m_e	electron mass
m_i	ion mass
Ne	electronic density
e	electrical charge
X	ordinary wave
Y	extraordinary wave
V_D	Zonal Drift
λ	Wave lenght
$\overline{\sigma_P}$	Pedersen conductivity

List of Abbreviation

ACE	Advanced Composition Explorer
ADRES	Automated Data Request Execution System
CDMA	Code Modulation Multiple Access
CH	Coronal Hole
CIRs	Corotational interaction region
CMEs	Coronal Mass Ejection
DDEFs	Disturbance Dynamo Electric Fields
DIDBase	Digital Ionogram Database
DPS	Digisonde Portable Sounder
EDP	Electron Density Profile
EEJ	Equatorial Electrojet
EIA	Equatorial Ionization Anomaly
EM	Electromagnetic Wave
EPB	Equatorial Plasma Bubbles
ESF	Equatorial spread F
EUV	Extreme Ultraviolet
EUV	Extreme Ultraviolet Radiation
EUV	Extreme ultraviolet radiation
FACs	Field-aligned currents
foF2	Critical plasma Frequency
GLONASS	Globalnaya Navigazionnaya Sputnikovaya Sistema
GNSS	Global Navigation Satellite System
GPS	Global Positioning System
GSM	Geocentric Solar Magnetospheric
GUVI	Global Ultraviolet Image
GUVI	Global Ultraviolet Imager
HF	High Frequency
HILDCAA	High-Intensity Long-Duration Continuous Auroral Electrojet Activity
hmF2	True height of F layer
h’F	Virtual height of F layer
HSS	High Speed Stream
HSSWs	High-Speed Solar Wind Stream
IBGE	Brazilian Institute of Geography and Statistics

IEF	Interplanetary electric field
IGS	International GNSS Service
IMF	Interplanetary magnetic field
IRI	International Reference Ionosphere
kp	Geomagnetic Activity Index
LISN	Low Latitude Ionospheric Sensor Network
LT	Local time
ND	No Data
NmF2	F2 Layer Maximum Electron Density
PCV	Polar Cap Potential
PD	Polar Disturbance
PPEFs	Prompt Penetration Electric Fields
PRE	Pre-reversal Enhancement
RAMSAC	Argentine Continuous Satellite Monitoring Network
RBMC	Brazilian Continuous Monitoring Network
RINEX	Receiver Independent Exchange Format
ROT	Rate of change of TEC
ROTI	Rate of TEC Index
ROTI	Rate of TEC Index
RTI	Rayleigh Taylor Instability
SAMA	South Atlantic Magnetic Anomaly
SAO	Standard Archiving Output
SD	Standard Deviation
SFU	Solar Flux Units
SMEI	Solar Mass Ejection Imager
SOHO	Solar and Heliospheric Observatory
SSC	Storm sudden commencement
SW	Solar Wind
SW	Solar Wind
Sym H	Ring Current Index
TEC	Total electron content
TID	Traveling ionospheric disturbance
TIMED	Thermosphere Ionosphere Mesosphere Energetics and Dynamics
UT	Universal time
Vsw	Solar Wind Speed

Contents

1 Introduction

Significant changes observed in the magnetosphere, ionosphere, and upper atmosphere during space weather events primarily occur during geomagnetic disturbances. These events are characterized by two main interplanetary structures: interplanetary coronal mass ejections (ICMEs) and corotating interaction regions (CIRs) (TSURUTANI et al., 1999; PRESTES et al., 2017).

ICMEs involve significant releases of plasma into interplanetary space and occur permanently on solar maximum, while CIRs primarily occur during the declining phase of the solar cycle as a result of interactions between High Speed Streams (HSSs) and slow solar winds. ICMEs, among the most spectacular transient events, give rise to intense-to-extreme magnetic storms through magnetic reconnection between the interplanetary magnetic field (IMF) and the geomagnetic field, fostering an electrodynamic coupling between solar wind plasma and the magnetosphere (ABDU, 1997; GONZALEZ et al., 1994; GONZALEZ; TSURUTANI; GONZALEZ, 1999; ECHER et al., 2011).

During the solar minimum and declining phases of the solar cycle, significant phenomena known as coronal holes emerge, inducing HSS/CIR geomagnetic storms. These events arise from the interaction between high-speed solar wind streams (>750-800 km/s) and low-speed solar wind streams (>300-400 km/s) near the ecliptic plane, forming a narrow region of compressed plasma known as a CIRs (TSURUTANI et al., 1995). These structures are characterized by high plasma density and strong, highly oscillatory magnetic fields. High-speed streams are embedded with highly fluctuating Alfvén waves, which produce phenomena called High-Intensity, Long-Duration, Continuous Auroral Electroject Activity (HILDCAA) events (GONZALEZ; TSURUTANI, 1987). Coronal holes are particularly pertinent in space weather forecasting due to their impact on Earth's environment, especially during the solar cycle's minimum or declining phases, as they constitute the primary source of HSS/CIRs geomagnetic storms (TSURUTANI et al., 2004).

Geomagnetic storms are severe disturbances in Earth's magnetosphere resulting from the efficient exchange of energy between the solar wind and Earth's magnetosphere, primarily driven by CMEs and HSS/CIR. During these disturbances, energetic particle precipitation, including ionospheric currents, accumulates to generate heat, affecting the distribution of neutral density and electron density in the upper atmosphere (GONZALEZ et al., 1994). These storms manifest due to the abrupt infusion of solar wind energy into the magnetosphere-ionosphere-thermosphere system. The geomagnetic storms are initiated by the significant accumulation of energy within the magnetosphere-ionosphere system, resulting from convection electric fields. This accumulation enhances the ring current to a level that surpasses certain critical thresholds used to quantify the storm's strength through the Dst index as indicated by Gonzalez et al. (1994) and Rezende et al. (2007).

The storm's sudden commencement (SSC) indicates one characteristic of geomagnetic storms, typically followed by main and recovery phases. During the main phase, there is an amplification in the nature of particle precipitation and the magnetospheric electric field, leading to intensification of the ring current. Conversely, during the recovery phase, there is a decay of energetic particles in the ring current due to the recombination loss processes such as charge exchange, wave-particle interaction, convection, etc. (KLAUSNER et al., 2021; GONZALEZ et al., 2006).

In Earth's magnetosphere, strong modifications in several plasma regions are attributed to electrical currents when geomagnetic storms occur (TSURUTANI et al., 2001). These modification mechanisms are linked to the intensification of the current system and contribute to an increased auroral ionospheric current at mid and high latitudes, as well as the build-up of the ring current generation at lower latitudes and associated phenomena such as HILDCAA. This phenomenon is linked to sudden changes in the IMF component Bz, occurring within interplanetary Alfvén waves. These changes are frequently accompanied by changes in polar cap potential, intensified auroral electrojets, and the development of symmetric or asymmetric ring current following magnetic reconnection (GONZALEZ; TSURUTANI, 1987; KLAUSNER et al., 2021).

HILDCAA occurs when charged particles collide with atmospheric gas molecules in polar regions, emitting light that appears as auroras due to interactions between the solar wind and the magnetosphere. Its occurrence is linked to multiple reconnections during the southward incursion of IMF-Bz, which is associated with interplanetary Alfvén waves embedded in HSS as mentioned by Klausner et al. (2021). During this declining phase, CIR/HSS-driven geomagnetic storm are noted for their prolonged recovery periods. When CIR storms have extended recovery phases, they can fall into another category known as HILDCAA.

HILDCAA are continuous and weaker compared to geomagnetic storms (GONZALEZ; TSURUTANI, 1987). The southward incursion of the IMF-Bz is one characteristic of Alfvén wave occurrence. High-speed streams are embedded with highly fluctuating Alfvén waves. These waves result from the reconnection process facilitated by the coupling mechanism between the IMF-Bz and the geomagnetic field, enhancing auroral activity (PRESTES et al., 2017). During CIR/HSS-driven geomagnetic storms and HILDCAA events, increased solar wind energy input enhances the convection of electric fields within the magnetosphere, as noted by Kozyra e Liemohn (2003). Furthermore, the density and composition of the ionosphere can undergo significant changes during CIR/HSS-driven geomagnetic storms, persisting for days even after geomagnetic activity ceases (HASTINGS, 1995).

Both theoretical and experimental investigations (GONZALEZ; TSURUTANI; GONZALEZ, 1999; REZENDE et al., 2007; ABDU et al., 1991; BATISTA et al., 2006; BLANC; RICHMOND, 1980; KELLEY et al., 2003; ABDU; BRUM, 2009) have elucidated the characteristics of prompt penetration electric field (PPEFs), aligned with magnetospheric convection electric fields from higher to lower latitudes, leading to adverse effects on low-latitude electrodynamics (FEJER; SCHERLIESS, 1997). During geomagnetic storm events, PPEFs disturbs the equatorial ionosphere, significantly impacting the equatorial ionization anomaly (EIA) (KELLEY et al., 2003). Disturbances in the equatorial ionosphere during geomagnetic activity, such as geomagnetic storms, arise from (a) PPEFs, commonly referred to as the “undershielding” scenario, (b) PPEFs, or the “overshielding” scenario, and (c) the disturbance dynamo electric field (DDEFs). The PPEFs serves as a contributing factor that may either enhance or not affect the $\vec{E} \times \vec{B}$ plasma drift, contingent upon the direction and magnitude of the field (CARTER et al., 2013). As noted by Wei et al. (2015), during a geomagnetic storm, high-latitude PPEFs into the equatorial ionosphere on the dayside due to the undershielding mechanism presented by the field-aligned currents system in Region 1 (R1), located at the outer edge of the aurora. This occurs as a result of the southward incursion of the IMF-Bz associated with magnetospheric convection, particularly during the main phase. At the end of the storm, or during the recovery phase, the overshielding electric field from Region 2 (R2), closer to the auroral equator, presents an opposite polarity. This abrupt northward turn of the IMF-Bz results in a westward electric field on the dayside.

Therefore, it’s important to conduct studies like this to examine ionospheric electrodynamics. This study aims to examine the response of the equatorial and low-latitude ionosphere to CIR/HSS geomagnetic storms and HILDCAA events and to compare these variations with those observed during geomagnetically quiet days using Digisonde data and Total Electron Content (TEC) derived from ground-based GNSS (GPS) receivers in the Brazilian sector.

1.1 Motivation

The ionosphere plays a crucial role in space weather monitoring, and understanding its response to geomagnetic storms generated by various sources, such as ICMEs or HSSs/CIRs, is vital to mitigating their impact on technological systems. Geomagnetic storms can disrupt satellite communications, GPS navigation, and power grids due to induced geomagnetically induced currents, highlighting the need for in-depth studies focused on the characteristics, evolution, and physical mechanisms present in the ionosphere during these events. During geomagnetic storms, significant changes occur in the ionosphere, particularly at low and equatorial latitudes. These variations, primarily attributed to electric fields, are particularly pronounced during periods of intense geomagnetic disturbance, such as those driven by HSSs/CIRs and HILDCAA phenomena. Despite their importance, the response of the equatorial and low-latitude ionosphere to geomagnetic storm driven by HSSs/CIRs from 12-23 October 2003, before the Halloween storm in 2003 in the Brazilian sector have not been specifically focused on until now.

The year 2003 was marked by intense geomagnetic activity related to HILDCAAs* events, making it a compelling period for further investigation. Therefore, this study aims to fill this gap by exploring and comparing the outcomes of our findings, specifically focusing on the influence of CIRs/HSSs-driven geomagnetic storms followed by HILDCAAs* events on the ionosphere in the Brazilian equatorial and low-latitude regions. By doing so, we seek to advance our understanding of ionospheric electrodynamics during geomagnetic storms in the declining phase of the solar cycle and contribute to improving space weather forecasting models, enhancing the resilience of technological systems to space weather impacts.

1.2 Scientific Questions

The following research questions aim to address gaps in our current understanding of ionospheric responses to moderate geomagnetic disturbances driven by CIR/HSS and associated HILDCAA events:

- How does the ionospheric F-layer respond to CIR/HSS-driven geomagnetic storms in comparison to extreme events such as the Halloween superstorms?

- To what extent do ionospheric variations during CIR/HSS-driven geomagnetic storms differ from those induced by CME-driven storms, considering their distinct physical drivers?

- What is the role of thermospheric composition particularly [O]/[N_2] variations in modulating TEC responses during CIR/HSS-driven storms and HILDCAA periods?

- What are the distinguishing features of electric field disturbances (PPEFs and DDEFs) observed in equatorial ionospheric parameters (e.g., h'F, hmF2 and f0F2) during the recovery phases of CIR/HSS-driven geomagnetic storms and HILDCAA events?

1.3 Objectives

General:

To investigate the Brazilian Equatorial and Low-Latitude ionospheric variability to distinct levels of geomagnetic disturbances in 2003, a very active year during the early descending phase of solar cycle 23.

Specific:

- To investigate the variation of the most important ionospheric parameters such as Critical plasma frequency (foF2), F-region Virtual and Peak height (h'F) and (hmF2), respectively, the vertical Total Electron Content (VTEC) taken from distinct representative regions in Brazil Magnetic equator equatorial and crest of the EIA (as available).
- To examine the role of Prompt Penetration Electron Field, PPEFs, and Disturbance Dynamo Electric Field, DDEFs, on the F-region vertical drift, using the empirical model developed by Fejer and Scherliess in 1997.
- To perform a statistical study of the ionospheric response to High-Intensity Long-Duration Auroral Electrojet Activity, HILDCAA* in 2003

1.4 Organization of the Research

To accomplish the stated objectives, the project follows the outlined structure below. This project comprises six main chapters, beginning with an abstract summarizing the research. Chapter one (1) provides the research background, motivation, and objectives. Chapter two (2) delves into the structure and composition of the Earth's ionosphere. Chapter three (3) offers a theoretical framework and a review of relevant literature. Chapter four (4) details instrumentation and methodology. Chapter four and five (4.5 and 5) presents the results, analysis, interpretation, and discussion. Finally, Chapter six offers conclusions, Summary and Recommendations.

2 Theoretical Review

This chapter delves into the theoretical framework and foundational literature relevant to the solar-terrestrial environment. It explores critical concepts such as solar activity and its principal drivers, the mechanisms governing solar-terrestrial coupling interactions, and the dynamics of geomagnetic storms. Particular attention is given to the effects of these storms, highlighting the distinguishing characteristics of ICME-driven and CIR-driven storms. Additionally, the chapter examines HILDCAA phenomena and their specific influences on the Earth's ionosphere, providing a comprehensive understanding of their role in space weather phenomena.

2.1 Concepts of solar-terrestrial environment

Short-lived solar disturbances such as sunspots, CMEs, flares, and prominences generate energetic particles and electromagnetic fields that can cause space weather effects through their interactions with Earth's atmosphere and magnetic field. The objective of this section is to present the fundamental concepts and principles of solar-terrestrial interaction. The solar wind (SW) serves as the primary conduit for this interaction between the Sun and the Earth's environment. The structure of the SW and its components experience disturbances due to interactions with CMEs, leading to ionosphere-magnetosphere disturbances. This section briefly describes some of the phenomena that contribute to geomagnetic storm events.

2.1.1 Sun

The Sun serves as the primary driver of our solar system, influencing energetic processes on Earth and regulating space weather. Periodically, the Sun emits matter into space through the solar wind. The following outlines the principal physical characteristics of the Sun, as documented by (LANG, 2001).

Table 1 – Physical features of the sun

Feature	**Value**
Age	4.5×10^9 years
Mass	1.99×10^{30} kg
Radius	696,000 km (109 Earth radii)
Mean distance from Earth	1 AU = 1.5×10^8 km
Emitted radiation (luminosity)	3.86×10^{26} W (or 3.86×10^{33} erg/s)
Principal chemical constituents	Hydrogen (92.1%), Helium (7.8%)
Volume	1.412×10^{27} m^3 (or 1.3 million Earths)
Density (centre)	1.513×10^5 kg/m^3
Pressure (centre)	2.334×10^{16} Pa
Surface temperature (photosphere)	5785 K
Magnetic field (Sunspots)	0.1 - 0.4 T

The heat source of the Sun originates from nuclear fusion reactions converting hydrogen into helium within its core as pointed by (STIX, 2004). This energy takes $\approx 10^7$ years to traverse through the radiative and convective zones before reaching the surface (LANG, 2001). The Sun consists of the core and the solar atmosphere. The core, occupying about 25% of the Sun's radius, exists in an ionized state (plasma) with extremely high temperatures (15 million K) and pressures (250 billion atmospheres) (MAROV; MAROV, 2015). The Sun's atmosphere is divided into three distinct layers: the photosphere, chromosphere, and corona, each exhibiting a stratified composition (LANG, 2001). The photosphere, the most prominent and visible layer, is about 300 km thick, with temperatures decreasing from approximately 10,000 K to about 5,000 K with height as noted by Chitta, Smitha e Solanki (2020).

The chromosphere, around 3,000 km thick, experiences a temperature increase from approximately 5,000 K to an average of 500,000 K with height (BOHM-VITENSE, 1984). The corona, the outermost layer, has a temperature of 10^6 K (JR, 1967). Its outer boundary is not well defined, merging with the interplanetary medium, and is visible during a total eclipse as highlighted by Wang et al. (2007).

The Sun's magnetic field arises from the movement of its plasma, with magnetic field lines accompanying the flow of solar material. This phenomenon, known as magnetic field line freezing, underscores the close connection between solar plasma motion and magnetic field dynamics (NANDY et al., 2023). A comprehensive understanding of solar dynamics depends on a deep understanding of solar magnetism. In fact, it is widely acknowledged that all solar activities stem from the presence and behavior of magnetic fields on the Sun, as indicated by Stix (2004), which is essential in influencing key solar phenomena such as sunspots, CMEs, and the solar wind.

2.1.2 Sunspots and Solar activity cycle

Sunspots are regions on the photosphere typically around 10,000 km in diameter that appear darker because they are cooler than their surrounding areas (CHITTA; SMITHA; SOLANKI, 2020). This cooling effect results from the strong magnetic fields associated with sunspots, which inhibit energy transfer by convection from the inner layers of the Sun. The central region of a sunspot, known as the umbra, has temperatures around 4000 K and magnetic field strengths of ≈ 0.3 T, with perpendicular field lines extending from it (ZAGAINOVA et al., 2022). Surrounding the umbra is the penumbra, characterized by a radial structure of dark and light filaments, where more horizontal field lines emerge.

Sunspots often appear in groups and can persist for up to two solar rotations. They are classified based on polarity (unipolar and bipolar), size, complexity, and the presence or absence of a penumbra. The Zurich magnetic classification system provides a formula for calculating the number of sunspots, expressed as $R = k(10g + f)$, where R represents the number of sunspots (ranging from 0 to 200), k is a correction factor accounting for differences among observatories (typically around 1), g is the number of sunspot groups, and f is the number of individual sunspots (ABD; MAJED; ZHARKOVA, 2010; KIL et al., 2011). The sunspot number follows an $\approx$ 11-year cycle, with the solar maximum characterized by a peak in sunspot number and a corresponding increase in solar activity, including more frequent solar eruptions (COWLEY, 1973; HATHAWAY, 2015; LEAN, 2010; VALIO et al., 2020).

A notable minimum in sunspot number, known as the Maunder Minimum, occurred from approximately 1650 to 1720. The magnetic fields of sunspots in opposite hemispheres exhibit reverse polarities, which invert every 22 years, as described by Hale (1924). Sunspots migrate across different latitudinal zones throughout the solar cycle. At the beginning of each cycle (solar minimum), sunspots appear around 40° away from the solar equator and gradually move towards it as the cycle progresses as noted by Das (1958), Makarov e Sivaraman (1989), Moore e Rabin (1985).

The well-known 11-year solar activity cycle is characterized by fluctuations in the Sun's average radiation intensity, including an increase in solar irradiance of approximately 0.07% in the solar maximum, as reported by Subedi, Adhikari e Mishra (2017), with peaks and troughs occurring roughly every 11 years. During periods of maximum solar activity (solar maximum), levels of ultraviolet solar radiation and atomic oxygen density are higher compared to periods of minimal solar activity (solar minimum). These conditions lead to elevated electron densities and reduced temperatures in the upper atmosphere (ABDU et al., 1995; KELLEY, 2009; ABDU et al., 2009; BATISTA et al., 2006). The increased electron densities during solar maximums result from higher production rates, while the lower temperatures are due to the inverse relationship between density and electron temperature. Figure 1 shows sunspots and solar activity over the last three cycles.

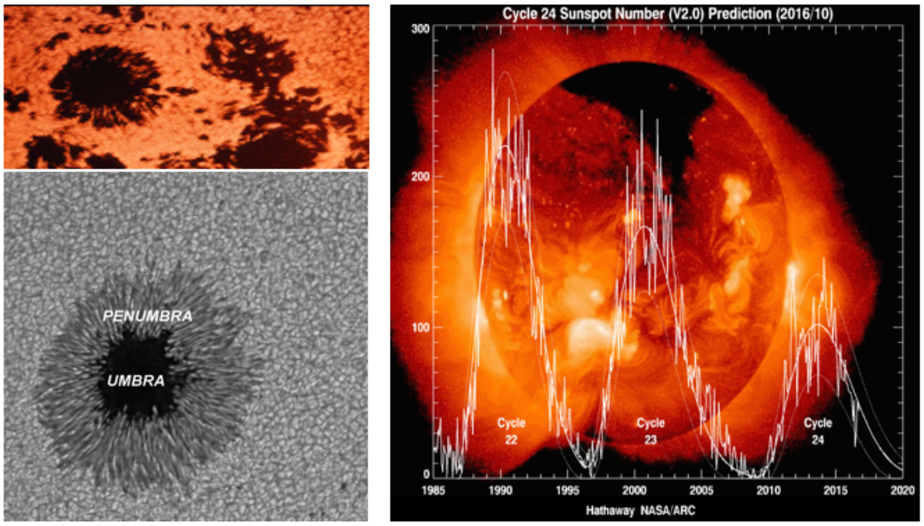
(a) Sunspot

(b) Solar cycle

Figure 1 – A image of sunspot and last three cycles of solar activity.
Source: Hathaway (2015)

At solar maximum, the Sun's magnetic field lines exhibit significant distortion due to differential rotation, where low latitude regions rotate faster than polar regions. This phenomenon contributes to the prominence of CMEs, which are eruptions of solar material observed emanating from the Sun's surface (MARIČIĆ et al., 2020). In contrast, the solar minimum, which marks the period of low solar activity within the 11-year solar cycle, is characterized by a notable decrease in sunspot and solar flare activity. During this phase, CMEs become less frequent, while coronal holes, which tend to be more prevalent, extend or migrate towards lower solar latitudes, increasing their geoeffective impact (GONZALEZ et al., 1994).

2.2 The solar drivers and their features

This section presents a review of past studies and their connections with solar activity. Solar activities from the Sun generate several disturbances, including coronal mass ejections, corotating interaction regions, solar energetic particles, and sunspots.

Solar eruptions, such as CMEs and coronal holes, release plasma into interplanetary space. The dynamics of these solar events differ based on their interactions, as observed ICMEs and CIRs respectively (MOUIKIS et al., 2019). However, both ICMEs and CIRs cause geomagnetic events that manifest in various forms of geomagnetic activity, including ring current, aurora, convection, and radiation belts (BOROVSKY; DENTON, 2006).

Borovsky e Denton (2006), Bargatze, McPherron e Baker (1986) highlighted that the value of v$\vec{B}$s of the solar wind, where v represents the solar wind speed and Bs indicates the southward component of the interplanetary magnetic field (in GSM coordinates), are factors driving geomagnetic activity. The morphology and strength of the magnetic field, the temporal profile of the velocity v, the durations of the v$\vec{B}$s drivers, and the presence of shocks, among other factors, exhibit variations (GONZALEZ; TSURUTANI; GONZALEZ, 1999; GONZALEZ et al., 2011).

ICMEs are eruptions of plasma and magnetic fields from the solar corona, traveling at speeds ranging from 250 kilometers per second (km/s) to nearly 3000 km/s (DEVRIESE, 2011). These eruptions occur when magnetic field structures, known as flux ropes, become highly twisted in the Sun's lower corona, resulting in stress and realignment into a less intense configuration through the magnetic reconnection process. Alternatively, CMEs can occur when denser plasma becomes trapped by magnetic flux stretching into the inner corona, forming filaments and prominences (GONZALEZ; TSURUTANI; GONZALEZ, 2002).

ICMEs have the potential to generate shock waves and accelerate charged particles, thereby increasing the intensity of radiation storms (WEBB; HOWARD, 1994; MANN; O'BRIEN; MILLING, 2004; GOPALSWAMY et al., 2004). These geomagnetic storms are driven by factors such as interplanetary shocks, the intense magnetic field within the sheath region, and the magnetic field associated with the ejecta. The occurrence pattern of CMEs is irregular, with high speeds typically observed during solar maximum periods and a relatively short recovery phase. Storm commencements are often attributed to strong interplanetary shocks as highlighted by Iucci et al. (1988), Russell et al. (1992). ICME-driven storms are characterized by denser plasma sheets, stronger ring currents, large Dst perturbation magnitudes, increased energetic particles in the radiation belts, intense auroras, and induced currents (BOROVSKY; DENTON, 2006).

CIRs-driven storms are another significant phenomena that occurs when fast solar wind streams, originating from coronal holes, interact with slower streams, creating a narrow region of compressed plasma in interplanetary space known as a CIRs. The source area, coronal holes, appears cooler than the surrounding plasma, with less density and open regions displaying unipolar magnetic fields, observed as dark regions in extreme ultraviolet (EUV) and soft X-ray solar images. These events are predominantly observed during the declining phase and persist for 27-day periods during years of low solar activity (KILPUA et al., 2017).

As noted by previous researchers, such as Jian et al. (2006), solar wind originating from coronal holes often result in compressed plasma at their leading edges, referred to as CIR-driven storms. These storms typically occur during the late declining phase of the solar cycle (GONZALEZ; TSURUTANI; GONZALEZ, 1999; GONZALEZ et al., 2011; YERMOLAEV; YERMOLAEV, 2002; RICHARDSON; CLIVER; CANE, 2001; RICHARDSON; CANE; CLIVER, 2002).

In addition, Venkatesan e Zhu (1991) highlighted that, CIR-driven storms are characterized by long recovery phases, moderate Dst perturbations, gradual sudden commencements, hotter plasma sheets, and higher fluxes of relativistic electron generation. Table 2 presents a brief comparison between CME-Driven Storms (Shock, Sheath, Ejecta, Cloud) and CIR-Driven Storms (CIRs, High-Speed Stream). In the heliosphere, these storms are large-scale structures predominantly found in the declining phase of the solar cycle, as noted by Balogh et al. (1999).

CIRs have the capability to generate shocks, which can accelerate energetically charged particles, as discussed by Lario e Roelof (2007). This is associated with recurrent geomagnetic activity, ultimately enhancing the intensity of non-recurrent geomagnetic storms, as indicated by Gosling et al. (1991a). Moreover, there is a perception among researchers that CIR phenomena may become accessible to physics-based prediction in the foreseeable future, as suggested by Riley, Linker e Mikić (2001). Therefore, the study of CIRs remains relevant.

Geomagnetic storms lead to disturbances caused by the substantial transfer of energy from the solar wind to the space environment (GONZALEZ et al., 1994). These disturbances are caused by variations in the solar wind's currents, plasmas, and fields within Earth's magnetosphere. A geomagnetic storm occurs following a ICMEs when the orientation of the Interplanetary Magnetic Field (IMF) $\vec{B}z$ changes from northward to southward (GONZALEZ et al., 1994). This change can last for hours and results in a reconnection with Earth's magnetic field (DUNGEY, 1961).

Conversely, coronal holes are noteworthy phenomena observed during the declining phase of solar activity. They emit high-speed solar wind streams, usually exceeding 750-800 km/s, which interact with slower solar wind streams, traveling at around 300-400 km/s, near the ecliptic plane. This interaction leads to the creation of region characterized by strong magnetic fields, termed CIRs (TSURUTANI et al., 2005). CIRs storms are typically

Table 2 – Comparison of CME-Driven and CIR-Driven Storms

Phenomenon	**CME-Driven Storms**	**CIR-Driven Storms**
Phase of the solar cycle when dominant	solar maximum	declining phase
Occurrence pattern	irregular	27-day repeating
Calm before the storm	sometimes	usually
Solar energetic particles (SEP)	sometimes	none
Storm sudden commencement (SSC)	common	infrequent
Mach number of the bow shock	moderate	high
β of magnetosheath flow	low	high
Plasma-sheet density	very superdense	superdense
Plasma-sheet temperature	hot	hotter
Plasma-sheet O^+/H^+ ratio	extremely high	elevated
Spacecraft surface charging	less severe	more severe
Ring current (Dst)	stronger	weaker
Global sawtooth oscillations	sometimes	no
ULF pulsations	shorter duration	longer duration
Dipole distortion	very strong	strong
Saturation of polar-cap potential	sometimes	no
Fluxes of relativistic electrons	less severe	more severe
Formation of new radiation belts	sometimes	no
Convection interval	shorter	longer
Great aurora	sometimes	rare
Geomagnetically induced current (GIC)	sometimes	no

Source: Borovsky e Denton (2006)

categorized as having low to moderate intensity because the z component of the Geocentric Solar Magnetospheric (GSM) magnetic field within the CIRs exhibits rapid flatuations, as noted by Tsurutani et al. (1995).

2.2.1 The solar wind (SW)

The solar wind is a stream of plasma primarily composed of charged particles, such as electrons and protons, emitted from the upper atmosphere of the Sun. The interplanetary medium is permeated by these fields and particles, originating mainly from the solar wind, along with the embedded interplanetary magnetic field (IMF). Fernández (2005) noted that the understanding of the dynamic phenomena of the solar wind in interplanetary space originated from observations of comet tails in the 1940s and 1950s. Brandt (1961) proposed the existence of a plasma flow with variable velocity based on the observed structure of comet tails. Nevertheless, Parker (1958) had previously developed the first successful SW model, which predicted a continuous high-speed solar wind using hydrodynamic theory. This model was further validated by observations from the Helios 1 and Helios 2 spacecraft between 1974 and 1976 (STIX, 2004).

According to Hundhausen (1970), charged particles from the solar wind gradually emanate outward from the solar corona, forming a supersonic wind. These particles escape the gravitational influence of the Sun due to their high kinetic energy and the corona's high temperature. In situ observations by spacecraft have reliably shown that the solar wind primarily consists of protons, electrons, and a small quantity of alpha particles (α particles, or H^+). The solar wind travels at supersonic speeds, with an average velocity of approximately 400 km/s, reaching Earth from the Sun in about four days.

The velocity and density of the SW exhibit significant fluctuations while maintaining a constant particle flux. Schwenn (1990) identified two main types of solar wind: fast and slow. Additionally, Tsurutani et al. (2006) categorized SW into three basic flow types: the background (slow) solar wind emerging from coronal helmet streamers, and high-speed solar wind, which often triggers geomagnetic disturbances during the descending phase of the solar cycle (GOPALSWAMY, 2009; TSURUTANI et al., 2006; TSURUTANI et al., 1999; GOPALSWAMY et al., 2004).

The fast solar wind is characterized by features such as low density compared to the slow solar wind, high variability, and turbulence. These fast wind streams originate from higher heliographic latitudes, while the slow component of the solar wind originates at low latitudes within the equatorial belt or Streamer during the minimum of the 11-year solar cycle (TSURUTANI et al., 2006; GOPALSWAMY et al., 2004; GOPALSWAMY, 2009). The fast solar wind, typically originating from coronal holes, can significantly impact geomagnetic conditions on Earth (GONZALEZ; TSURUTANI, 1987; KLAUSNER et al., 2021; ECHER et al., 2011; TSURUTANI et al., 2006; HAJRA et al., 2014).

2.2.2 Coronal Hole (CH)

Coronal holes are prevalent during the declining and solar minimum phases of solar activity, emitting HSSs that traverse the interplanetary medium at speeds of 500–800 km/s (TSURUTANI et al., 2006). These coronal holes are characterized by dark, low-density regions in the corona and behave as collisionless plasma in the outer solar atmosphere. During more active periods of the solar cycle, coronal holes can exist at all solar latitudes but may persist for only several solar rotations before evolving into different magnetic configurations (BATISTA et al., 2006).

Their measurement can be based on various criteria: firstly, from the darkest blotches on the solar surface; secondly, from the lowest-intensity regions observed during a total solar eclipse or with an occulting coronagraph, as mentioned by Cranmer (2009) and thirdly, based on a theory matching all open-field ends from solar winds within a steady timeframe. During periods of solar minimum, the magnetic field is dominated by rotationally-aligned dipole components, with a coronal hole often covering the north and south polar caps of the Sun (CRANMER, 2009; HEWINS et al., 2020; WEBB; DAVIS; MCINTOSH, 1984; KOSUGI; ISHIGURO; SHIBASAKI, 1986). Coronal holes, as indicated in figure 2, are associated with the acceleration of the solar wind, which can impact Earth's magnetosphere and potentially cause geomagnetic storms, such as those driven by CIRs or HSSs (TSURUTANI et al., 2006; ECHER et al., 2011; GONZALEZ; TSURUTANI, 1987; KLAUSNER et al., 2021; PRESTES et al., 2017; TSURUTANI et al., 1995; BOROVSKY; DENTON, 2006).

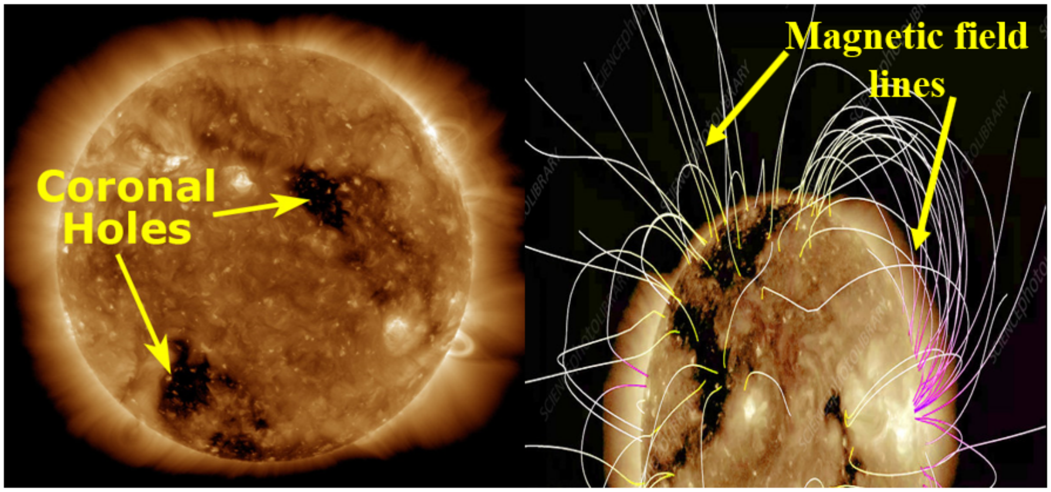

Figure 2 – The source region of HSS (Coronal Holes) and Magnetic field lines flowing into interplanetary space.
Source: Harvey e Jr (1979)

According to Cranmer (2009), the study of coronal holes is significant for several reasons: (i) their low-density state allows for the easy study of collisionless kinetic processes, (ii) coronal holes and their associated HSS are responsible for CIRs geomagnetic storms, and (iii) their ambient, time-steady state nature facilitates theoretical modeling.

2.2.3 Coronal Mass Ejections (CMEs)

Coronal Mass Ejections are massive eruptions of plasma, typically ranging from 10^{12} to 10^{13} kilograms, expelled from the Sun. These eruptions form extensive arcs that expand into space at speeds ranging from hundreds to several thousand kilometers per second. Shock waves associated with CMEs usually reach Earth within ≈ 2 days (SCHWENN, 1986). They are caused by intensifications in particle flux, which develops into solar wind. Approximately half of CMEs are believed to be associated with eruptive prominences, although the exact source of their initiation remains unclear (LUGAZ, 2015; GRECHNEV; KUZMENKO, 2020; CHEN, 2011). CMEs were initially discovered on December 14, 1971, using the white-light coronagraph aboard NASA's seventh Orbiting Solar Observatory (OSO 7), and they were definitively identified in 1973 (YASHIRO et al., 2004). Since then, various missions, including the Solar Maximum Mission (SMM), Yohkoh, Solar and Heliospheric Observatory (SOHO), Transition Region and Coronal Explorer (TRACE), and Solar Terrestrial Environment Observatory (STEREO), have enabled reliable observations, providing detailed information about the morphology and properties of CMEs (MIKIĆ; LEE, 2006).

Since 1996, coronagraphs (C1, C2, and C3) aboard the LASCO instrument on SOHO have been operational, detecting over 10,000 CMEs during Solar Cycle 23 (GOPALSWAMY et al., 2012; CYR et al., 2000). The source region of CMEs is typically an active region on the Sun, often corresponding to sunspots. According to Low (2001) CMEs eruptions are associated with a large-scale reconfiguration of the coronal magnetic field, playing a crucial role in magnetic polarity reversal over the solar cycle.

The structure of a typical CMEs is divided into three parts: the leading bright edge (or frontal rim), the void (or dark cavity), and the bright core, also known as a prominence (UWAMAHORO, 2011). This prominence-corona structure suggests that CMEs morphology is rooted in the pre-eruption magnetic field configuration. The frontal edge marks the leading boundary of the erupting structure, while the cavity represents a large magnetic flux rope filled with low-density plasma, which appears as dark regions in coronagraph images (BIESECKER et al., 2002).

Figure 3 illustrates the eruption of CMEs, detected by analyzing coronagraph data capturing Thomson-scattered photons within plasma structures moving outward. Additionally, Table 3 presents a summary of CMEs features as described by Gopalswamy (2009).

Table 3 – The main features of Coronal Mass Ejections

Property	Range	Average
Speed	20 km/s to $>$ 3000 km/s	470 km/s
Mass	10^{12} g to $> 10^{16}$ g	4×10^{14} g
Kinetic energy	10^{27} erg to 10^{33} erg	5×10^{29} erg
Angular Width	$< 5°$ to 360°	54°
Daily Occurrence rate	$<$ 0.5 to $>$ 6 CMEs	Solar min - solar max

Source: Gopalswamy (2009)

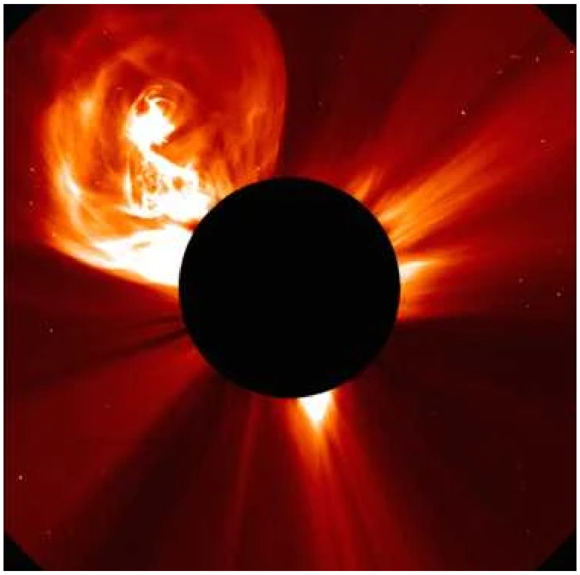

Figure 3 – An image from SOHO/LASCO C2 coronagraph on 4th January 2002 depicting the coronal mass ejection.

Source: Green et al. (2018)

2.2.4 Corotation interaction Region (CIRs)

Krieger, Timothy e Roelof (1973) noted that coronal holes are open magnetic structures in the solar corona that emit high-speed solar wind streams. These holes are recognized as sources of high speed solar wind (750-800 km/s), exceeding the typical solar wind velocities of less than 500 km/s, while coronal streamers are identified as sources of low solar wind. When fast solar wind streams intersect with slower streams, an interface region or interaction region is formed. This generates shock waves and intense magnetic fields that rotate with the Sun (TSURUTANI et al., 2006).

Gosling et al. (1991a) highlighted that at large heliocentric distances, these streams form an interface region bounded by fast forward and fast reverse shocks. Coronal holes may persist beyond a single solar rotation, facilitating the reappearance of HSS from the same area within a solar rotation, leading to recurrent streams. The configuration created by these streams takes the form of spirals, which are distorted by solar rotation. This distortion leads to the formation of an interaction region with slower streams, known as a CIRs, as shown in Figure 4.

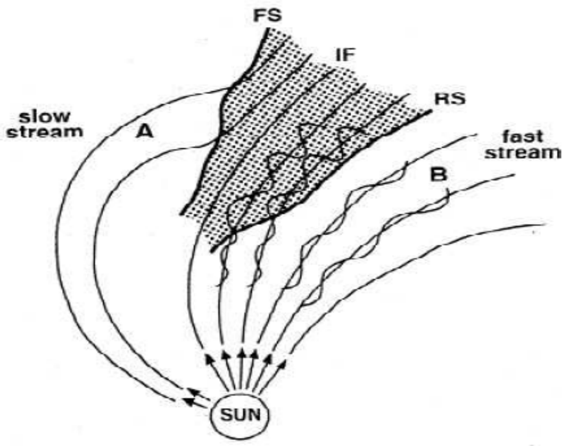

Figure 4 – The formation of a CIRs is depicted in the schematic diagram, (A) and (B), illustrating the interaction between a slow-speed stream and a high-speed stream. The shaded region represents the CIR, with FS, IF, and RS denoting the forward shock, interface surface, and reverse shock, respectively.
Source: Kamide et al. (1998)

2.2.5 Interplanetary coronal mass ejection (ICMEs)

After a CMEs erupts from the solar corona, it takes about one to three days for its interaction with the solar wind to reach Earth's magnetosphere. Within the heliosphere, CMEs manifest as plasma and magnetic field structures in the interplanetary medium, referred to as ICMEs, as highlighted by Gosling et al. (1991b). ICMEs are characterized by low plasma beta, smooth field rotation, strong magnetic fields, and regions with lower than usual solar wind proton temperatures (NIEVES-CHINCHILLA et al., 2018; KILPUA et al., 2017; GOOD et al., 2023). Occasionally, ICMEs can generate shock waves and large southward IMFs, which can cause geomagnetic perturbations such as geomagnetic storms, disrupting power grids and satellite operations, and producing spectacular auroras at high latitudes. Therefore, understanding the propagation of ICMEs is essential for forecasting such events (GOSLING et al., 1991a). Figure 5 depicts a schematic representation of an ICMEs.

Heliospheric images containing ICMEs structures have been extensively studied by instruments such as the Solar Mass Ejection Imager (SMEI), which tracked over 300 ICMEs during its 6-year operational period starting in February 2003 (HARRISON et al., 2010). However, observations of ICMEs date back to the late 1970s and early 1980s with the zodiacal light experiments aboard the Helios spacecraft as noted by Jackson et al. (2010), Tucker-Hood et al. (2015). Over the past two decades, several spacecraft, including NASA's WIND mission and others following the Interplanetary Monitoring Platform (IMP) series, have detected interplanetary signatures of CMEs in the solar wind.

ICMEs have been identified as flux rope formations that remain magnetically linked to the Sun while being transported outward by the solar wind (BURLAGA, 1988; KUMAR; RUST, 1996; BOTHMER; SCHWENN, 1997). Additionally, ICMEs can become disconnected from the Sun and transform into plasmoids, as suggested by Vandas et al. (1993). These two potential structures of ICMEs have been extensively discussed and documented in the literature (GOPALSWAMY, 2009; BOTHMER; SCHWENN, 1997; BURLAGA, 1988).

ICMEs are referred to as driver gas, ejecta, and plasma clouds when originating from the Sun's closed field region (TSURUTANI et al., 1988). Moreover, according to Webb et al. (2009), the structures of ICMEs and associated shocks interact with Earth's magnetosphere, inducing moderate to severe geomagnetic storms through magnetic reconnection (GONZALEZ et al., 2011).

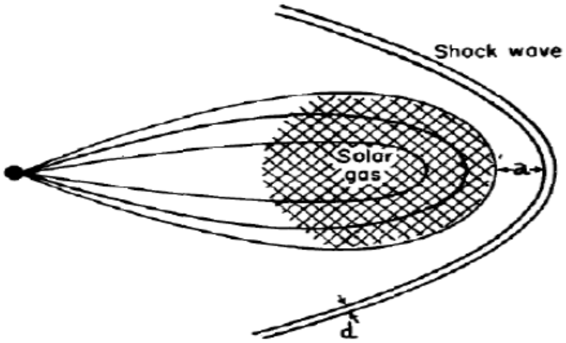

Figure 5 – The structure of an ICME is illustrated in the schematic diagram.
Source: Gopalswamy (2009).

During coupling interaction, the Earth's magnetosphere is distorted by supersonic ionized plasma eruptions, formed by the interaction of the solar wind with Earth's magnetic field (see Figure 6). Davies (1990) mentioned that the magnetosphere extends in a long tail opposite to the direction of the Sun.

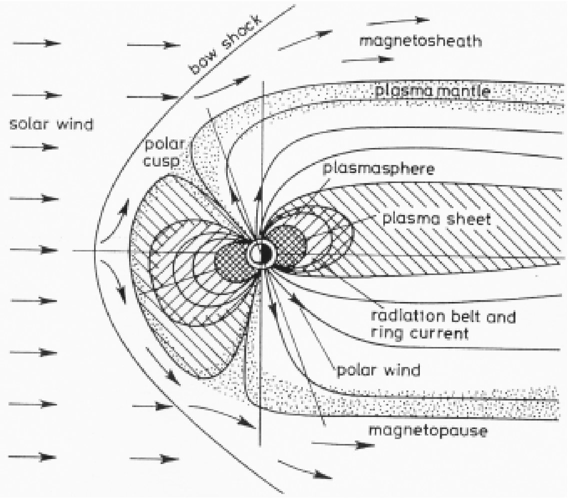

Figure 6 – The reconnection process of magnetic field (IMF) and geomagnetic field
Source: Davies (1990)

The ring current is sufficiently strong to quantify the storm time Dst index (GONZALEZ et al., 1994) which is carried mainly by energetic ions trapped by the geomagnetic field lines and undergo an azimuthal drift (DAGLIS et al., 1999). The forces due to the curvature and gradient of the Earth's magnetic field (GANUSHKINA; LIEMOHN; DUBYAGIN, 2018) influence the energetic particles in the inner magnetosphere on the nightside. The force turns to drift the proton westward from nightside toward dusk and the electron to drift eastward from nightside towards dawn and the effect is noticed in the ring current encircling the Earth westward (KAMIDE; CHIAN, 2007).

The momentum and energy from the solar wind create an intensification of the convection electric fields and in effect, enhance the particle precipitation and currents in the high-latitude ionosphere. The magnetospheric shielding layer is ineffective in shielding magnetospheric electric fields during magnetically disturbed periods that penetrate directly and dominate the low latitudes.

The increase in ionospheric conductivity, Joule heating, and ion drag in the upper atmosphere of high latitudes impacts the structure and dynamics of the thermosphere and ionosphere. The westward electric field, resulting from disturbance dynamo, can remain for up to 30 hours after the end of the storm's main phase.

Within Earth's magnetosphere, the movement of plasma, primarily composed of protons and electrons, is largely influenced by the magnetic field. The shape of magnetic flux lines is elongated on the opposite side due to the influence of the solar wind. The magnetosphere spans from approximately 1000 km (ionosphere) to the magnetopause, where the magnetic field governs the movement of plasma (RUSSELL, 1972). This magnetospheric cavity contains the magnetosphere. On the side facing the Sun, it extends to approximately $10R_E$, while on the anti-solar side, it forms a cylindrical shape with a long extension (up to $60R_E$) known as the magnetospheric tail (KELLEY, 2009). The geomagnetic field strength near the equator, at the Earth's surface, is approximately 3.1×10^{-5} Tesla. However, as the field lines extend farther from the Earth, the field weakens while remaining sufficiently strong to shield the Earth from the solar wind force. Approximately $10R_E$ away from the Earth on the dayside, the solar wind exerts pressure on the magnetosphere, forming a boundary known as the magnetopause. This boundary separates the regions of the interplanetary magnetic field from the region of the geomagnetic field. The high-speed impact of the solar wind on the magnetosphere causes a shock wave to form in the sub-solar region (AKASOFU, 2011).

The magnetosheath, a region of significant turbulence following the shock wave, serves as a transitional region between the shock wave and the magnetosphere itself (KELLEY, 2009). The polar cusp is a region where plasma from the magnetosheath has direct access to the ionosphere as seen in Figure 6, regardless of whether the interplanetary magnetic field (IMF) is oriented southward or northward. In a non-reconnected magnetosphere, the size of the Polar cusp depends on the shape of the magnetopause.

When magnetic reconnection occurs in the magnetosphere, triggering a geomagnetic storm, it alters the position of the polar cusp. This shift facilitates the direct penetration of charged particles from the external solar wind environment into Earth's magnetosphere. The plasma sheet, also referred to as the neutral sheet, is an unstable region characterized by intense electrical currents. In areas with open magnetic field lines connecting the polar regions to the magnetospheric tail, charged particles can precipitate into the upper atmosphere, giving rise to phenomena such as polar auroras (SCHULZ, 1991).

2.3 Geomagnetic storms

The interaction between the Sun and Earth leads to magnetic disturbances such as geomagnetic storms and other phenomena like HILDCAA (GONZALEZ et al., 2006). During this interaction, complex magnetospheric current systems are established, primarily composed of magnetopause current, tail current, ring current, and field-aligned current (ANTONOVA et al., 2018). The magnetopause current is primarily identified by the presence of the bow shock, a shock wave standing in the supersonic solar wind flow in front of the magnetosphere. Considerable changes in solar wind characteristics, including plasma density, flow velocity, and magnetic field strength, are observed across the bow shock. As electrons and protons penetrate the magnetopause, they experience bending from their trajectories due to the Lorentz force, resulting in gyration in opposite directions around the magnetic field lines.

According to Baumjohann et al. (2010) and Gombosi (1998) the varying gyro-radii of protons and electrons contribute to the formation of the magnetopause current, also known as the Chapman-Ferraro current. However (GOMBOSI, 1998) further explains that terrestrial dipole fields are prevented from penetrating the solar wind, thereby influencing the magnetic field outside the magnetopause and leading to an increase in the current system's strength inside.

The magnetosphere contains a significant amount of plasma and energy, particularly within the geomagnetic tail, leading to disturbances in the geomagnetic field as it interacts with the inner magnetosphere. This tail consists of two distinct parts: the northern lobe, facing Earth's northern hemisphere, and the southern lobe, extending outward from Earth's southern hemisphere, separated by a plasma sheet.

These lobes exhibit opposite orientations to the magnetic field, as observed in Baumjohann et al. (2010). The magnetotail's current system divides it into two adjacent hemispheres with contrasting magnetic field polarities, driven by dawn-dusk-directed neutral sheet currents, as discussed in Alexeev (1986). Variations in the geomagnetic field are linked to the behavior of the ring current. This westward-flowing electric current, known as the ring current, contributes to the weakening of the geomagnetic field at distances from 4 to 9 Earth radii (R_E), according to Daglis et al. (1999).

According to Daglis (2006) positive ions, with energies ranging from around $\approx$ 1 keV, undergo an azimuthal drift, generating a current that counters the primary geomagnetic field. This current consists partly of ions that have direct convective access to low L-values (near Earth's radius) and partly of higher-energy ions that follow closed drift paths, gradually migrating inward under the influence of oscillating electric and magnetic fields, as outlined by Kozyra e Liemohn (2003).

The penetration of positive ions from the supersonic solar wind and the Earth's ionosphere into the inner magnetosphere creates electric fields linked to the intensification of magnetospheric activity or substorms. This current has minimal impact during quiet periods but significantly affects geomagnetic disturbances, producing a magnetic field countering Earth's horizontal magnetic field. The strength of the ring current is assessed by measuring the reduction in Earth's surface magnetic field, caused by the accumulation of charged particles drifting in the magnetosphere. The field-aligned current, following magnetic field lines, connects the magnetosphere with the ionosphere, fostering strong coupling between these two regions.

This coupling is directly affected by solar wind and the IMF. Physical phenomena such as magnetic reconnection, acceleration of field-aligned currents, auroral activities, and plasma convection are linked to field-aligned currents. Throughout the coupling process between the magnetosphere and ionosphere, a significant amount of energy is deposited in the polar regions. This energy is quantified as a polar cap potential parameter. The effects of space weather on Earth are primarily due to geomagnetic disturbances. However, the main focus is on understanding their origin, which stems from the interaction between the Sun and Earth. This interaction leads to events like solar flares and CMEs. The concept of Earth as a large magnet was first proposed in 1600 by A. D. William Gilbert, as documented by Lakhina et al. (2012). This hypothesis led to the development of geomagnetism, enabling navigation. In the eighteenth century, Edmund Halley created the primary map of magnetic field declination. These maps assisted Alexander von Humboldt in recording local magnetic declination in Berlin every half hour from midnight to morning, spanning from May 1806 to June 1807. During a magnetic storm in December 1806, von Humboldt observed a significant magnetic deviation for six hours and noted the presence of northern lights (aurora) overhead. He concluded that magnetic disturbances on the ground and auroras in the polar sky were linked to the same phenomenon. On the night of December 21, 1806, he termed this phenomenon "Magnetische Ungewitter" or magnetic storm (LAKHINA; TSURUTANI, 2016).

Schröder (1997) noted that "magnetic storms" were recognized as phenomena by the global network. Independent studies on geomagnetic activities and solar activity, including sunspot observations, were conducted in the early nineteenth century. In 1851, Lamont reported a variation of magnetic declination close to $\approx$ 10-11 year solar cycle periodicity on a daily basis at the Munich Observatory. However, this variation was linked to the sunspot cycle, as stated by Lamont (1866) and Schröder (1997).

Geomagnetic activity was then investigated and found to correlate with the sunspot cycle, initially by Sabine (1851) and Sabine (1852). This discovery led to the establishment of a connection between geomagnetic activity and sunspots. According to Rostoker, Lam e Hume (1972) and Menvielle e Berthelier (1991), geomagnetic activity is categorized based on summaries of the K index, a scale ranging from 0 to 9, which reflects the magnitude of magnetic disturbances observed in each 3-hour interval of universal time. According to Gonzalez et al. (1994) a magnetic storm occurs when significant energy within the magnetosphere-ionosphere system, as a result of a convection electric field, effectively enhances the ring current, allowing for the estimation of the storm-time Dst index.

The primary characteristic of a magnetic storm is a distinct decrease in horizontal intensity of the Earth's magnetic field followed by subsequent recovery [e.g., (JACOBS, 2016)].

Trapped magnetospheric particles undergo enhancement due to dynamics, leading to a decrease in the intensity of the Dst index (GONZALEZ et al., 1994). A geomagnetic storm is marked by a main phase during which the horizontal component of the Earth's phase-latitude magnetic fields is efficiently depressed over some time, followed a recovery that may last for several days. The development of the ring current is a defining feature of a magnetic storm, generating a magnetic field disturbance opposite in direction to the Earth's dipole field at the equator. The strength of this disturbance field is approximately described by the Dessler-Parker-Sckopke relationship (DESSLER; PARKER, 1959; SCKOPKE, 1966):

$$Dst^* \left(\frac{t}{B_o} \right) = \frac{2E\left(t\right)}{3E_m} \tag{2.1}$$

where, Dst^* is the decrease in the geomagnetic field associated with the ring current, B_o is the mean equatorial surface field, E(t) is the overall energy of the ring current particles, and E_m (= 8 x 10^{24} ergs) is the overall magnetic energy of the geomagnetic field outside the Earth. For a complete review, see Carovillano e Siscoe (1973). The Dst^* index is the measured Dst value after correction for magnetopause currents. It expresses the intensity of the ring current on an hourly basis, hence the estimation of geomagnetic disturbances is determined, either by (Dst) or Sym-H index which is a 1-Min estimate of the ring current intensity (IYEMORI, 1990). Both SYM-H and Dst indexes are the same, just that the SYM-H index has a high resolution as compared to Dst based on computerization (e.g. 1 min instead of 1 hour used for Dst). As observed in equation 2.1, the field decrease is linearly related to the overall energy of the ring current particles. The overall energy deposited into the inner magnetosphere is estimated via the Dst index which defines the magnetic storm intensity indicated by Gonzalez et al. (1994).

The general relationship of energy balance for the ring current is given by

$$\frac{dE(t)}{dt} = U(t) - \frac{E(t)}{\tau} \tag{2.2}$$

Where, $U(t)$ is the rate of energy input into the ring current and τ is the decay time. Using equation 2.1, equation 2.2 can be written in terms of Dst^* as

$$\frac{dDst^*(t)}{dt} = Q(t) - \frac{Dst^*(t)}{\tau} \tag{2.3}$$

and where, $Q(t) = 2.5 \times 10^{21}\, U(t)$ in Gaussian units.

When there is no energy input, as during the (ideal) recovery phase of the storm, equation 2.2 has the following simple solution:

$$E(t) = E_o e^{-\frac{(t-t_o)}{\tau}} \tag{2.4}$$

From this one can obtain reasonably accurate values for the decay time τ. A formal solution for equation 2.2, or equation 2.3, can be written as;

$$Dst^*(t) = e\frac{-t}{\tau}\left[Dst^*(t) + \int_0^t Q(Z)e\frac{z}{\tau}dz\right] \tag{2.5}$$

However, the results become much more significant when the analytical input function Q is known. Otherwise, the equation 2.2 must be computed numerically as mentioned by many authors (BURTON; MCPHERRON; RUSSELL, 1975; GONZALEZ; TSURUTANI, 1987). The development of geomagnetic storms has been considerably classified into the 'standard' type and the 'gradually commencing' type. Akasofu e Chapman (1963) noted intrinsic differences between solar streams that go beyond their pressure, depending on the type of geomagnetic storm development. The behavior of these intrinsic differences is currently unknown. In respect to standard type, features such as the storm's sudden commencement (SSC), a discontinuous increase in horizontal (H) component in the low latitude, and remaining in its initial level for some period are attributed to its sustained elevation for a period of time. (GONZALEZ et al., 1994). The initial phase is known as the positive phase and is followed by the growth rate as the main phase and characterized by a decrease in the H component, with greater magnitude compared to the initial phase. The recovery phase emerges when the H horizontal component recovers slowly from its minimum value. This happens due to the decay of the ring current as a result of charge exchange, wave-particle interactions, Coulomb collisions, and ring current energetic particle convection out of the magnetopause (LAKHINA; TSURUTANI, 2016).

As proposed by Lakhina e Tsurutani (2016) a geomagnetic storm is attributed to the ring current intensification, as a result of the depression in the H-component of the geomagnetic field. The gradually commencing type of geomagnetic type shows no evidence of sudden onset as compared to the standard type. Furthermore, Gonzalez, Tsurutani e Gonzalez (2002) indicated the initial, main, and recovery phases as the three phases of the geomagnetic storm. These phases are characterized by different time scales. These phases have different time scales. The initial phase happens when the solar wind ramps pressure as an interplanetary shock wave, and strikes the frontside magnetosphere. In the southward direction of the interplanetary magnetic field, IMF is marked as the storm's main phase onset and consequential associated with the enhanced magnetic reconnection. In addition, the decay of ring currents in the belt of energetic particles is applied to the recovery phase. A geomagnetic storm is classified into recurrent or non-recurrent. The recurrent storms occur every 27 days and mostly occur in the declining phase of the solar cycle. As mentioned by Gonzalez et al. (1994) and Tsurutani et al. (2001) they result from the interaction of low and high-speed solar wind streams co-rotating emanating from the coronal hole while non-recurrent geomagnetic storms happen most frequently near solar maximum, and are caused by fast interplanetary ICMEs (GONZALEZ et al., 2011).

Magnetic field undergo significant changes during storms, which are typically caused by increased solar wind activity. Its density can range from 10^6 to 10^7 m^{-3} particles per cubic meter, while its velocity can vary from 300 up to 900 or 1000 kms^{-1}. Aurora luminosity tends to rise during periods of disturbance. The increase in the velocity and density of the solar wind causes compression of Earth's magnetosphere on the side facing the Sun (the dayside), leading to an intensification of the geomagnetic field in that region.

2.3.1 Geomagnetic variations

As the geomagnetic field undergoes strong compression by enhanced solar wind pressure, the magnetic field strength at the magnetopause increases, causing its boundary—typically located near 10 terrestrial radii 6 (R_E) to contract inward to about 6 R_E (GONZALEZ et al., 1994). This sudden intensification of the magnetic field ($\vec{B}$) is referred to as a sudden storm commencement (SSC). However, SSCs are not always clearly visible in ground magnetograms, as their signatures may be weak or gradual. The variations associated with SSCs can be recognized by their characteristic shapes, which correspond to distinct storm phases illustrated in Figure 7.

The initial phase arises from the compression of magnetospheric field lines by the impinging solar wind. The main phase is characterized by a sharp decrease in the horizontal component of the geomagnetic field, primarily due to the intensification of the magnetospheric ring current system. Finally, the recovery phase represents the gradual return of the geomagnetic field to its quiet-time level. Minor perturbations during the main phase are attributed to secondary current systems, particularly polar electrojet activity and polar disturbances (PD), which are closely linked to substorm processes (CHAPMAN, 1918).

In addition to ring current dynamics, magnetospheric activity is also modulated by changes in thermospheric winds and ionospheric conductivities in the dynamo region. Auroral electrojets serve as critical channels of current, coupling field-aligned currents with the outer

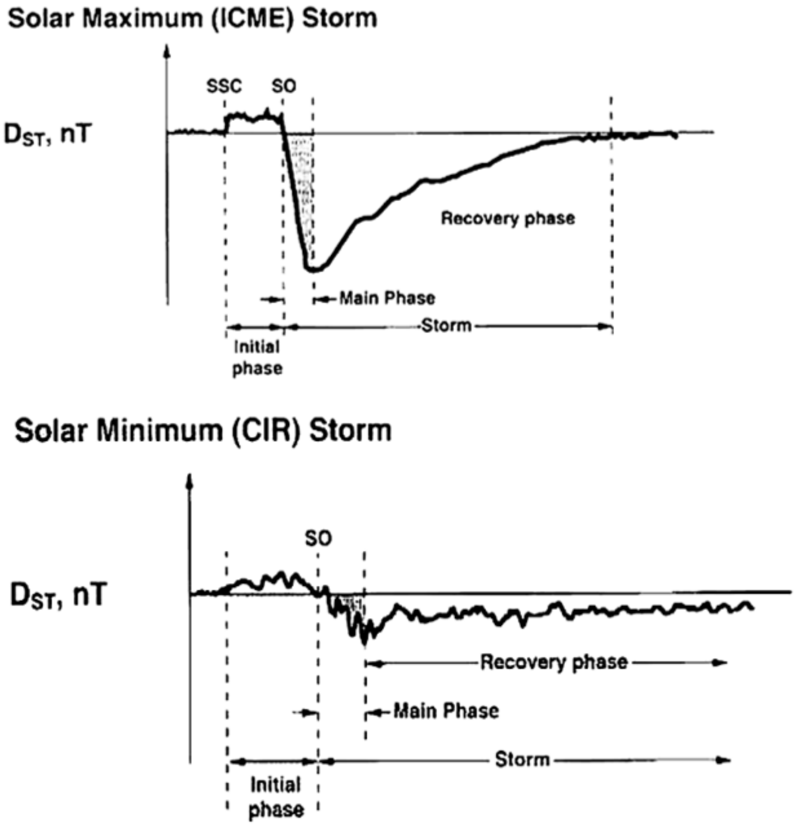

Solar Maximum (ICME) Storm

Solar Minimum (CIR) Storm

Figure 7 – Illustration of the phases of a magnetic storm.
Source: Tsurutani et al. (2006)

magnetosphere (BURESOVA et al., 2014). At low and mid-latitudes, magnetic perturbations observed on the ground are primarily driven by a combination of magnetopause currents, field-aligned currents, and the ring current system (RICHMOND, 2017). These current systems account for geomagnetic disturbances that can persist even during nighttime when ionospheric conductivity is minimal.

Daytime disturbances, on the other hand, are significantly influenced by the equatorial electrojet (EEJ), where disturbance electric fields penetrate effectively to low latitudes, amplifying perturbations near the magnetic equator (YAMAZAKI; KOSCH, 2015). Daily variations in geomagnetic activity are evident during both quiet and disturbed conditions but show only weak longitudinal correlation across widely separated stations (KANE, 1972). These longitudinal differences are largely attributed to variability in atmospheric tide propagation into the dynamo region from below (RICHMOND, 2017). Furthermore, strong modulations in geomagnetic activity during stratospheric sudden warming events have been linked to enhanced solar and lunar tidal influences (YAMAZAKI; KOSCH, 2015).

2.4 High-Intensity Long-Duration Continuous Auroral Electrojet Activity (HILDCAA)

The solar minimum and the declining phase of the solar cycle have garnered significant attention due to notable features such as CIRs and HSSs, along with the HILDCAA phenomenon, which have adverse impacts on Earth's environment. During this period, high-speed solar wind streams that form CIRs are accompanied by oscillating Alfvén waves (TSURUTANI et al., 1995; GONZALEZ; TSURUTANI, 1987; PARKS, 2019; KLAUSNER et al., 2021). These waves propagate parallel to the magnetic field lines within the plasma, arising from the interaction between the magnetic field and electric currents, causing ions to fluctuate as noted by Alfvén (1977), Tsurutani et al. (1999), Alfvén (1942) and Parks (2019). This fluctuation may result in shocks that enhance geoeffectiveness, leading to increased geomagnetic activity (ECHER et al., 2011; HAJRA et al., 2013; ALFVÉN, 1942; GUO et al., 2016).

According to Gonzalez e Tsurutani (1987), HILDCAA is a specific type of geomagnetic activity. This phenomenon was identified during the analysis of geomagnetic storms characterized by prolonged recovery phases, where the Dst index did not return to its usual values for days or even weeks (GONZALEZ; TSURUTANI, 1987; TSURUTANI et al., 1999; GONZALEZ; MOZER, 1974). Such activity occurs particularly during the declining phase of the solar cycle and differs from classical geomagnetic activities due to these extended recovery phases (KLAUSNER et al., 2021; TSURUTANI et al., 2001; GONZALEZ; TSURUTANI, 1987).

The main physical processes explaining the decay of the ring current include charge exchange between ions and neutrals, Coulomb collisions, ion convection through the magnetopause, and wave-particle interactions. These processes have time scales ranging from hours to just a fraction of days. According to Gonzalez e Tsurutani (1987), the HILDCAA phenomenon is characterized by four main criteria: (i) the AE index must reach or exceed 1000 nT at its peak intensity; (ii) the AE index should not fall below 200 nT for more than 2 continuous hours; (iii) the event must last at least 2 days; and (iv) the HILDCAA event should occur outside the main phase of geomagnetic storms, specifically during the recovery phase. This empirical characterization allows for the identification of HILDCAA events even if one or more of the criteria are not strictly met (GONZALEZ; TSURUTANI, 1987).

The fourth criterion aims to separate the mechanism responsible for a HILDCAA event from those that generate the main phase of a magnetic storm, as no known physical hypothesis can explain recovery phases lasting for days or weeks (GONZALEZ; TSURUTANI, 1987; KLAUSNER et al., 2021; PRESTES et al., 2017). Søraas et al. (2004), Klausner et al. (2021), Echer et al. (2011) explained that the prolonged recovery phase during a HILDCAA event is due to the injection of protons into the outer portion of the ring current, preventing its natural decay and delaying the recovery of the Dst index. The criteria proposed by Gonzalez e Tsurutani (1987) are quite restrictive to minimize the number of events to be studied, but the same physical process associated with a HILDCAA event may occur even if one or more of these criteria are not met (TSURUTANI et al., 1995; GONZALEZ; TSURUTANI, 1987). In addition to the traditional criteria, new criteria have been suggested. Koga et al. (2011), Prestes et al. (2017) propose the following additional criteria to identify a HILDCAA event: a moderate variation of the SYM-H index (not less than -100 nT), the presence of high solar speed streams, and a high-frequency oscillation of the Bz component of the IMF around zero, with amplitudes of ± 10 nT.

Prestes et al. (2017); Prestes et al. (2016) and Klausner et al. (2021) modified one of the HILDCAA criteria in order to identify HILDCAA* events. The HILDCAA* events are defined as follows: (1) AE peak values must exceed 1000 nT at least once during each event; (2) the event should last at least two days; (3) the AE values should never drop below 200 nT for periods longer than 4 hours at a time; and (4) HILDCAAs* must occur outside of the main phases of magnetic storms. Only main phases where Dst > -50 nT are disregarded from the HILDCAA* interval. According to Gonzalez e Tsurutani (1987) and Klausner et al. (2021) these criteria were imposed to illustrate the physical process related to the aforementioned solar energy transfer into the magnetosphere during HSSs, and therefore the physical process associated with HSS/CIR events (HSS + CIR and their combination) occurs even when one of the four HILDCAA criteria is not strictly followed.

The relationship between the HILDCAA phenomenon, AE index intensity, and the Alfvénic oscillations in the presence of the IMF-Bz is described by the expression:

$$\delta V_A = \frac{\delta B_z}{\sqrt{\mu_o n_i M_i}}$$

where δV_A is the speed of the Alfvén wave in the medium, δB_z is the IMF Bz fluctuation amplitude, μ_o is the magnetic permeability, and n_i and M_i are the ion density and mass, respectively (PARKS, 2019; ALFVÉN, 1942; ALFVÉN, 1977). These oscillations are more frequent and thus more commonly observed during the descending phase and solar minimum phases (KOZYRA et al., 2006; GUARNIERI, 2006; GONZALEZ et al., 2006).

According to Hajra et al. (2013), 94% of HILDCAA events, as defined by the criteria outlined by Gonzalez e Tsurutani (1987), are attributed to CIRs and HSSs, while the remaining events are caused by the passage of ICMEs. The geomagnetic perturbations observed during the descending phase and solar minimum result from the recurrent emergence of HSSs from coronal holes. These high-speed streams are characterized by highly fluctuating Alfvén waves and travel at velocities much greater than those of the solar wind. They interact with the slower solar wind streams, forming an interface region in the interplanetary medium known as CIRs, as highlighted by Tsurutani et al. (1995), contributing to the formation of HILDCAA activity.

Alfvénic fluctuations, as described by Alfvén (1942), represent continuous and weaker activity compared to geomagnetic storms. These fluctuations are a type of magnetohydrodynamic (MHD) motion in magnetic fluid plasma, characterized by rapid fluctuations where ions propagate along magnetic field lines, with the restoring force provided by magnetic tension (IWAI et al., 2003).

The phase velocity of Alfvén waves is estimated to be approximately 1200 km/s, decreasing to 50-70 km/s (ADHIKARI, 2015). According to (DAVIS; SUGIURA, 1966), AE index parameters are utilized to monitor auroral activities, reflecting the horizontal component of the perturbed magnetic field in the auroral zone. Tsurutani et al. (2004) suggested that HILDCAA is an independent phenomenon, differing mechanism from geomagnetic storms, particularly during their main phase, and may occur independently of geomagnetic storms. However, HILDCAAs often coincide with the recovery phase of geomagnetic storms, leading to moderate geomagnetic responses at low and medium latitudes, as discussed by Tsurutani et al. (2004), Gonzalez e Tsurutani (1987), Tsurutani et al. (2006) and Guarnieri (2006).

During HILDCAA events, it is noteworthy that the PPEFs and the disturbance DDEFs contribute to a combined ionospheric response, particularly during the prolonged recovery phase. The PPEFs results from the sudden reconfiguration of the magnetosphere due to solar wind pressure variations, leading to rapid changes in the electric field that penetrates into the ionosphere (HAJRA et al., 2013; SOBRAL et al., 2001). On the other hand, the DDEFs is generated by the enhanced thermospheric winds and ionospheric currents driven by geomagnetic activity (HAJRA et al., 2013; SOBRAL et al., 2006; GUARNIERI, 2006). The interplay between these electric fields causes significant ionospheric perturbations, as discussed by Yeeram (2019).

Sobral et al. (2006) presented evidence of the PPEFs during the ionospheric response to HILDCAA events. Disturbed dynamo electric fields and disturbed thermospheric winds exhibit characteristics similar to those observed during geomagnetic storms (ABDU et al., 1995; GUARNIERI, 2006). Wei et al. (2008) noted numerous instances of electric field penetrations into the equatorial ionosphere associated with HILDCAA phenomena. The dynamo action of thermospheric winds arises from auroral heating during storms, resulting in ionospheric disturbance dynamo effects (ABDU et al., 1995; SOBRAL et al., 2006). These winds alter the circulation patterns, generating disturbed ionospheric electric fields, particularly in low and middle latitudes, as described by Blanc e Richmond (1980). This process causes variations in thermospheric composition and densities (RICHMOND, 1979).

2.5 Magnetospheric and ionospheric dynamos effects on the Earth's ionosphere

Equatorial and low-latitude regions experience disturbances primarily induced by magnetospheric and ionospheric dynamo activities, along with geomagnetic active conditions. Prompt penetration electric fields occurs due to magnetospheric dynamics, influenced by ionospheric conductivity and magnetospheric plasma properties (BLANC; RICHMOND, 1980; JAGGI; WOLF, 1973). Magnetospheric dynamo activity, driven by the solar wind, converts its energy into electromagnetic energy through magnetic reconnection processes, intensifying the penetration of electric fields as the solar wind interacts with the planetary magnetosphere and ionosphere, resulting in various plasma motion patterns in the ionosphere.

According to Kelley (2009), internal currents generated by neutral winds and gravity, along with externally applied potentials, contribute to electric fields in the low and middle-latitude ionosphere. In the equatorial ionosphere, two main disturbance electric fields are observed: PPEFs and DDEFs, originating externally in the mid and low-latitude ionosphere of Earth. External electric fields propagate towards the equator along magnetic field lines due to the coupling between the ionosphere and inner magnetosphere, a phenomenon termed "penetration." However, the external source can be attributed to the outer magnetosphere or driven by the solar wind.

Nishida (1968) emphasizes the existence of the electric field penetration phenomenon between geomagnetic oscillations and interplanetary magnetic field (IMF) fluctuations within the north-south components. Jaggi e Wolf (1973) provides a theoretical explanation known as the "shielding" mechanism to describe prompt penetration, which is based on solar and magnetospheric processes. This mechanism considers charge accumulation in the ring current region or the Alfven layer. Wei et al. (2015) also discuss the origin of PPEFs and shielding electric fields based on polarization electric fields in the ring current region and convection electric fields in the outer magnetosphere, respectively. These electric fields exhibit opposite polarities that nullify each other. The terms "undershielding" and "overshielding" denote two degrees of electric field imbalance by the Alfven layer, as proposed by Kelley, Fejer e

Gonzales (1979). These concepts result in the influence of interplanetary electric field (IEF) on ionospheric electrodynamics in the low-latitude ionosphere during intense geomagnetic storms. The penetration of IEF is influenced by hot magnetospheric plasma, and its effect defines the origin of Region-2 field-aligned currents (FACs).

The southward incursion of the interplanetary magnetic field component (IMF Bz), associated with magnetospheric convection due to the reconnection process and an intensified dawn-to-dusk IEF, characterizes the undershielding phenomenon. This weakens the shielding layer, allowing the penetration of IEF into the inner magnetosphere and augmenting the calm ionospheric zonal electric field (dawn-to-dusk). Conversely, overshielding occurs when magnetospheric convection suddenly weakens due to the transition of the IMF from southward to northward.

As noted by Huang, Foster e Kelley (2005) the dusk-to-dawn electric fields are linked to shielding charges within the inner magnetosphere, generating an eastward electric field on the nightside ionosphere and a westward electric field on the dayside. The prompt penetration effects have been extensively studied by many authors (KELLEY; FEJER; GONZALES, 1979; GONZALEZ; TSURUTANI, 1987; TSURUTANI et al., 2004; VERKHOGLYADOVA et al., 2008; FEJER; SCHERLIESS, 1997). Wei et al. (2008) also demonstrated this phenomenon based on a comparison study of a 5-day-long HILDCAA event. The coupling between the magnetosphere and equatorial ionosphere during HILDCAA phenomena has been investigated by Sobral et al. (2006), Kelley (2009) highlighting that energetic particle precipitation alters the coupling process and dynamics of the thermosphere-ionosphere system, consequently modifying the electron density. According to Yeeram (2019) this modification can extend to low latitudes involving electric field disturbances, such as PPEFs and DDEFs. Electric fields play a significant role in the coupling between the solar wind and ionosphere during prolonged external driving mechanisms within HILDCAA intervals, as noted by Verkhoglyadova et al. (2013) and Negreti, Paula e Candido (2017). Their variations are attributed to the influence of the IEF and have been emphasized by Yeeram (2017) indicating variations of solar wind IEF as part of the contributing factor causing the change. Furthermore, the authors pointed out that PPEFs is the immediate response to a variation of IEF. Wei et al. (2008) stated that during certain periods, a penetration of the IMF Bz and IEF into the ionosphere can occur, allowing these fields to directly affect ionospheric conditions. Wei et al. (2008) also pointed out that the penetration of the electric field occurs mainly when IMF Bz fluctuates between the southward and northward direction. The dayside positive ionospheric storm is attributed to PPEFs as said by Tsurutani et al. (2004) and Tsurutani et al. (2008).

Figure 8 illustrates the connection between magnetospheric electric fields and the ionosphere via Region 1 (R1) and Region 2 (R2) field-aligned currents (FACs). The eastward-westward magnetic field disruptions observed at mid-latitudes are attributed to these FACs, (SUN et al., 1984) while equatorial and auroral electrojets primarily cause perturbations at low and high latitudes. The penetration of the electric field is associated with R1 FACs, whereas R2 FACs are linked to the shielding electric field. Consequently, the causes of penetration electric fields in the mid and low-latitude ionosphere are also explained based on the imbalance status of these FACs.

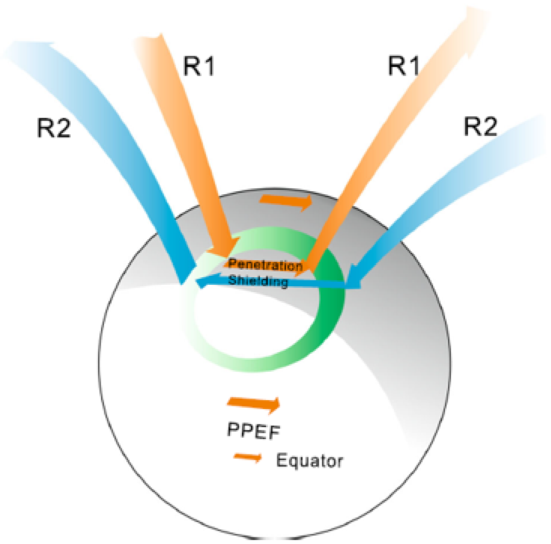

Figure 8 – Origin of magnetospheric electric field penetration and shielding generated by R1 and R2.

Source: Wei et al. (2015)

According to Blanc e Richmond (1980) during ionospheric disturbance periods, the electric field comprises various components, including the background electric field present in the mid and low latitudes, which are linked to the solar-quiet (Sq) current system, PPEFs, and disturbance dynamo electric fields. Siqueira et al. (2011) pointed out that PPEFs and long-lasting ionospheric disturbances serve as the primary sources of plasma drift and current perturbations during geomagnetically disturbed conditions. Ren et al. (2008) and Yue et al. (2008) emphasize PPEFs during intense storms based on several factors: (i) the smoothness of the Sq electric field, which may change if solar activity (LIU et al., 2011) remains similar to calm days; (ii) the duration of effectiveness of the disturbance dynamo, which can last several hours (FEJER; SCHERLIESS, 1997) and (iii) rapid fluctuations in PPEFs under external drivers, often exhibiting distinct patterns compared to Sq electric fields and disturbance dynamo electric fields.

A study conducted by Kelley et al. (2003) suggested that pulses in the equatorial electric field are attributed to PPEFs, resulting from fluctuations in the IEF, listed as one of the external drivers. During the main phase, these pulses can have a prolonged duration. It is suggested that electric field penetration can persist for tens of minutes when the IMF Bz remains southward or oscillates between northward and southward directions, as noted by Gonzalez et al. (1994). Huang, Foster e Kelley (2005) mentioned that PPEFs can endure for many hours during storm conditions based on observational evidence. Quantitatively, electric field penetration serves as an estimate for its occurrence and effect. Huang et al. (2007) provided an estimated average value of 0.096 mV/m.

Additionally, Zhang et al. (2013) highlighted estimated efficiency values of 0.16 and 0.13 at the dusk sector during a superstorm on November 20, 2003, attributed to the PPEFs mechanism. This mechanism often stems from solar winds or the magnetosphere. Zhang et al. (2013) also highlighted that dynamic pressure from solar wind influences plasma distribution in the inner magnetosphere, leading to an enhancement of PPEFs (YUAN; DENG, 2007; ZONG et al., 2010). PPEFs is identified as a cause of uplift in the equatorial ionosphere to higher altitudes, resulting in decreasing plasma density at the bottom side. During events such as the "Bastille Day Storm" and "Halloween Storm," as discussed by Zhao, Wan e Liu (2005), Vlasov, Kelley e Kil (2003), **??**) and Tsurutani et al. (2004) PPEFs has exhibited strong fountain effects, accompanied by plasma density bite-outs (density troughs) over latitudinal ranges near 30° close to the magnetic equator, and significant total electron content (TEC) variations extending to magnetic latitudes of up to about 40°. The mechanism of positive storm effects resulting from significant PPEFs at low to middle latitudes has garnered considerable attention.Tsurutani et al. (2004) and Tsurutani et al. (2008) proposed that the movement of equatorial plasma to higher magnetic latitudes plays a pivotal role in generating strong storms at low to middle latitudes. During geomagnetic storm periods, the equatorial and low-latitude ionospheric regions undergo significant alterations due to PPEFs and ionospheric disturbance dynamo activities, favoring the development of Rayleigh-Taylor instability (RTI) and resulting in the occurrence of Equatorial Spread F (ESF) irregularities. Additionally, highly disturbed electric fields and thermospheric winds dominate these regions (ALEXEEV, 1986). According to Wei et al. (2008) the sudden southward turning of the IMF Bz resulted in a high-latitude convection electric field penetrating the low-latitude ionosphere (undershielding condition), leading to the creation of an eastward PPEFs during the day and a westward PPEFs during the night.

Abdu (2012) highlighted that the development of ESF can be either inhibited or initiated at nighttime, depending on whether the PPEFs is of undershielding or overshielding type.

During an undershielding mechanism, PPEFs contributes to vertical uplift of the equatorial F layer and growth of Rayleigh-Taylor (R-T) instability, leading to the formation of plasma bubbles associated with irregularities. These irregularities are directed eastward during the pre-reversal enhancement. Conversely, during an overshielding mechanism, PPEFs influences the low-latitude ionosphere when the IMF-Bz turns northward. However, overshielding PPEF of eastward polarity can also lead to plasma bubble development at night, as highlighted by Abdu et al. (2009).

On the other hand, DDEFs occurs when magnetic disturbances induce electric fields through electromagnetic induction, driven by the current system generated by interactions with solar wind (ABDU et al., 2007). Abdu et al. (2007) emphasizes that DDEFs in the equatorial ionosphere arise from the interaction between neutral winds and ionospheric plasma. Blanc e Richmond (1980) highlights that DDEFs result from disturbance winds via the dynamo process. They are attributed to intensified Joule and particle heating when a magnetic storm occurs and progresses toward the equatorial region along magnetic field lines. DDEFs typically commence 3 hours after geomagnetic activity and reach peak disturbance levels up to 6 hours later in the equatorial region (HUANG, 2013). Huang (2013) further note that factors such as solar flux, season, and local time determine the strength and direction of Disturbance Dynamo Electric Fields. Quantitatively, it is observed that vertical drift velocity is highest in CME-driven storms compared to CIR-driven storms.

2.6 Influence of solar wind-magnetosphere coupling on the Earth's ionosphere

The solar wind, an ionized stream of plasma originating from the Sun, transfers energy and momentum into the magnetosphere and ionosphere, driving them as an interconnected system. The solar wind consists of alpha particles and low densities of highly ionized heavy ions (such as C, N, O, Ne, Mg, Si, S, Fe, etc.). These alpha particles and heavy ions travel at high velocities along field-aligned directions from the Sun, generally moving at similar or slightly slower speeds compared to the proton wind (NěMEčEK et al., 2020; ĎUROVCOVá; ŠAFRáNKOVá; NěMEčEK, 2021).

High-speed solar wind streams, classified based on their flow, induce substantial geomagnetic storm activity in the ionosphere. These streams originate from coronal holes and give rise to CIRs due to interactions with slow-speed solar wind streams, accompanied by fluctuations in interplanetary Alfvén waves (TSURUTANI et al., 1995; BELCHER; JR, 1971). According to Tsurutani et al. (2006), HSS significantly impact the magnetosphere and ionosphere during storms caused by CMEs and CIRs, leading to variations in particle energy density. Liu et al. (2019) noted that typical HSS events are characterized by phenomena such as: (i) an increase in solar wind pressure lasting for extended periods, (ii) an intensification of magnetospheric convection persisting for days, generating high-amplitude oscillations in the magnetic IMF Bz, (iii) an enhancement due to wave-particle interactions building up in the inner magnetosphere, and (iv) enhanced particle precipitation in the auroral regions, with large amounts of energy injected through the Joule heating process, followed by variations in ionospheric TEC. In addition, Borovsky e Denton (2006) emphasized that the energy transported by HSS into the ionosphere and thermosphere adversely affects thermospheric temperature, density, and ionospheric plasma number density. The effects of HSS can propagate down to middle and low latitude regions due to electrodynamic perturbations, causing variations in thermospheric neutral wind circulation and enhanced magnetospheric convection. This leads to an increase in NmF2 and hmF2, as mentioned by Lyon (2000).

Also disruptions to both space-based and ground-based systems are attributed to variations in the solar wind, resulting in enhanced currents flowing into the ionosphere and increased ionization in the near-Earth environment (BAKER et al., 1998). Furthermore, Adhikari et al. (2018) mentioned that as the solar wind flow passes the magnetopause of the Earth's magnetosphere, an electric field is produced via magnetic reconnection between the southward-directed IMF-Bz and the geomagnetic field. Consequently, a portion of this electric field is deposited in the polar ionosphere, creating a cross polar cap potential. This potential arises from the difference in the ionospheric electric convection potential, specifically between the maximum and minimum polar cap potential values (i.e., PCVmax - PCVmin). The southward component of Alfvén waves triggers a magnetic reconnection mechanism, leading to substorms (DUNGEY, 1961; GONZALEZ; MOZER, 1974; TSURUTANI et al., 1995). Additionally, it regulates magnetospheric convection and geomagnetic activity extending into the ionosphere.

The coupling process between the solar wind and the magnetosphere is driven by magnetic field lines through magnetic reconnection. Earth's magnetic field within the magnetosphere acts as a shield against the solar wind, which encounters it primarily on the dayside. As the solar wind flows across the bow shock, it creates a curl in the magnetic field $\vec{B}$, generating currents. On the nightside, there is an expansion of magnetic field lines, resulting in a low-pressure zone and the formation of the magnetotail. The tail region serves as a reservoir for a large number of energetic particles and is dominated by a magnetic field with low density. In contrast, the tail lobes are characterized by higher density, a plasma sheet, and a lower field region surrounding its (FEDDER; LYON, 1987).

The region where the pressure of the solar wind equals the pressure of the magnetic field is known as the magnetopause. The magnetosheath is located between the bow shock and the magnetopause. The bow shock forms from the collision between the supersonic solar wind and the magnetosphere. Magnetic field lines serve as pathways for plasma to travel between different regions connected by these lines. Energy and momentum from the solar wind flow into the inner magnetosphere through magnetic reconnection, connecting with the polar ionosphere and contributing to the coupling process as shown in figure 9. The oppositely directed magnetic fields of the solar wind and the geomagnetic field merge and combine, resulting in plasma flow along the same field lines from these two different regions.

After magnetic reconnection in the tail, the magnetic fields generally move in a sunward direction until they reach the dayside. This brings the fields closer to Earth's ionosphere, which contains plasma and interacts with the neutral atmosphere. Collisions between neutral atoms and molecules with ions determine how magnetospheric convection responds due to collisional drag, influencing the motion of ion flow. These collisions allow solar wind plasma to be transported into the ionosphere along open field lines and also cause currents to flow within the ionosphere (refer to figure 9 C). The flow extends far from the sun across the topside of the polar cap and returns at lower latitudes on both the dawn and dusk sides. This pattern indicates the two-cell ionospheric convection highlighted in figure 9 C. Solar wind energy drives ionospheric and magnetospheric convection, enhancing plasma circulation within the magnetosphere. This process is particularly intensified near the polar caps, where solar wind flow interacts with the magnetospheric boundary, known as the magnetopause, and the magnetosheath.

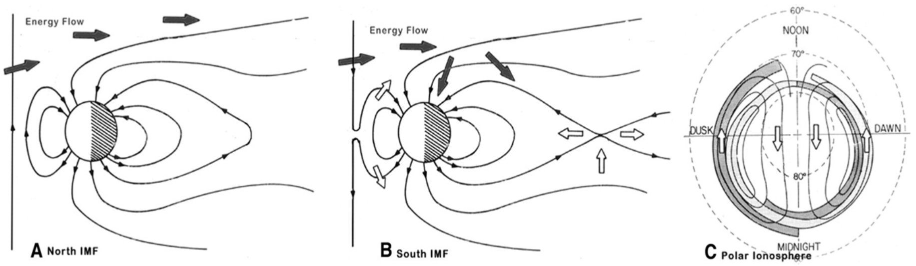

Figure 9 – The schematic diagram illustrates the process of reconnection in the magnetosphere. In (A), no reconnection occurs, and there is no energy flow, as indicated by the absence of solid arrows. (B) depicts the initiation of reconnection and the opening of the magnetosphere, showing magnetospheric convection with an arrow. (C) indicates the flow of current moving into the polar ionosphere due to a southward IMF. The shaded area represents the currents flowing between the magnetosphere and ionosphere, with lighter shading indicating upward current and darker shading indicating downward current.

Source: Fedder e Lyon (1987)

The enhancement in the southward Interplanetary Magnetic Field (IMF) strengthens magnetospheric convection, which can lead to geomagnetic storms (TSURUTANI et al., 1995). This enhanced convection extends towards the ionosphere at mid and low latitudes. Moreover, the energy carried by high-speed solar wind can lead to the relaxation of the magnetic field in the magnetotail towards a more dipolar configuration, causing auroral displays and intense ionospheric currents. Foster (1984) emphasized that ionospheric ionization is linked to sunward magnetospheric convection, peaking at dusk and reaching its minimum at dawn due to low nighttime density. This results in plasma at the dawn and dusk electric fields moving to high latitudes, away from the daytime ionization. According to Pedatella e Forbes (2011), the two-cell convection pattern at high latitudes is associated with geomagnetic storms and is affected by the southward incursion of the interplanetary magnetic field. During geomagnetic storms, the interaction between the solar wind and the magnetosphere causes ionospheric disturbances (BURNS et al., 2007). This interaction significantly affects the ionosphere-thermosphere (I-T) system (BUONSANTO, 1999; LYON, 2000) regulated by variation in thermospheric composition and ionospheric disturbance dynamo electric fields, which affect the low-latitude electric field (BLANC; RICHMOND, 1980; FEJER; LARSEN; FARLEY, 1983), especially in the recovery phase of geomagnetic storm.

The occurrence of geomagnetic storms generates energetic particles and enhances the solar wind, often associated with solar phenomena such as CMEs and HSS. These interactions with Earth's magnetosphere and ionosphere are accompanied by an increase in extreme ultraviolet (EUV) solar radiation (TSURUTANI; GONZALEZ, 1987; ABDU et al., 1991).

The heightened solar radiation, particularly below 10 10Å in the X-ray range, correlates with an increase in the Hα line, leading to intensified ionization at altitudes around 80 km (BANKS; KOCKARTS, 2013). This surge in ionization triggers a series of phenomena known as sudden ionospheric disturbances (SIDs), which are most intense in regions directly beneath the solar zenith. During such events, electromagnetic wave propagation undergoes significant attenuation. The electron density in the D-region sharply increases but typically returns to baseline levels within a few hours (KELLY, 2012).

Additionally, DDEFs, driven by thermospheric winds, can significantly influence the EIA. These fields alter the latitudinal distribution of the ionosphere by shifting it poleward in either the northern or southern hemisphere, as discussed by Liu et al. (2019). This anomaly is characterized by a non-uniform latitudinal distribution of ionospheric electron density, exhibiting two prominent crests near the magnetic equator (LI et al., 2018; APPLETON, 1946).

3 The Earth´s ionospheric structure and composition

The ionosphere, a weakly ionized fluid within the neutral atmosphere, is distinguished by a significant presence of free ions and electrons that influence radio-wave propagation. Essentially, it constitutes a plasma with an overall neutral net charge. It extends roughly from 60 to 1000 km altitude, with each layer containing distinct ions (KELLEY, 2009). The quantity of neutral particles present is higher compared to charged particles, yet it still significantly influences the electrical properties of the medium. Photoionization processes, involving the absorption of solar radiation such as extreme ultraviolet and x-ray wavelengths—by neutral atmospheric elements, are responsible for generating free electrons and ions within the ionosphere. The absorption of solar radiation causes collisions between neutral elements, leading to increased ionization and the loss of electrons, resulting in the formation of positive ions and the release of free electrons. The ionization of the ionosphere is also caused by the collision of charged energetic particles from solar or galactic sources, particularly noticeable at high latitudes and in the South Atlantic Magnetic Anomaly region (SAMA). Figure 10 illustrates the vertical distribution profiles of electron density during both day and night. Various factors, such as season, solar cycle, local time, latitude, and magnetic activity as indicated by Abdu et al. (2007), influence the variation in maximum density peak height and total electron content. Additionally, the chemical composition of the atmosphere exhibits significant variability, contributing to the complexity of the profile, as depicted in figure 11.

During the night, the recombination processes becomes predominant, leading to a decrease in electron density, especially at lower altitudes, as solar radiation ceases to induce photoionization. Transport processes play a role in sustaining the nocturnal ionosphere at higher altitudes. These electrically conductive mediums, located between 50 km and 150 km (refers to figure 10), exhibit a change in electron concentration (n_e) from 10^7 particles per m³ at 50 km to a peak of 10^{12} particles per cm³ at 250-300 km.

The ionospheric plasma is produce from the energetic electromagnetic and particle radiation emitted by the sun. Even at altitudes where n_e reaches its maximum, the ratio between electron density and the density of neutral air does not exceed 10^7 (KELLY, 2012). Regular ionospheric layers are formed by X-ray and extreme ultraviolet (EUV), solar radiation characterized by variations over the course of the day and with latitude. In polar regions, ionization

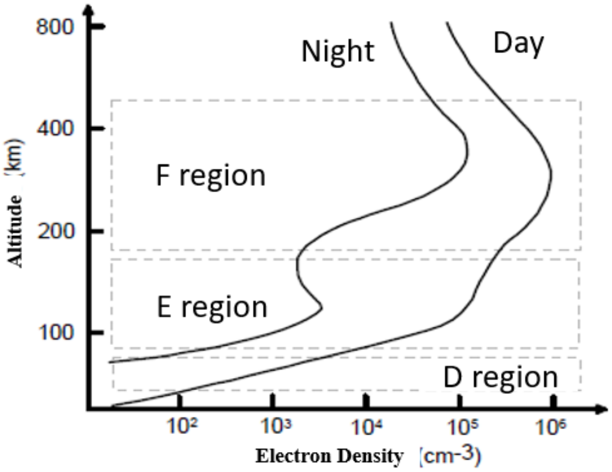

Figure 10 – The electron density vertical distribution profiles during the day and night
Source: Rishbeth e Garriott (1969)

occurs due to the precipitation of energetic particles along magnetic flux lines. The diurnal variation of the ionospheric layers reveals that the F layer is divided into F1 and F2, with the E layer preceding it, and the D layer.

The region above the F region (> 500 km) is known as the magnetosphere, where the magnetic field predominantly influences electrically charged particles (STERN, 1977). The ionosphere is further categorized into three distinct layers: the D layer (50-95 km), the E layer (95-150 km), and the F layer (150-500 km), as illustrated in figure 10. The electron concentration in these layers varies depending on solar radiation type, recombination, and transport processes, diverging from the ideal Chapman layer due to diurnal, latitudinal, and altitudinal variations. These layers persist even during nighttime, when the sun is below the horizon, due to scattered radiation and transport mechanisms facilitating the movement of plasma from sunlit to dark regions.

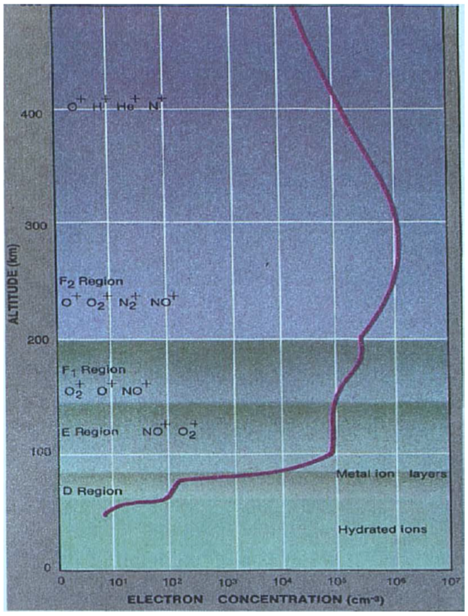

Figure 11 – A temperature profile of the Earth's ionosphere.
Source: Heelis (2004)

The ions and electrons present within the F region (150-500 km) are generated through the absorption of EUV radiation by O and N_2, which are major components of the atmosphere with wavelengths ranging from 10 nm to 90 nm. The primary ions predominantly consist of O^+ and N_2^+, which react with molecules and neutral atoms. The F1 region is more prevalent during summer than in winter and disappears at night. The primary source of ionization is solar radiation in the EUV range, specifically at wavelengths of $\lambda = 58.4$ nm and 30.4 nm. The F2 region's electron density varies with magnetic latitude, with an average peak value occurring at approximately 300 km and a maximum density on the order of 160 cm^{-3}. Density fluctuations depend on the solar zenith angle and solar activity.

The upper and lower ionosphere, associated with the regions above and below the F2 peak, respectively, are characterized by diffusion as the dominant process. In these regions, the vertical distribution of electrons cannot be solely described by the balance between production and loss, as the ratio of collision frequency to gyro frequency for ions and electrons is negligible. This results in their velocities perpendicular to the magnetic field being nearly equal, thus defining a unique plasma flow associated with the electric field. The thermospheric wind system, driven by pressure inequalities from solar EUV heating, acts as the primary force behind the F-region dynamo. The absorption process leads to temperature variations, creating a pressure gradient and ultimately generating winds for plasma interactions.

The E region, ranging from 95 km to 150 km, exhibits behavior akin to Chapman's model. Ion production within the typical E-layer is triggered by X-rays (1 nm to 10 nm) and ultraviolet radiation (100 nm to 150 nm), which dissociates O_2 and N_2 into O_2^+ and N_2^+, respectively, with the latter quickly disappearing through charge exchange. Unlike molecular ions, metallic ions in the E-region have a longer lifespan, persisting even into the night once formed. Ionization primarily occurs due to soft X-rays (1-10 nm) and far-ultraviolet radiation, which ionizes molecular oxygen (O_2), reaching a peak density of 150 cm^{-3} (KELLEY, 2009). The prevalent ions are O^{+2} and NO^+. The vertical structure of the E layer is influenced by both ionization and recombination processes. In the E-region, metallic ions like Na^+, Mg^+, and Fe^+ often lingers and undergos charge changes, leading to the formation of irregular layers known as sporadic layers. These regions can vary greatly in density and thickness and may appear intermittently during both day and night.

The D region ranges from 60 km to 90 km in altitude. Electron density within the D-layer fluctuates primarily due to the influence of various ionization radiations. H-Lyman-α radiation ($\lambda = 121.5$ nm) is the predominant ionizing radiation that penetrates and ionizes NO to a significant extent. Solar L-α (121.6 nm) radiation plays a crucial role in ionizing NO, while solar X-rays (< 0.8 nm) ionize N_2, O_2, and Ar. Solar ultraviolet (UV) radiation ($\lambda < 111.8$ nm) ionizes unstable O_2, and galactic cosmic rays ionize all constituents within the D region. Daytime maximum density typically ranges from 10^2 to 10^4 cm^{-3}. Main chemical reactions involve O, O_3, O_2, NO_2, CO_2, and H_2O. The production rate of ions and recombination mechanisms are fairly complex, particularly between 50 km and 95 km. This production mechanism is dominant around 70-90 km, mainly attributed to solar X-ray radiation. Around 70 km altitude, cosmic radiation becomes the predominant ionizing radiation source. Recombination processes are therefore dependent on both altitude and temperature.

3.1 The ionospheric electrical conductivity

Balfour Stewart, in 1882, inferred the electrical conductivity in the upper atmosphere based on the solar daily geomagnetic variation. Stewart noted that while the lower atmosphere displayed negligible variation associated with the sunspot cycle, there was a discernible electrical current present in the upper atmosphere. Balfour Stewart proposed that the movement of conducting air across the geomagnetic field lines, driven by dynamo action, rendered the ionospheric conductivity anisotropic. Ionization in the upper atmosphere occurs through the absorption of solar ultraviolet and X radiation, as well as the precipitation of energetically charged particles from the magnetosphere due to solar wind interaction (GONZALEZ et al., 2006). Nighttime ionization is initiated by galactic and cosmic rays, typically occurring at low altitudes. The primary ions generated include N^{+2}, O^{+2}, N^{+}, and O^{+}.These ions undergo reactions with neutral gases and nitrogen ions, leading to the production of O^{+2} and NO^{+} through the charge dissociation process. NO^{+}, O^{+2}, and O^{+} are the predominant ions, whereas those below 150 km are observed as molecular ions. O^{+} are also noticed above 200 km. Negative and positive ions become significant only below 90 km, where conductivity is relatively low. Between 90 km and 150 km, the densities of NO^{+} and O^{+2} are equivalent to the electron number density, N. According to Kelley (2009) molecular ions recombine with electrons at a rate represented by the reaction coefficient α. These ions are close to photochemical equilibrium. If Q_e represents the electron production rate, then within the altitude range of 90 km to 150 km, the photochemical equilibrium implies that

$$Q_e = \alpha N^2 \tag{3.1}$$

or

$$N = \sqrt{Q_e/\alpha} \tag{3.2}$$

The mean value of the two ions (NO^{+} and O^{+2}) is weighted upon the densities of α in 3.1 and 3.2 since the recombination coefficient varies. In addition, α is inversely proportional to the temperature of the electron of about 3 x 10^{-13} m^3s^{-1}. Furthermore, O^{+} at high altitudes reacts with molecular neutral elements to become molecular ions before the recombination process with electrons commences, and due to such reason equation 3.1 and 3.2 become invalid at high heights. At maximum heights, neutral density is insignificant and O^{+} ions loss is less rapid. The photochemical equilibrium breaks down as a result of transferring ions to a greater distance. The primary ionization source during the day varies based on solar activity.

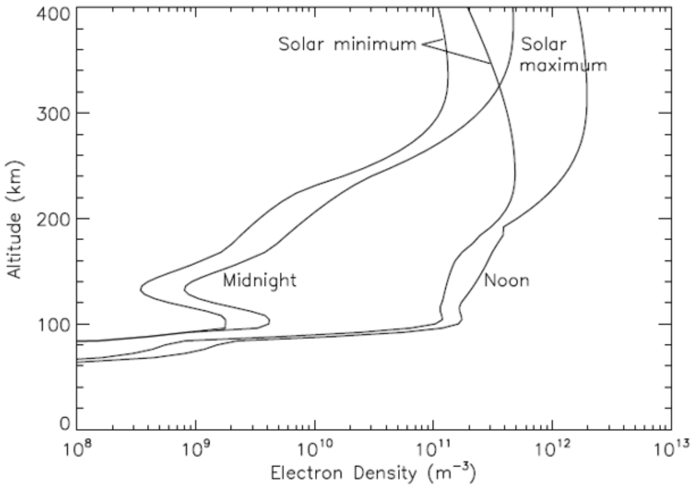

Figure 12 – High and low solar activity effects on electron density vertical profiles observed during day and night time.
Source: (BANKS; KOCKARTS, 2013)

In the E region, the peak density is often seen around 105 km, whereas the larger-density region above 150 km is attributed to the F region. However, the E region undergoes greater variations as compared to the upper F region during the day and night. The ionization in the auroral regions, driven by significant variations in the precipitation of energetic particles, is much higher compared to that caused by solar radiation (NEWELL; SOTIRELIS; WING, 2009). To deal with the conductivity within these regions, the ions, and the electrons are considered fluids in force balance as mentioned by Richmond (2017). The magnitude of electron charge and ions are equivalently the same at heights above 90 km and all ion species are treated as a single fluid (thus, number density equals electrons, N).

The ion mass m_i, velocity v_i, temperature T_i and the collision frequencies of ions with neutrals v_{in} and with electrons v_{ie} then indicate the mass-density-weighted mean overall ion species by ((RICHMOND, 2017)). The current density $\vec{J}$ is associated to N, the ion and electron velocities v_i and v_e by

$$\vec{J} = Ne\left(v_i - v_e\right) \tag{3.3}$$

For ions and electrons, the force-balance conditions are respectively:

$$Ne\left(E + v_i x B\right) - Nm_i v_{in}\left(v_i - v_n\right) - Nm_i v_{ie}\left(v_i - v_e\right) + Nm_i g - \nabla\left(NkT_i\right) = 0 \tag{3.4}$$

$$-Ne\left(E + v_e x B\right) - Nm_e v_{en}\left(v_e - v_n\right) - Nm_e v_{ei}\left(v_e - v_i\right) + Nm_e g - \nabla\left(NkT_e\right) = 0 \tag{3.5}$$

where m_e and T_e are the electron mass and temperature, v_n is the velocity of the neutral gas, v_{en} and v_{ei} are the electron-neutral and electron-ion collision frequencies, $\vec{E}$ and $\vec{B}$ are the electric and magnetic fields, g is the acceleration of gravity, and k is the Boltzmann constant. As mentioned by Shkarofsky, Johnston e Bachynski (1966) and Hill e Bowhill (1977), in the presence of a magnetic field, collision frequencies are tensors. According to Gagnepain, Crochet e Richmond (1977), electron-neutral collision frequency is $\approx$ 1.4 times as large for motion perpendicular to $\vec{B}$ above 80 km. For horizontal motion along the magnetic field ($\vec{B}$) below, the off-diagonal term in the collision-frequency tensor is considered significant. v_{ei} is similarly anisotropic, concentrating on the value of its motion along $\vec{B}$. The anisotropy of an ion is irrelevant to its collision frequency.An expression for current density parallel to $\vec{B}$ is obtained from the component of 3.8 parallel to $\vec{B}$, which in rearranged form is

$$Nm_e v_{en\|}\left(v_e - v_n\right) + Nm_e v_{ei\|}\left(v_e - v_i\right) = -Ne\left(E_{\|} - E_{\alpha}\right) \tag{3.6}$$

$$E\alpha = \frac{1}{N_e}\frac{\delta\left(NkT_e\right)}{\delta_s} \tag{3.7}$$

Where the subscripts $\|$ indicate the direction along B and s is the distance along $\vec{B}$. E_{α} is known as the ambipolar electric field, which from 3.30 is seen to be the value of $E_{\|}$ in the absence of collisional drag on the electrons. The electron-neutral collision terms are important. In addition, the motion of ions along the magnetic field ($\vec{B}$) is strongly influenced by collisions with neutrals. In low-latitude regions, the parallel velocities of ions and neutrals are effectively treated as being the same. Hence, $v_{n\|}$ can be replaced by $v_{i\|}$, and the electron-ion velocity deviates along B and is found to be

$$\left(v_e - v_i\right)_{\|} = \frac{e\left(E_{\|} - E_{\alpha}\right)}{m_e\left(v_{en\|} - v_{ei\|}\right)} \tag{3.8}$$

The electric current parallel to $\vec{B}$ is then

$$\vec{J}_{\|} = \sigma_{\|}\left(E_{\|} - E_{\alpha}\right) \tag{3.9}$$

The electric current parallel to $\vec{B}$ is then

$$\sigma_{\|} = \frac{Ne^2}{m_e\left(v_{en\|} - v_{ei\|}\right)} \tag{3.10}$$

Where $\sigma_{\|}$ is the parallel conductivity.

To derive expressions for motions and currents perpendicular to the magnetic field, we ignore the collision effect between ions and electrons in 4.1 and 3.8. This turns out to be a great approximation because the magnetic component of Lorentz's force is greater than the rate of momentum transfer between electrons and ions as indicated by Allis (1956). Now denoting velocities and electric fields in the frame of reference of the neutral air, i.e.,

$$v^{|}{}_{ie} = v_{ie} - v_n \tag{3.11}$$

$$\vec{E}^{|} = \vec{E} + v_n \times \vec{B} \tag{3.12}$$

the component of 4.1 perpendicular to $\vec{B}$, upon rearrangement, gives

$$-N_{ev^{|}{}_{i}} xB + Nm_i v_{in} v^{|}{}_{i\perp} = -NeE^{|}{}_{\perp} + F^{|}{}_{\perp} \tag{3.13}$$

$$F_i = Nm_{ig} - \nabla\left(NkT_i\right) \tag{3.14}$$

where the subscript $\perp$ signifies the component perpendicular to $\vec{B}$, and F_i is the force per unit volume on the ions due to the ion pressure gradient and gravity by Kelley (2009). To solve 3.13 for $v^{|}{}_i$ take its cross product with $\frac{e\vec{B}}{m_i v_{in}}$, add the result to 3.13, and rearrange, yielding

$$v^{|}{}_{i\perp} = \frac{v_{in\perp}\Omega_i E^{|}{}_{\perp} - \Omega^2{}_i bxE^{|}{}_{\perp}}{B\left(v^2{}_{in\perp} - \Omega^2{}_i\right)} + \frac{v_{in\perp}F^{|}{}_{i\perp} - \Omega^2{}_b xF^{|}{}_{i\perp}}{Nm_i\left(\Omega^2{}_b - v^2{}_{in\perp}\right)} \tag{3.15}$$

Where **b** is a unit vector in the direction of $\vec{B}$ and where

$$\frac{e\vec{B}}{m_i v_{in}} \tag{3.16}$$

is the angular gyrofrequency for the ions, describing their gyration in the geomagnetic field. Similar equations are obtained for electrons:

$$v^{|}{}_{e\perp} = \frac{-v_{en\perp}\Omega_e E^{|}{}_{\perp} - \Omega^2{}_e bxE^{|}{}_{\perp}}{B\left(v^2{}_{en\perp} - \Omega^2{}_e\right)} + \frac{v_{en\perp}F^{|}{}_{e\perp} - \Omega^2{}_b xF^{|}{}_{e\perp}}{Nm_e\left(\Omega^2{}_b - v^2{}_{en\perp}\right)} \tag{3.17}$$

$$F_e = -\nabla\left(NkT_i\right) \tag{3.18}$$

$$\frac{e\vec{B}}{m_e} \tag{3.19}$$

Figure 13, Shows the height variations of the collision frequencies v_{in}, $v_{en\perp}$ and ($v_{en\|} - v_{ei\|}$) for daytime solar-minimum conditions, along with the angular gyro frequencies of the ions and electrons.

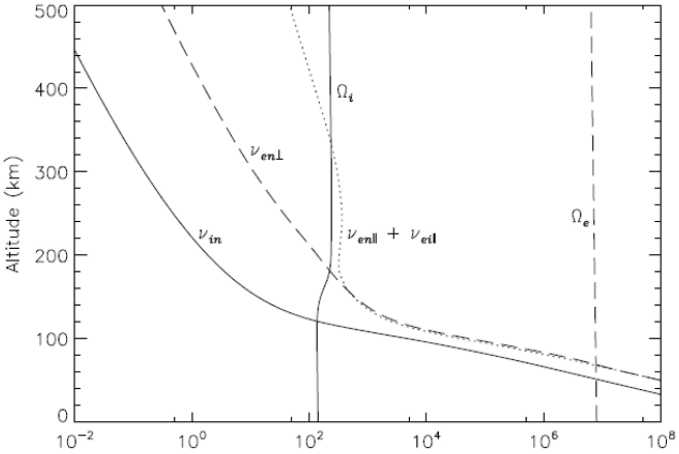

Figure 13 – Variation of collision frequencies and gyro frequencies (s^{-1})with altitude. Source: (BANKS; KOCKARTS, 2013)

Richmond (2017) highlighted that ion-neutral and electron-neutral collision frequencies are directly proportional to neutral density, which decreases exponentially with increasing altitude in the upper atmosphere, varying by a factor of approximately 10^5 between 80 km and 300 km. Moreover, ion-electron and electron-ion collision frequencies are roughly proportional to the electron number density, N, peaking near the altitude of maximum electron density. In the F region, gyro frequencies greatly exceed collision frequencies for both ions and electrons, and the first terms on the right-hand sides of equations 3.15 and 3.17 are typically much larger than the second terms related to F_i or F_e, as mentioned by Banks e Kockarts (2013). In such cases, the approximate solutions for ion and electron velocities are

$$v_{i\perp} \sim v_{e\perp} \sim \frac{\vec{E} \times \vec{B}}{B^2} \equiv v_E \tag{3.20}$$

where v_E is the so-called "$\vec{E} \times \vec{B}$" velocity.

By subtracting 3.17 from 3.15 we obtain the velocity difference $v_{i\perp}$-$v_{e\perp}$, which, when multiplied by N_e, gives the electric current density perpendicular to $\vec{B}$. According to Richmond (2017), an expression for Ohm's Law can then be obtained that expresses the total current density J in terms of the electric field that exists in the frame of reference of the moving neutral gas, $\vec{F}^{|}$, and the current density $\vec{J}_{pg}$ associated with gravity and plasma pressure gradients:

$$\vec{J} = \sigma_P \vec{E}^{|}_{\perp} + \sigma_H B \times \vec{E}^{|}_{\perp} + \sigma_{\|} \left(E_{\|} - E_{\alpha}\right) b + \vec{J}_{pg} \tag{3.21}$$

$$\sigma_P = \frac{Ne}{B}\left(\frac{v_{in}\Omega_i}{{v^2}_{in} - \Omega_i^2} + \frac{v_{en\perp}\Omega_e}{v_{en\perp}^2 - \Omega_e^2}\right) \tag{3.22}$$

$$\sigma_H = \frac{Ne}{B}\left(\frac{\Omega_e^2}{v_{en\perp}^2 - \Omega_e^2} + \frac{\Omega_e^2}{v_{in}^2 - \Omega_i^2}\right) \tag{3.23}$$

$$\vec{J}_{pg} = \frac{v_{in}\Omega_i F_{i\perp} - \Omega_i^2 bxF_{e\perp}}{B\left(\Omega_i^2 + v_{in}^2\right)} + \frac{v_{en\perp}\Omega_e F_{i\perp} - \Omega_e^2 bxF_{e\perp}}{B\left(\Omega_e^2 + v_{en\perp}^2\right)} \tag{3.24}$$

σ_P and σ_H are know as Pedersen and Hall conductivities, respectively. For currents perpendicular to $\vec{B}$, the Pedersen conductivity gives the component in the direction of ${E^{|}}_{\perp}$, while the Hall conductivity gives the component perpendicular to both $E^{|}$ and $\vec{B}$ as mentioned by Richmond (2017). The component $v_n \times \vec{B}$ of $E^{|}$, indicates the deviate between the electric field of the moving neutrals and the electric field in the Earth reference frame respectively, often noted as the dynamo electric field. The above expressions rely on the fact that collision frequencies are independent of the fluid velocities, when thermal velocities are minimal in order of 300 to 1000 m/s for neutrals and ions, depending on the composition and temperature of the gases. However, the differential velocities of the ion and neutral gases can often be comparable to the thermal velocities, especially in the auroral regions, where strong electric fields associated with magnetospheric processes can exist (RICHMOND, 2017). The altitude distributions of the direct, Pedersen, and Hall conductivities are shown in figure 14.

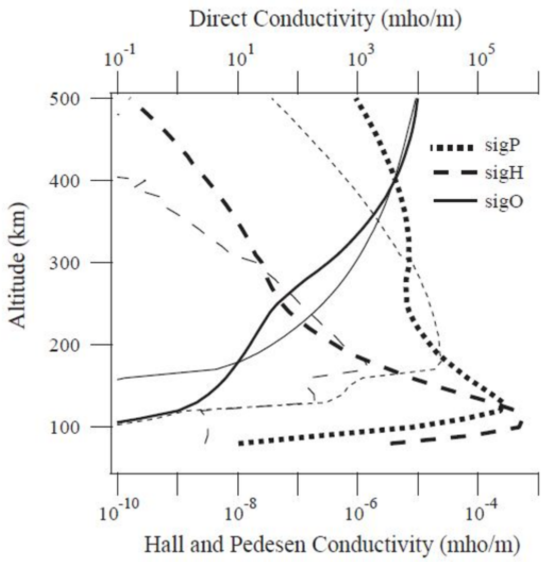

Figure 14 – Altitude profiles of the direct conductivity SigO and the Hall and Pedersen conductivities SigH and SigP.Heavy curves denote daytime values. Lighter curves denote nighttime values.

Source: Heelis (2004)

The current components in relation to the magnetic field and force are characterized by conductivities. Specifically, the Pedersen conductivity delineates two peaks corresponding to the daytime E and F regions. During nighttime, the conductivity of the F-region surpasses that of the E-region, resulting in significantly lower conductivity in that region. While the Hall conductivity is comparable to the Pedersen conductivity in the lower E-region, it diminishes rapidly with increasing altitude compared to the Pedersen conductivity above $\approx$ 200 km. Direct conductivity exceeds both Pedersen and Hall conductivities at all altitudes [e.g see (KELLEY, 2009)].

In contrast, ions exhibit motion in the direction of the wind at low altitudes, while at high altitudes, their motion becomes perpendicular to both the wind and the magnetic field, albeit with a significantly reduced magnitude. Conversely, electric fields propel electrons in the E×B direction at altitudes above approximately 100 km. In the ionosphere, this conductivity arises from the drift motion of electrons ($\vec{E} \times \vec{B}$ drift), reaching its maximum in the E region where electrons predominantly drift in the direction of E×B. However, ions move at very low velocities in the direction of the electric field at low altitudes and nearly align with $\vec{E} \times \vec{B}$ at higher altitudes.

The conductivity of the E region following sunset initiates the F region dynamo (RICHMOND, 1979), thus establishing a distinct lower boundary for the F region, as depicted in the configuration shown in Figure 15. Within the slab, the plasma is characterized by a constant finite Pedersen conductivity, while outside the slab, the conductivity is zero. Additionally, a constant zonal wind (u) exists within the slab. At the equatorial F region, vertical polarization electric fields develop, resulting in a zonal plasma drift ($V_D = \frac{\vec{E} \times \vec{B}}{B^2}$), which aligns in both direction and magnitude with the neutral wind during nighttime (KELLEY, 2009).

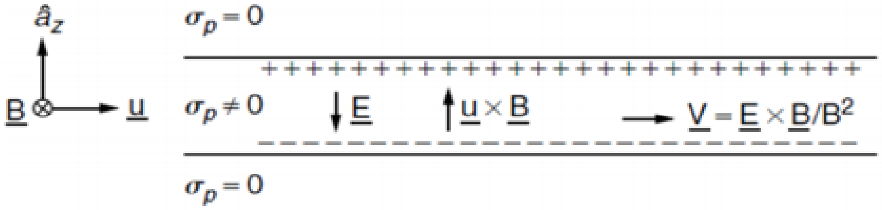

Figure 15 – Electrodynamics of the equatorial F-region.
Source: (Kelley (2009))

The charge separation occurs in such a way that the overall current (J_z) is zero. Thus ;

$$J_z = \sigma_p E_z + \sigma_p uB = 0 \tag{3.25}$$

This means that $E_z = E_Z = -\vec{u} \times \vec{E} = -uB$. Thus, the ideal F-region dynamo can be generalized as,

$$E + U \times B = 0 \tag{3.26}$$

During the night, the thermospheric wind is dominant and drives the plasma without ion drag. The conductivity variations between the E-region and F-region during the daytime, serve as a building mechanism influencing ion drag to remain high (HEELIS et al., 1974). The daytime conductivity in the E-region driven by wind determines the magnitude of the zonal electric field. Figure 15, depicts the motion of wind-driven current between the F-region and the E-region, attributed to divergence in the F-region current.

$$E_z = \frac{(U(z)B)\Sigma_P^F(z)}{\Sigma_P^F + 2\Sigma_P^F(z)} \tag{3.27}$$

The diurnal deviation in the vertical electric field motions from the E- to F-region can be express and explained detailed by the model. The Hall conductivity is negligible at the low latitudes since the F-region meridional winds constituent is parallel to the magnetic field. The current is generated perpendicular to the wind and the magnetic field near the equator. The field-aligned currents loop is indicated by the dashed line. The current driven by the F-region dynamo in the magnetic meridian is associated with Pedersen conductivity.

The electric field polarization embedded in the magnetic meridian follows:

$$\Sigma_F^P(E + U_F X B) = \Sigma_F^P E \tag{3.28}$$

When the horizontal current is divergent at the edges of the regions by assumption. Thus,

$$E = \frac{\Sigma_F^P}{\Sigma_F^P + \Sigma_F^P}(U_F X B) \tag{3.29}$$

Hence the physical mechanism describing the process is as follows.

In the E-region, the Pedersen conductivity generated is much larger as compared to the F-region as a result of negligible polarization field, thus during the sunset hours. However, at night time, this polarization field is directly proportional to the F-region dynamo wind. For this reason, it creates divergence in the F-region current leading to height gradients in the flux-tube integrated Pedersen conductivity. The F-region zonal wind which is constant with altitude and latitude shown as a function of local time distribution in figure 17 including flux-tube integrated Pedersen conductivity as a function of height for daytime and nighttime conditions. The polarization charges accumulated at nighttime conditions are responsible for creating the electric field and as a result, generating a $\vec{E} \times \vec{B}$ zonal drift of the charged particles in the F-region. During the nighttime, the polarization field is labeled as the maximum whereas E-region conductivity is minimal. According to Richmond (1979) eastward nighttime drifts in the F-region peaked at maximum and are aided by E-region dynamo winds by Richmond (1979). The polarization field in the magnetic meridian serves as one resolving mechanism in the F-region dynamo process. The existence of the F3 layer (G-layer) is located at the latitude near the magnetic equator depends on the phenomena such as Equatorial Anomaly and the meridional wind. It is situated between 500 km and 700 km altitude.

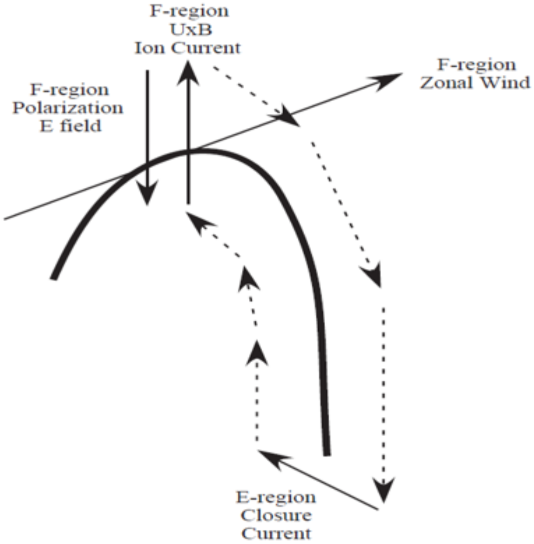

Figure 16 – Electrodynamics of the equatorial F-region.
Source: Rishbeth (1977)

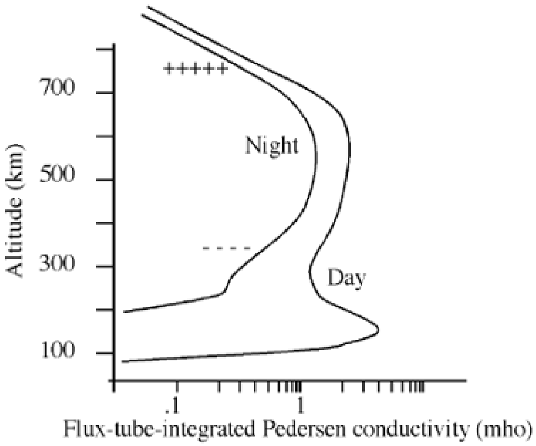

Figure 17 – The peak and ledge of F and E regions ion concentration during daytime and nighttime.

Source: Heelis (2004)

3.2 Electromagnetic waves in ionospheric plasma

A significant portion of Earth's atmosphere, known as the ionosphere, facilitates communication through various mechanisms within its different regions, owing to its conductive nature as noted by Heelis e Maute (2020). This layer, transformed into a plasma by the absorption of solar radiation through photoionization, alters or reflects radio waves, particularly those around 30 MHz, from transmitter to receiver via ground waves, sky waves, free space waves, and open field waves (BERTONI, 1999). Hence, understanding the characteristics of ionospheric plasma media is essential (REINISCH, 2004). The characteristics of the ionosphere are determined by estimating the refractive index and waveform in the medium at any frequency, thus altering the nature of wave energy and propagation through polarization (YEŞIL; ÜNAL, 2011). These waves exhibit frequency dependence, being either reflected or refracted based on the frequency of the electrons in the plasma and the refractive index of the medium (YEŞIL; ÜNAL, 2011). Its characteristics vary depending on the time of day, season, longitude on Earth, and the multiyear cyclic production of sunspots on the sun (ABDU et al., 2007). The ionosphere's horizontal stratified structure maintains equilibrium between photoionization and various loss mechanisms, thus establishing a balanced density of free ions and electrons. This electron density varies with altitude above the Earth's surface and is particularly influenced by sunrise and sunset, especially at lower altitudes. Free electrons are a crucial characteristic of the F region. While the ionosphere is typically divided into D, E, and F regions, the F region can further subdivide into F1 and F2 during the daytime, but at nighttime, these regions merge into one layer (KELLEY, 2009).

The maximum plasma density in the F-region is observed during daytime at altitudes of around one hundred kilometers, attributed to the decrease in densities of neutral atoms and molecules, coupled with an increase in the intensity of solar ultraviolet radiation. This leads to a variation in the ratio of charged particles to neutral particles concentration, ranging from 10^{-8} at 100 km to 10^{-4} at 300 km and 10^{-1} at 1000 km altitude. The spatial distribution of the refractive index in the ionosphere influences electromagnetic wave propagation. Unlike the lower atmosphere, where the refractive index remains constant, electromagnetic waves in the ionosphere may experience deviations from a straight-line trajectory. At an altitude of 50 km, free ions generated by solar radiation begin to appear, a process elucidated by the Chapman Layer model.

The Chapman Layer model describes the ion production rate as a function of height and zenith angle, considering assumptions about the atmospheric structure and incoming solar radiation (CHAPMAN; CHAPMAN, 1993). Furthermore, it elucidates the diminishing of electrons due to either attachment or recombination processes, necessary for studying electron density distribution, particularly within the ionized layer. Budden (1988) highlighted that radio waves are refracted in the High-Frequency (HF) range, thus enabling long-range HF propagation. The theory underlying the formation of the Chapman Layer, the constitutive relation, and the Appleton-Lassen equation serve as the foundation for comprehending ionospheric propagation. Since Guglielmo Marconi's trans-Atlantic radio wave experiment in 1901, the reflection of transmitted radio waves has been instrumental in long-range communications, particularly concerning ionospheric propagation.

Yeh e Liu (1982) provided a more comprehensive mathematical approach to understanding electromagnetic waves in the ionosphere. However, the function of the ionospheric layer is impeded by several factors that degrade radio wave propagation to some extent, thereby affecting signal efficiency. The ionosphere, as described by Kelley (2009), is the region of the atmosphere where free electrons and ions are present in sufficient numbers to influence radio wave propagation. These free electrons and ions result from the photoionization process, which occurs due to interaction between incoming solar radiation and atmospheric elements, and they are organized into nearly horizontally stratified layers extending from 50 kilometers to several thousand kilometers in altitude. The ionosphere consists of distinct layers, namely D, E, and F, each exhibiting distinct peaks in electron density. The structure of the ionosphere varies depending on seasonal, geographical, diurnal, and Sunspot Number (SN) variations. Figure 18 illustrates the differences between the typical daytime and nighttime ionospheres.

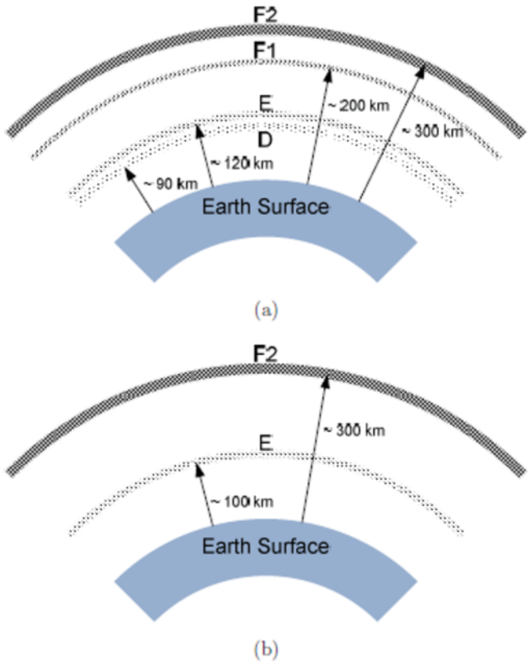

Figure 18 – The various distinct ionospheric regions and their respective altitude during the Day-time (a) and Night-time (b).
Source: Budden (1988)

The F region is divided into F1 and F2, with the F2 region exerting the most significant influence on the propagation of HF radio waves within the 3 to 30 MHz frequency range. Incoming electromagnetic (EM) waves interact with the ionized layer, influenced by the movements of free electrons in a prescribed electromagnetic field. The frequency of oscillations of an electron in an induced electric field, caused by the displacement of plasma, is determined by the angular plasma frequency ω_p:

$$\omega_p^2 = \frac{Ne^2}{\epsilon_o m} \tag{3.30}$$

where N is the electron density per cubic meter, e and m are the charge and mass of an electron respectively. The angular gyrofrequency ω_H is the frequency of oscillations of an electron in an imposed magnetic field and is given by:

$$\omega_H = \frac{e\vec{B}}{m} \tag{3.31}$$

where $\vec{B}$ is the magnitude of the magnetic flux density of the imposed magnetic field. The magnetic field of the Earth has a strong effect on ionospheric radio-wave propagation. The constitutive relations in magneto-ionic theory combine the forces imposed on the free electrons (which includes the electric force from the incoming electromagnetic wave, the force imposed on the moving electron by the Earth's magnetic field and the force exerted when an electron collides with a neutral particle), and the resulting set of Maxwell's equations can be solved for waves propagating in an ionized medium with an external magnetic field. This results in the Appleton formula for the refractive index of the ionospheric propagation medium as highlighted by Hartree (1931). The complex refractive index n is given by

$$n^2 = \frac{X}{1 - jZ - \frac{Y_T^2}{2(1-X-jZ)} \pm \sqrt{\frac{Y_T^4}{4(1-X-jZ)^2} + Y_L^2}} \tag{3.32}$$

where;

$$X = \frac{\omega_p^2}{\omega^2} \tag{3.33}$$

$$Y_L = \frac{e\vec{B}_L}{m\omega} \tag{3.34}$$

$$Y_T = \frac{e\vec{B}}{m\omega} \tag{3.35}$$

$$Z = \frac{v}{\omega} \tag{3.36}$$

where ω is the angular frequency of the radio wave, v is the collision frequency between the electrons and neutral molecules, and the L and T subscripts refer to the transverse and longitudinal components of the magnetic field (referred to as the direction of the wavefront normal as shown in figure 19. The plus and minus sign in equation 3.32 indicates that the complex refractive index may take two different values, the result of which is that the medium can support the propagation of two characteristic modes. The two modes

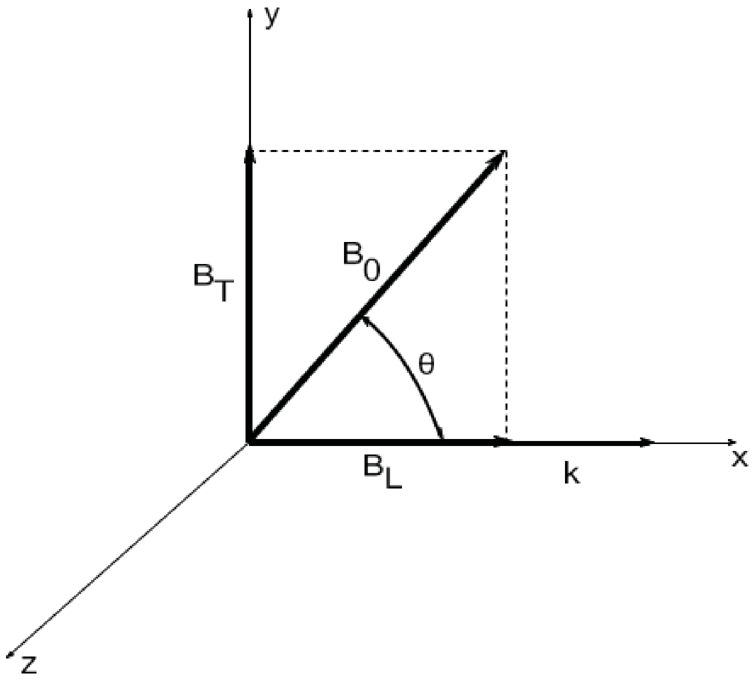

Figure 19 – Magnetic field orientation showing the Transverse (T) and longitudinal (L) components of B_0 relative to the wave normal vector k.
source: Hartree (1931)

are know as the Ordinary (O) wave and the Extraordinary (X) wave. For the case when the wave frequency is low (comparable to or below the gyrofrequency), there will be a third propagation mode. The simplest ionospheric propagation medium for analysis is one with the absence of the imposed magnetic field $(Y_L = Y_T = 0)$ and without collision (Z = 0). In such case, the refractive index has only a real part:

$$\Re\{n\}^2 = 1 - X = 1 - \frac{\omega_p^2}{\omega^2} \tag{3.37}$$

and only a single propagation mode is present. Using equation 3.37 and Snell's law ($n_1 \sin\varphi_1 = n_2 \sin\varphi_2$, where φ_1 and φ_1 are angles between the wave normal and normal of the boundary), it is possible to calculate the path of wave propagation, and the height at which the wave is reflected is when the refractive index is given by

$$n = \sin\varphi_o \tag{3.38}$$

where φ_o is the angle of incidence of the wave as it enters the ionosphere. It is the refraction of HF radio waves back toward the Earth by the ionosphere that allows the propagation of radio waves over long distances.

3.3 Equatorial and low latitude ionospheric phenomena

The equatorial and low latitude ionosphere has many special important phenomena such as the Equatorial Ionization Anomaly (EIA), Pre-reversal enhancement (PRE), and Spread F. However, these phenomena are strongly latitude, longitude, season, solar flux, and geomagnetic activity-dependent (ABDU et al., 2007; PANDA; GEDAM; JIN, 2015; LIU et al., 2011).

3.4 The equatorial ionization anomaly (EIA)

The electric fields of dynamo that are generated in the region E by tidal winds are transmitted along the magnetic field lines to the F region, because of the high parallel conductivity. During the day the dynamo electric field is directed to the east. In the equatorial F region, an electric field to the east, in the presence of the magnetic field directed northwards, causes an upward electromagnetic drift, given by $\frac{\vec{E}\times\vec{B}}{B^2}$. At night the electric field reverses directions and the drift is downward. Plasma that is elevated to high altitudes during the day can diffuse, driven by the force of gravity and the pressure gradient, but this movement is restricted along the magnetic field lines. This combination of electromagnetic drift and diffusion produces a plasma movement similar to the movement of a fountain and therefore received the name of fountain effect. Figure 20 illustrate this mechanism.

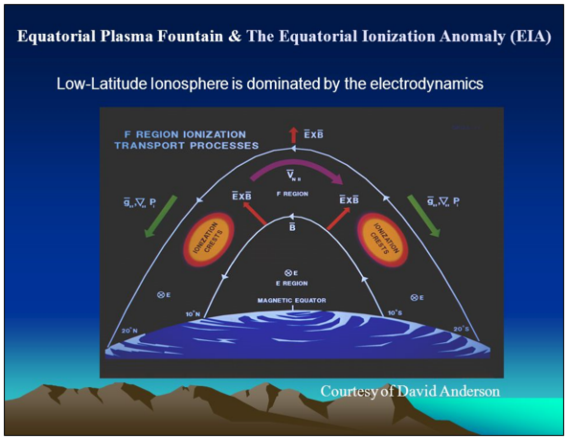

Figure 20 – Schematic diagram showing how plasma is transported from the equatorial region to high altitudes and subsequently to approximately 20° magnetic latitude through the action of electric and magnetic fields ($\vec{E} \times \vec{B}$), gravity and pressure gradients. Source: Basu et al. (2009)

3.5 The Pre-reversal enhancement (PRE)

During the day, plasma motion within the equatorial ionosphere is directed westward and upward due to E×B drift, while at night, it reverses direction to eastward and downward. The interaction of neutral winds stemming from temperature gradients facilitates the E-region dynamo, which generates the polarization electric field. However, this electric field is negligible in the F region. As night falls, the zonal drift intensifies, resulting in a vertical upward plasma drift at dusk, hence earning the moniker "evening enhancement" or "Prereversal Enhancement" (ABDU et al., 1991). This enhancement is associated with a high conductivity gradient across the day-night terminator after sunset. Key factors such as the F region, neutral wind, and electrical conductivity of the E region act as initiators for the process of prereversal enhancement, as illustrated in Figure 21. The eastward electric field driven by neutral wind interaction solely drifts ions upward, leading to charge separation due to perturbation. Moreover, this electric field, resulting from charge separation and sharing the same direction as thermospheric winds, extends into the E region along magnetic field lines with high conductivity, forming equipotential lines (KELLY, 2012). Before sunset, the F region experiences a short circuit due to the high Pedersen conductivity generated in the E region. However, at night, the conductivity diminishes significantly, leading to a decrease in electron density and the formation of a downward electrical field in the F region. At the terminator, the eastward electrical field experiences enhancement immediately before the reversal of the electrical field drift.

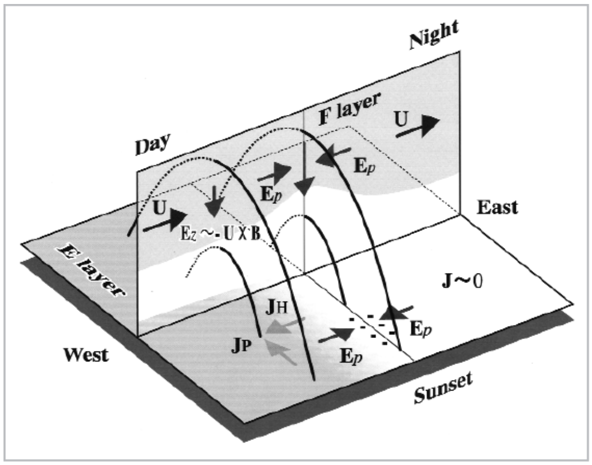

Figure 21 – The electric field evening enhancement driven by the F-region dynamo. Source: Farley et al. (1986)

3.6 Ionospheric irregularities

Both theoretical and experimental research conducted over the past decades have revealed that plasma instability mechanisms contribute to the development of ionospheric irregularities. These irregularities manifest as small structures ranging from meters to hundreds of kilometers, leading to ionospheric scintillation (HOLLING, 1992). They are predominantly observed in two distinct regions on Earth: the polar or auroral regions, and the equatorial regions (EZEKOYE; OBODO, 2007). In polar regions, ionospheric irregularities arise due to particles precipitating into the ionosphere from the magnetosphere, which are the same particles responsible for producing the visible aurora.

The influx of energetic particles from the magnetosphere into the ionosphere typically triggers the generation of irregularities in polar regions. These ongoing particle emissions lead to the formation of bubbles, which intensify to produce scintillations, particularly visible during daytime. However, they become notably prominent during periods of high geomagnetic activity and at nighttime. In equatorial regions, after sunset, ionization bubbles form at the lower edge of the ionosphere and ascend during the night. Equatorial and low-latitude irregularities can occur from post-sunset until pre-dawn hours, predominantly at night. In the literature, irregularities are generally classified into two main categories: large patches and individual field-aligned irregularities (LIDDLE; LYTH, 2000). According to Koster (1963) irregularities appear smaller during nighttime but exhibit gradual pattern changes over time. Yokoyama e Stolle (2017) highlight that ionospheric irregularities are small-scale structures in plasma density generated by the gravitationally driven Rayleigh-Taylor instability. (SULTAN, 1996) specifies that the instability growth rate (γ_{RT}), neglecting chemical recombination, can be expressed as;

$$\gamma_{RT} = \frac{\Sigma_P^F}{\Sigma_P^E + \Sigma_P^F} \frac{\overrightarrow{\nabla} N}{N} \cdot \left[\frac{\overrightarrow{E} x \overrightarrow{B}}{B^2} - \frac{\overrightarrow{g}}{v_{in}} - \overrightarrow{U_n} \right] \tag{3.39}$$

The irregularities development involves two enabling factors and three driving effects which are shown in the equation 3.39 above. At sunset, the enabling condition occurs, When the F region Pedersen conductivity ratio $[\frac{\Sigma_P^F}{\Sigma_P^E+\Sigma_P^F}]$, approaches unity and the electron density gradient, $[\frac{\overrightarrow{\nabla}N}{N}]$ is large. The upward EXB drifts $\left[\frac{\overrightarrow{E}x\overrightarrow{B}}{B^2}\right]$ have been marked as the key drivers for the irregularity's developments. As mentioned by Fejer, Scherliess e Paula (1999) and Martinis, Mendillo e Aarons (2005) a strong upward drift in the post-sunset period remains the essential condition for irregularities to occur. The ionosphere moves to higher altitudes, during the period of the enhancement effects and these reduce the collisional frequency between ions and neutrals v_{in} and thus causing $\left[-\frac{\vec{g}}{v_{in}}\right]$ to be large. The neutral wind term $\left[\overrightarrow{U_n}\right]$ is defined as the component perpendicular to the magnetic field.

According to Sultan (1996) and Woodman (2009) the gravitational Rayleigh-Taylor instability mechanism is a significant factor in the development of irregularities in the equatorial and low latitude ionosphere. Additionally, Fejer, Scherliess e Paula (1999) emphasizes that vertical ExB drift is a primary driver of this phenomenon.

During daytime, the magnetic field aligns parallel to the Earth's surface, while the eastward electric field generated by the E-region dynamo prevails at these latitudes. Consequently, plasma drifts upward over the geomagnetic equator, and under the influence of gravity and pressure gradient forces, moves along magnetic field lines. This gives rise to the equatorial anomaly, resulting in minimal ionization density in the F region at the magnetic equator, with maxima observed at the two crests, situated near the magnetic latitudes to the north and south, as noted by Abdu et al. (1995).

Booker e Wells (1938) observed that the most intense ionospheric irregularities occur in low-latitude regions near the magnetic equator. These irregularities were initially detected as the spreading of F layer echo traces on ionograms obtained with ionosondes, a phenomenon subsequently referred to as equatorial spread F. Irregularities in the F region are often referred to as 'spread F,' a term derived from the appearance of ionograms under conditions when irregularities occur. These irregularities predominantly occur during nighttime and during periods of geomagnetic activity (HERMAN, 1966).

This phenomenon affects the performance of space weather instruments and navigational signals, leading to disruptions in satellite-to-ground communications. Its impact varies depending on local time, season, latitude, and longitude, as well as solar and geomagnetic activity, as highlighted by Abdu (2012); Haridas, Manju e Arunamani (2018) and Balan, Liu e Le (2018). During periods of low solar activity, possible initiators of irregularities include gravity waves, TIDs, thermospheric winds, and other factors. The likelihood of their occurrence is also influenced by ionospheric variabilities driven by various mechanisms. One such mechanism is the coupling between the magnetosphere and ionosphere, which induces magnetic disturbances and consequently enhances the growth rate of irregularities. At low latitudes, ionospheric disturbances such as PPEFs and DDEFs, as discussed by Blanc e Richmond (1980) and Ram et al. (2016) predominantly occur during geomagnetically active periods. Kelley, Fejer e Gonzales (1979) highlighted that electric field perturbations induced by PPEFs are rapid and short-lived. The emergence of irregularities is also linked to thermospheric winds, both meridional and zonal in nature. DDEFs, on the other hand, stem from auroral heating processes triggered by dynamo action.

4 Instrumentation and methodology

This chapter outlines both the instrumentation and methodology employed in this study. The instrumentation will primarily utilize the Digisonde Portable Sounder (DPS) and the Global Navigation Satellite System (GNSS). The adaption of analog ion probes was widespread in the past due to their low maintenance costs and effectiveness in conducting ionospheric measurements and monitoring. However, ionospheric probing techniques have undergone significant technological advancements, with Digisondes replacing ion probes. This transition allows for greater control over data processing and storage through digital systems (REINISCH, 2004).

Figure 22 represents Digisonde and global map of Lowell Digisonde in the world. Digisonde facilitates the comprehension of radio wave behavior as they propagate through the ionosphere, providing information to grasp the factors directly influencing ionospheric phenomena.

The development of Digisondes has facilitated the expansion of ionospheric data collection and has concurrently lowered maintenance costs compared to analog ionosondes. When extrapolating the trajectories of the incident and reflected waves linearly, they intersect at a specific point, denoted as point A (refer Figure 23), known as virtual height.

For instance, the virtual height of the F2 layer typically ranges from 250 to 400 km, whereas for the F1 layer, it ranges from 200 to 250 km. However, it's acknowledged that the propagation speed of waves varies as they traverse the ionosphere, which acts as a dispersive medium. Consequently, the virtual height (h^I) differs from the real height (h).

With the development of Digisondes, it was possible to expand the amount of ionospheric data and reduce maintenance costs for analog ionosondes (GONÇALVES; FERREIRA; BATISTA, 2007). When the trajectories of the incident wave and the reflected wave are extrapolated linearly, they converge at a certain point A (23), at a height of reflection called virtual height. The virtual height of the F2 layer varies between 250 and 400 km, for example, while for the F1 layer the virtual height has a value between 200 and 250 km as indicated by Reinisch et al. (2005). However, it is known that the wave propagation speed varies when it propagates through the ionosphere, which acts as a dispersive medium. In this way, the virtual height (h^I) will differ from the real height (h).

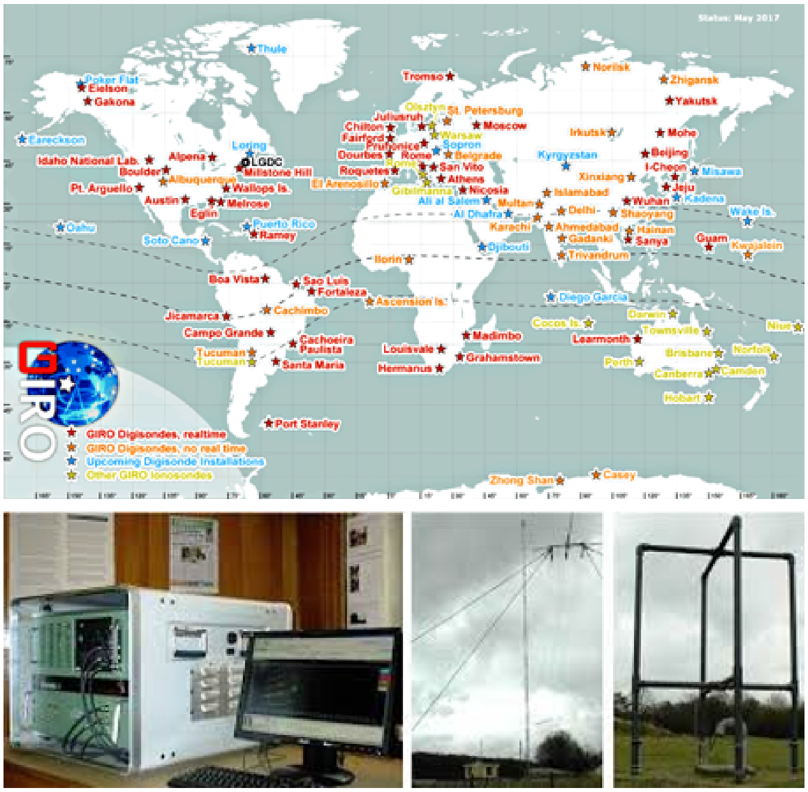

Figure 22 – Global Ionosphere Radio Observatory in the world including Digisonde, transmitter, and receiver.
Source: <https://giro.uml.edu/>

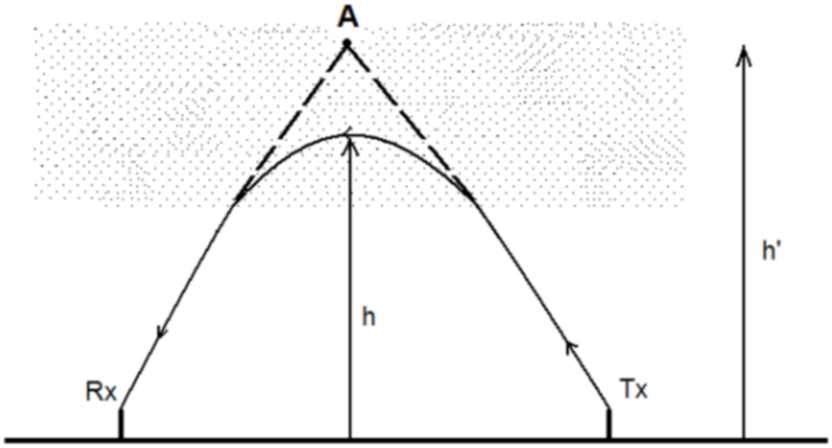

Figure 23 – Virtual height (h^I) of an ionospheric layer.
Source: Reinisch (2004))

The wave transmitted by the Tx antenna, when propagating through the ionosphere, undergoes refractions and delays with its initial speed. Point A represents the location where the wave would reflect if its speed of propagation was equivalent to the speed of light (REINISCH, 2004). The virtual height can be calculated as follows:

$$h^I = \frac{1}{2}ct \tag{4.1}$$

where c is the speed of light in a vacuum, and t is the transit time between the transmitted pulse and the received signal.

The Digisonde measures the ionosphere's F2 peak, offering real-time on-site processing and analysis to enhance radio signal propagation for communication purposes and to advance ionospheric research (REINISCH, 2004). Davies (1990) emphasizes that Digisonde transmits electromagnetic energy at frequencies in order from 0.5 to 30 MHz. It is designed to measure the transit time, that a pulse of radio waves takes to propagate at the transmitter-ionosphere-receiver interface, depending on the frequency. The electronic density profile, the plasma drift speed, and the polarization are obtained based on its measurements. These parameters are derived from frequency spectra as a function of altitude, which are represented by ionograms (WRIGHT; ARGO; PITTEWAY, 1996). The radio frequency signals emitted by the Digisonde are reflected in the ionosphere when the pulse frequency equals to the natural resonance frequency of the ionospheric plasma (REINISCH, 2004). Through measurement, various conditions such as the time elapsed between signal transmission and reception, the propagation speed of the wave in a vacuum, and the distance between the point of reflection and the Earth's surface are determined. This distance, known as virtual height, represents the electromagnetic pulse's travel distance to the region of maximum resonance in the ionosphere, accounting for interactions with regions possessing intermediate resonance frequencies (KOUBA; KNÍŽOVÁ, 2012).

4.1 Digisonde online databasing and quality control via SAO explore

The ionogram serves as a quality control measure to validate auto-scaling for ionosonde data. Consequently, significant attention has been directed towards its advancement, particularly in automated quality control techniques (REINISCH et al., 2005). It plays a vital role in refining ionospheric features through human inspection in both research and applied projects. Hence, an enhanced data management system is imperative to ensure the quality of ionogram-derived characteristics. This includes the utilization of key elements such as the "SAO Explorer," a tool for editing and visualizing Digisonde data; "DIDBase" (Digital

Ionogram Database), serving as a repository for both raw and derived Digisonde data under a database management system; and "ADRES" (Automated Data Request Execution System), facilitating the processing of specific data requests including periods and locations, along with data acquisition, verification, and reporting. In our investigation, the SAO Explorer demonstrated superior reliability and efficiency compared to alternatives, capable of analyzing thousands of ionograms. It is employed for manual verification and editing of automatically scaled Digisonde ionograms, as well as various visual representations to extract ionospheric features. The SAO-X workstations offer access to DIDBase, enabling comprehensive, platform-independent, remote operations for both data retrieval and storage over the internet (REINISCH et al., 2005). Previews of typical SAO explorer output are shown in Figure 24 and available at <https://ulcar.uml.edu/Installation/SAO-X/install.htm.>

Connecting to jdbc:firebirdsql://129.63.134.212//ext/db/ib/didb

SAOExplorer v 3.5.1

Copyright (c) UMLCAR 1998-2012

Loading complete

University of Massachusetts Lowell
Center for Atmospheric Research

```
2018.09.21 13:49:23.171: SAOExplorer 3.5.1 started...
```

No files opened for reading

Figure 24 – Interface of ionogram s data processing using SAO explorer.
Source: <https://ulcar.uml.edu/Installation/SAO-X/install.htm.>

4.1.1 Ionogram analysis using SAO Explorer

Ionograms display echo amplitudes versus virtual height (time-of-flight) and frequency (BERTONI, 2004). Each ionospheric layer is characterized by virtual heights (h’E, h’F, h’F2) and critical frequencies (foE, foF1, foF2). The widely adopted Automatic Real-Time Ionogram Scaling with True-height (ARTIST) and the True Height Profile Inversion Tool

(NHPC) are utilized for real-time calculation of electron density profiles, as described in Reinisch e Xueqin (1983) and Xiao et al. (2020). The illustration in Figure 25 shows a sample ionogram depicting the reflections of echoes, with frequency (including noise) plotted on the horizontal axis and virtual height on the vertical axis. This ionogram indicates the presence of the sporadic E layer (Es) and F1, F2, and F3 representing reflections. The signal amplitude is represented by curve pixel count, Doppler shift by curve color, and polarization by color gradient.

Figure 25 – The sporadic layer E (Es), and Reflections (F1, F2, and F3)of the F region are display in the ionogram interface.

Source: <https://giro.uml.edu/ionogram-data.html>

Digital ionograms offer several parameters categorized into three main groups: (i) E Region Group, denoted by the prefix "E" in the parameter code, (ii) Region F Group, identified by the acronyms F1 and F2 as prefixes in the parameter codes, and (iii) Independent Group, which provides parameters irrespective of the region and lacks a prefix in the parameter code. However, the independent ionospheric parameters include: (i) fmI, indicating the minimum frequency at which scattering traces are observed in layer F, and (ii) fmin, denoting the minimum frequency at which the "echo" trace is observed on the ionogram.

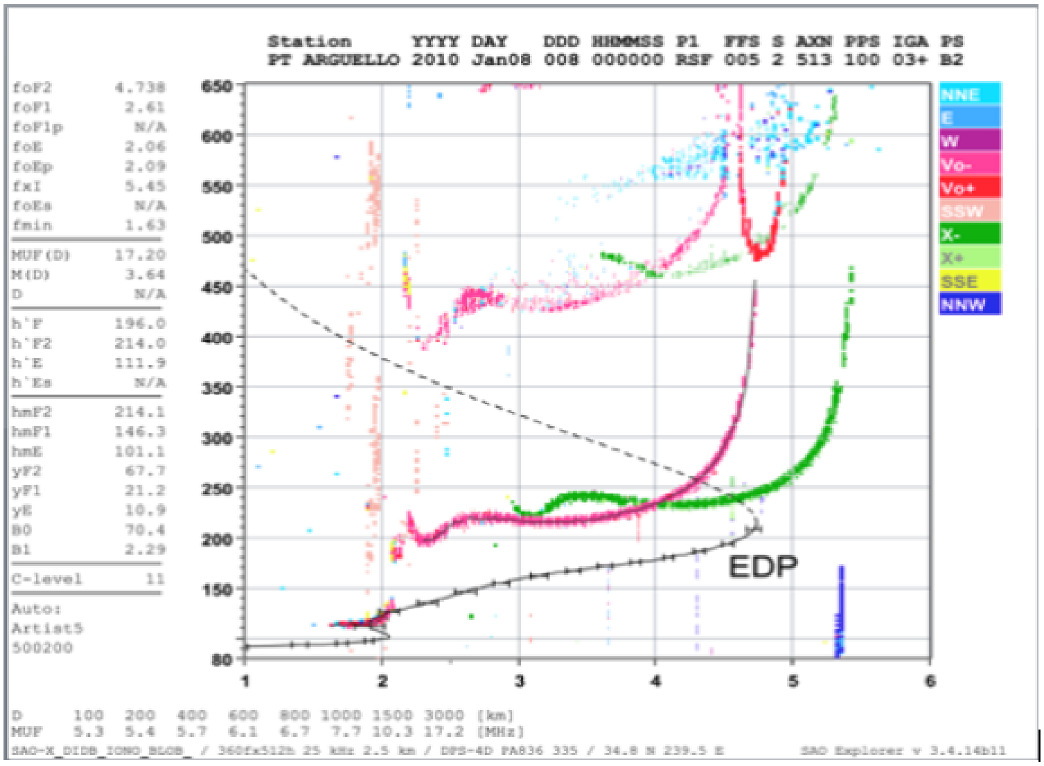

```
Station      YYYY DAY   DDD HHMMSS P1  FFS S AXN PPS IGA PS
PT ARGUELLO 2010 Jan08 008 000000 RSF 005 2 513 100 03+ B2
```

```
foF2      4.738
foF1       2.61
foF1p       N/A
foE        2.06
foEp       2.09
fxI        5.45
foEs        N/A
fmin       1.63
MUF(D)    17.20
M(D)       3.64
D           N/A
h`F       196.0
h`F2      214.0
h`E       111.9
h`Es        N/A
hmF2      214.1
hmF1      146.3
hmE       101.1
yF2        67.7
yF1        21.2
yE         10.9
B0         70.4
B1         2.29
C-level      11
Auto:
Artist5
500200
```

```
D      100  200  400  600  800 1000 1500 3000 [km]
MUF    5.3  5.4  5.7  6.1  6.7  7.7 10.3 17.2 [MHz]
SAO-X_DIDB_IONO_BLOB_ / 360fx512h 25 kHz 2.5 km / DPS-4D PA836 335 / 34.8 N 239.5 E          SAO Explorer v 3.4.14b11
```

Figure 26 – shows the various reflections on the ionogram interface.
Source: <https://giro.uml.edu/ionogram-data.html>

The Digisonde ionogram exhibits signals reflected from the ionosphere in a frequency versus travel time format, where signal intensity is represented by pixel intensity, wave polarization, angle of arrival, and Doppler frequency displayed in various colors. Each sounding frequency unveils distinct reflected signals (echoes), forming traces within the ionogram image. Red (green) colors denote vertical echoes with O-polarization (X-polarization). The ARTIST software scales the ionogram and conducts real-time calculations of the vertical Electron Density Profile (EDP). Thin black lines depict ARTIST-identified O-traces, while the black line with uncertainty bars illustrates the calculated bottom-side EDP. The extraction and interpretation of signal traces in ionogram images present a complex challenge in feature recognition.

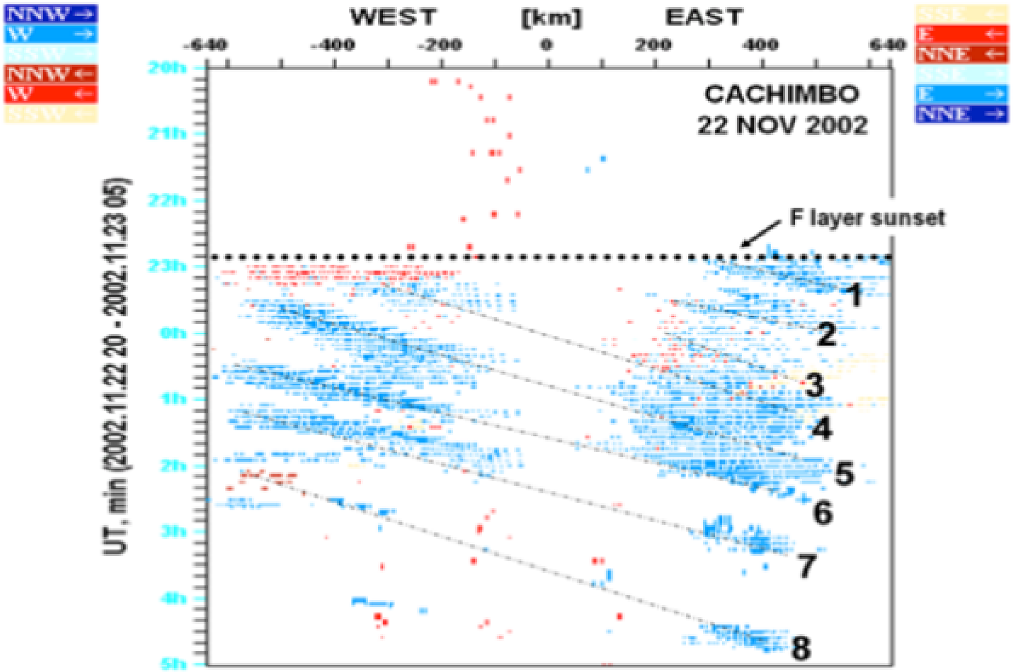

Figure 27 – shows a sample of spread F Directogram in Brazil.
Source: <https://giro.uml.edu/ionogram-data.html>

The Digisonde Spread F Directogram displays the temporal information of echoes resulting from reflections propagating vertically after encountering irregular plasma structures. The Y-axis represents time, while the X-axis denotes the horizontal distance in the ionosphere to the reflection point, with 0 indicating the location of the sounder. Vertical echoes are not depicted; a blank directogram indicates the reflections of the echoes of the transmitted wave into the ionosphere. The development of Spread F conditions is illustrated by the signatures in the directogram (see figure 27). The Doppler shift of echoes is analyzed to distinguish plasma structures approaching on one side and departing on the other, with the same color scheme applied (BHARGAVA; BHARGAVA, 2019). In a sample directogram, an eastward drift of 8 plasma bubbles' development is detected by the Cachimbo Digisonde in Brazil.

4.2 Global navigation satellite system (GNSS)

GNSS systems provides navigation, positioning, and timing services on a global or regional basis. It comprises constellations of satellites that provide global coverage for geospatial positioning, allowing electronic receivers on the Earth's surface to determine their locations (latitude, longitude, and elevation) using temporal signals transmitted via radio waves from satellites in line of sight. The four GNSS systems currently in operation are; the Global

Positioning System (GPS) from the United States [<https://www.gps.gov/systems/gps/>], the European Space Agency's Galileo [<https://www.esa.int/Applications/Satellite_navigation/Galileo_and_EGNOS>], Russia's GLONASS [Globalnaya Navigazionnaya Sputnikovaya Sistema) [<https://www.ehttps://glonass-iac.ru/en/about_glonass/>], and China's BEIDOU [<https://novatel.com/an-introduction-to-gnss/gnss-constellations/beidou>]. These GNSS systems utilize a constellation of orbiting satellites in coordination with a network of ground stations. However, this research confines its discussion solely to the GPS. In the South American sector, the GNSS receiver network includes the Brazilian Continuous Monitoring Network (RBMC), which belongs to the Brazilian Institute of Geography and Statistics (IBGE), the Argentine Continuous Satellite Monitoring Network (RAMSAC), the Low Latitude Ionospheric Sensor Network (LISN), and the International GNSS Service (IGS).

4.2.1 Global positioning system (GPS)

The Total Electron Content (TEC) is determined by the concentration of free electrons along the path of the electromagnetic wave between satellite and the receiver, given by

$$TEC = \int_{receiver}^{satellite} N.ds \tag{4.2}$$

according to Ya'acob, Abdullah e Ismail (2010).

where N and ds represent the electron density and distance respectively, It serves as an important parameter for navigation measurements for single-frequency receivers. According to Calais e Minster (1996), TEC measurements are based on the Faraday Rotation effect on a linear polarized propagating plane wave. This was traditionally accomplished by utilizing unique transmitters in geostationary and non-geostationary satellites over decades. However, nowadays, TEC measurements are primarily conducted using GPS data, providing at least 4 and potentially up to 9 TEC values within a 1000 km radius from the receiving station simultaneously every 30 seconds (the usual period). The sole objective of GPS is to determine the position and velocity of a fixed or mobile object located on or near the Earth's surface. The GPS system consists of space, control, and user segments, comprising 32 operational satellites distributed across six orbital planes (with 8 satellites in each plane). These satellites orbit at an altitude of around 20,200 km with an inclination of 55°, resulting in an orbit period of approximately 12 sidereal hours (CAMPOS; WANNINGER; SEEBER, 1993). Satellite information is processed at the master control station to determine satellite orbital positions, clock errors, and other navigation data parameters. Each signal transmission from a GPS satellite depends on two L-band frequencies with code modulations. By comparing these signals with a reference code, it becomes possible to measure the travel time of both the code and the carrier between the satellite and the receiver, yielding the following four observables: thus P_{L1}, Φ_{L1}, P_{L2}, Φ_{L2} (pseudorange with modulation P and phase Φ for L_1 and L_2). The pseudoranges from the code travelling time is express as

$$P = \rho + c.(dT - dt) + \Delta i_i^{iono} + \Delta^{trop} + b_i^{p,r} + b_i^{p,s} + m_i^p + \varepsilon_i^p \tag{4.3}$$

and the carrier phases express as

$$\phi_i = \lambda_i.\phi_i = \rho + c.(dT - dt) + \phi_i N_i - \Delta_i^{iono} + \Delta^{tro} + b_i^{\phi,r} + b_s^{\phi,r} + m_i^{\phi} + \varepsilon_i^{\phi} \tag{4.4}$$

where i = 1, 2 corresponding to carrier frequencies L1 and L2, P is the code. pseudorange measurement (in distance units), ρ is the geometrical range between satellites and receiver, c is the vacuum light speed, dT, dt are the receiver and satellites clock offsets from GPS time, Δ^{iono} = 40.3 TEC/fi 2 is the ionospheric delay, fi is the carrier frequency L_i, Δ^{tro} is the is the tropospheric delay, b_i are the receiver and satellite instrumental delays on P and Φ, m_i are the multipath on P and Φ_i measurements, ε_i are the receiver noise on P and Φ, ϕ_i are the carrier phase observation (in distance units), Φ_i are the carrier phase observation (in cycles), λ = c/f is the wavelength, N_i are the unknown L_i integer carrier phase ambiguities as noted by (ALLEN, 1998). By combining P_{L1}, Φ_{L1}, P_{L2}, Φ_{L2}. TEC value are obtained for modulation and phase in the below expression;

$$TEC_p = 9.52.(P_2 - P_1) + instr.delays + multipath + noise \tag{4.5}$$

Which is considered highly noisy and

$$TEC_{\phi} = 9.52.[(\Phi_1 - \Phi_2) - (N_1\lambda_1) - N_2\lambda_2)] + instr.delays + multipath + noise \tag{4.6}$$

which is less noisy than TEC_p, but ambiguous. However, the ambiguity is eliminated by averaging ($TEC_P - TEC_{\phi}$) across a satellite pass (phase connecting arc), thus

$$TEC_{Levelled} = TEC_{\phi} - (TEC_{\phi} - TEC_P) \tag{4.7}$$

This process "levels" the TEC to the unambiguous TEC_P, incorporating the TEC information from the less noisy TEC_{ϕ} while also accounting for instrumental delays, multipath, and noise.

The geographic location of the VTEC is determined by the position of the piercing point, which is the intersection between the satellite receiver's path and the thin layer. The vertical

TEC (VTEC), [1TECU= 10^{16} electron/m^2], which depends solely on geographical location and time is given by

$$\chi = \frac{\pi}{2} - El - arcsin\left(\frac{R_e}{R_e + 300}\right) Xcos\,(El) \tag{4.8}$$

Where, χ represents the elevation angle of the satellite as observed from the receiver's perspective, aiding in estimating the ionospheric piercing point (IPP) within the F2 region.

Additionally, TEC at the IPP, referred to as VTEC, is also expressed by Lyon (2000) as:

$$VTEC = STEC.\left[1 - \left(\frac{R_e cos\,(\theta)}{R_e + H_{ipp}}\right)\right]^{-\frac{1}{2}} \tag{4.9}$$

R_e denotes the radius of the Earth, while El represents the elevation angle with average height of IPP considered to be 300 km, thus H_{ipp} and θ is elevation angle in radians.

The table 4 displays the three L-band frequencies used by GPS satellites along with their corresponding wavelengths.

Table 4 – Frequencies and their respective Wavelengths for GPS.

L-Band	Frequency (Hz)	Wavelength (cm)
L1	f_1 = 1575.42	λ_1 = 19.05
L2	f_2 = 1227.60	λ_2 = 24.45
L5	f_5 = 1176.45	λ_5 = 25.49

Source: Calais e Minster (1996)

The present study utilized data from the GNSS, sourced from the RBMC operated by the IBGE. The locations of the GNSS and Digisonde stations employed in this research are depicted on a map of Brazil in Figure 28, with a black line indicating the magnetic equator and the triangles representing various stations. The GNSS and ionospheric sounding stations considered in this study were São Luís, Cachoeira Paulista, and GNSS (GPS) observations covering the South American sector from Fortaleza to Uruguaiana in 2003, all operating on the same local time. Detailed information regarding the stations utilized can be found in Table 6.

Table 5 – Stations used for digital ionospheric sounding (Digisonde) and GPS measurements, including their codes, observational methods, geographical coordinates (latitude and longitude), and dip latitudes. The stations are organized by dip latitude and instrument type, covering the Brazilian low-latitude region from the equatorial to the southern crest zones of the EIA.

Location	Symbol used	Obs.	Geog. Lat.	Geog. Long.	Dip Lat.	Local Time (LT)
Sao Luis	SL	DIGISONDE	2.6°S	44.2°W	1.5°S	LT=UT-3h
Fortaleza	FZ	GPS	3.8°S	36.9°W	6°S	LT=UT-3h
Creara	CRATO	GPS	7.23°S	39.41°W	1.75°S	LT=UT-3h
Imperatriz	IMPZ	GPS	5.53°S	47.48°W	2.64°S	LT=UT-3h
Recife	RECF	GPS	8.05°S	34.93°W	2.88°S	LT=UT-3h
Salvador	SALV	GPS	12.97°S	38.50°W	11.23°S	LT=UT-3h
Bom Jesus da Lapa	BOMJ	GPS	13.25°S	43.42°W	9.76°S	LT=UT-3h
Brasilia	BRAZ	GPS	15.9°S	47.93°W	10.3°S	LT=UT-3h
Cuiaba	CUIB	GPS	15.60°S	56.10°W	12.11°S	LT=UT-3h
Cachoeira Paulista	CP	DIGISONDE	22.5°S	45°W	31.7°S	LT=UT-3h
Para de Minas	PARA	GPS	19.86°S	44.61°W	18.0°S	LT=UT-3h
Vicosa	VICO	GPS	20.76°S	42.88°W	16.12°S	LT=UT-3h
Rio de Janeiro	RIOD	GPS	22.91°S	43.20°W	19.8°S	LT=UT-3h
Porto Alegre	POAL	GPS	30.03°S	51.23°W	23.07°S	LT=UT-3h
Santa Maria	SMAR	GPS	29.68°S	53.81°W	45.0°S	LT=UT-3h
Uruguaiana	UEPP	GPS	29.76°S	57.08°W	23.75°S	LT=UT-3h

(<https://latitudelongitude.org/>)

4.3 Data sets and methodology

Data sets

To understand the solar, interplanetary, and geomagnetic conditions during both the geomagnetic storm and the chosen quiet day, we utilized the 5-minute average data of various parameters. These include the solar wind speed (Vsw), interplanetary magnetic field (IMF-Bz), electric field (Ey), symmetric disturbance index (Sym-H, equivalent to Dst), and auroral electrojet index (AE). Additionally, we considered the solar flux F10.7 in $Wm^{-2}s^{-1}$, proton density (Np) in $\frac{1}{cm^3}$ obtained from measurements at the L1 Lagrangian point, 1 AU, by the ACE satellite and geomagnetic index (kp) from ground based magnetometers.

These measurements were accessible through the OMNI web NASA website at <https://omniweb.gsfc.nasa.gov/form/dx1.html>. Furthermore, we incorporated ionospheric parameters such as virtual F region height (h'F), F-layer peak height (hmF2), and plasma frequency (foF2), obtained from Digisonde measurements, along with VTEC data from GNSS. These data sets provide insight into the ionospheric variation of electron density during geomagnetic storms.

We utilized ionograms obtained from a Digisonde installed at the equatorial station in São Luís and at the south crest of the Equatorial Ionospheric Anomaly (EIA) in Cachoeira Paulista as well as VTEC using GPS from a chain of GNSS stations covering the South American sector in 2003 from Crato to Presidente Prudente, Brazil. We established a baseline using the five quiet days avarage (5QD) data based on the Kp index obtained at <http://wdc.kugi.kyoto-u.ac.jp/qddays/>, which serves as a control. This data provides the background behavior during undisturbed periods. For the CIR/HSS-driven geomagnetic storm and HILDCAA* events, the average of the five quietest days (5QD) in each month in 2003 was selected to calculate deviations from the disturbed days.

The GPS data are provided by the RBMC, which is operated by the IBGE. Finally, we included the thermospheric neutral composition O/N_2 ratio obtained from <http://guvitimed.jhuapl.edu/> to verify its relationship with TEC changes.

Methodology

- During each daily interval, we manually analyzed ionograms from 00:00 UT to 23:45 UT, examining ionospheric parameters such as foF2, hmF2, and h’F. Raw data was processed at 15-minute intervals using the SAO explorer software to deduce ionospheric variations in the equatorial and low latitude regions. Ionospheric parameter values were extracted, and the ionograms from the analysis period were manually reviewed and edited as needed to ensure accurate data extraction.

  The average of 5QD was calculated to examine the background behavior compared to the disturbed days. The VTEC was derived using the GPS-TEC retrieval algorithm developed by Gopi Krishna Seemala from the Institute for Scientific Research at Boston College, USA. This software incorporates DCB values provided by the RBMC, operated by the IBGE, to calculate TEC over the monitoring stations (SEEMALA, 2009; ESSIEN et al., 2021; CHINGARANDI et al., 2023).

- The percentage deviation caused by the geomagnetic disturbance in the foF2, hmF2, h’F and VTEC was computed using the method described by (ADEBIYI; ADIMULA; OLADIPO, 2015), defined as: $(\frac{foF2-foF2(5QD)}{foF2(5QD)}) \times 100$, $(\frac{hmF2-hmF2(5QD)}{hmF2(5QD)}) \times 100$, $(\frac{h'F-h'F(5QD)}{h'F(5QD)}) \times 100$, where $foF2$, $hmF2$, $h'F$ represents the plasma density, F layer true height, F layer virtual height (current days) measured during the storm time, and $foF2(5QD)$ represents the average of five quiet days. whereas VTEC as; $\frac{VTEC-VTEC(5QD)}{VTEC(5QD)}X100$, where $VTEC$ represents the disturbed days (current days), and$VTEC(5QD)$ the average of five quiet days. The deviation (Δ) in foF2, hmF2, h'F and VTEC was calculated as: Δ= foF2-foF2(5QD), hmF2-hmF2(5QD), h'F-h'F(5QD); Δ= VTEC-VTEC(5QD) as adapted from Liu et al. (2013) and Koga et al. (2011).

- Tracking the time derivative of the rate of change of TEC (ROT) is crucial for detecting ionospheric irregularities. ROT represents a measure of phase fluctuation activity and is obtained by computing the time derivative of STEC through an algorithm developed in MATLAB. ROT values are estimated for each selected GNSS station and then detrended for individual satellite tracks with elevation angles $\geq 45^o$. These values were mathematically expressed as follows: ROT(t)= $\frac{STEC(t+\Delta t)-STEC(t)}{\Delta t}$ as defined by Chingarandi et al. (2023); where Δt is the change in time in minutes. The Rate of TEC Index (ROTI), defined as the standard deviation of the detrended ROT values which can effectively characterize ionospheric fluctuation activity was also expressed as ROTI= $\sqrt{\langle ROT^2\rangle - \langle ROT\rangle^2}$ as defined by Pi et al. (1997). Based on the retrieved ROT values, ROTI was calculated over 5-minute periods using a sliding window to reveal the spatial structure of ionospheric irregularities over the Brazilian sector.

- The storm drift calculation was performed by using an empirical model developed by Fejer e Scherliess (1997) (i.e., implemented in Fortran). The total disturbance vertical drifts were expressed as:

$$
\begin{aligned}
V(t, AE) = \sum_{i=1}^{9} \Big[& a_1\, \Delta AE(t - 30\,\text{min}) \\
& + a_2\, \Delta AE(t - 90\,\text{min}) \\
& + a_3\, AE_d(1\text{–}6\,\text{h}) \\
& + a_4\, \alpha\, AE_d(7\text{–}12\,\text{h}) \\
& + \big(a_5\, \beta\, AE_d(22\text{–}28\,\text{h}) - 200\,\text{nT}\big)\, N_{i,4}(t) \Big].
\end{aligned}
$$

Where:

$$
\begin{aligned}
\Delta AE(t - 30\,\text{min}) &= AE(t) - AE(t - 1\,\text{h}), \\
\Delta AE(t - 90\,\text{min}) &= AE(t) - AE(t - 1\,\text{h}) - AE(t - 2\,\text{h}).
\end{aligned}
$$

The short-long term coupling was described by; $\alpha\binom{0}{\frac{AE(1-6hours)}{100nT}-2}$, thus for $AE(1-6hours) < 200nT$ and $200nT < AE(1-6hours) < 300nT$ respectively. β is determined using the formula $\beta = exp[\frac{-AE(1-12hours)}{90nT}]$ and $N_{i,4}(t)$, indicating cubic B-splines. The values of a_i and AE represent different factors or quantities that affect the calculation of V_d. The first two terms account for Prompt penetration drifts at time t and are based on the variation in the AE indices with average time delays of 30 and 90 min. The last three terms are used to account for ionospheric Disturbance dynamo effects.

- HILDCAAs* events were selected using the four criteria defined by (PRESTES et al., 2017) in 2003, as listed below;
  - AE peak values must exceed 1000 nT at least once per event.
  - The event should last at least two days.
  - AE values should not fall below 200 nT for more than four hours.
  - The HILDCAA* event must occur outside the main phase of the storm, with its onset considered until Dst index > -50 nT.
- In the quantitative analysis, we examined 143 geomagnetically disturbed days associated with 26 HILDCAA intervals. To calculate the monthly proportion of HILDCAA × days, we divided the number of disturbed days in each month by the total number of HILDCAA days and multiplied the result by 100, hence given us the percentage occurrence of HILDCAA* events.

  Furthermore, to assess and compare the distributions of disturbed and quiet days during HILDCAA intervals, we applied Gaussian (normal) fits to the normalized histograms, which serve as approximations of the probability density function (PDF). The histograms were normalized such that the total area under each curve equals one, thereby satisfying a fundamental property of a PDF. The PDF was estimated using the following equation: $\text{PDF} = \frac{\text{Frequency in bin}}{\text{Total number of samples} \times \text{Bin width}}$

  This approach ensures that the distribution accurately represents the relative probability of different parameter values within the dataset, enabling robust statistical comparisons between disturbed and quiet conditions during HILDCAA events.

4.3.1 Case Study of Pre-Halloween Geomagnetic Disturbances Induced by a CIR-Driven Storm and HILDCAA Event

In this section, we review the scientific contributions of the article “CIR-Driven Geomagnetic Storm and High-Intensity Long-Duration Continuous AE Activity (HILDCAA) Event: Effects on the Brazilian Equatorial and Low-Latitude Ionosphere—Observations and Modeling” by Abaidoo et al. (2025), recently accepted for publication in Atmosphere. The study presents a comprehensive case analysis of a moderate geomagnetic storm driven by a Corotating Interaction Region (CIR)/High-Speed Stream (HSS), which occurred from October 13 to 23, 2003—immediately preceding the well-known Halloween superstorm. This event, with a minimum Sym-H index of –100 nT, featured a prolonged recovery phase (∼9 days) and persistent disturbances associated with a HILDCAA event.

Using multi-instrument observations, including ground-based Global Navigation Satellite System (GNSS) receivers, Digisondes, and satellite data from the Advanced Composition Explorer (ACE), NASA’s Thermosphere Ionosphere Mesosphere Energetics and Dynamics (TIMED) mission, and the Solar and Heliospheric Observatory (SOHO), in conjunction with empirical modeling by Fejer e Scherliess (1997), the authors investigated ionospheric and thermospheric effects over the Brazilian sector. The results reveal F-layer uplifts of up to 120 km, expansion of the Equatorial Ionization Anomaly (EIA) beyond -20° dip latitude, and prolonged Total Electron Content (TEC) enhancements and plasma irregularities linked to the HILDCAA event. The storm also induced changes in thermospheric composition, notably enhancements in the $[O]/[N_2]$ ratio over Brazil, coinciding with TEC intensifications. Small-scale plasma irregularities, identified through the Rate of TEC Index (ROTI) below 0.05 TECU/min, expanded poleward from low latitudes into the South Atlantic Magnetic Anomaly (SAMA) region, indicating weak but persistent ionospheric disturbances.

4.3.2 CIR/HSS-Driven Geomagnetic Storm on October 12–23, 2003 and Dataset Description

On 13 October 2003, a moderate geomagnetic storm was initiated by a CIR followed by a HSS, characterized by a minimum Sym-H value of approximately –100 nT. The storm’s prolonged recovery phase—lasting nearly nine days—was sustained by continuous energy input into the magnetosphere, largely driven by multiple episodes of magnetic reconnection associated with strong southward excursions of the interplanetary magnetic field (IMF-Bz). These southward turnings were modulated by Alfvén waves embedded in the high-speed solar wind streams, which enhanced dayside reconnection when IMF-Bz remained negative for extended periods (TSURUTANI; GONZALEZ, 1987; GONZALEZ et al., 1994).

The auroral electrojet (AE) index increased sharply on 14 October, signaling the onset of enhanced auroral activity. From 15 to 22 October, a HILDCAA event was identified, reflecting persistent magnetospheric and auroral disturbances throughout the storm's recovery phase. This continuous AE activity highlighted the sustained impact of CIR/HSS structures on geospace, resulting in long-lasting moderate geomagnetic storm conditions.

To characterize the heliospheric and geomagnetic environment associated with this event, we analyzed 5-minute average data of the solar wind speed (V_{sw}), IMF-Bz component, interplanetary electric field (E_y), the Sym-H index (a high-resolution analog of Dst), and the AE index. These parameters were obtained from the ACE spacecraft at 1 AU via the OMNIWeb interface (<https://omniweb.gsfc.nasa.gov/form/dx1.html>). We also included solar flux F10.7 (in W m^{-2} Hz^{-1}), proton density (N_p, in cm^{-3}), and the planetary Kp index.

To investigate ionospheric responses, we analyzed ionograms from Digisondes located at two Brazilian stations: São Luís (2.6°S, 44.2°W; dip latitude: 1.5°S), located near the magnetic equator, and Cachoeira Paulista (22.5°S, 45°W; dip latitude: 17°S), located near the southern crest of the EIA. The ionospheric parameters—virtual F-layer height (h′F), F-layer peak height (hmF2), and critical frequency (foF2)—were manually scaled using the SAO Explorer software (<https://ulcar.uml.edu/SAO-X/SAO-X.htm>). To provide a quiet-time baseline, we utilized the 5 Quietest Days (5QD) reference, determined using the Kp index and available at <http://wdc.kugi.kyoto-u.ac.jp/qddays/>.

The VTEC was computed using the GPS-TEC software developed by Gopi Seemala, based on dual-frequency GPS data collected at GNSS stations in Fortaleza (3.8°S, 38.4°W; dip latitude: 6°S) and Rio de Janeiro (22.9°S, 43.2°W; dip latitude: 19.8°S). The GNSS data were provided by the Brazilian Network for Continuous Monitoring (RBMC), operated by the Brazilian Institute of Geography and Statistics (IBGE).

Figure 28 presents the spatial distribution of Digisonde and GNSS stations used in this study. Blue markers denote the GNSS stations, while red markers represent Digisonde locations. The magnetic equator and geomagnetic inclination lines are also included to contextualize the stations relative to the EIA region.

Additionally, we incorporated thermospheric composition data from the Global Ultraviolet Imager (GUVI) onboard the TIMED satellite, specifically the column-integrated [O/N_2] ratio. These data provide valuable insights into the thermospheric dynamics and composition changes during the geomagnetic storm and are available from the GUVI project website (<http://guvitimed.jhuapl.edu/>).

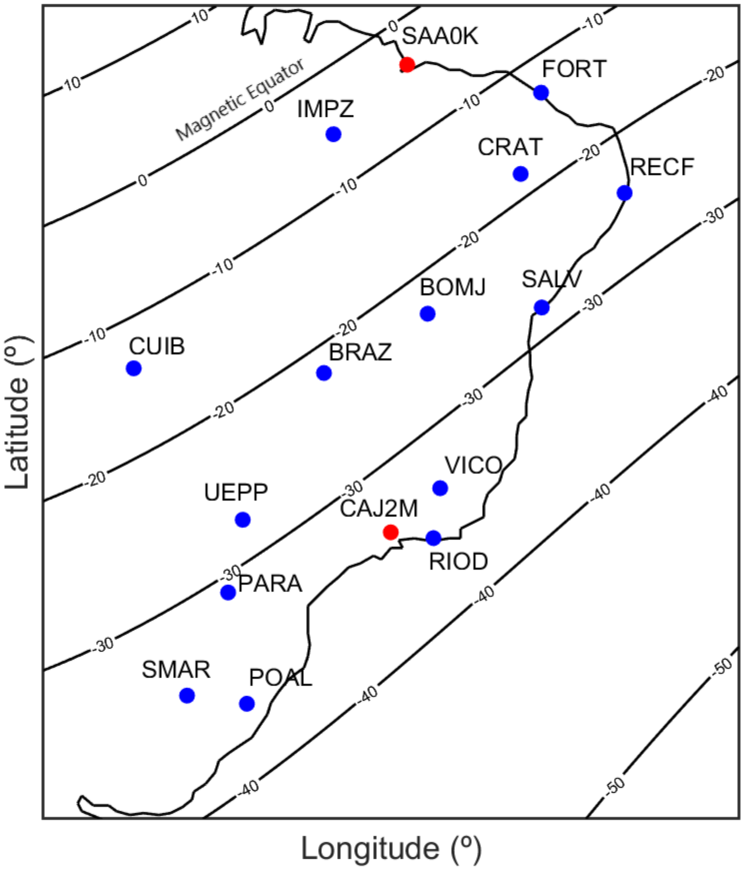

Figure 28 – Geographical distribution of ionospheric monitoring stations used in this study. The equatorial station São Luís (SL) is located at a dip latitude of 1.5°S, while Cachoeira Paulista (CP), situated near the southern crest of the Equatorial Ionization Anomaly (EIA), is at 17°S. Red dots indicate the locations of Digisonde instruments, and blue dots represent GNSS stations used to derive Total Electron Content (TEC) datasets. Black lines denote geomagnetic inclination, with the 0° line marking the magnetic equator, serving as a reference for the EIA region.

4.3.3 Coronal Hole, Solar wind and Interplanetary Way Parameter

Figure 29 shows a sequence of solar disk images in the extreme ultraviolet wavelength, captured between October 12 and 23, 2003. These images highlight transequatorial coronal holes (CHs), visible as dark regions that co-rotate with the Sun.

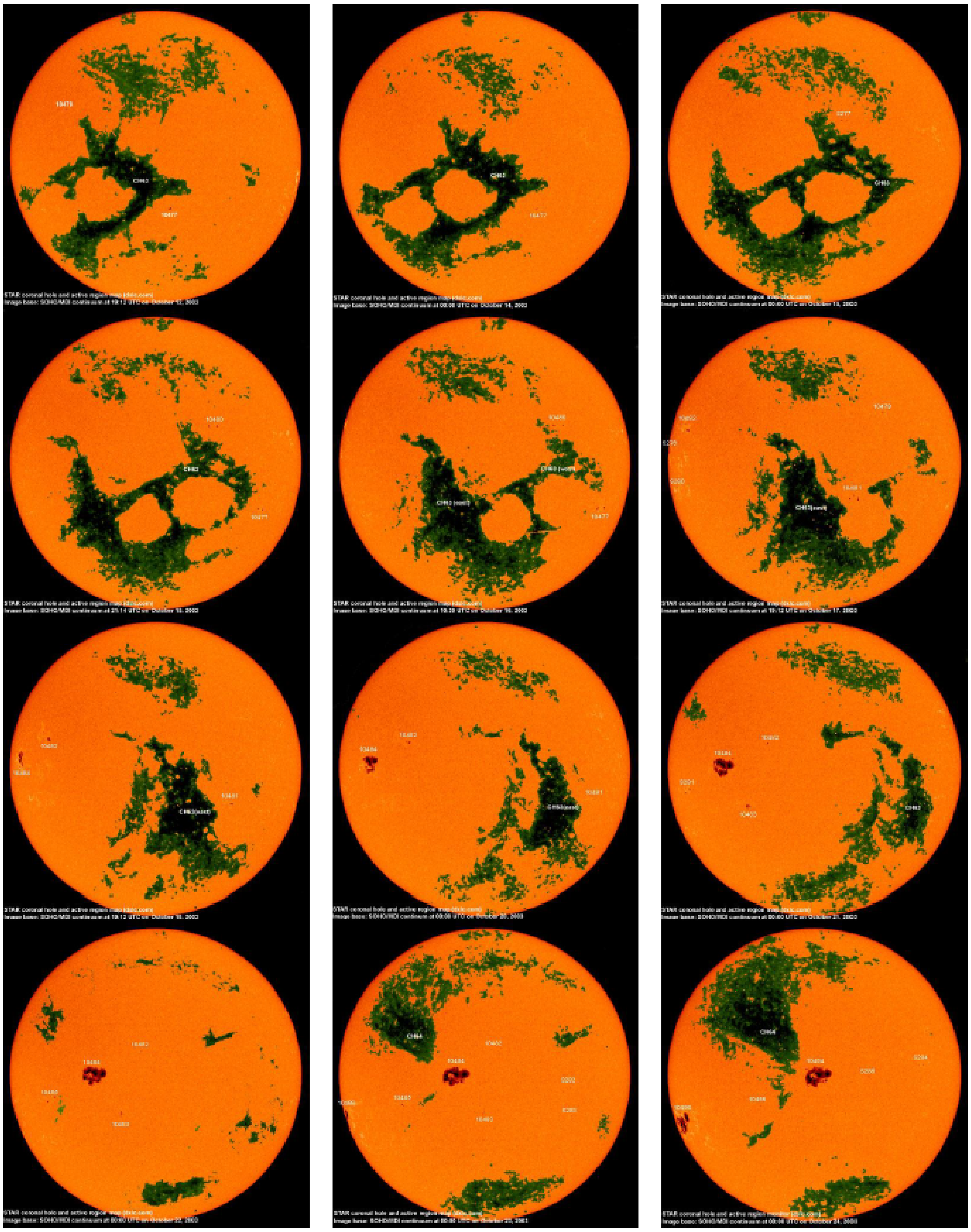

Figure 29 – SOHO images showing the coronal hole CH63 from October 12 to 23, 2003. The green areas represent the coronal hole structure as it evolves, with active regions labeled across different dates. These observations were captured in the ultraviolet emission spectrum, highlighting key coronal features.

As is well-known, CHs are most geoeffective when aligned near the solar disk's central meridian and around the solar equator, allowing for maximal interaction with Earth's magnetosphere (TSURUTANI; GONZALEZ, 1987). In the images, a large transequatorial coronal hole, designated CH63, crossed the center of the solar disk and reached the central meridian between October 12 and 18. Subsequently, it showed a reduction in area compared to its previous solar rotation, losing much of its extent in the northern hemisphere and merging with remnants of coronal hole CH59 in the southeastern quadrant.

During this period, HSS and CIR directed toward Earth were detected by ACE onboard instruments. These interactions led to enhanced coupling with Earth's magnetosphere, resulting in a moderate (Sym-H = -100 nT) and prolonged geomagnetic storm from October 13 to 23, associated with a HILDCAA event, as defined by Gonzalez e Tsurutani (1987), Prestes et al. (2016), Koga et al. (2011).

After October 17, as the coronal hole rotated westward and moved out of direct alignment with Earth, its geoeffectiveness gradually diminished, leading to a decrease in geomagnetic storm activity and reduced impacts on Earth's environment.

To characterize the interplanetary and geomagnetic conditions associated with this CIR-driven storm, we utilized 1-minute average datasets of the solar wind speed (V_{sw}), the proton density (N_{sw}), the Z-component of the interplanetary magnetic field (Bz), the interplanetary electric field component (E_y), the geomagnetic symmetric disturbance index (Sym-H, an analog of the Dst index), and the auroral electrojet index (AE). These data are displayed in Figure 30.

Between October 12 and 23, 2003, HSSs were detected, evidenced by a significant rise in solar wind speed, which exceeded 400 km/s on October 13 and peaked at 800 km/s on October 15. The corresponding peak in N_{sw} indicates the presence of a CIR—a compressed plasma region formed at the interface between fast and slow solar wind streams. Proton density showed substantial variability, with a major peak on October 13 exceeding 40 cm^{-3}, signaling the arrival of the CIR (TSURUTANI et al., 1999). The Bz component of the interplanetary magnetic field fluctuated significantly, ranging between -20 and 20 nT, particularly on October 14 during the storm's main phase.

It is crucial to highlight that during geomagnetic storms, particularly when the interplanetary magnetic field Bz is directed southward ($Bz < 0$), the impacts of PPEFs and DDEFs become especially prominent. During the main phase of the storm, a PPEF event is often observed, characterized by conditions where $Bz < 0$ and $Ey > 0$ due to magnetic reconnection processes as we observed in Figure 30. These reconnection events allow the solar wind to couple directly with Earth's magnetosphere, resulting in the rapid penetration of high-latitude electric fields to low-latitude and equatorial regions. PPEF can quickly alter its polarity and direction, influencing both daytime and nighttime ionospheric dynamics (FEJER; SCHER-

LIESS, 1997; BATISTA et al., 2006).

The Sym-H index reached a minimum of -100 nT, indicating a moderate geomagnetic storm. Sym-H measures the ring current intensity, which correlates with the energy stored in the magnetosphere during geomagnetic storms (GONZALEZ et al., 1994). The storm's prolonged recovery phase was driven by sustained energy input, resulting from multiple magnetic reconnection events triggered by large fluctuations in Bz. These fluctuations were associated with Alfvén waves embedded in the high-speed solar wind streams. Magnetic reconnection occurs when the IMF is oriented southward for extended periods, enabling direct coupling with Earth's geomagnetic field (TSURUTANI; GONZALEZ, 1987; GONZALEZ et al., 1994). An intense southward IMF can lead to enhanced plasma sheet convection, strengthening the ring current and intensifying the geomagnetic storm.

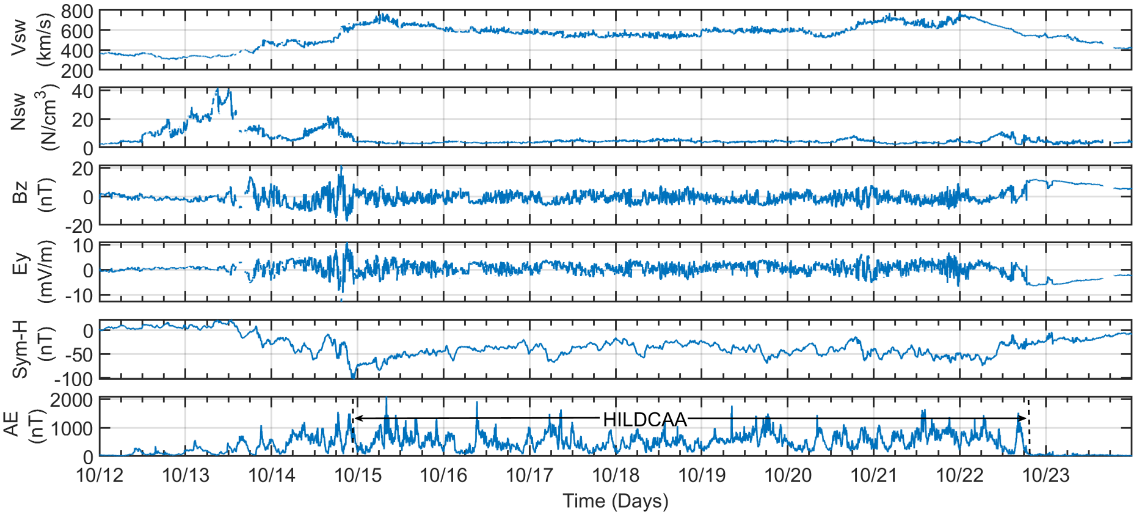

Figure 30 – Solar Wind and Geomagnetic Conditions during the CIR-driven storm from October 12 (00:00 UT) to October 24 (00:00 UT), 2003. The figure presents, from top to bottom: solar wind speed (Vsw, km/s), proton density (Nsw, cm^{-3}, the Z-component of the interplanetary magnetic field (Bz, nT), the Electric Field (Ey, mV/m), the symmetric disturbance index (Sym-H, nT), and the auroral electrojet index (AE, nT). A HILDCAA event is highlighted, beginning on October 15, 2003, and persisting until October 22, 2003.

A HILDCAA event was recorded between 15 and 22 October, indicating continuous, long-lasting auroral disturbances during this period. It is possible to observed that the AE index exceeds 1000 nT and remains predominantly above 200 nT for the remainder of the interval, with only brief drops. The elevated AE levels persist for approximately nine days, fulfilling the minimum duration requirement. Moreover, the Sym-H index indicates that the main phase of the geomagnetic storm ended on 14 October, confirming that the HILDCAA occurred during the subsequent recovery phase. The recovery phase of the storm extended from 22:21 UT (19:21 LT) on October 14 to 23:59 on October 23, lasting approximately 9 days. In addition to satisfying the traditional criteria, this event also aligns with the complementary parameters proposed in more recent studies, including sustained high-speed solar wind streams, moderate Sym-H fluctuations (remaining above -100 nT), and IMF B$_z$ oscillations of approximately ±10 nT. These observations collectively support the classification of this interval as an HILDCAA event (GONZALEZ; TSURUTANI, 1987; KOGA et al., 2011; PRESTES et al., 2016).

4.3.4 F-Layer Analysis

The F layer of the ionosphere plays a central role in determining ionospheric density and radio wave propagation, particularly during geomagnetic disturbances. This section presents a detailed investigation of F-layer behavior during the CIR/HSS-driven geomagnetic storm from October 12 to 23, 2003. Using data from Digisonde soundings at both equatorial and low-latitude stations in Brazil, we examine the temporal evolution of the ionospheric parameters such as virtual and peak F-layer heights and the critical plasma frequency. These diagnostics provide informations about the vertical transport and redistribution of ionospheric plasma under the influence of storm-time electric fields and thermospheric dynamics, with particular attention given to the impact of Prompt Penetration Electric Fields (PPEFs), Disturbance Dynamo Electric Fields (DDEFs), and the associated HILDCAA event.

Figure 31 presents a series of time-series plots from October 12 to 23, 2003, highlighting key ionospheric parameters derived from Digisonde measurements at the equatorial station of São Luís (SAA0K). The top panel shows the Sym-H index, a proxy for the intensity of geomagnetic activity.

The subsequent panels display h'F and hmF2 (in km), and foF2 (in MHz). During the storm's main phase on October 14, a significant F-layer uplift occurred, with increases up to 120 km compared to the 5-day quiet average (5QD), particularly around local sunset (22:21 UT / 19:21 LT). Concurrently, the $foF2$ values exhibited a reduction of approximately 3 MHz, likely due to plasma redistribution and depletion at lower altitudes.

To aid interpretation, the lower panels in Figure 31 illustrate deviations ($\Delta h'F$, $\Delta hmF2$, $\Delta foF2$) from quiet-time baselines, alongside normalized indices expressed as percentiles. The uplift patterns in $h'F$ and $hmF2$ persisted beyond the main phase into the extended recovery phase, correlating with variations in Sym-H. Negative deviations in $foF2$ remained during these periods, suggesting persistent low-altitude plasma depletion.

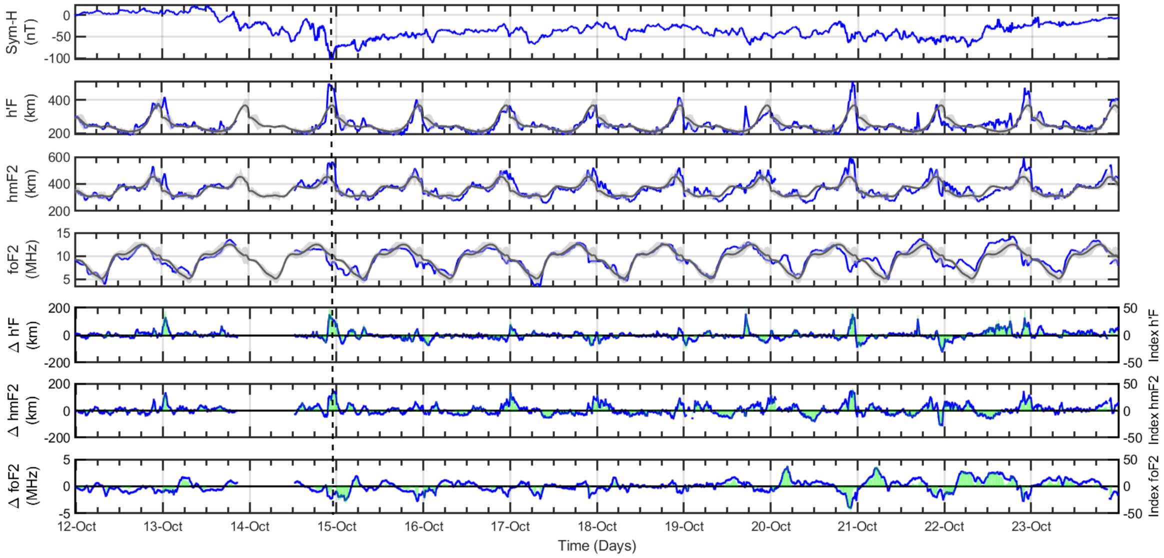

Figure 31 – Temporal variation of Sym-H and ionospheric parameters ($h’F$, $hmF2$, $foF2$) and their respective deviations at São Luís from October 12–23, 2003. Black lines show the 5QD means, with standard deviation bands in light gray. Green lines show indices expressed as percentiles. Dashed line marks the onset of the HILDCAA event.

The observed F-layer uplifts are closely tied to post-sunset ionospheric dynamics, particularly to the pre-reversal enhancement (PRE) of the zonal electric field. Under quiet-time conditions, PRE is caused by the sharp conductivity gradient across the day-night terminator, which enhances eastward electric fields in the E-region (ABDU, 2019). However, during disturbed periods, dawn-dusk electric fields originating from high latitudes can rapidly penetrate to the equator due to under-shielding of the Region-2 current system (JAGGI; WOLF, 1973; TSURUTANI et al., 1995).

PPEFs, with polarity influenced by local time (RICHMOND; PEYMIRAT; ROBLE, 2003), enhance the background eastward electric field and thereby intensify the vertical $E \times B$ plasma drift (KELLEY, 2009; ABDU et al., 1995). These storm-time PPEFs can significantly modify ionospheric dynamics, with effects visible in the uplift and reshaping of the EIA and in the generation of plasma irregularities.

The enhanced vertical drift at PRE time, observed during the storm main phase, can create favorable conditions for irregularity formation. In equatorial regions, these irregularities can evolve into Equatorial Plasma Bubbles (EPBs), particularly between October and March when their occurrence rate is seasonally higher. The strong vertical uplift can lead to EPBs reaching higher apex altitudes and extending toward higher latitudes than typical EIA crest positions. Although spread-F traces were consistently observed at São Luís (not shown), further assessment of EPB latitudinal extent requires GPS-based TEC data and the derived ROTI, to be discussed later.

Figure 32 presents similar parameters measured at Cachoeira Paulista, near the southern EIA crest. As in São Luís, several F-layer uplifts are observed throughout the storm period. Simultaneous uplifts at both locations suggest the action of under-shielding PPEFs, particularly during strong southward IMF Bz excursions. These electric fields strengthen the $\vec{E} \times \vec{B}$ drift, intensifying the fountain effect and pushing the EIA crests poleward.

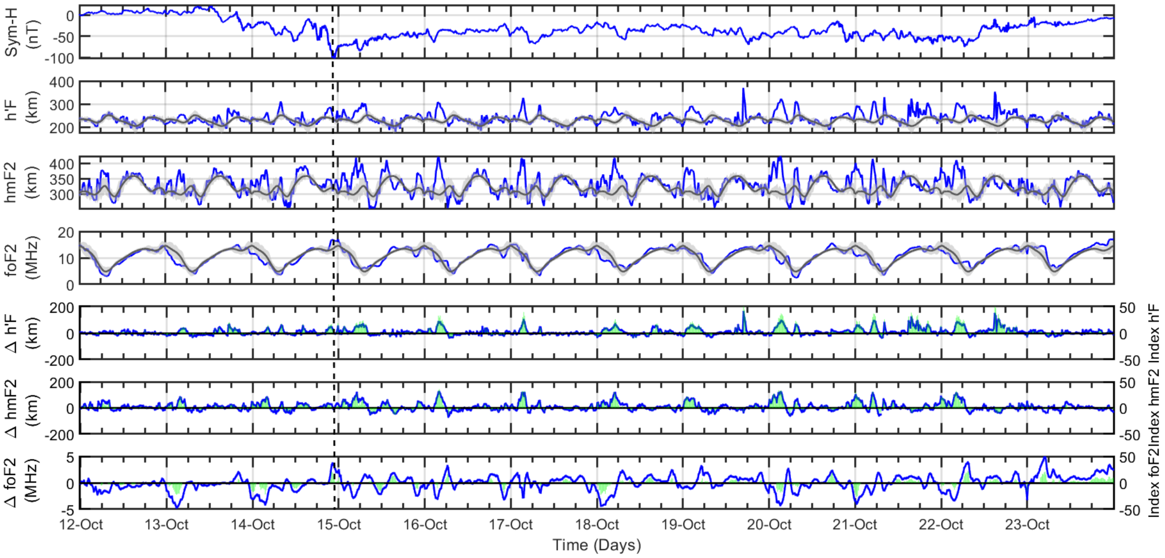

Figure 32 – Same as Figure 31, but for Cachoeira Paulista near the southern crest of the EIA. Deviations and indices highlight storm-time modifications in the low-latitude ionosphere.

However, caution is required in interpreting $hmF2$ and $foF2$ under strong spread-F conditions. Spread-F can distort ionograms, complicating automatic scaling and potentially introducing errors. As discussed further, this limitation affects confidence in parameter estimation during disturbed intervals.

Interestingly, nighttime increases in $foF2$ may also reflect the interaction of vertical and zonal plasma transport. Westward plasma drift dominates during post-sunset hours, while the daytime dynamics are influenced by equatorward meridional winds and downward drift due to wind reversal (ABDU et al., 1991). These effects are governed by the E-region dynamo and modulated by neutral wind patterns (KELLEY, 2009).

4.3.5 Empirical Modeling of Vertical Plasma Drifts

To investigate the impact of geomagnetic disturbances on equatorial plasma dynamics, we employed the empirical model developed by Scherliess and Fejer (1999), which estimates vertical plasma drifts based on auroral activity levels, particularly the AE index. This model distinguishes between the contributions from PPEF and DDEF, offering a robust framework for interpreting the electrodynamic response of the low-latitude ionosphere under storm-time conditions.

Figure 33 presents, from top to bottom panel: the vertical component of IMF, Bz, and the Sym-H index, in nT. From the third to bottom panel are presented: the calculated mean (quiet) vertical drift, (V$_{mean}$); the disturbed vertical drift, (V$_{d\ storm}$), the total vertical drift, (V$_{d\ total}$); the PPEF-Vd (PPEF) and DDEF-Vd (DDEF) components, respectively, in m/s for the whole storm interval. The mean vertical drift velocity (V$_{d\ mean}$) during quiet time exhibited its typical pattern, with an upward drift during the day and a downward drift at night.

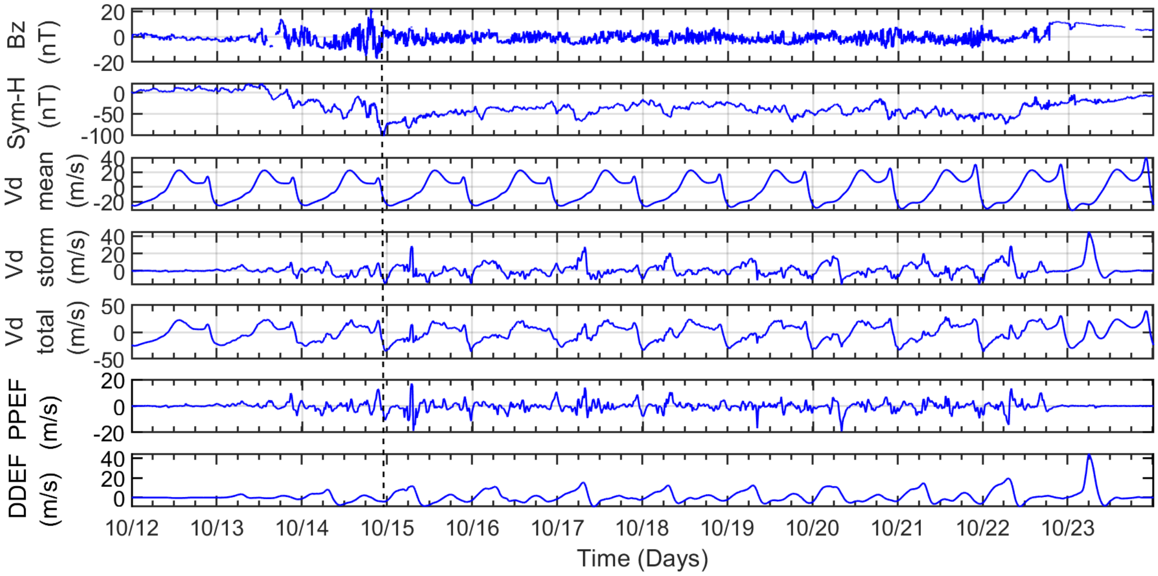

Figure 33 – Temporal variations of interplanetary and geomagnetic parameters during the CIR-driven geomagnetic storm from October 12 to 23, 2003. From top to bottom: IMF Bz (nT), Sym-H index (nT), modeled quiet-time vertical drift (V_d-mean), total disturbed vertical drift (V_d-total), and the respective PPEF and DDEF vertical drift components (m/s).

During the main phase of the storm on October 14, the total disturbed drift reached 10 m/s at around 23:00 UT (20:00 LT), closely aligning with the expected time of the PRE. This behavior is consistent with the F-layer uplift observed at São Luís, where the virtual height $h'F$ rose by approximately 120 km relative to the quiet-day mean, while $foF2$ decreased—indicative of plasma depletion from the lower F-layer.

As reported by Tsurutani et al. (2001), such sudden uplifts in the F-layer are frequently linked to rapid plasma motion induced by penetrating electric fields. Zonal electric fields play a dominant role in regulating vertical $E \times B$ drifts, especially during the pre-sunset and post-sunrise transitions, when steep conductivity gradients in the E-region and thermospheric winds are more influential (FEJER et al., 1991a).

The disturbed-time electric field contributions from DDEF arise from modified neutral wind patterns and storm-induced conductivity changes, which can persist long after the main storm phase (FEJER et al., 1979; BUONSANTO; WITASSE, 1999). According to Batista et al. (2006), storm-time downward drifts at the equator can be attributed to westward electric fields originating in the inner magnetosphere, whereas upward drifts are typically linked to the generation of post-sunset irregularities such as equatorial spread F.

Additionally, Rishbeth (1971) and Heelis et al. (1974) emphasized that nocturnal enhancements in F-layer height are strongly modulated by the eastward electric field generated via the F-region dynamo mechanism. The pre-reversal enhancement in vertical drift, which usually peaks around sunset, is known to provide favorable conditions for the onset of plasma instabilities, including equatorial plasma bubbles and scintillations (BHATTACHARYYA, 2022). This enhancement is a typical feature of solar maximum periods but becomes less prominent or even absent during solar minimum years, as shown by Fejer et al. (1979).

4.3.6 TEC Variations and EIA Evolution

In this section, we present a comprehensive analysis of TEC dynamics and the development of the EIA across Brazil during the geomagnetic storm induced by a CIR and HSS from October 12 to 23, 2003.

TEC variations were examined using GPS data from multiple stations spanning the geomagnetic equator, the southern EIA crest, and the SAMA region. Figure 34 compares observed TEC (blue line) with quiet-day averages (5QD, black line). Throughout the event, positive TEC anomalies dominated, particularly over the southern EIA crest (e.g., PARA) during the main storm phase on October 14. These enhancements are attributed to increased $E \times B$ vertical drifts driven by eastward PPEFs.

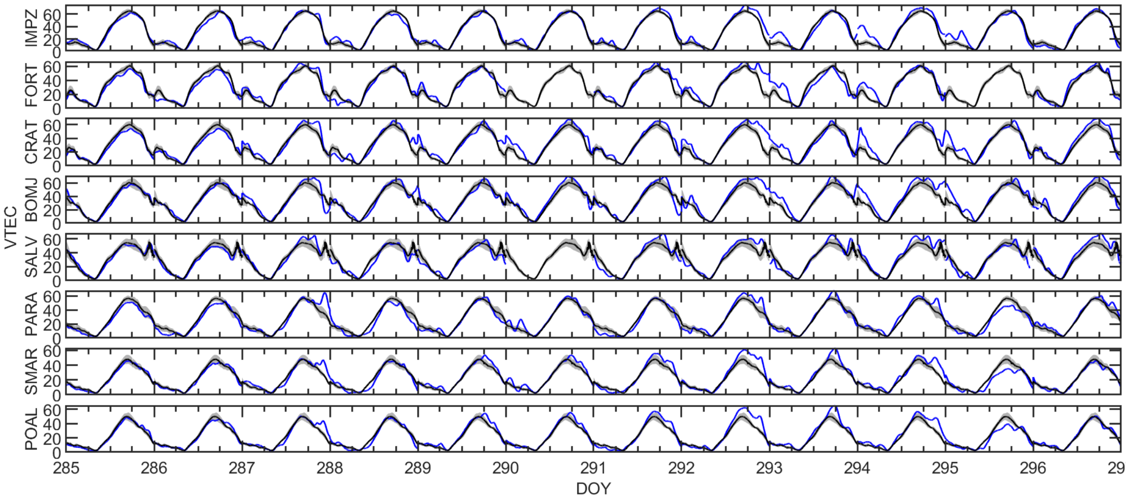

Figure 34 – VTEC variations from equator to southern EIA crest during the CIR/HSS-driven storm (October 12–23, 2003). Blue lines represent observed TEC; black lines show 5QD baselines.

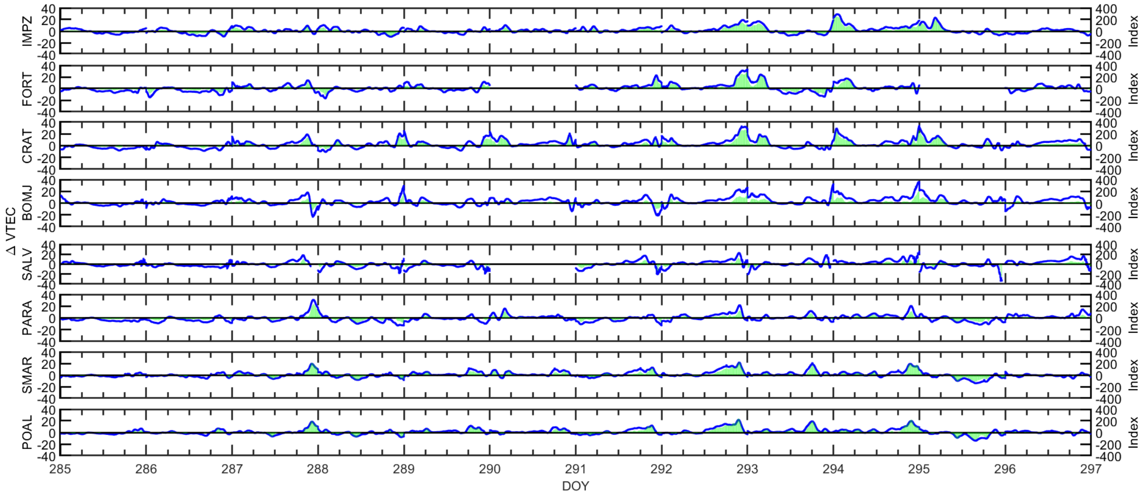

Figure 35 – Latitudinal distribution of ΔVTEC and normalized VTEC Index during the CIR-driven storm of October 12–23, 2003.

During the storm recovery phase (October 19–21), additional TEC intensifications occurred, consistent with DDEF activity. Sustained solar wind speeds and recurring geomagnetic perturbations contributed to prolonged TEC enhancement across all latitudes. This period also featured reinforced Pre-Reversal Enhancements (PREs), amplifying upward plasma drifts.

A sharp transition to negative storm conditions occurred on October 22, with TEC depletions observed across stations near the SAMA. Figure 35 presents the latitudinal distribution of VTEC deviations (ΔVTEC), percentile variations (δVTEC), and normalized indices, highlighting poleward EIA expansion and subsequent contraction.

To further illustrate EIA development, Figure 36 presents time-latitude contour plots of daily TEC variation. The EIA is consistently present, intensifying during the main and recovery phases, reaching latitudes as far as POAL (∼–20° dip). Elevated TEC values are closely linked to PPEF during storm onset and DDEF throughout the HILDCAA event.

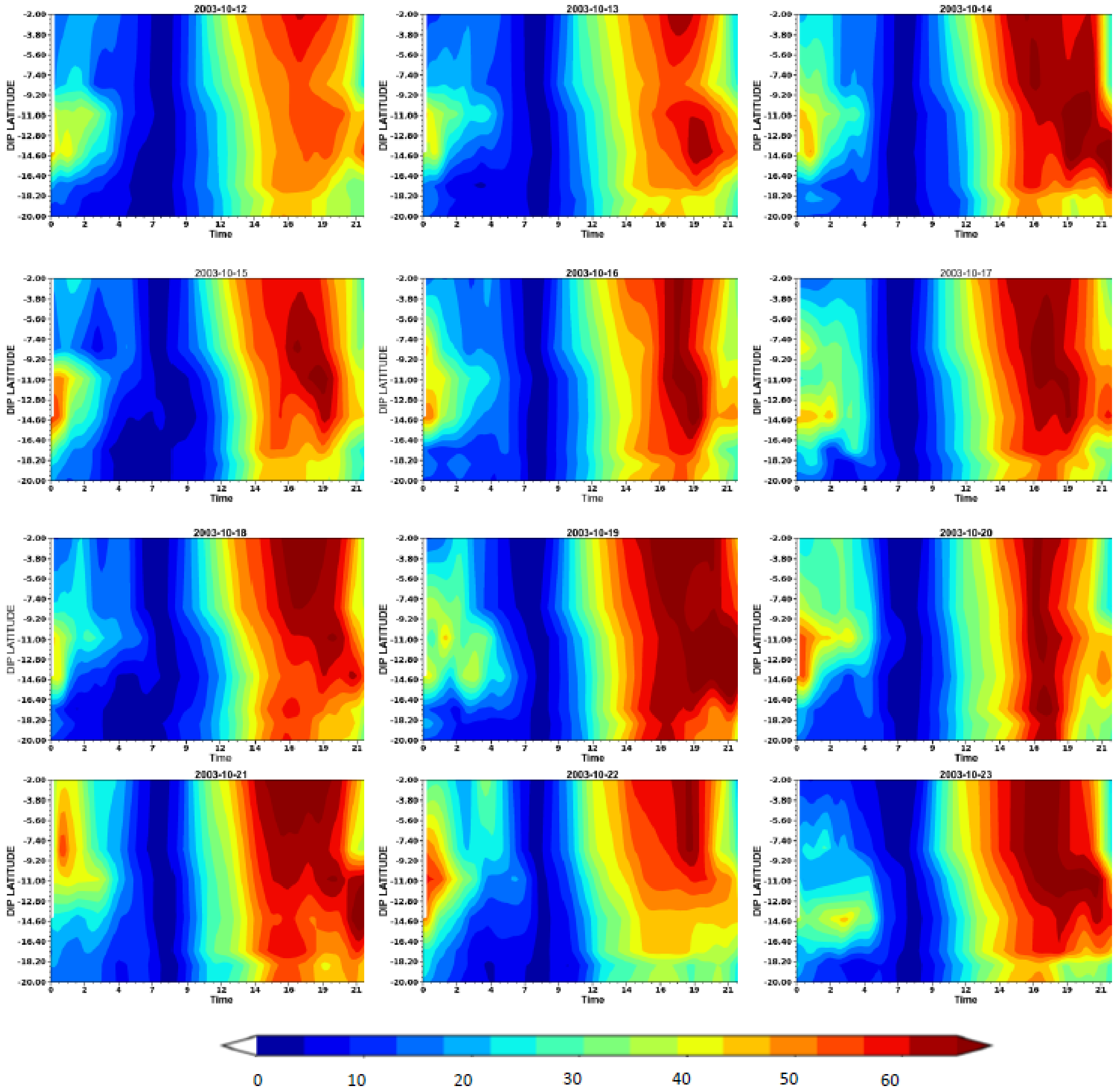

Figure 36 – Daily temporal GPS-TEC average contour plots for October 12–23, 2003, across the Brazilian sector.

Changes in thermospheric composition, revealed by $[O]/[N_2]$ ratios from GUVI/TIMED observations (see Figure 37), further explain the ionospheric response. These shifts reflect a coupling between magnetospheric energy input and neutral atmospheric dynamics, which collectively sustain the EIA beyond its typical boundaries.

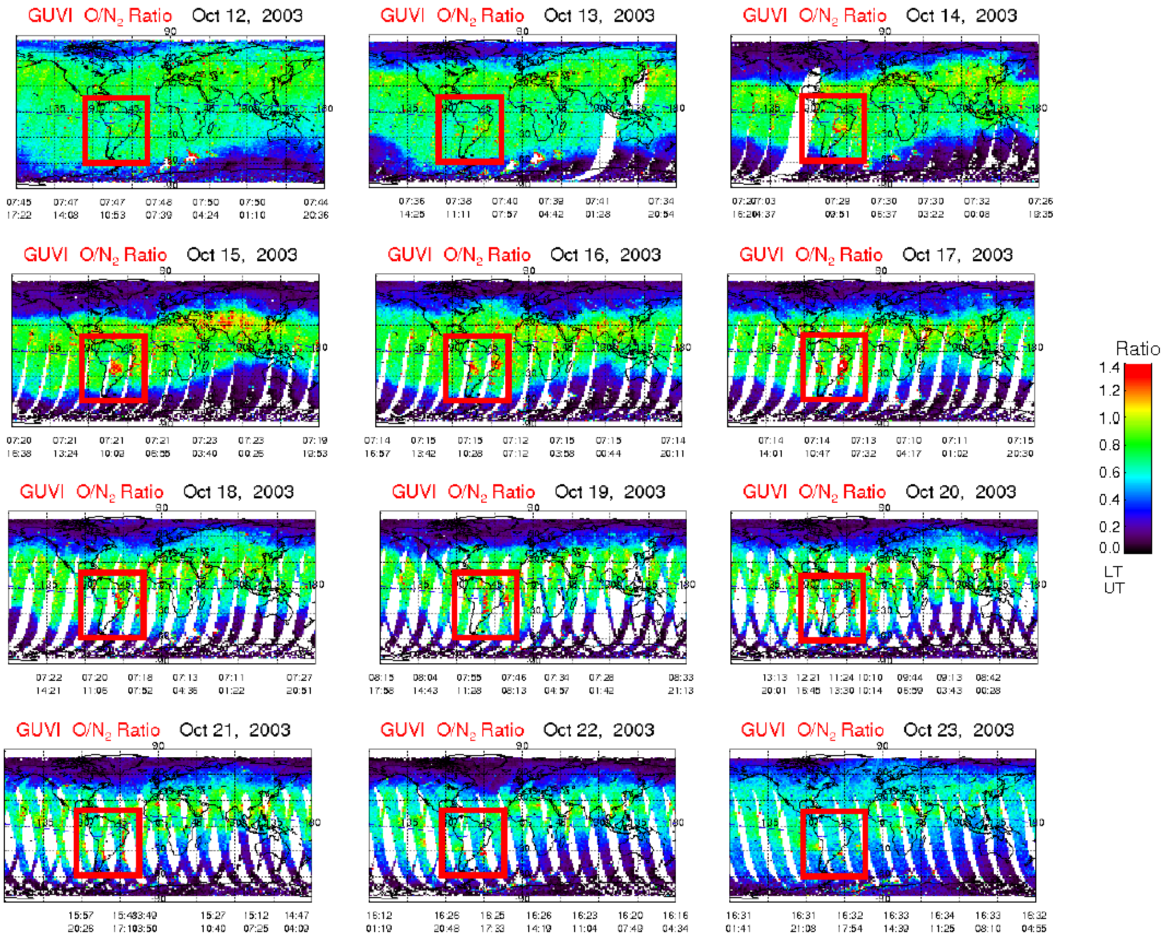

GUVI O/N_2 Ratio Oct 12, 2003

GUVI O/N_2 Ratio Oct 13, 2003

GUVI O/N_2 Ratio Oct 14, 2003

GUVI O/N_2 Ratio Oct 15, 2003

GUVI O/N_2 Ratio Oct 16, 2003

GUVI O/N_2 Ratio Oct 17, 2003

GUVI O/N_2 Ratio Oct 18, 2003

GUVI O/N_2 Ratio Oct 19, 2003

GUVI O/N_2 Ratio Oct 20, 2003

GUVI O/N_2 Ratio Oct 21, 2003

GUVI O/N_2 Ratio Oct 22, 2003

GUVI O/N_2 Ratio Oct 23, 2003

Figure 37 – Global maps of the [O]/[N_2] ratio obtained from the GUVI experiment onboard the TIMED satellite for a geomagnetically quiet day (October 12) and disturbed days (October 13-23). The red rectangle indicates the region of South America, where Brazil is located.

4.3.7 Equatorial Plasma Irregularities and EPB Activity

Equatorial plasma irregularities were assessed through the ROTI, derived from GPS observations across Brazilian stations ordered by dip latitude. Figure 38 displays temporal ROTI variation from October 12 to 24, 2003.

Initial irregularities (ROTI $<$ 0.05 TECU/min) were detected around 21:00 UT, persisting into post-midnight hours, extending poleward to $\sim$20°S dip. Peak activity occurred between 10° and 15°S, where strong TEC gradients are typical. These irregularities intensified during storm-driven PPEF events and remained significant throughout the HILDCAA recovery period.

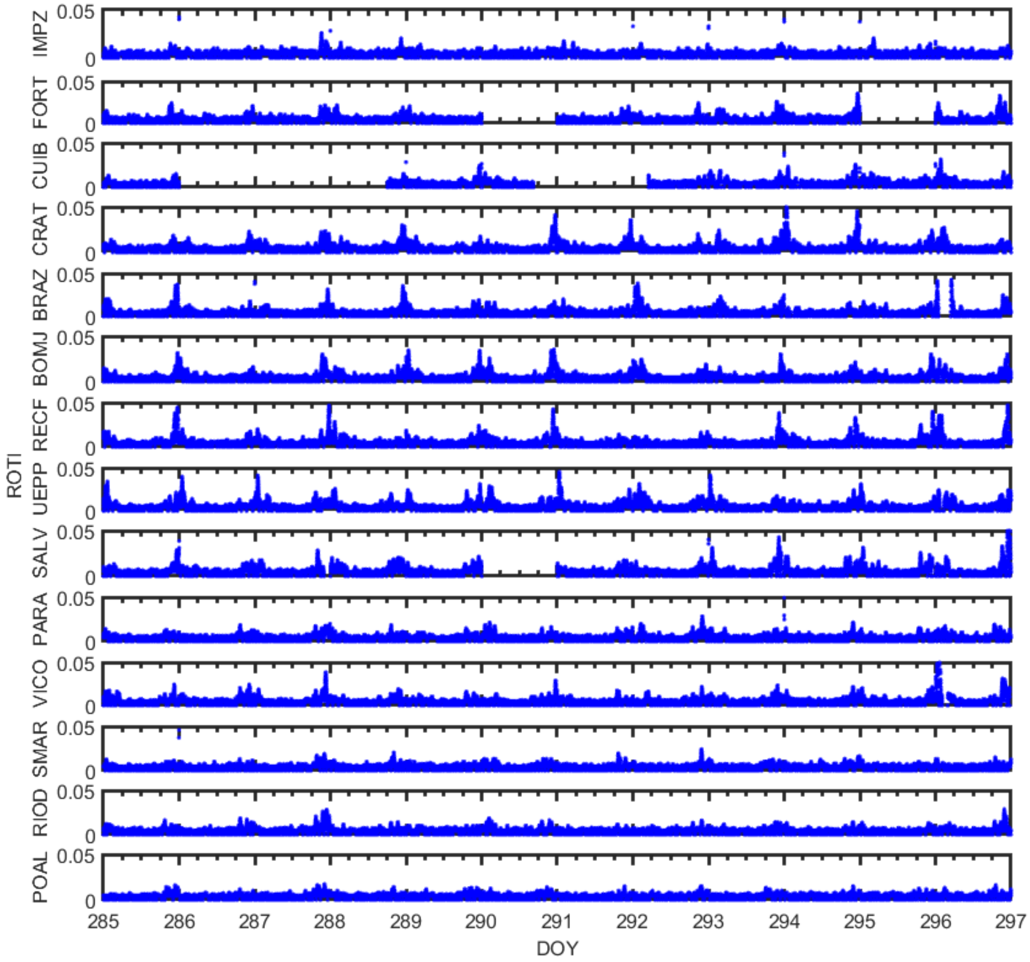

Figure 38 – Temporal variation of the Rate of TEC Index (ROTI) from October 12th to 24th, 2003, across multiple Brazilian stations ordered by dip latitude. Blue intensity indicates the presence and strength of ionospheric irregularities.

Although Spread-F signatures were consistently observed at São Luís and Cachoeira Paulista, GPS-based ROTI offers superior spatial and temporal resolution, revealing latitudinal irregularity propagation. The findings align with previous works highlighting South America as a hotspot for ionospheric disturbances, especially during equinoctial months.

These results confirm that even moderate CIR/HSS-driven storms, particularly when accompanied by HILDCAA activity, are capable of generating extended and structured ionospheric disturbances across the Brazilian sector. The interplay of PPEFs, DDEFs, thermospheric modulation, and neutral wind dynamics governs the evolution of both large-scale TEC features and small-scale plasma irregularities.

4.3.8 CIR/HSS-driven storm and HILDCAA vs Hallowen storm in October 2003

The year 2003 was one of the most geomagnetically active periods in recent space-age history, marked by intense solar activity and significant space weather events. Numerous solar flares, CMEs, and CIRs triggered a wide range of geomagnetic storms, substantially impacting Earth's magnetosphere, thermosphere, and ionosphere, as well as critical space- and ground-based technological systems. The most intense geomagnetic storm of that year occurred on October 29–30, driven by a series of solar flares and CMEs. This storm, characterized by a Sym-H index reaching -400 nT and AE index values up to 3600 nT, generated extreme perturbations in the low-latitude ionosphere over Brazil. Notably, the storm caused an unusual strengthening of the $E \times B$ vertical drift, with speeds around 700 m/s (ABDU et al., 2008), facilitated by strong eastward PPEFs.

This intense uplift led to an exceptional expansion of the EIA to latitudes well beyond the usual 20°S dip, indicative of a "Super Fountain Effect" (ABDU et al., 2008; SAHAI et al., 2009; BATISTA et al., 2006). As reported by Sahai et al. (2009), EPBs extended to approximately 33°S magnetic latitude over the South American sector, reaching apex altitudes around 2500 km above the equator. Additionally, Batista et al. (2006) documented early morning development of the EIA. During this storm, TEC values increased by up to 1000%. Despite these substantial disturbances, the ionosphere returned to quiet conditions within a few days in early November.

In this study, we analyzed ionospheric conditions in the weeks preceding the Halloween storm, focusing on the period from October 13 to 20, when an intense CIR/HSS-driven storm occurred, associated with a large transequatorial CH on the Sun. Although this storm was less intense than the Halloween storm, it generated prolonged and impactful ionospheric disturbances over the Brazilian longitudinal sector, particularly in the low-latitude region, where persistent electrodynamic processes influenced the EIA and equatorial EPBs. Continuous energy injection into the auroral region sustained geomagnetic disturbances for approximately nine days, resulting in cumulative effects such as periodic ionospheric uplifts, plasma irregularities, and persistent TEC enhancements.

Storm-time PPEFs intensified the equatorial $\vec{E} \times \vec{B}$ vertical drift, triggering a pronounced fountain effect that expanded the EIA to latitudes near the SAMA region. It is well-established that simultaneous TEC enhancements and plasma irregularities after sunset create favorable conditions for intense plasma gradients near the EIA crest, leading to strong ionospheric scintillations. This interplay of factors, along with thermospheric changes induced by auroral heating, sustains complex and prolonged electrodynamic processes, posing risks to technological systems, particularly those reliant on navigation and positioning accuracy.

4.3.9 Summary of the Ionospheric Response to the October 2003 CIR/HSS-Driven Storm

In this work, we investigated the response of the Brazilian equatorial and low-latitude ionosphere to a CIR/HSS-driven geomagnetic storm occurring from October 13 to 23, 2003. We also examined the relationship between HILDCAA events and the low-latitude ionosphere. Our findings are summarized as follows:

1. The CIR/HSS-driven storm resulted in significant ionospheric disturbances over Brazil, with the strengthening of the $\vec{E} \times \vec{B}$ vertical drift in the equatorial region and prolonged TEC intensifications that extended for several days during the storm's recovery phase, coinciding with a HILDCAA event in this study.
2. During the storm's main phase, the F-layer experienced a significant uplift due to PPEF action, causing the southern crest of the EIA to extend poleward to latitudes higher than typically observed.
3. Thermospheric composition changes, indicated by measurements of the $[O]/[N_2]$ ratio, were observed during the storm interval. These changes reflect the interplay between Joule heating and plasma/neutral redistribution, impacting the low-latitude ionosphere over Brazil.
4. Periodic fluctuations in F-layer heights were detected during the recovery phase, influenced by both PPEFs and DDEFs, contributing to the prolonged ionospheric disturbances associated with the HILDCAA event.
5. TEC measurements revealed the development of a stronger fountain effect during the storm's main phase, with the EIA extending to higher latitudes (up to -20° dip latitude) and persisting throughout the prolonged recovery phase ($\sim$9 days).
6. Plasma irregularities, detected using the GNSS-derived ROTI, were most prominent between 10° and 15° dip latitude and expanded poleward during the storm interval.

5 Equatorial Ionospheric Responds to HILDCAA* Events in 2003 Over Brazilian Longitudinal sector

This section presents a comprehensive analysis of the ionospheric response to HILDCAA events over the Brazilian equatorial and low-latitude ionosphere during the declining phase of solar cycle 23, with a particular focus on events occurring in 2003. The study utilizes 15-minute resolution ionosonde data from São Luís (2.6°S, 44.2°W, dip latitude 1.5°S), complemented by GNSS-derived TEC observations from a longitudinal chain of stations extending from Fortaleza to Uruguaiana, Brazil.

The investigation integrates the analysis of dTEC to varify the plasma enhancement level and ROTI, serving as proxies for identifying ionospheric irregularities and small-scale plasma fluctuations. In addition, empirical calculations of vertical plasma drift were performed using the model proposed by Fejer e Scherliess (1995), facilitating a better understanding of the electrodynamic response of the equatorial ionosphere during these events.

To characterize the coupling between solar wind and ionospheric parameters during HILDCAA intervals, the study applies rigorous statistical methods, including Gaussian distribution analysis, to evaluate the variability and distribution of solar wind parameters (e.g., velocity, dynamic pressure, IMF components etc.), geomagnetic indices (e.g., AE, Sym-H etc.), and ionospheric parameters (foF2, h'F, hmF2 and TEC). These statistical techniques enable an overview assessment of the underlying processes that govern ionospheric behavior during extended geomagnetically active periods.

5.1 Interplanetary and Geomagnetic Disturbance Conditions in 2003

Figure 39 presents the temporal variations of key solar wind and geomagnetic parameters during 2003. From top to bottom, the panels display: from top to bottom panels indicate, F10.7: solar flux in $Wm^{-2}s^{-1}$, Vsw: Solar Wind Speed, in km/s, Np: Proton density, Np, in $\frac{1}{cm^3}$, Tp: Plasma temperature in K, |IMF|: Interplanetary Magnetic Field, |IMF|, in nT; Sym H: the Ring Current index, in nT, AE: Auroral electroject index in nT, taken from measurements at libration or Lagrangian point L1, at 1 AU, by the satellite ACE and available in <https://omniweb.gsfc.nasa.gov/> and geomagnetic activity index (Kp) from ground based magnetometers. The solar wind and interplanetary magnetic field (IMF) parameters were obtained from measurements at the Lagrangian point L1 (1 AU) by the ACE satellite and accessed via the OMNI database obtain at <https://omniweb.gsfc.nasa.gov/>.

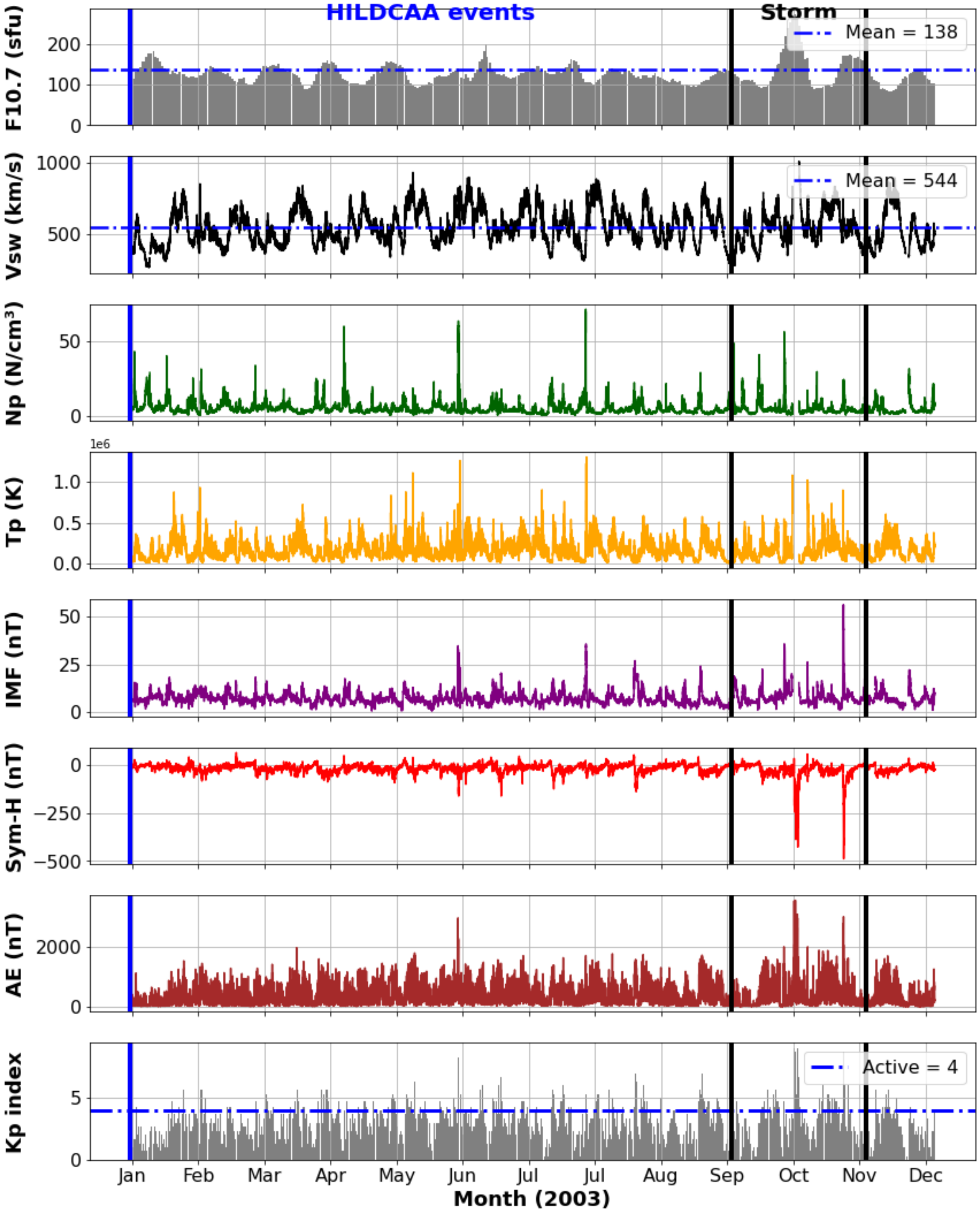

Figure 39 – Variation of geomagnetic and solar parameters observe in period of 2003.

A peak in solar radio flux observed in October may have caused intense geomagnetic disturbances during the Halloween storm period. During the descending phase of solar cycle 23 in 2003, the F10.7 index maintained an average value of ≈ 138 SFU, where $1SFU = 10^{-22}\ Wm^{-2}s^{-1}$. This period was characterized by elevated solar energetic particle (SEP) emissions and increased ionospheric ionization. High-Speed Solar Wind Streams were observed with velocities exceeding 400 km/s, and significant southward fluctuations in the IMF-Bz component. The horizontal dashed blue line in the figure denotes the average Vsw of ≈ 544 km/s, commonly associated with HILDCAA events.

Enhanced proton densities and elevated plasma temperatures hallmarks of CIR structures were observed, indicating interactions between fast and slow solar wind streams in the interplanetary medium. The Sym-H index reached values around –50 nT, signifying a moderate geomagnetic storm.

Meanwhile, the Kp index, which averaged around 4 during this interval, measures the global geomagnetic activity level and short-term fluctuations in the magnetosphere.

5.2 List of HILDCAAs for 2003

To better understand the nature and signatures of HILDCAA events, we analyzed corresponding quiet geomagnetic periods and assessed interplanetary drivers for each selected event on a monthly basis. Magnetic quiet days were obtained from the Kyoto World Data Center for Geomagnetism (<[http://wdc.kugi.kyoto-u.ac.jp/qddays/>) and represent the undisturbed background state of geomagnetic activity. For each event in 2003, the average of the five quietest days was computed to serve as a reference for quantifying deviations observed during HILDCAA intervals. During these quiet periods, responses to solar perturbations are assumed to be minimal, allowing the magnetospheric and auroral ionospheric currents to return to a baseline state. The quiet-time behavior is largely driven by thermospheric wind dynamo effects, as discussed by Chapman (1951), Bargatze, McPherron e Baker (1986), and Sobral et al. (2006).

These HILDCAA events are marked by persistently elevated auroral electrojet activity and are characterized by a lack of significant disturbance in the Dst index, even during geomagnetic storms (GONZALEZ; TSURUTANI, 1987). The AE index was chosen as the primary indicator for identifying HILDCAA events, as it offers detailed insights into high-latitude ionospheric dynamics driven by Joule heating and particle precipitation.

Additionally, we incorporated supporting interplanetary and geomagnetic parameters to characterize HILDCAA intervals. These include the 5-minute averaged vertical component of the interplanetary magnetic field, the symmetric disturbance index, and the interplanetary electric field. The 2003 HILDCAA event was selected using the four standard criteria, consistent with the classification provided by Prestes et al. (2017) (see Table 6)

Table 6 – List of HILDCAA* events driven by CIR/HSS geomagnetic storms during the declining phase of solar cycle 23.

No. of HILDCAA*/ Year	HILDCAA events Interval	Duration (Days)	Five Quiet Days (Used)	Mechanism
H1_2003	19 Jan 05:46 - 23 Jan 05:38	5d	6, 8, 9, 16, 17	CIR
H2_2003	23 Jan 09:44 - 27 Jan 02:19	5d	6, 8, 9, 16, 17	CIR or ICME
H3_2003	06 Feb 05:22 - 11 Feb 18:12	6d	12, 13, 23, 24, 25	CIR
H4_2003	16 Feb 05:24 - 21 Feb 11:10	6d	12, 13, 23, 24, 25	CIR/ICME
H5_2003	04 Mar 09:59 - 07 Mar 23:34	4d	8, 12, 24, 25, 26	CIR
H6_2003	14 Mar 03:01 - 16 Mar 17:16	3d	8, 12, 24, 25, 26	CIR
H7_2003	15 Apr 19:10 - 17 Apr 21:06	3d	6, 7, 12, 13, 19	CIR
H8_2003	20 Apr 15:45 - 24 Apr 12:22	5d	6, 7, 12, 13, 19	CIR or ICME
H9_2003	25 Apr 22:59 - 28 Apr 14:31	4d	6, 7, 12, 13, 19	CIR
H10_2003	01 May 08:59 - 04 May 14:35	4d	16, 17, 18, 19, 20	CIR or ICME
H11_2003	05 May 08:50 - 09 May 07:59	5d	3, 4, 16, 17, 18	CIR/ICME
H12_2003	10 May 19:59 - 16 May 14:23	6d	3, 4, 17, 18, 19	ICME
H13_2003	22 May 08:50 - 29 May 11:27	8d	3, 4, 16, 17, 18	CIR
H14_2003	02 Jun 13:59 - 12 Jun 18:25	11d	5, 20, 22, 25, 26	ICME/CIR
H15_2003	13 Jun 16:55 - 16 Jun 05:59	4d	5, 12, 20, 22, 25	ICME/CIR
H16_2003	24 Jun 14:59 - 06 Jul 17:28	13d	5, 12, 13, 20, 22 / 8, 9, 10, 21, 22	ICME/CIR
H17_2003	12 Jul 19:59 - 15 Jul 12:10	4d	8, 9, 10, 21, 22	CIR
H18_2003	18 Jul 16:56 - 21 Jul 07:51	4d	1, 8, 9, 10, 22	CIR or ICME
H19_2003	29 Jul 23:59 - 04 Aug 10:46	7d	8, 9, 10, 21, 22 / 5, 16, 26, 27, 31	CIR
H20_2003	07 Aug 21:59 - 14 Aug 11:09	8d	5, 16, 26, 27, 31	CIR
H21_2003	23 Aug 14:59 - 25 Aug 18:19	3d	5, 16, 26, 27, 31	CIR
H22_2003	10 Sep 08:02 - 12 Sep 17:39	3d	7, 14, 28, 29, 30	CIR
H23_2003	19 Sep 07:59 - 22 Sep 20:02	4d	7, 14, 28, 29, 30	CIR or ICME
H24_2003	01 Nov 06:59 - 04 Nov 06:16	3d	5, 8, 27, 28, 29	ICME
H25_2003	14 Nov 06:59 - 19 Nov 18:46	6d	5, 8, 27, 28, 29	ICME/CIR
H26_2003	10 Dec 19:59 - 17 Dec 06:36	8d	3, 18, 19, 25, 29	CIR

Source: Prestes et al. (2017)

5.3 HILDCAA* Events Description using Digisonde Data

Figures A.1 to A.6, as referenced in Appendix A, display the following parameters from top to bottom: the auroral electrojet index, the symmetric disturbance index, the electric field, the interplanetary magnetic field component, the virtual height of the F-layer, the peak height of the F-layer, and the critical frequency of the F-layer.

In January 2003, two HILDCAA events were identified: the first occurred from 19 January, 05:46 UT to 23 January, 05:38 UT, and the second followed shortly after, spanning from 23 January, 09:44 UT to 27 January, 02:19 UT. During the first event, the AE index peaked at

≈ -1240 nT on January 23, and the Sym-H index reached a minimum of about -45 nT on January 19 and 22 at 03:00 and 00:00 UT, respectively. However, the AE index remained minimal between January 19 and 22. During this period, the F-layer uplift aligned with the five quiet-day averages at ≈ 23:16 UT (20:16 LT) during the PRE but diverged on January 23.

From January 23 at 09:44 UT to January 27 at 02:19 UT, the AE index reached a peak of ≈ -1502 nT on January 25, while Sym-H hit a minimum of ≈ -60 nT. During this period, Bz and Ey oscillated significantly, especially around January 27 at 00:00 UT, when Bz < 0 and Ey > 0 became prominent, signaling reconnection attributed to interplanetary conditions. The F-layer uplift, similar to the first event, aligned with the five quiet-day averages during PRE at ≈ 22:43 UT (19:43 LT). Throughout this HILDCAA period, the ionospheric F-layer exhibited a notable uplift in h'F, aligning more closely with the five quiet-day average during PRE time and developing spread F. The elevated h'F is attributed to increased auroral activity due to Joule heating and particle precipitation at high latitudes, propagating into the equatorial ionosphere and enhancing the nighttime critical frequency.

During the HILDCAA days in January, foF2 values exceeded those of quiet days during the post-midnight hours on January 20, 21, 24, and 25, while both remained in phase during daytime. The F10.7 cm solar flux was also elevated throughout January, indicating enhanced photoionization and higher critical plasma densities, which contribute to daytime foF2 intensification, as previously noted by Batista et al. (2006) and illustrated in Figure 39.

A similar pattern was observed during the HILDCAA events identified in February. The first event occurred from 06 February, 2003 at 05:22 UT to 11 February at 18:12 UT, and the second from 16 February at 05:24 UT to 21 February at 11:10 UT. During the first event (February 6–11), the AE index reached a peak of approximately -1121 nT on February 9, while the Sym-H index dropped to a minimum of around -40 nT, with frequent fluctuations. These fluctuations indicate multiple reconnection processes associated with Alfvén waves observed in Ey and Bz, as described by Guarnieri et al. (2006) as noted from February 6 until February 10 around 02:35 UT. During this period, the F-layer exhibited uplift above the five quiet-day average at ≈ 23:30 UT (20:30 LT), with notable deviations in the peak ionospheric height, h'F, of ≈ 73 km and ≈ 72 km observed on February 6 and 9, respectively, at ≈ 23:30 UT. The foF2 showed significant enhancement above the five quiet-day average during nighttime, while the daytime frequency remained relatively unaffected.

For the second event (February 16–21), the AE index peaked at ≈ -1021 nT on February 20, and Sym-H decreased to a minimum of around -25 nT. This event was characterized by intense ionospheric activity at the equator, evidenced by high AE-index oscillations.

According to Guarnieri et al. (2006), this HILDCAA event was preceded by a CIR-driven storm, during which the IMF-Bz displayed strong Alfvénic fluctuations. F-layer uplift was slightly above the five quiet-day average around ≈ 22:39 UT (19:39 LT), with a deviation of ≈ 64 km in h'F observed on February 16 at ≈ 22:39 UT. Spread F development was observed throughout this period, attributed to plasma instabilities indicated by the horizontal bar.

Figure A.3 highlights the HILDCAA events occurring on March 4–7, March 14–16, April 15–17, April 20–24, April 25–28 in 2003, and May 1–4. Specifically for March, we observe 04 March, 2003 09:59 UT to 07 March, 15:44 UT and 14 March, 2003 03:01 UT to 16 March, 17:16 UT as HILDCAA interval.

During the first HILDCAA interval (March 4–7), the AE index varied from ≈ 200 nT to 1314 nT on 06 March. The symmetric disturbance index, Sym-H, reached a minimum of ≈ -75 nT on 04 March at 00:00 UT, indicating the onset of a geomagnetic storm influenced by the HSSs event. The B magnitude was ≈ -8 nT, and Bz exhibited typical high-frequency fluctuations of Alfvén waves for much of the time, as discussed by Tsurutani e Gonzalez (1987).

The ionospheric F layer parameters in general, during this HILDCAA period exhibited an uplift. h'F remained considerably higher than the five quiet day's average during both nighttime at ≈ 22:46 UT (19:46 LT) and in the storm phase at the daytime. Notice that the h'F rises above the average curve are consistent with each other, that is, they present similar time progress of amplitude variations in all the days, especially on 05 March after sunset. This effect is primarily caused by the other complex processes related to the magnetospheric and ionospheric coupling processes.

The foF2 observed during the HILDCAA days was generally enhanced relative to the five quiet days during daytime hours. At night, foF2 values tended to decrease, although some variability was observed depending on the balance between upward plasma transport and recombination losses. Notably, the F10.7 cm solar fluxes were elevated during the month, contributing to enhanced photoionization rates and increased plasma densities, particularly around equinox, as reflected in the foF2 values in March (see Figure A.3). Moreover, the elevated h'F and foF2 may also result from intensified auroral activity and associated Joule heating, which drives equatorward thermospheric winds and enhances disturbance DDEFs. These modified electric fields can reinforce upward drifts, contributing to F-layer uplift. These findings are consistent with previous studies by Sobral et al. (2006) and Hajra et al. (2013).

However, referring to the second event, the HILDCAA interval spanned from March 14 at 03:01 UT to March 16 at 17:16 UT. During this period, the AE index reached a maximum of ≈ -1253 nT on March 15, while the Sym-H index dropped to a minimum of around -60 nT, marking the onset of geomagnetic disturbance on March 15 and again on March 16 at ≈ 02:00 UT. Throughout this interval, Bz and Ey (with Bz < 0 and Ey > 0) exhibited frequent oscillations influenced by HSSs. Bz displayed typical high-frequency oscillations characteristic of Alfvén waves, as noted by Tsurutani et al. (1995). The F-layer uplifted above the five quiet-day average at approximately 22:35 UT (19:35 LT), with a minor deviation in h'F of ≈ 56 km observed on March 16 around the same time. Spread F development was observed on all days during the PRE time. Additionally, foF2 values for the HILDCAA days showed intensification above the five quiet-day average during daytime hours.

In April, three HILDCAA events were observed; as occured in April 15 at 19:10 UT to April 17 at 21:00 UT, April 20 at 15:45 UT to April 24 at 12:22 UT and 25 April, 22:59 UT to 28 April, 11:05 UT. The first event, from April 15 at 19:10 UT to April 17 at 21:00 UT, saw the AE index peaking at ≈ -1293 nT on April 15. Subsequent days showed high fluctuation levels, with multiple magnetic reconnection processes reflected in Bz and Ey indices and a minimum Sym-H value of about -35 nT. F-layer uplift was recorded above the five quiet-day average at around 23:41 UT (20:41 LT). On April 16, there were periods with no data (ND), possibly due to instrument error or geomagnetic conditions. Spread F development was evident on all days within this interval. The foF2 values intensified during daytime hours, mirroring the behavior observed in ionospheric peak heights.

For the second April event, the AE index peaked at around -1240 nT on April 23, with Bz and Ey showing similar fluctuation patterns as those observed during April 15–17. Sym-H dropped to ≈ -60 nT, while the F-layer uplift exceeded the five quiet-day average at ≈ 22:18 UT (19:18 LT), deviating by about 104 km from the quiet-day average on April 24 at around 22:35 UT, as indicated by the h'F parameter. Similarly, from 25 April, 22:59 UT to 28 April, 11:05 UT, a storm onset was noted on 25 April at ≈ 02:52 UT, followed by a decrease in Sym-H to about -60 nT.

The magnetic field Bz and electric field Ey exhibited a series of oscillations throughout the HILDCAA days until the storm onset on 28 April at 06:14 UT. This was caused by a northward turning of Bz (Bz < 0 and Ey > 0) due to the presence of Alfvén waves (GUARNIERI et al., 2006). These magnetic fluctuations are corroborated by the multiple magnetic reconnection processes between the solar wind and the interplanetary magnetic field. The eastward interplanetary electric field, Ey, also showed a drop to negative intensity (dusk-to-dawn direction) at this time. The decrease in Sym-H to ≈ -60 nT is not expected to create severe detectable disturbance effects in the equatorial ionosphere. Throughout the period, Bz presented high-frequency oscillations that are possible signatures of Alfvén waves.

The F layer during the HILDCAA days showed an uplift compared to the five quiet days around 22:56 UT (19:56 LT). On 4 April, the h'F rise was significantly elevated above the five quiet day average and persisted into post-midnight hours.

According to Abdu et al. (1995), Sobral et al. (2001) and Abdu (1997), during post-midnight hours, both hmF2 and h'F increase until 05:00 LT, attributing these effects to dynamo eastward electric field effects as observed at equatorial stations in Brazil. Notice that the AE index was quite high. Spread-F was observed on all the days in April during the HILDCAA period. This indicates that auroral activity was not strong enough to generate a DDEFs to inhibit spread-F formation, as occurs during intense storms. The parameter foF2 was slightly above the five quiet day averages during the daytime on 3, 4, 5, and 6 April, which may not conclusively represent a HILDCAA effect. The increase in height or uplift suggests the presence of a disturbance dynamo electric field similar to that observed during storm activity, as noted by Sobral et al. (2006).

Subsequently during the month of May 2003, HILDCAA events were observed from May 1 at 08:09 UT to May 4 at 14:35 UT, May 5 at 08:50 UT to May 9 at 07:59 UT, May 10 at 19:59 UT to May 16 at 14:23 UT, and finally from May 22 May at 08:50 UT to 29 May, 11:27 UT as highlighted in A.2 as referenced in A and A.3 respectively. The first event occurred from May 1 at 08:09 UT to May 4 at 14:35 UT. During this interval, the AE index reached a peak of $\approx$-1344 nT on May 1, with smaller fluctuations in subsequent days. Sym-H dipped to around -95 nT during periods of high AE index, indicating the level of geomagnetic disturbance attributed to HSSs and multiple magnetic reconnection events. The ionospheric F-layer uplift exceeded the five quiet-day average at approximately 05:16 UT (02:16 LT), with a significant deviation of $\approx$ 159 km observed in h'F on May 2. Spread F development was present each day, with foF2 intensifying during daytime hours. However, only on May 1 did foF2 levels exceed the five quiet-day average, while on other days, it remained below as observed in A.3.

The second May event exhibited minimal AE index fluctuations on May 5 and 6, followed by a peak reaching $\approx$ -1593 nT on May 8. Sym-H reached a minimum of around -55 nT on May 9, with high fluctuations in Bz and Ey indicating strong oscillatory activity. The F-layer was uplifted above the five quiet-day average at $\approx$ 02:53 UT (11:53 LT), with a significant deviation in h'F of approximately 116 km observed on May 7 in the post-midnight hours. Spread F was evident throughout the period, and foF2 exhibited daytime enhancement, remaining below the five quiet-day average.

In the third May event, the AE index reached a maximum of around -1709 nT on May

10, indicating strong auroral activity and particle precipitation, which subsided slightly in subsequent days. Also, the Sym-H dropped to approximately -95 nT on May 10, with Bz and Ey showing significant oscillations due to solar turbulence and magnetic reconnections. The F-layer peak height rose above the five quiet-day average at ≈ 23:14 UT (20:14 LT), with a minimum deviation of ≈ 96 km in h'F observed on May 15 at ≈ 06:23 UT. Spread F development was also recorded during the PRE period, and foF2 followed a trend similar to the May 5–9 event.

A storm onset was noted on 22 May at ≈ 02:15 UT, followed by a decrease in Sym-H to about -68 nT. AE index oscillations peaked at around 1174 nT, with a higher peak of ≈ 1354 nT at 14:43 UT on the same day. Bz < 0 and Ey > 0, indicating the magnetic reconnection process. These oscillations were observed throughout the HILDCAA days. The magnetic perturbation indicated in Sym-H was insufficient to produce severe detectable disturbance effects. Around 23:30 UT (20:30 LT), the F-layer during HILDCAA days showed an uplift over the five quiet days after sunset on 22 and 25 May. The horizontal dashed rectangles below the h'F curves represent the development of spread F. The foF2 parameter was slightly above the five quiet day averages during the daytime on all the days.

The increase in height or uplift suggests the presence of a disturbance dynamo electric field similar to that observed during storm activity. From 26 May 18:47 UT to 29 May, 11:27 UT. The storm onset occurred on 26 May at 18:00 UT. AE oscillations peaked at around 2284 nT at 19:14 UT on 29 May, with Sym-H decreasing to approximately 100 nT. Kamide et al. (1998) pointed out that large deposits of energy and charged particles are injected into the magnetosphere and ionosphere, leading to geomagnetic perturbations that expand and intensify the current system, as also noted by Jankovičová et al. (2002).

Furthermore, three distinct HILDCAA events were observed in June 2003. These events occurred during the following periods: June 2 at 13:59 UT and June 12 at 18:25 UT, June 13 at 16:55 UT to June 16 at 05:59 UT, and June 24 at 14:59 UT to July 6 at 17:28 UT. During the first interval, the AE index exhibited significant fluctuations, peaking at ≈ -1421 nT on June 10 at 08:07 UT. Sym-H reached a minimum of ≈ -85 nT, indicating moderate geomagnetic disturbances. The F-layer uplift in HILDCAA days exceeded the five quiet-day average, particularly on June 8 and 9 at ≈ 00:39 UT (03:39 LT) and on June 7 and 12 at ≈ 03:20 UT (12:20 LT), with an average deviation of ≈ 64 km. Spread F development persisted throughout the PRE period. Notably, foF2 during HILDCAA days showed a significant daytime enhancement over the five quiet-day average.

In the second June event, the AE index peak reaches about -1210 nT on June 14. During this peak in auroral electrojet activity, Bz and Ey displayed high fluctuations due to Joule heating and particle precipitation. The F-layer uplift exceeded the five quiet-day average during the PRE period at ≈ 23:14 UT (20:14 LT), with increased spread F attributed to plasma instabilities. foF2 showed an enhancement, mirroring the trend observed in the ionospheric peak height during daytime.

In the third June event, the AE index ranged between 200 and 1500 nT, with a peak observed on June 28. Sym-H reached a minimum of ≈ -98 nT, with Bz and Ey displaying minimal fluctuations from solar wind turbulence, though a strong oscillation pattern was noted on June 26. The storm onset was recorded at ≈ 06:59 UT on June 27. In HILDCAA days, the h'F rose above the five quiet-day average during post-midnight hours on June 27, 30, and July 3 and 5, with an average deviation of ≈ 75 km. Spread F development was indicated in the horizontal bar below h'F. FoF2 showed the highest intensification of HILDCAA days over the five quiet-day average in June, while July foF2 values were generally lower, except on July 1, 4, and 5 during the day.

For the period between July 12 at 19:59 UT and July 15 at 12:10 UT, the AE index reached a peak of ≈ -1305 nT on July 12 before subsiding into lower auroral activity, with Sym-H dropping to a minimum of around -90 nT the same day, indicating geomagnetic disturbance. Bz and Ey exhibited rapid fluctuations on July 12, followed by minor oscillations over the subsequent days due to reduced geomagnetic activity. h'F showed a significant uplift with HILDCAA days consistently exceeding the five quiet-day average, particularly during post-midnight hours around 03:31 UT (12:31 LT). Spread F development was observed during the PRE time, extending into the post-midnight period. FoF2 displayed daytime enhancements, with the five quiet-day average exceeding HILDCAA values at certain times. Notably, data were unavailable for certain time frames on July 12.

Moreover from July 18 at 16:56 UT to July 21 at 07:51 UT saw the AE index peaking at ≈ -1133 nT on July 20, with minimal fluctuations on other days indicating low auroral activity levels. Sym-H decreased to a minimum of approximately -56 nT. The F-layer uplift during HILDCAA days exceeded the five quiet-day average, particularly around 23:41 UT (20:41 LT) on July 21 and from ≈ 03:41 UT (12:41 LT) to ≈ 08:21 UT (05:21 LT) on July 19–20. An estimated deviation in ionospheric peak height of around 65 km on July 19–20 and 128 km during the PRE time on July 21 was observed in h'F. Spread F development followed this uplift, as indicated by the horizontal bar below h'F. Enhanced foF2 values occurred during the daytime, with HILDCAA values surpassing the five quiet-day average on July 19 and 21, while subsequent days showed a reversal in this trend.

These characteristics were similary seen from July 29 at 23:59 UT to August 4 at 10:46 UT were the AE index peak at ≈ -1500 nT on July 29, with Sym-H reaching a minimum of around -53 nT that day. The F-layer uplift during HILDCAA days slightly exceeded the five quiet-day average around ≈ 00:00 UT (21:00 LT) on July 30. However, from July 31 to August 3, the F-layer uplift extended into post-midnight hours around ≈ 02:30 UT (11:30 LT). Spread F signatures persisted throughout the period, starting from the PRE time and continuing into the post-midnight hours. FoF2 intensified during the daytime, with the five quiet-day average generally higher than HILDCAA values.

Subsequently, from August 7 at 21:59 UT to August 14 at 11:09 UT, elevated auroral activity was observed, with the AE index peaking at approximately 1407 nT on August 7. This intense activity was followed by a gradual decline in auroral intensity over the subsequent days. Concurrently, the Sym-H index reached a minimum of about –62 nT, indicating a moderate geomagnetic storm. These conditions were accompanied by pronounced fluctuations in the IMF Bz component and the dawn-dusk electric field, suggesting ongoing magnetic reconnection processes. In the following days, these fluctuations diminished significantly.

During this HILDCAA interval, the F-layer exhibited a noticeable uplift compared to the five quiet-day average, particularly around 23:00 UT (20:00 LT), with average deviations in h'F reaching approximately 85 km—most prominently on August 9 and 14. Spread-F signatures, indicative of equatorial plasma irregularities, developed consistently during the PRE period on each day. Additionally, daytime foF2 values were generally enhanced throughout the interval; however, the five quiet-day averages often exceeded the corresponding HILDCAA values, possibly due to variations in solar flux and recombination dynamics.

This increased level of auroral activity persisted in the event from August 23 at 14:59 UT to August 25 at 18:19 UT were AE index peaked at ≈ -1407 nT on August 23, with lower auroral activity in the following days. Sym-H reached a minimum of around -42 nT on August 25, while Bz and Ey exhibited substantial fluctuations during this period. The F-layer uplift during HILDCAA days slightly exceeded the five quiet-day average at ≈ 22:56 UT (19:56 LT), with a minimum deviation of ≈ 90 km observed on August 24 and 25 in h'F. Spread F generation was observed. FoF2 enhancements during the daytime exceeded the five quiet-day average for this interval, contrasting with the behavior observed from August 7–14.

In September, the HILDCAA events occurred from September 10 at 08:02 UT to September 12 at 17:39 UT and from September 19 at 07:59 UT to September 22 at 20:02 UT as shown in Figures A.5 and A.6. During the first interval, the AE index peaked at ≈ -1107 nT on September 10, with minimal auroral activity noted on the following days. Bz and

Ey exhibited significant oscillations, indicating high levels of auroral activity. The F-layer uplift during the HILDCAA days was slightly above the five quiet-day average at around 23:06 UT (19:06 LT), with a minimum deviation of $\approx$ 60 km observed on September 12, as represented by the h'F. Spread F generation was also observed during this period. FoF2 showed intensification during both daytime and nighttime, with negligible deviations between the HILDCAA days and the average of the five quiet days.

For the second September event, the AE index reached a peak of ≈ -1404 nT on September 19, while the disturbance index, represented by Sym-H, measured around -72 nT on the same day. The geomagnetic and interplanetary conditions during this period were dominant, with Bz and Ey displaying high levels of oscillation throughout. Development of spread F was noted during the PRE time, as indicated by the horizontal bar. The F-layer uplift for the HILDCAA days was above the five quiet-day average at $\approx$ 23:16 UT (02:16 LT), particularly on September 21 and 22. The variation in height compared to the five quiet days average was about 123 km, as indicated by the h'F parameter. FoF2 exhibited a similar behavior pattern as observed in the September 10-12 case.

A comparable ionospheric behavior is observed in November, during the periods from November 1 at 06:59 UT to November 4 at 06:16 UT and November 14 at 06:59 UT to November 19 at 18:46 UT. During the first event, the AE index showed a series of oscillations beginning on November 1, peaking at $\approx$ -1884 nT. This peak coincided with a minimum dip in Sym-H, which measured around -98 nT on November 4.

Significant fluctuations were observed in Bz and Ey, clearly indicating the magnetic reconnection process ($Bz < 0$ and $Ey > 0$), while the other days exhibited negligible variation. A notable feature of this event is the correlation between the negative incursions of the IMF-Bz and decreases in Sym-H, demonstrating a direct relationship consistent with the findings of Tsurutani et al. (2006). Additionally, for significant negative incursions of IMF Bz, a corresponding increase in the AE index can be observed.

The F-layer uplift during the HILDCAA days was above the five quiet-day average at $\approx$ 23:16 UT (23:16 LT), with a deviation of about 98 km noted on November 4, as indicated by the ionospheric peak height, h'F. Spread F development was also observed during this period. The enhancement of foF2 during the HILDCAA days exceeded the average of the five quiet days during the daytime, with a significant deviation of 3 MHz.

In the second case of HILDCAA events in November, the AE index peaked at $\approx$ -1500 nT on November 17, accompanied by a series of oscillations indicative of low levels of auroral activity. Sym-H dipped to a minimum of about -55 nT, reflecting the strength and duration of magnetic disturbances due to solar wind and magnetosphere coupling processes. During this period, Bz and Ey oscillations were significant compared to the intervals observed on November 18 and 19, attributed to the magnetic reconnection process as seen in previous events. The F-layer of the ionosphere during the HILDCAA days and the five quiet days was in phase at ≈ 22:42 UT (19:42 LT), without any significant deviation. The spread F signature was observed throughout the entire period during the PRE time. FoF2 intensified over the five quiet-day average on November 15, while a reverse trend was observed on the subsequent days.

The HILDCAA event in December commence from December 10 at 19:59 UT to December 17 at 06:36 UT, as illustrated in figure A.6. AE- index continue to show a significant peak of ≈ -1500 nT. Sym-H dipped to a minimum value of about -71 nT, indicating that there were no severe disturbances in the equatorial ionosphere. A significant amplitude of variation was noted in Bz and Ey (Bz < 0 and Ey > 0) on the same day, while minimal variations were observed from December 15 to 17, which aligns with the magnetic reconnection process mentioned in previous events. Generally, the fluctuations in Bz have been shown to be Alfvén waves, which have large nonlinear amplitudes in HSS (BELCHER; JR, 1971; TSURUTANI; GONZALEZ, 1987; TSURUTANI et al., 2008; MA et al., 2021). It is observed that whenever the IMF Bz is negative (southward), there is a corresponding increase in the AE index and a decrease in Sym-H. This has been interpreted as being due to magnetic reconnection between the southward components of the Alfvén waves and the Earth's magnetopause. The F-layer uplift during the HILDCAA days was above the five quiet-day average at ≈ 22:17 UT (19:17 LT). During this period, there was a signature of spread F development. The uplifts of h'F during nighttime coincide with the presence of strong disturbance dynamo electric fields and disturbed neutral winds generated by intensified Joule heating.

5.3.1 Characteristics and low-Latitude Impacts of HILDCAA Events

As highlighted by Kamide et al. (1998), interplanetary structures observed on the Sun play a important role in geomagnetic disturbances, with HILDCAA events being one example. These events result from magnetic reconnection involving the southward component of interplanetary Alfvén waves within solar interplanetary structures. During these events, the AE index shows a high level of intensification and continuous activity. HILDCAA events occur when solar winds, composed of Alfvén waves, interact without disturbance. Alfvén waves are defined by the extent of southward penetration of the IMF-Bz. These waves are a type of magnetohydrodynamic wave, oscillating with periods on the order of a few minutes, where ions move along magnetic field lines under the influence of magnetic tension as the restoring force (ECHER et al., 2011).

These persistent wave structures enhance the coupling between the IMF and Earth's magnetosphere, promoting magnetic reconnection processes that lead to elevated values of the AE index (GONZALEZ et al., 1994). The HILDCAA events analyzed in this study correspond to prolonged periods of heightened AE index activity that closely match the empirical criteria established by Prestes et al. (2017), although earlier identification schemes were proposed by Gonzalez e Tsurutani (1987). Notably, Tsurutani et al. (2004) emphasized that HILDCAA events can still occur even when not all these criteria are strictly satisfied, as previously observed by Tsurutani e Gonzalez (1987).

Sobral et al. (2006) demonstrated strong magnetospheric-ionospheric coupling between auroral and equatorial regions during HILDCAA intervals. In particular, variations in the h'F serve as a reliable proxy for estimating vertical plasma drifts during the PRE period. These variations are modulated by multiple factors, including changes in electron density profiles driven by enhanced photoionization, which is strongly correlated with increases in the solar F10.7 cm flux—especially affecting the foF2 (SOBRAL et al., 2006).

According to Sandanger et al. (2005), Søraas et al. (2004) and Gonzalez et al. (2006), the variability observed in ionospheric parameters is also linked to energy transfer during HILDCAA activity. The primary mechanism facilitating this energy transfer during geomagnetic activity between the solar wind and Earth's magnetosphere is magnetic reconnection, although it is not the sole mechanism involved. During HILDCAA events, the injection of ions and energetic electrons into the westward ring current is a factor that increases energization, prolonging periods of elevated activity beyond normal decay phases. A significant influx of charged particles and energy occurs through magnetic field lines (KAMIDE et al., 1998), expanding and intensifying existing current systems within the magnetosphere and ionosphere during geomagnetic disturbances (JANKOVIČOVÁ et al., 2002). Consequently, ring currents dominate at low and middle latitudes, while ionospheric electrojet currents prevail in higher latitudes within the auroral oval.

The equatorial region is characterized by the equatorial electrojet, a system of currents flowing towards the equator, which can produce daily variations of up to 200 nT. However, on quiet days, variations are influenced by atmospheric tides, the phase of the sunspot cycle, seasonal changes, movement of the solar quiet zones, and longitude. These factors often generate two large vortices of electric currents in the dayside ionosphere (HEELIS; MAUTE, 2020), driven by dynamo currents within the ionosphere. Particle precipitation during the daytime also plays a significant role.

During HILDCAA events, the influx of energy modifies the orientation of electric fields, resulting in variations in the height and density peak of the F2 layer (GUARNIERI et al., 2006). PPEFs and DDEFs may also affect these intervals, mapping along magnetic field lines from high to middle and low latitudes (SILVA et al., 2023). Negreti, Paula e Candido (2017) and Yeeram (2019), studied ionospheric electric field configurations during HILDCAA events and identified the critical roles of both PPEFs and DDEFs. Wei et al. (2008), also reported multiple electric field penetrations to the equatorial ionosphere associated with HILDCAA phenomena, and Negreti, Paula e Candido (2017) suggested that hmF2 variations relate to IEF penetrations, which may explain elevated electron density peak heights in these latitudes during HILDCAA periods. This could explain the high values of the electron density peak height in this latitudinal region during the HILDCAA interval. Continuous ionosphere-magnetosphere coupling during HILDCAAs is modulated by the Bz polarity, potentially enhancing coupling efficiency.

DDEFs serve as a predominant mechanism during HILDCAA events, contrasting with the role of PPEFs in typical storm conditions. DDEFs play a significant part in solar wind-magnetosphere-ionosphere coupling, especially during the prolonged external driving characteristic of HILDCAA events, as highlighted by Verkhoglyadova et al. (2013), Negreti, Paula e Candido (2017). PPEFs, which arise from the solar wind-magnetosphere interaction, are understood to be influenced by variations in the IEF, as noted by Huang et al. (2006), Vasyliunas (1970), Vasyliunas (1972), and Manoj et al. (2008). Manoj et al. (2008) observed that abrupt and quasi-periodic fluctuations in the solar wind IEF correlate with variations in equatorial ionospheric electric fields. DDEFs emerge at equatorial latitudes after a delay of several hours following initial high-latitude energy inputs and the onset of PPEFs. The nighttime vertical drifts discussed here consider the combined effect of PPEFs and DDEFs, or either factor individually, applying empirical models during HILDCAA periods. When these electric fields penetrate into lower latitudes, they contribute to ionospheric storms observed through the h'F parameter.

5.4 Comparative Analysis of Latitudinal Variations in Total Electron Content (TEC) during HILDCAA* Events in 2003

To deepen our understanding of how CIR/HSS-driven geomagnetic storms affect the low-latitude region of Brazil, we perform a comprehensive analysis of the latitudinal variations in

TEC during HILDCAA events. Ionospheric parameters such as TEC exhibit complex and often unpredictable responses to variations in solar flux, electrodynamic drifts, and electric fields generated by disturbances like HILDCAAs and geomagnetic storms.

The equatorial and low-latitude ionospheric regions are significantly influenced by global thermospheric disturbances originating from high-latitude heat and momentum sources, driven by solar wind–magnetosphere coupling processes. This study aims to compare the ionospheric morphological variations between equatorial and low-latitude stations in Brazil during HILDCAA events that occurred throughout various months of 2003. To investigate latitudinal TEC variations, we analyzed GPS-derived TEC measurements from selected stations across the Brazilian sector. These include the equatorial site Fortaleza (FZ, dip latitude: 6°S) and multiple stations near the southern crest of the Equatorial Ionization Anomaly (EIA): Bom Jesus da Lapa (BOMJ, 9.76°S), Brasília (BRAZ, 19.8°S), Viçosa (VICO, 16.12°S), Rio de Janeiro (RIOD, 16.32°S), Porto Alegre (POAL, 23.07°S), and Presidente Prudente (UEPP, 23.75°S). The results of this comparative analysis are presented in Figures A.7 through A.12, with further discussion provided in Appendix A.

Additionally, the O/N_2 column density ratios retrieved from the GUVI instrument onboard the TIMED satellite were employed to investigate their relationship with ionospheric variability. These ratios are crucial for assessing changes in the neutral composition of the upper atmosphere during geomagnetic disturbances, as discussed in earlier sections. TEC variations are particularly sensitive to alterations in the thermospheric composition, especially in the O/N_2 ratio, since atomic oxygen is a primary contributor to ionization at F-region altitudes. The TIMED mission provides essential data on the energetics and dynamics of the mesosphere and lower thermosphere, spanning altitudes from ≈ 60 to 180 km (III; MLYNCZAK; GORDLEY, 1994). Although GUVI measurements focus primarily on the thermosphere, they offer indirect information into processes affecting the F-region ionosphere, particularly through composition-driven changes in ion production and loss rates.

In the following paragraphs, we present an analysis of the HILDCAA* events that occurred throughout 2003, covering the period from January to December. The discussion emphasizes ionospheric behavior over the equatorial region and the southern crest of the EIA, focusing on intervals associated with the summer solstice, winter, and equinox seasons. The behavior of the TEC during each HILDCAA event is depicted in the corresponding plots. For comparison, TEC variations during each HILDCAA interval are contrasted with the average of the 5QDs, providing a baseline for identifying storm-time deviations.

As shown in A.7, TEC observed during the HILDCAA events, which occurred between

19-23 January 2003, at the equatorial GPS station FZ and low-latitude stations such as BOMJ, BRAZ, VICO, RIOD, POAL, and UEPP, reveals that on January 19, higher TEC enhancement were observed during HILDCAA days over the south crest of EIA compared to the five quiet days, particularly relative to the equatorial region. High geomagnetic disturbance levels were noted on 19 January at 18:00 UT (15:00 LT), influencing TEC enhancement. However, TEC variations on 20-21 January behaved oppositely to those on 19 January. On 22 January, the maximum TEC value recorded was $\approx$ 97 TECU for RIOD, compared to 62 TECU for FZ at 18:00 UT (15:00 LT) during the day. Weak but effective disturbances were present, and the action of DDEFs likely caused the TEC enhancements during this hour since these stations are located on the EIA crests, representing a stronger EIA. These enhancements are not associated with geomagnetic storms but show significant TEC responsiveness compared to typical geomagnetic storm effects. No GPS TEC responses were observed over the equatorial station FZ on 22 January due to data unavailability. Conversely, only VICO showed higher TEC over the six GPS stations analyzed for the southern crest of EIA on 23 January at 17:35 UT (14:35 LT), attributed to elevated auroral activity, as noted by Sobral et al. (2006).

Between January 23 and 27, the TEC values were slightly lower than the five quiet-day average, particularly at low latitudes on January 23. On January 24, an enhancement in TEC was observed over the southern crest of the EIA at 18:00 UT (15:00 LT), reaching approximately 65 TECU during the HILDCAA period—significantly above the quiet-time baseline. Although no GPS data were available for the equatorial station FZ, a substantial TEC increase was recorded on January 26, with peak values reaching $\approx$85 TECU at the VICO and RIOD stations and $\approx$60 TECU at FZ around 18:00–21:00 UT (15:00–18:00 LT), especially at low latitudes.

The F10.7 solar flux in January remained elevated, with values around 130 SFU, indicating increased photoionization and background ionospheric density. Notably, a sharp TEC peak observed around 21:00 UT over VICO and RIOD is likely linked to an intensified PRE.

The PRE enhances the EIA by lifting the F-layer to higher altitudes, where the recombination rate is lower, thereby promoting an increase in TEC. Under disturbed conditions, this mechanism can be amplified by PPEFs, intensifying the equatorial fountain effect and resulting in stronger EIA crests. Furthermore, during the recovery phase of the geomagnetic storm, the effects of DDEFs, driven by equatorward thermospheric winds resulting from Joule heating at high latitudes, also contributed to the observed TEC enhancements.

TEC continued to increase significantly at both latitudes relative to the five quiet-day average on 6 February during the daytime as observed within the HILDCAA interval of 6-11

February 2003 and 16-21 February as indicated in Figure A.7. This sharp increase can be attributed to strong geomagnetic disturbances, which led to electric field penetration into the equatorial and low-latitude ionosphere.

According to Bagiya et al. (2009), the day-to-day variability of TEC is influenced by factors such as EUV flux, geomagnetic activity, electrojet strength, and local atmospheric conditions in the thermosphere. Additionally, Liu, Zhao e Liu (2010), Zhao et al. (2007) and SUN et al. (2017) noted that positive storms in the equatorial region and the southern EIA crest are mainly driven by eastward PPEFs.

On 6 February, elevated auroral activity due to joule heating and particle precipitation also contributed to the TEC increase. The maximum TEC enhancement reached around 68 TECU on average over the south crest of EIA and $\approx$ 55 TECU in the equatorial region around 18:00 UT, compared to the five quiet-day average.

In low-latitude regions, the highest daytime peak TEC values are heavily dependent on the strength of the EIA. The TEC enhancement persisted throughout 7-11 February, though the magnitude of the increase was less pronounced than on 6 February at both latitudes.

On 7-8 February, the TEC values in geomagnetically quiet days were observed to align with those in the equatorial region, differing from those at the south crest of EIA, although data were unavailable for some stations. TEC intensification on HILDCAA days relative to the five quiet-day average was notably reduced around 19:00 UT on 10 February.

The TEC increase observed on 11 February can be attributed to the influence of a weak storm. The presence of a geomagnetic storm indicates solar wind-magnetosphere interaction, which triggers global disturbances in the geomagnetic field and ionospheric TEC, as observed during this period.

During the interval from 16-21 February, TEC enhancement was higher during the daytime around 18:00 UT at both latitudes, reaching a peak value of $\approx$ 65 TECU relative to the five quiet-day average on 16 February. This TEC behavior persisted over the following days, especially during daytime hours.

However, on 18 February, TEC enhancement over the south crest of EIA continued from daytime into nighttime around 23:45 UT (20:45 LT). The significant TEC increase observed over VICO and BRAZ on 19 February resulted from a greater PRE time.

The F10.7 solar flux remained stable during 20-21 February, with significant daytime TEC enhancements, particularly at POAL, where TEC reached $\approx$ 67 TECU. On 21 February, TEC intensified over the equatorial region during HILDCAA days, nearly equaling the five quiet-day average and then enhancing sharply over the southern crest of EIA.

Similarly, as shown in Figure A.8, the period from March 4–7, 2003, exhibits contrasting ionospheric behavior. During the HILDCAA days, minor TEC enhancements were observed around 17:00 UT (14:00 LT), particularly over stations near the southern crest of the EIA. In contrast, the equatorial region displayed weaker TEC responses compared to the five quiet-day average on March 3, likely due to geomagnetic disturbances preceding the HILDCAA onset.

From March 5 to 7, significant TEC intensifications were observed over the southern crest of the EIA around 18:00 UT (15:00 LT), when compared to the quiet-time baseline. This behavior was more pronounced at low latitudes than at the equator. On March 7, peak TEC values reached approximately 70 TECU at RIOD and about 60 TECU at FZ. These enhancements may be attributed to elevated solar flux levels during the period, which enhanced atomic oxygen ionization and increased electron density. Additionally, moderate Joule heating and particle precipitation associated with ongoing geomagnetic disturbances may have contributed, although the magnitude of these effects was not sufficient to induce severe storm-time ionospheric changes.

In contrast, during the HILDCAA event from March 14–16, TEC intensification was predominantly observed on March 14. A significant increase was recorded over the southern crest of the EIA relative to the five quiet-day average. TEC peaked at $\approx$88 TECU around 20:00 UT (17:00 LT) over UEPP and $\approx$73 TECU at the equatorial station FZ. The mechanisms driving these enhancements are similar to those observed in January and include enhanced photoionization, Joule heating, and coupling to high-latitude processes.

Auroral electrojet activity exhibited strong oscillations, likely reflecting enhanced geomagnetic activity linked to solar wind turbulence. On March 15, TEC enhancements over the southern crest (notably at VICO, RIOD, and POAL) showed strong variability compared to the quiet-day average. Meanwhile, the equatorial station FZ exhibited either weaker or opposite-phase responses. Despite low Sym-H variability during this time, the TEC response can be attributed to sustained auroral activity, consistent with the presence of interplanetary Alfvén waves embedded in HSSs traveling at $\approx$800 km/s, as described by Hajra et al. (2013).

On March 16, TEC values at southern EIA crest stations were nearly in phase with the five quiet-day average, except for BOMJ and BRAZ, which displayed notable increases around 19:00 UT (16:00 LT). In contrast, the equatorial region (FZ) showed minimal deviations, suggesting that low-latitude electrodynamic responses were spatially dependent and possibly modulated by local conditions or weaker coupling to high-latitude drivers on that day.

Additionally, for the HILDCAA events that occurred from 15–17 April, 20–24 April, and

25–28 April 2003, TEC behavior showed notable enhancements across both equatorial and low-latitude regions, particularly during periods of heightened auroral activity.

On 15 April, a TEC enhancement was observed at approximately 19:23 UT (16:23 LT) at both latitudinal regions. Interestingly, the five quiet-day average exceeded the HILDCAA-day values at the southern crest of the EIA, while the opposite was observed at the equatorial region. This suggests differing responses to auroral-driven disturbances. During geomagnetically active periods, auroral heating generates strong thermospheric winds, which drive the ionospheric disturbance dynamo, modulating electric fields and plasma transport. Under quiet conditions, however, the regular increase in TEC around 18:00 UT (15:00 LT) is primarily driven by solar photoionization, as reported by Rastogi, Iyer e Sharma (1977) and Sethia et al. (1978).

On 16 April, a pronounced TEC enhancement occurred over the southern crest of the EIA around 19:14 UT (16:14 LT), with peak values reaching approximately 65 TECU at VICO and 54 TECU at FZ, relative to the five quiet-day average. This continued on 17 April, when TEC began to rise around 15:23 UT (12:23 LT) and remained elevated until 19:21 UT (16:21 LT), particularly over the southern crest of the EIA. The maximum TEC peak recorded was $\approx$ 80 TECU at BRAZ and 56 TECU at FZ. These enhancements are consistent with increased auroral activity, as indicated by elevated AE index values during this period. Geomagnetic disturbances can modulate TEC by altering electric fields, thermospheric composition, and plasma drifts, resulting in latitude-dependent variations (MENDILLO, 2006; TITHERIDGE; BUONSANTO, 1988; ZHAO et al., 2007; JAKOWSKI et al., 1999).

During the HILDCAA event from 20–24 April, TEC enhancements relative to the quiet-day average were particularly evident on 20 April, with a peak around 18:45 UT over the southern EIA crest. Maximum average TEC values reached approximately 85 TECU, while the equatorial station FZ recorded $\approx$60 TECU. On 21 April, a similar pattern emerged, with a TEC peak of $\approx$74 TECU at BRAZ around 18:00 UT, although lower than previous enhancements at FZ. Throughout this interval, TEC remained elevated, especially over the southern crest of the EIA during daytime hours.

However, the moderate TEC response to the HILDCAA event observed over the southern EIA crest on 25 April was likely due to high fluctuations in the auroral electrojet, associated with solar wind turbulence and the magnetic reconnection process, as indicated by the Bz and Ey interplanetary indices. The geomagnetically quiet-day average was in phase with HILDCAA days during the daytime, around 18:00 UT. Around 23:35 UT, TEC intensification was attributed to plasma drift during PRE. TEC enhancement persisted moderately across both latitudes, with a drastic increase on 27 April, reaching a peak of ≈ 88 TECU around 18:00 UT over BRAZ and ≈ 63 TECU at FZ relative to the five quiet-day average. The local time variation of PPEF may account for longitudinal differences in TEC disturbances.

The HILDCAA events in May 2003 induced significant variations in TEC, reflecting dynamic ionospheric responses during the intervals centered on 01–04 May, 05–09 May, 10–16 May, and 22–29 May. On 01 May, a notable TEC enhancement was observed over the southern crest of the EIA, particularly at BOMJ and BRAZ, with peak values reaching ≈ 85 TECU at 19:00 UT, compared to the ≈60 TECU measured at the equatorial station FZ. This intensification is attributed to strong geomagnetic disturbance levels, as indicated by a pronounced drop in the Sym-H index and elevated auroral activity.

The TEC enhancement persisted on 02 May, despite the Sym-H index indicating low geomagnetic disturbance. However, elevated auroral activity—reflected in the AE index—likely contributed to continued ionospheric effects. On average, TEC peaks at the southern EIA crest were around 80 TECU at 18:00 UT, while equatorial TEC values remained near 50 TECU, relative to the five quiet-day average.

In the subsequent days, TEC remained elevated, though at slightly lower levels compared to 01–02 May. Throughout the analyzed period, the TEC variations on HILDCAA days often followed the same phase as the quiet-day reference, with less pronounced positive enhancements. This in-phase behavior was more apparent at the equatorial station than at the southern EIA crest.

As shown in Figure A.9, the TEC pattern on 05 May closely resembled the trends observed on 03–04 May, with the maximum TEC at the EIA crest reaching ≈ 65 TECU around 18:34 UT at BOMJ, and ≈ 50 TECU recorded at FZ. During this period, solar wind turbulence and multiple magnetic reconnection episodes—evident from fluctuations in IMF-Bz and Ey—likely triggered moderate auroral activity, which in turn influenced the observed TEC enhancements.

A similar TEC pattern was observed on 06 May, although the enhancement relative to the five quiet-day average was minor. This modest intensification may be attributed to the presence of Alfvén waves embedded within the HSSs, which can contribute to moderate energy input into the ionosphere without producing a major geomagnetic storm.

According to Hajra et al. (2013), during magnetospheric disturbances, the maximum number of energetic particles populates the high latitudes due to the action of Alfvén waves.

On 07 and 08 May, around 18:00 UT, a pronounced TEC enhancement was detected over the southern crest of the EIA, particularly at stations VICO, RIOD, POAL, and UEPP.

These stations recorded an average peak of approximately 65 TECU, significantly higher than the corresponding five quiet-day average. In contrast, the equatorial station FZ displayed lower TEC values during the HILDCAA days—about 52 TECU—compared to its quiet-day average.

From 09 to 14 May, TEC behavior remained similar to the quiet-day reference levels at both latitudes, despite the presence of moderate to intense geomagnetic activity. This finding is consistent with the results of Deng et al. (2012), who reported that TEC can exhibit significant day-to-day variability even under quiet geomagnetic conditions, as supported by earlier studies such as Fejer et al. (1991b) and Xiong et al. (2023). During this period, the maximum mean TEC values reached approximately 55 TECU at the southern EIA crest and 45 TECU at FZ, peaking around 18:23 UT.

On 15 May, TEC intensified markedly around 18:00 UT at VICO, RIOD, POAL, and UEPP, reaching up to 62 TECU relative to the five quiet-day average. However, no significant enhancement was observed at the equatorial station FZ. A similar latitudinal pattern persisted on 16 May, with clear intensification at mid-latitude sites and minimal changes at equatorial latitudes.

Between 22 and 28 May, solar and geomagnetic indices indicated minimal fluctuations, resulting in generally low TEC levels. TEC enhancements during this interval were negligible compared to the reference baseline. Additionally, data gaps were noted at FZ and BOMJ, possibly due to GPS receiver outages or other instrumental issues.

On 29 May, around 18:28 UT, a significant TEC increase was observed over the southern EIA crest, with mean values peaking at approximately 60 TECU.

During 06–12 June, a negative TEC deviation was observed at both equatorial and low-latitude stations compared to the five quiet-day average. Notably, geomagnetic quiet conditions were prevalent throughout most of the period, especially around 18:00 UT, which corresponds to local afternoon.

At the equatorial station FZ, TEC values typically peaked around 40 TECU, while at the southern crest of the EIA, average peaks reached approximately 50 TECU. However, on 09 June, a significant TEC enhancement was detected over the southern EIA crest around 23:00 UT (20:00 LT). This localized intensification could be attributed to the action of DDEFs or PPEFs. As established by Abdu (1997), Huang et al. (2006), Sobral et al. (2006) and Fejer (2011), equatorial electric fields are drivers of TEC variability under both geomagnetically quiet and disturbed conditions. Specifically, during HILDCAA events, intermittent penetration of the interplanetary electric field into the equatorial ionosphere has been documented (WEI et al., 2008).

As illustrated in Figure A.10, on 13 June, TEC enhancements were observed around 18:00 UT at BOMJ, BRAZ, VICO, and RIOD, while the equatorial station FZ showed a corresponding reduction. The maximum TEC peak on this day reached approximately 50 TECU, despite minimal geomagnetic activity, suggesting that the enhancement may have been driven primarily by increased solar EUV flux, leading to higher ionization rates during daytime hours.

Later, around 19:23 UT (16:23 LT), only minor TEC enhancements were noted in both latitude regions, possibly influenced by auroral activity and rapid fluctuations in IMF Bz and Ey, which were evident in solar wind data on both 13 and 16 June. Overall, TEC responses during this HILDCAA period were negligible, with HILDCAA days and quiet-day profiles largely in phase at both equatorial and low-latitude stations.

During the final HILDCAA interval, from 24 June to 06 July, TEC behavior mirrored the earlier 06–12 June period, showing generally low intensities with few deviations from the quiet-day baseline. However, on 01 July, a notable TEC enhancement was observed over the southern EIA crest, particularly at UEPP, around 19:20 UT, with a peak of 48 TECU, exceeding the five quiet-day average. In contrast, the equatorial station showed minimal response. It is important to note that GPS data gaps were present between 24–30 June for several stations, including VICO, RIOD, POAL, and intermittently for FZ, which limits the completeness of the analysis during this interval.

The HILDCAA events of July 12–15, July 18–21, and July 29–August 4, 2003, exhibited distinct ionospheric responses across equatorial and low-latitude regions. On 12 July, no significant TEC enhancement was observed over the equatorial station (FZ) relative to the five quiet-day average. However, over the southern crest of the EIA, a pronounced TEC increase was detected between 00:00 UT and 05:00 UT (03:00–02:00 LT), with an average deviation of $\approx$ 35 TECU above the quiet-time reference level. This behavior suggests that geomagnetic disturbances—likely driven by weak to moderate fluctuations in IMF Bz, Ey, and Sym-H triggered enhanced ionospheric electrodynamics, resulting in elevated TEC at low latitudes.

On 13 July, moderate daytime TEC enhancement was observed at both latitudes around 18:00 UT, reaching values of approximately 55 TECU over the southern EIA crest and 50 TECU at the equatorial station. In contrast, on 14 July, the TEC response was negligible across all stations, consistent with minimal geomagnetic activity and quasi-periodic variations in the AE index, suggesting weak magnetospheric-ionospheric coupling. However, on 15 July, a significant increase in TEC was observed at VICO, RIOD, and POAL near 14:20 UT (11:20

LT), with peak values around 50 TECU, while the equatorial station recorded approximately 45 TECU. This behavior may be attributed to localized enhancements in PRE-related vertical drifts or remnant effects of auroral heating.

During the next HILDCAA event, on 18 July around 19:20 UT, moderate TEC enhancement was again observed at both latitudes. The southern EIA crest showed average peak values of $\approx$ 50 TECU, while the equatorial region exhibited an even stronger response with $\approx$ 60 TECU, surpassing the five quiet-day baseline. This trend continued through 21 July, though 19 July itself showed a negative TEC deviation, meaning that TEC values were lower during the HILDCAA days than on quiet days. This behavior resembled that observed on 14 July, when Bz, Ey, and the AE index exhibited low-amplitude, low-frequency fluctuations, insufficient to drive strong ionospheric responses.

On 20 July at 18:00 UT, a notable enhancement occurred across both latitudes, with peak TEC values of approximately 63 TECU over the southern crest of the EIA and 55 TECU at the equator, indicating an efficient interplanetary energy transfer possibly via PPEFs.

Later, during the HILDCAA interval of 29 July–04 August, TEC enhancement was recorded over the southern EIA crest at 18:30 UT on 29 July, particularly over RIOD, where values peaked at $\approx$ 45 TECU relative to the quiet-day reference. This enhancement coincided with weak-to-moderate auroral activity, suggesting the influence of Alfvénic turbulence in HSS. However, from 30 July to 04 August, TEC values during HILDCAA days were consistently lower than the quiet-day averages at both latitudes, indicating a negative response, as shown in Figure A.11. This suggests that quiet-day solar flux and ionospheric conditions were more favorable for TEC production than during the disturbed period.

The behavior of TEC variations observed during the intervals of 07–14 August and 23–25 August followed a pattern similar to that seen on 04 August, showing predominantly negative TEC enhancements at both latitudes relative to the five quiet-day average, as illustrated in Figure A.11. Despite the overall subdued ionospheric response, a slight positive deviation in TEC was noted from 09–12 August over the southern crest of the EIA, particularly at BRAZ and BOMJ around 18:20 UT, suggesting localized enhancements during the daytime.

This modest TEC behavior persisted into the next HILDCAA interval beginning on 23 August, during which no significant enhancement was detected across most stations during the daytime. However, a slight rise in TEC was observed around 00:00 UT on 24 August at BRAZ and BOMJ, indicating a weak positive deviation from the quiet-time average. On 25 August, a localized peak in TEC of $\approx$ 40 TECU was recorded at UEPP around 17:00 UT, while other stations at comparable latitudes exhibited only minimal TEC increases.

On average, TEC values over the equatorial region reached approximately 55 TECU, while the southern crest of the EIA exhibited around 45 TECU, pointing to a relatively modest enhancement. These variations may be attributed to eastward PPEFs during periods of low geomagnetic disturbance. This interpretation is supported by the presence of small fluctuations in the IMF-Bz, interplanetary Ey, and AE index, which indicate weak but persistent coupling between the solar wind and the magnetosphere.

The ionospheric response observed during the 07–14 August interval may also reflect the influence of auroral and magnetospheric activity, as suggested by the variability in the interplanetary electric and magnetic field components and modest Sym-H fluctuations, consistent with previously reported HILDCAA signatures.

The associated ionospheric responses were particularly prominent during the period from 10–12 September, where a daytime TEC enhancement was observed from approximately 12:00 UT to 23:00 UT throughout the interval. The peak values recorded were about 55 TECU over the southern crest of the EIA and approximately 45 TECU over the equatorial region. Notably, this intensification occurred during geomagnetically quiet days across both latitudes and, despite representing an increase in TEC, it is classified as a negative storm effect, as the enhancement remains below the quiet-day average. As emphasized by Sahai et al. (2009), both positive and negative TEC effects are commonly observed in the equatorial and low-latitude ionosphere during geomagnetic disturbances, depending on the prevailing electrodynamic and thermospheric conditions.

As depicted in Figure A.12, a modest TEC intensification was detected on 19 September around 18:00 UT over the southern EIA crest, while a weaker response was noted over the equatorial region. This enhancement is likely associated with geomagnetic disturbances and solar wind fluctuations, which contributed to elevated auroral activity, as reflected in the AE index. On 20 September, significant TEC increases were observed at BOMJ and BRAZ from around 12:00 UT to 00:00 UT, with peak values reaching $\approx$ 64 TECU, while no notable enhancement was recorded at FZ (equatorial region), suggesting a latitude-dependent ionospheric response to the HILDCAA conditions.

On 21 September, TEC enhancements were generally negligible across both latitudes, with the TEC variations for HILDCAA and quiet days remaining in phase, except at BOMJ, where a local TEC peak of $\approx$ 60 TECU occurred around 23:35 UT, representing an isolated positive deviation. This type of behavior aligns with previously observed localized ionospheric responses during HILDCAA intervals.

On 22 September, the TEC behavior mirrored that observed on 19 September; however, magnetic activity introduced latitudinal variability in the ionospheric response. Over UEPP, TEC peaked at approximately 62–65 TECU around 18:00 UT, exceeding values from earlier days. In contrast, the equatorial station (FZ) continued to exhibit minimal TEC response, underscoring the spatial heterogeneity of ionospheric perturbations during these HILDCAA events.

The HILDCAA intervals from 1–4 November and 14–19 November 2003, as illustrated in Figure A.12, exhibited notable TEC enhancements during the daytime, particularly from 12:00 UT to 00:00 UT (09:00 to 21:00 LT), over both the southern crest of the EIA and the equatorial region, relative to the five quiet-day averages. On 1 November, VTEC peaked at $\approx$ 90 TECU at the southern crest of the EIA and around 60 TECU at the equatorial station, indicating a strong response to geomagnetic disturbances and associated auroral activity.

The TEC enhancement persisted until 2 November, with maximum values averaging 60 TECU around 18:20 UT over the southern crest of the EIA. In contrast, the equatorial region exhibited weaker enhancements, and by 3 November, the TEC responses had largely diminished. On this day, the HILDCAA and quiet-day TEC patterns appeared largely in phase at both latitudes, except for a slight deviation observed over BRAZ during the daytime.

On 4 November, a positive TEC enhancement was recorded between 12:00 UT and 22:00 UT, with deviations above the quiet-day average. These variations are likely associated with solar wind-driven PPEFs.

By contrast, on 14 November, a negative TEC enhancement was observed in the equatorial region and at selected low-latitude stations (BOMJ, BRAZ, VICO). From 15–19 November, the VTEC values during HILDCAA days closely resembled the quiet-day averages, with slightly lower magnitudes at low latitudes, except for RIOD, which exhibited a modest daytime enhancement. The maximum VTEC value recorded was approximately 65 TECU on 15 November at low-latitude stations, whereas equatorial TEC remained relatively unchanged, thus constituting a negative storm effect.

During the period from 10 to 17 December, TEC values during the geomagnetically quiet days were observed to be higher than those during the HILDCAA days, as shown in Figure A.12, indicating a negative TEC enhancement trend relative to the reference level. This negative deviation in TEC suggests a suppression of ionospheric electron content during HILDCAA intervals.

Despite the moderate intensity of the geomagnetic activity, auroral indices (AE) were elevated (see Figure A.6), accompanied by decreases in Sym-H, and Kp values indicating enhanced global geomagnetic conditions (Figure 39). These combined factors reflect the presence of substorm activity and energy input from the solar wind into the magnetosphere–ionosphere system.

The maximum average TEC observed over the southern crest of the EIA was approximately 50 TECU, while values near 40 TECU were recorded at the equatorial station. The suppression of TEC during HILDCAA days in December contrasts with the behavior observed in March and April, where TEC surges were recorded. These surges were likely driven by DDEFs or PPEFs arising from southward IMF-Bz intrusions, which facilitated magnetospheric energy transfer to the ionosphere via magnetic reconnection and enhanced auroral particle precipitation.

Additionally, the potential contribution of changes in thermospheric neutral composition specifically the O/N_2 ratio during HILDCAA events was investigated, as presented in Figures A.13 and A.14 (see also Appendix A).

Analysis of O/N_2 data indicates that no significant variations in neutral composition occurred over South America during the HILDCAA intervals of 2003, as reflected by the stability of the O/N_2 ratio. This observation supports the interpretation that thermospheric composition changes were not a dominant driver of the observed TEC variations during these events. The inclusion of the O/N_2 ratio in this study serves to exclude the possibility that changes in neutral composition substantially contributed to the ionospheric electron density responses recorded during the HILDCAA periods. No clear correlation was identified between variations in the O/N_2 ratio and the enhancements in TEC observed during the events. This suggests that thermospheric composition changes were not the dominant driver of the ionospheric response. Instead, other mechanisms—particularly electrodynamic drivers—appear to have played a more significant role. Similar results have been reported in previous studies, such as Mannucci et al. (2009), which documented cases of anti-correlation between O/N_2 variations and storm-time TEC behavior.

The thermospheric composition, including the O/N_2 ratio, is primarily governed by photochemistry and diffusive processes:

(a) Production of atomic oxygen Atomic oxygen is produced mainly through the photodissociation O_2: $O_2 + hv(EUV) \rightarrow 2O$ A minor contribution arises from N_2 dissociation at higher altitudes: $N_2 + hv \rightarrow 2N$ (b) Loss of atomic oxygen Atomic oxygen undergoes loss via chemical reactions with O_2 and N_2:

$O + O \rightarrow O_2$

$O + N_2 \rightarrow NO + N$ These processes regulate the vertical distribution of [O] in the thermosphere.

(c) Diffusive separation At higher altitudes, molecular diffusion dominates, leading to separation by mass: lighter species (O, H, H_e) rise, while heavier species (N_2, O_2) settle. Consequently, the O/N_2 ratio increases with altitude, particularly above $\approx$ 200 km.

Given the weak linkage between composition changes and the observed TEC variations, further emphasis was placed on electrodynamic processes. To investigate this, we employed an empirical model to quantify the combined effects of DDEFs and PPEFs on equatorial plasma drift dynamics. The results, associated with variations in both vertical and zonal drifts, are presented in Section 5.8.

5.5 Statistical Characterization of Solar Wind, Geomagnetic Activity, and Ionospheric Conditions Associated with HILDCAA* Events in 2003

HILDCAA events are characterized by periods of enhanced geomagnetic activity, typically driven by HSS occurring during the recovery phase of geomagnetic storms. These events impact the coupled magnetosphere–ionosphere system, resulting in significant changes in key space weather parameters. Such parameters naturally fluctuate in response to solar, geomagnetic, and atmospheric influences. Understanding their statistical behavior is essential for identifying anomalies, establishing quiet-time baselines, and ensuring quality control in ionospheric modeling efforts.

Assuming a normal (Gaussian) distribution is a fundamental step in both descriptive and inferential analysis of geospace data, as deviations from Gaussian patterns may signal the presence of underlying physical processes or disturbances. In this context, Gaussian histogram analysis is employed to examine the distribution and variability of solar wind, geomagnetic, and ionospheric parameters associated with HILDCAA events throughout 2003. This approach provides deeper insight into the characteristic behavior of these parameters during such disturbances.

To establish the link between solar wind parameters and geomagnetic indices or ionospheric variations, Gaussian distributions were employed to gain valuable insights into the underlying physical processes. Figures 40, 41, and 42, along with Figures 44 and 43, provide a statistical comparative analysis of various parameters. These include the average magnetic field magnitude (B_o), the vertical component of the magnetic field (B_z), solar wind parameters such as speed (V_{sw}), proton density (N_{sw}), temperature (T_{sw}), and dynamic pressure (P_{sw}). Additionally, auroral geomagnetic indices (AE, AL, AU, AO), the Sym-H geomagnetic index, and ionospheric parameters (TEC, foF_2, $h'F$, and hmF_2) are analyzed during disturbed days (HILDCAA events) and quiet days to verify the role of HSS/CIR events in driving HILDCAA phenomena.

This analysis spans periods of geomagnetic disturbances to assess the contribution of HSS/CIR events to HILDCAA events. The histogram below illustrates these parameters for the year 2003. Specifically, Figures 40, 41, and 42 present the histograms of the average magnetic field magnitude (B_o), the vertical component of the magnetic field (B_z), solar wind speed (V_{sw}), proton density (N_{sw}), temperature (T_{sw}), and dynamic pressure (P_{sw}); auroral indices (AE, AL, AU, AO); the geomagnetic Sym-H index; and the average IMF magnitude.

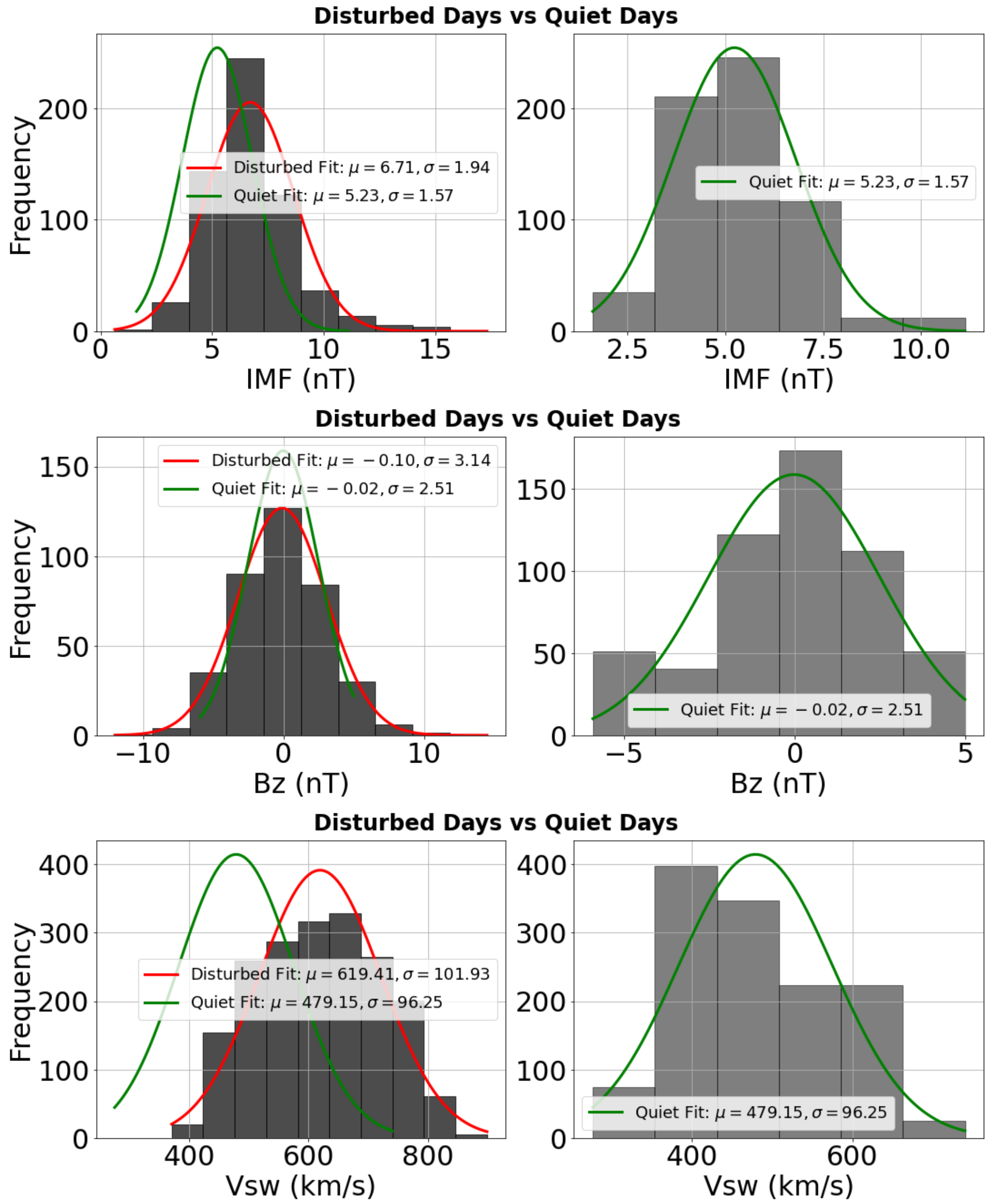

Figure 40 – Histogram of interplanetary magnetic field (IMF) parameters; IMF magnitude (Bo, in nT), Bz component in the GSM coordinate system (Bz, in nT), solar wind speed (Vsw, in km/s) are shown for disturbed days (HILDCAA* events) and quiet-day conditions in 2003. Gaussian distribution fits are depicted in red for disturbed days (HILDCAA* events) and in green for quiet days.

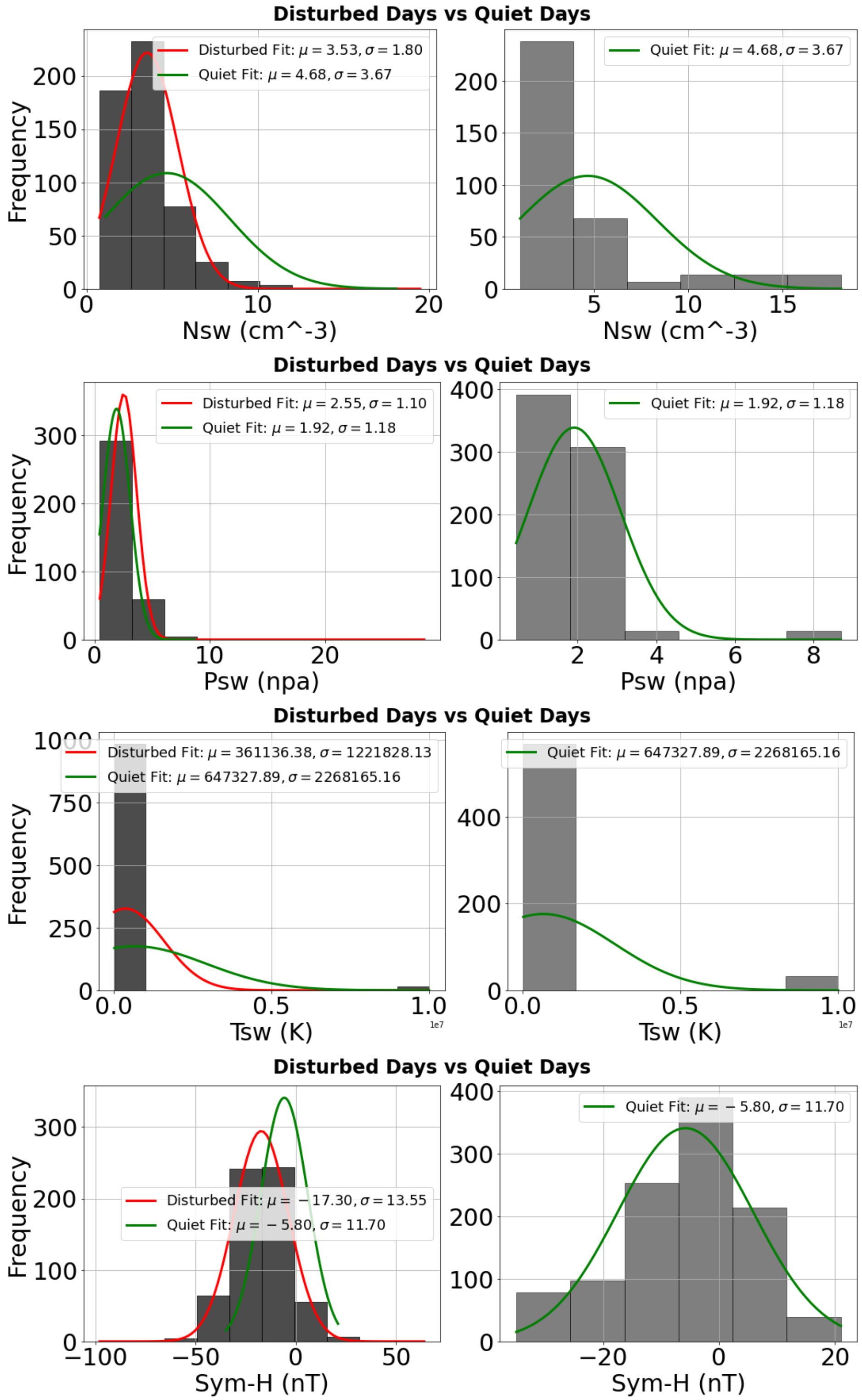

Figure 41 – Histogram of proton density (N_{sw} in cm^{-3}), flow pressure (Psw, in nPa), temperature (Tsw, in K) and the Sym-H index in nT are shown for disturbed days (HILDCAA* events) and quiet-day conditions in 2003. Gaussian distribution fits are depicted in red for disturbed days (HILDCAA* events) and in green for quiet days.

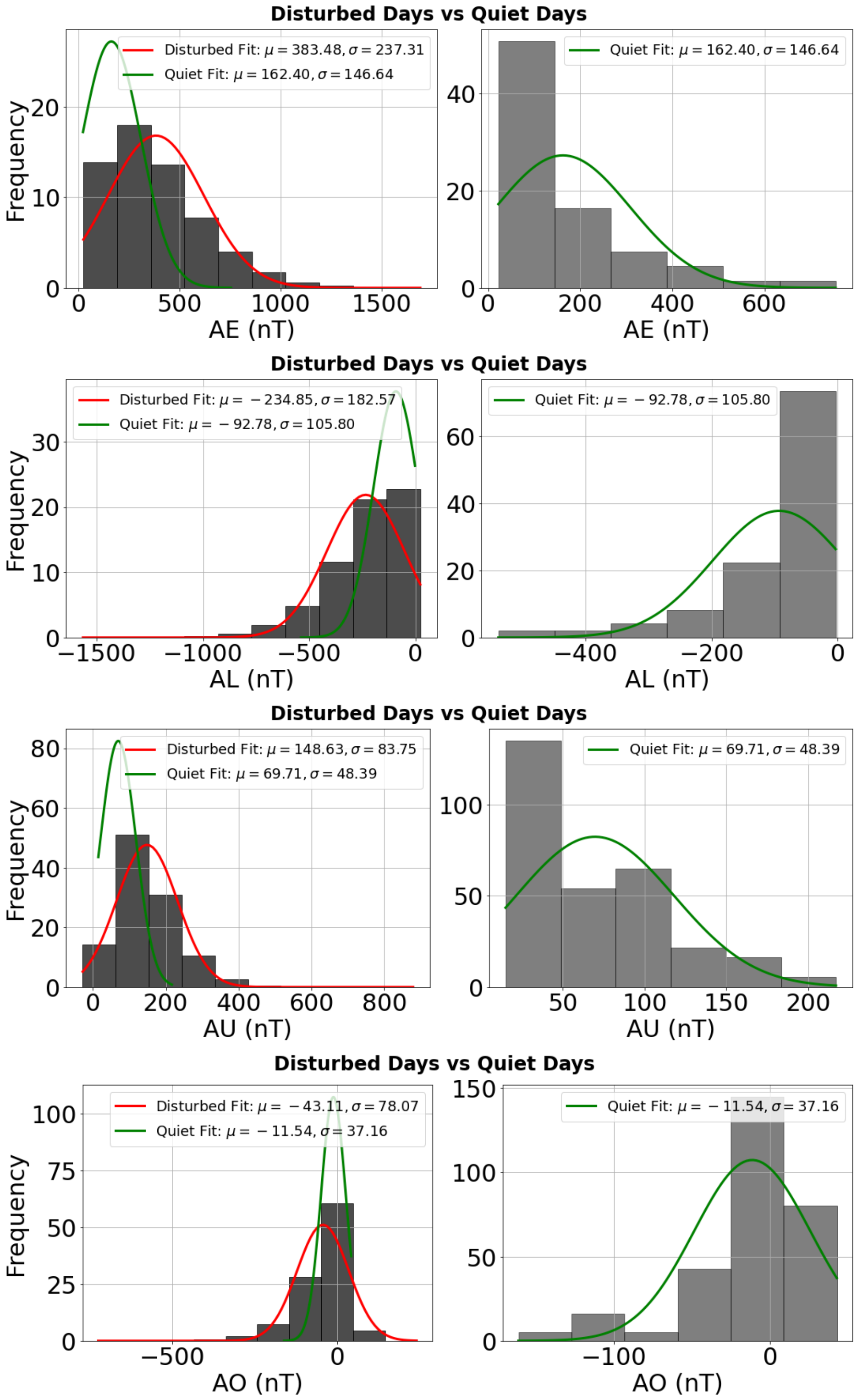

Figure 42 – Histogram of auroral electrojet indices in nT; AE, AU, AL, and AO are shown for disturbed days (HILDCAA* events) and quiet-day conditions in 2003. Gaussian distribution fits are depicted in red for disturbed days (HILDCAA* events) and in green for quiet days.

During the HILDCAA* events of 2003, the IMF exhibited moderate strength, with values between 5 and 7 nT. The B_z component fluctuated between 5.0 and 7.5 nT, predominantly in the positive direction, indicating weak southward IMF. This limited magnetic reconnection at the magnetopause. A notable enhancement in the IMF strength during disturbed periods showed higher peak distributions than during quiet days, where values were subdued, reflecting subdued energy transfer into the magnetosphere during geomagnetic storms. Solar wind speed ranged between 500 and 750 km/s, likely originating from coronal holes.

The proton density (N_{sw}) was relatively low, averaging 2.5–3.0 cm^3. However, N_{sw} and T_{sw} increased significantly during disturbed periods, contributing to geomagnetic activity. In contrast, quiet days displayed narrower distributions with lower values, indicative of calm solar wind conditions. The AE index peaked between 400 and 600 nT during disturbed periods, while the AL index reached -400 nT, indicating moderate substorm intensity. The AU index decreased to below 300 nT, and the Sym-H index peaked around -60 nT, signifying stronger geomagnetic storm activity.

Higher values of AE and AL during disturbances indicate intensified auroral activity and stronger westward electrojet currents. In contrast, quiet days were characterized by low Sym-H values, reflecting minimal auroral and ring current activity. The mean Sym-H index during disturbed days was -17.30 nT, compared to -5.80 nT during quiet days. Standard deviations of 13.55 nT (disturbed) and 11.70 nT (quiet) indicated moderate variability. Similarly, during quiet days, IMF values peaked at 4–6 nT, and B_z components remained minimally southward, around -6 nT. This narrower distribution is consistent with reduced geomagnetic activity.

The mean (V_{sw}) during disturbed days (619.41 km/s) was significantly higher than during quiet days (479.15 km/s), with respective standard deviations of 101.93 km/s and 96.25 km/s. These results align with estimates by Klausner et al. (2016) of 250–450 km/s during quiet periods. The (P_{sw}) during disturbances ranged from 1 to 5 nPa, with a mean value of 2.55 nPa, compared to 1.92 nPa during quiet days. These findings align with the average value (2.6 nPa) reported by Kivelson e Russell (1995), III, Mlynczak e Gordley (1994) across solar cycles.

The high auroral activity during 2003 was linked to long-term solar wind fast streams, as noted by Hajra et al. (2014), which increased HILDCAA* occurrences. A total of 26 HILDCAA* events, spanning 144 days, were observed in 2003. The mean AE index during disturbed days (383.48 nT) was significantly higher than during quiet days (162.40 nT), reflecting intense auroral activity characteristic of HILDCAA* events. The mean AL index during disturbed days (-234.85 nT) was greater than during quiet days (-92.78 nT), while the mean AU index during disturbances (148.68 nT) surpassed quiet days (69.71 nT). The AO index also followed this trend, averaging -43.11 nT during disturbances compared to -11.54 nT during quiet days.

These findings align with prior studies, such as Ahn e Moon (2003), which reported average AU, AL, and AE values of 84.6 nT, -135.1 nT, and 213.7 nT, respectively, for both disturbed and quiet periods. During HILDCAA* events, westward auroral electrojets are stronger than during quiet periods but weaker than during more intense geomagnetic disturbances. Enhanced solar wind speed and temperature during HILDCAA* events suggest a connection to HSS/CIR events, which amplify energy input into the ionosphere, perturbing currents and impacting TEC. (N_{sw}) remained lower on average during HILDCAA* events, a feature also noted by Hajra et al. (2014), where brief increases in N_{sw} occurred near the HILDCAA* onset but decreased throughout the event's duration. Conclusively, the southward B_z component observed during HILDCAA* events facilitates magnetic reconnection, as described by Dungey (1961), Gonzalez e Mozer (1974).

The coupling between the magnetosphere and ionosphere, primarily driven by magnetic reconnection processes, plays a fundamental role in modulating ionospheric parameters such as the F2-layer peak height. To gain a deeper scientific understanding of these interactions, it is essential to perform monthly statistical analyses. Such analyses allow for the extraction of systematic trends and the identification of anomalous behaviors by filtering out short-term fluctuations, which are often characterized as Gaussian noise. Notably, ionospheric parameters including hmF2, h′F, foF2, and TEC exhibit distinct monthly modulations during HILDCAA intervals, underscoring the persistent influence of high-speed solar wind streams on ionospheric variability.

Furthermore, Figure 43 displays a comparative analysis of the Gaussian distributions for ionospheric parameters; h'F, hmF2, and foF2, during geomagnetically disturbed intervals associated with HILDCAA events and quiet conditions in 2003. Histograms for both cases are overlaid with Gaussian fits to emphasize statistical distinctions: the red curve (left panel) denotes disturbed periods, while the green curve (right panel) represents quiet days.

During HILDCAA events in 2003, the mean h'F value for disturbed days (268.91 km) was higher than that for quiet days (260.00 km), indicating geomagnetic disturbances (e.g., HILDCAA) uplift the ionospheric layer to higher altitudes. The standard deviation for disturbed days (65.86 km) was also greater than that for quiet days (58.69 km), highlighting increased ionospheric variability caused by geomagnetic activity. Both histograms display a positive skew, with most values concentrated at lower heights but extending to higher altitudes.

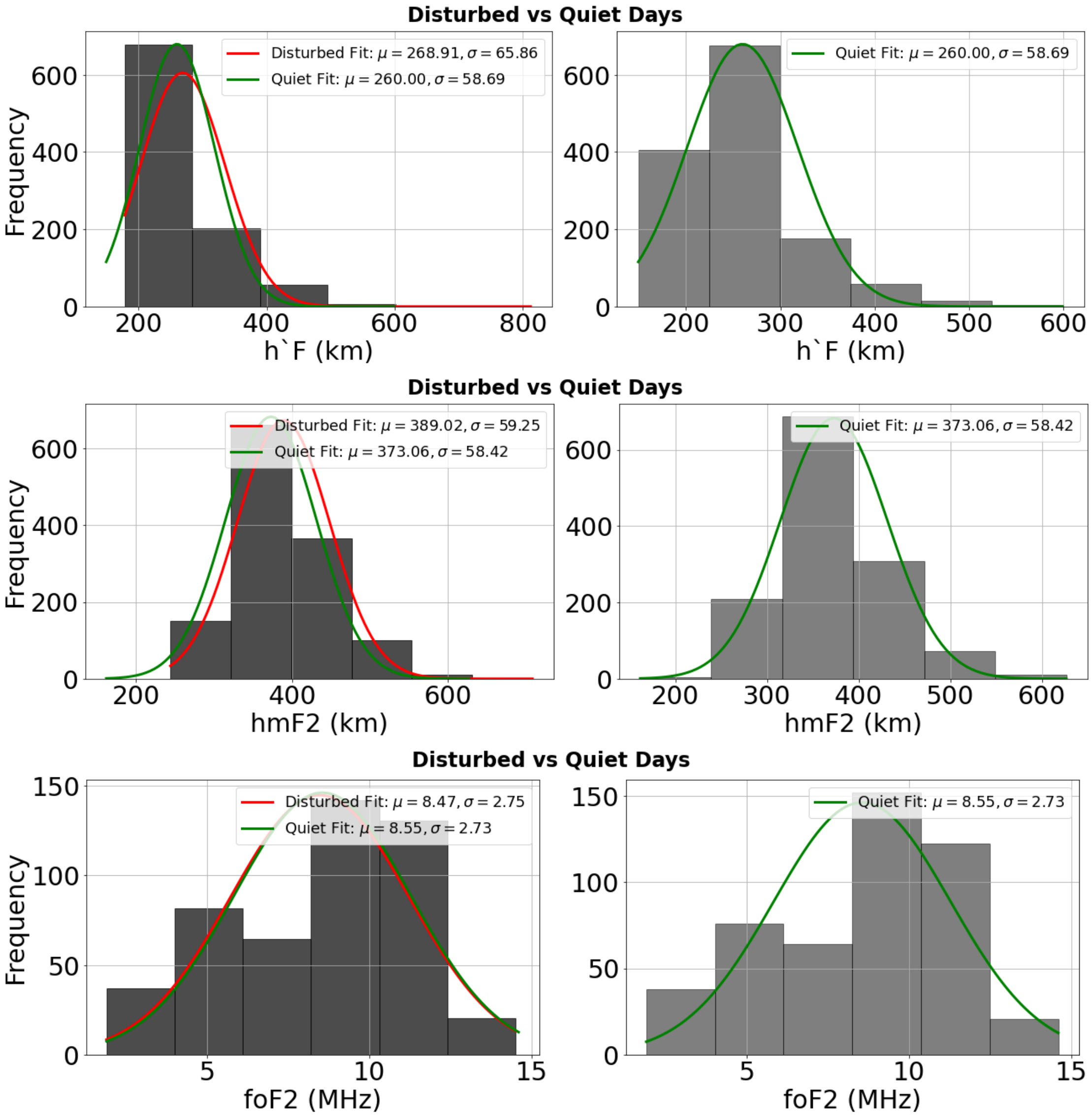

Figure 43 – Histogram of h’F, hmF2, foF2 are shown for both disturbed days (HILDCAA* events) and quiet-day conditions in 2003.

The distribution for disturbed days (red Gaussian fit) is broader and slightly shifted compared to quiet days (green fit), suggesting more significant ionospheric variability.

For hmF2, the Gaussian distribution reveals that the mean hmF2 during disturbed days (389.02 km) exceeded that during quiet days (373.06 km), reflecting the impact of geomagnetic disturbances on the ionospheric F2-layer peak height. Geomagnetic forcing processes during disturbed conditions drive this increase. The standard deviation for disturbed days (59.25 km) was marginally larger than that for quiet days (58.42 km), suggesting slightly greater fluctuations in the F2-layer peak height under geomagnetic activity. The histograms for both conditions are approximately symmetric with clear peaks, but the Gaussian fit for disturbed days (red) is shifted to the right, indicating higher hmF2 values than quiet days. This shift reflects dynamic changes in the ionosphere due to geomagnetic activity, with disturbed days showing higher altitudes and greater variability in F2-layer peak heights.

The increase in h′F during disturbed days can be attributed to geomagnetic storm effects. Energy input during disturbances heats the thermosphere, causing atmospheric expansion that raises the F-layer height. These disturbances also alter ionospheric dynamics, such as neutral winds and electric fields, which uplift ionized plasma and contribute to vertical movement of the F2-layer. Enhanced $\vec{E}$E×B drifts during geomagnetic disturbances further elevate the F-layer. The greater variability (σ) observed on disturbed days reflects the dynamic response of the ionosphere to geomagnetic activity, characterized by thermospheric expansion and vertical plasma drifts.

Regarding foF2, the data showed a Gaussian-like distribution, as illustrated by the fitted curves. The mean foF2 during disturbed days (8.47 MHz) was slightly lower compared to quiet days (8.55 MHz). This decrease is attributed to enhanced ionospheric disturbances caused by geomagnetic activity during HILDCAA events. Factors such as changes in thermospheric composition (e.g., increased molecular species like N_2 and O_2) and enhanced recombination processes due to energy input from geomagnetic storms lead to reduced ionization levels in the F2 region. The standard deviation for disturbed days (2.75 MHz) was marginally higher than that for quiet days (2.73 MHz), indicating slightly greater variability in ionospheric conditions during geomagnetic disturbances. While both histograms are similarly shaped, the Gaussian fit for disturbed days (red) shows a minor leftward shift, representing lower foF2 values compared to quiet days (green).

The observed decrease in foF2 during disturbed days reflects the impact of geomagnetic activity, including electron density irregularities and modifications in thermospheric winds and composition. The slightly larger spread during disturbed days signifies increased fluctuations in the ionosphere, consistent with the effects of geomagnetic disturbances. Although the overall distribution of foF2 remains relatively similar between disturbed and quiet days, the observed differences underscore the influence of geomagnetic activity on ionospheric behavior.

The Gaussian distribution of TEC on disturbed days versus quiet days for seven stations (FORT, BOMJ, BRAZ, POAL, RIOD, UEPP, VICO) during geomagnetic disturbances, such as HILDCAA phenomena in 2003, is illustrated in the figure in 44. Notably, the TEC values for disturbed days exhibit higher means (μ) and broader spreads (σ) compared to quiet days at all stations. The frequency distribution of TEC during disturbed days demonstrates broader

Gaussian-like distributions, whereas quiet days are heavily skewed towards lower TEC values.

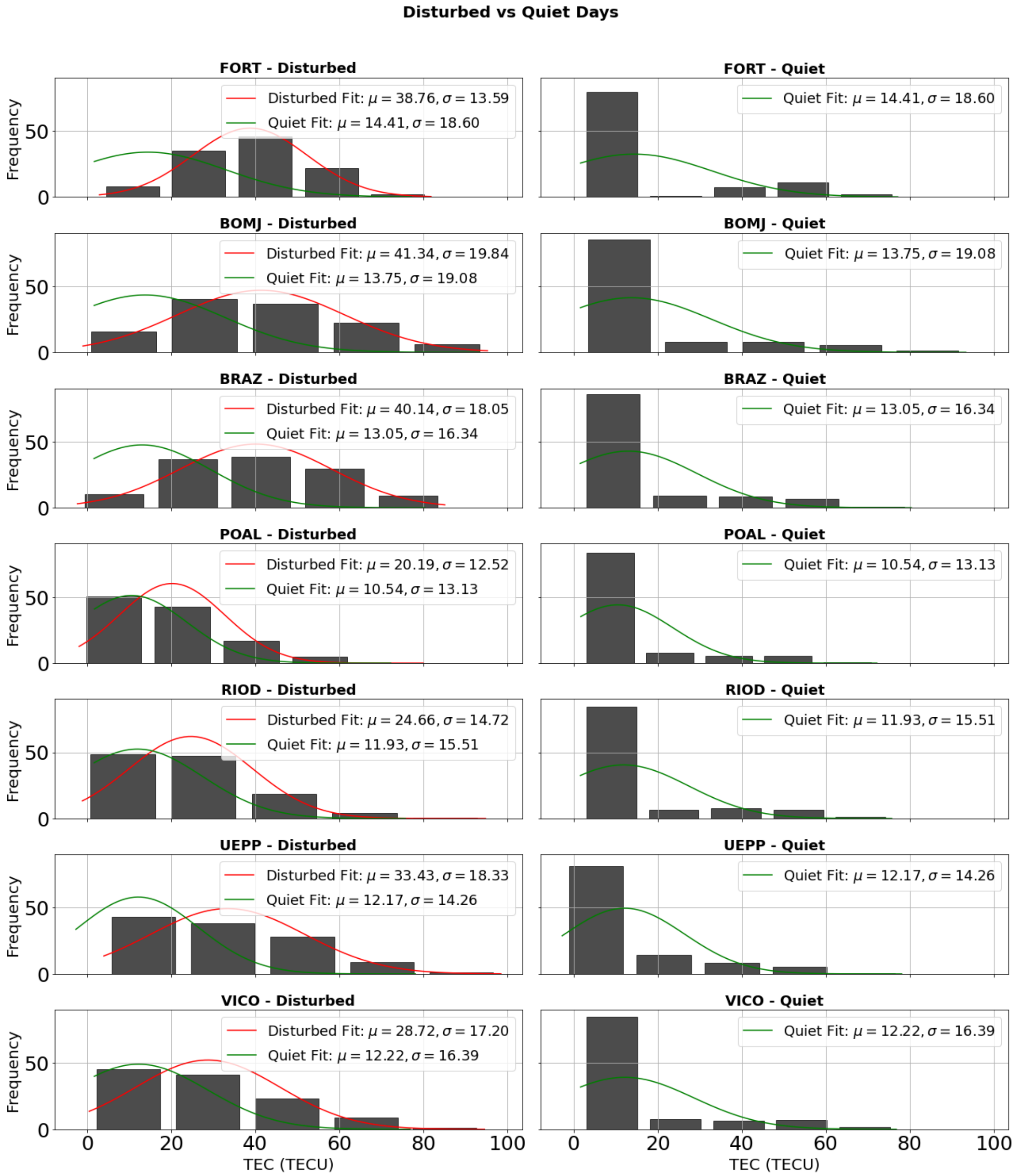

Figure 44 – Histogram of TEC are shown for both disturbed days (HILDCAA* events) and quiet-day conditions in 2003.

During HILDCAA-associated disturbed days in 2003, TEC exhibited significantly higher mean values and broader statistical distributions across all stations when compared to quiet days. This reflects enhanced ionization and increased variability in the ionosphere due to geomagnetic activity. At FORT and BOMJ, TEC values during disturbed days were notably elevated and widely dispersed, while quiet-day distributions were narrow and concentrated at lower values, indicating relatively undisturbed ionospheric conditions.

BRAZ similarly showed broader TEC distributions and elevated values on disturbed days, contrasting with the more constrained distributions observed during geomagnetically quiet periods. POAL and RIOD, located at slightly higher latitudes, exhibited moderate TEC enhancements during disturbed days, with POAL showing a relatively narrower distribution. On quiet days, TEC at these stations was strongly skewed toward lower values. At UEPP, disturbed days produced a significant TEC increase with a near-Gaussian distribution, whereas quiet days remained low and concentrated. VICO showed moderate enhancement and increased variability on disturbed days, with quiet-day values concentrated at the lower end of the distribution.

These observations suggest that HILDCAA events lead to systematic TEC enhancements driven by energy input from high-speed solar wind streams and associated interplanetary electric fields. The broader Gaussian-like distributions on disturbed days highlight the increased ionospheric variability and dynamic plasma transport processes induced by geomagnetic activity. The most pronounced effects were observed at stations closer to the EIA, such as BOMJ, BRAZ, and FORT, while higher-latitude stations exhibited more moderate responses.

5.5.1 Electrodynamic and Thermospheric Drivers of TEC Variability During HILDCAA Events

The Bz component of IMF exhibits significant fluctuations during periods of HSS following CIRs. This variability is closely correlated with AE index fluctuations during HILDCAA events. Additionally, major negative excursions of IMF-Bz correspond to increases in AE indices. Studies by Huang, Foster e Kelley (2005), Tsurutani et al. (2004), Tsurutani et al. (2008) and Mannucci et al. (2009) suggest that prolonged southward IMF Bz events prompt long-duration penetration of ionospheric electric fields, leading to uplift of ionospheric plasma and enhanced TEC at EIA crests. Enhanced electric fields transport plasma to higher altitudes, facilitating the expansion of EIA towards mid-latitudes (BATISTA et al., 2006).

According to studies (VERKHOGLYADOVA et al., 2008; TSURUTANI et al., 2005; KELLEY et al., 2003; HUANG et al., 2005), significant southward incursions of IMF-Bz can lead to sudden penetration of ionospheric electric fields, resulting in increased TEC at the EIA crest. Additionally, daytime photoionization also contributes to TEC enhancements. One of the primary mechanisms driving TEC enhancement is the uplift of the ionospheric F region to higher altitudes, where reduced neutral densities lead to slower recombination rates

(KELLEY, 2009). Our results are consistent with the findings of Negreti, Paula e Candido (2017).

Additionally, our analysis reveals significant differences in TEC behavior between the Brazilian equatorial and low-latitude regions. The southern crest of EIA experiences more pronounced TEC fluctuations, while the equatorial region generally exhibits greater TEC stability during nighttime. However, post-sunset TEC enhancements are frequently observed at the south crest of EIA, driven by the intensification of pre-reversal electric fields. Overall, low-latitude regions show stronger TEC enhancements compared to the equatorial zone, largely due to the EIA, where plasma density maxima are located away from the magnetic equator. The findings of this study contrast with those reported by Denardini et al. (2021), Wang et al. (2024). During HILDCAA events, increased electric fields and particle precipitation enhance TEC levels and strengthen ionospheric currents, as described by Denardini et al. (2021).

TEC enhancements during HILDCAA events could likely due to DDEFs or PPEFs influenced by the oscillatory behavior of IMF Bz. Verkhoglyadova et al. (2013) highlighted the role of PPEFs and DDEFs as significant contributors to VTEC changes during HILDCAA events associated with CIRs and solar wind forcing. Another contributing factor to these enhancements is the observed increase in F10.7 solar flux (referenced in 39), which enhances atmospheric ionization. During this period, the average F10.7 solar flux was noted to be ≈ 138 Solar Flux Units. The changes observed in the EIA represent one aspect of the equatorial thermosphere-ionosphere system's response to magnetospheric disturbances (ABDU et al., 1995). These variations can arise from alterations in ionospheric electric fields and thermospheric winds (VOLLAND, 1995; PRÖLSS; ROEMER; SLOWEY, 1988).

It is important to emphasize that both PPEFs and DDEFs might occur during a HILDCAA event, hence contributing to the combined ionosphere response during the long recovery phase. Auroral heating during storm times generates dynamic thermospheric winds which result in ionospheric disturbance dynamo due to the overshielding mechanism as presented by the R2 current system (WEI et al., 2015). These thermospheric winds influence the globalized movement, producing disrupted ionospheric electric fields at middle and low latitudes causing changes in composition and densities of thermosphere as highlighted by Blanc e Richmond (1980) and Rishbeth (1975), which contribute to TEC enhancement. According to Negreti, Paula e Candido (2017) TEC over South America increased during HILDCAA events and was linked to the PPEFs.

Mostly, at equatorial and low latitudes, TEC characteristics are shaped by the geomagnetic field, responding to three primary storm-time processes: (1) prompt effects, (2) delayed effects, and (3) changes in composition, as outlined by Mendillo (2006), all of which are ultimately connected to magnetospheric input. Prompt penetration effects occur during geomagnetic storms, where the magnetospheric electric field penetrates and transports low-latitude plasma to higher altitudes due to the under-shielding mechanism, creating what is known as the "fountain effect" at the magnetic equator. This phenomenon results in a decrease in TEC over the equatorial region while enhancing TEC at the southern crest of the EIA. This latitudinal variation significantly influences the TEC of the ionosphere, linking it to the position of the subsolar point and specific dynamical processes occurring in the Earth's upper atmosphere (YASYUKEVICH et al., 2023). The structure of the EIA at various latitudes is also affected by electric field disturbances that can be detected by TEC measurements within the EIA belt (BATISTA et al., 1991; ASTAFYEVA, 2009). Low latitudes absorb the highest levels of solar energy (ABDU et al., 1995), resulting in increased ionization in these areas. The ambient ionization level here is sensitive to changes in the electric field at the magnetic equator as well as to the dynamics of the thermosphere and neutral atmosphere, depending on the timing and intensity of geomagnetic storms. This distribution of ionization is referred to as the ionization equatorial anomaly or Appleton anomaly. Consequently, the equatorial low-latitude region displays a variety of unique phenomena, including the equatorial electrojet , EIA, plasma fountain, equatorial wind, and temperature anomalies (JAYACHANDRAN et al., 1997). As noted by Abdu (1997), the formation of the EIA can experience significant enhancement or suppression due to the influence of disturbance electric fields (i.e., delayed effects) during storms.

The delayed effect is linked to short-lived electric field disturbances (KOTADIA, 1965; SOMAYAJULU, 1963; KAN; LEE, 1979) that suppress the fountain effect, resulting in longer-lived impacts. This leads to a delay in the electrodynamics caused by winds from auroral heating reaching low latitudes, a phenomenon referred to as the "disturbance dynamo" mechanism (BLANC; RICHMOND, 1980), which diminishes eastward electric fields at equatorial latitudes. The disturbance fountain extends over a broader latitudinal range compared to the normal fountain driven by the E/F-layer dynamo electric field. The formation of latitudinally displaced crests is a result of the diffusion process following the initial disturbance fountain associated with the expansion of the EIA (ABDU, 1997). The DDEFs can suppress both the vertical E×B drift and the fountain effects, leading to a weaker EIA (characterized by lower TEC values on the crests) or even reversing the fountain effects from the perspective of the EIA, as seen during certain HILDCAA intervals.

The third mechanism of magnetospheric origin is related to changes in composition, which also stem from auroral heating. Joule heating at high latitudes triggers neutral circulation toward lower latitudes, which enriches O/N_2 concentrations at mid-latitudes and increases densities at low latitudes as presented in figure A.13 as referenced in A.

This process enhances TEC near the equator, adding a nonelectrodynamical component when the fountain effect is not predominant. It is recognized that equatorward winds, driven by heightened Joule and particle heating, elevate the ionospheric layers to greater altitudes and across pressure surfaces and as a results in observable positive changes in ionospheric conditions (WERNER; PRÖLSS, 1997; PRÖLSS, 1997). These findings highlight the influence of equatorward neutral winds, which elevate the F-layer height by transporting ionization to areas with lower losses during the daytime, thereby increasing TEC values.

A combination of these processes especially intense Lorentz coupling and joule heating causes an upwelling of the atmosphere around the auroral oval or simply thermospheric expansion of the atmosphere which results in the motion of perturbed plasma composition. The redistribution of depleted O/N_2 ratio by thermospheric winds influences ionospheric variability in mid- to low-latitude regions as mentioned by Lee et al. (2013), Prölss, Roemer e Slowey (1988), Fuller-Rowell et al. (2016).

5.5.2 Monthly Analysis of HILDCAA* Event Occurrences and Their Relationship with Solar Wind Characteristics, Geomagnetic Indices, and Ionospheric Parameters in 2003

A comprehensive comparative analysis was performed to explore the relationship between the monthly percentage occurrence of HILDCAA* events and the corresponding monthly mean peak values of solar and geomagnetic parameters, as well as ionospheric characteristics over Brazil in 2003. The ionospheric variables considered include F2 layer parameters h′F, hmF2, and foF2in addition to TEC. A total of 143 disturbed days, associated with 26 HILDCAA* intervals, were identified and analyzed. The monthly percentage of HILDCAA* days was computed as the ratio of disturbed days per month to the total number of disturbed days, multiplied by 100.

In Figures 45 and 46, the distribution of HILDCAA* days is represented by gray bars, while the red line with markers indicates the monthly average values of the examined parameters during the HILDCAA* intervals.

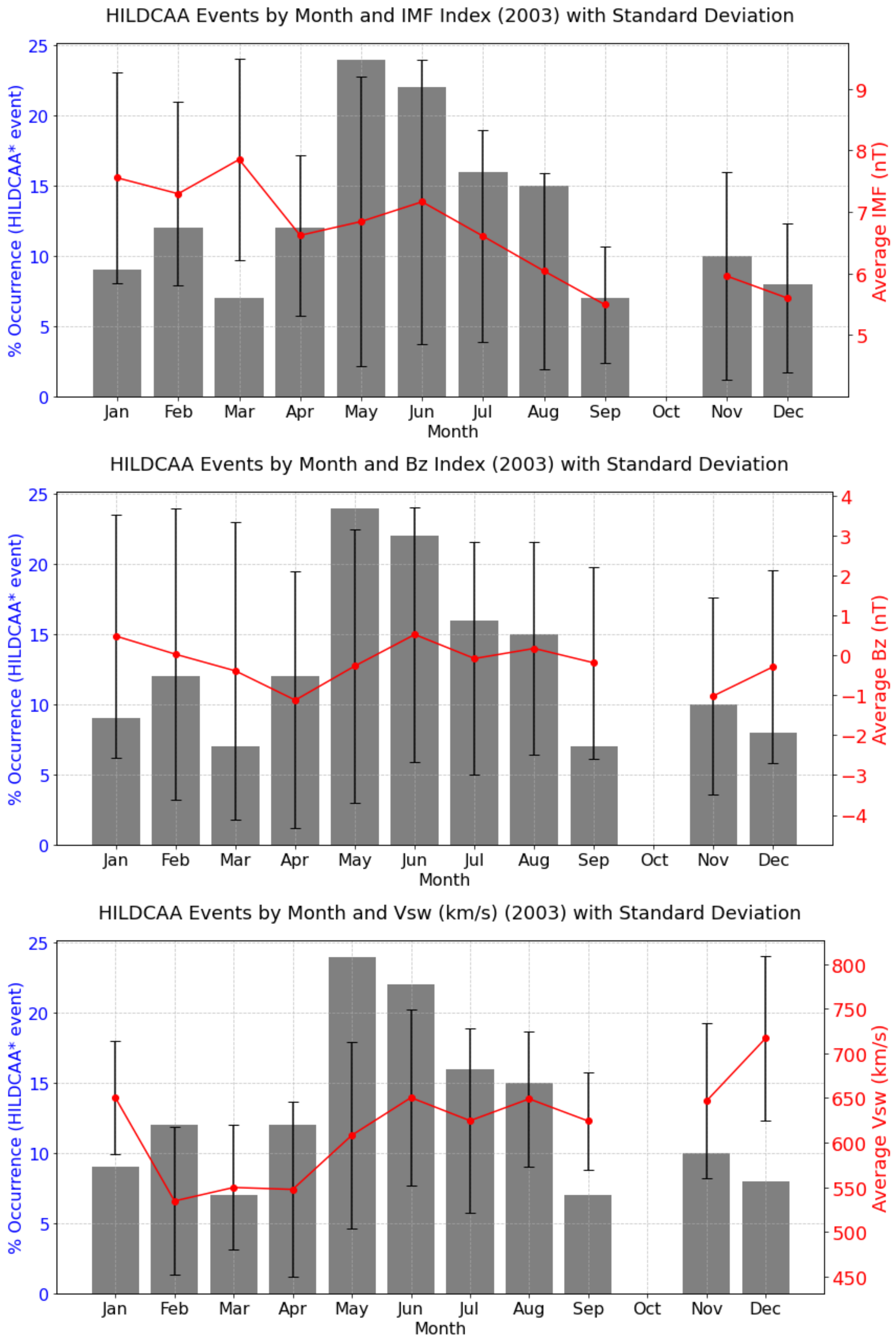

Figure 45 – Histograms of interplanetary magnetic field (IMF) parameters; IMF magnitude (Bo, in nT), Bz component in the GSM coordinate system (Bz, in nT), solar wind speed (Vsw, in km/s) are shown for disturbed days (HILDCAA* events) conditions in 2003.

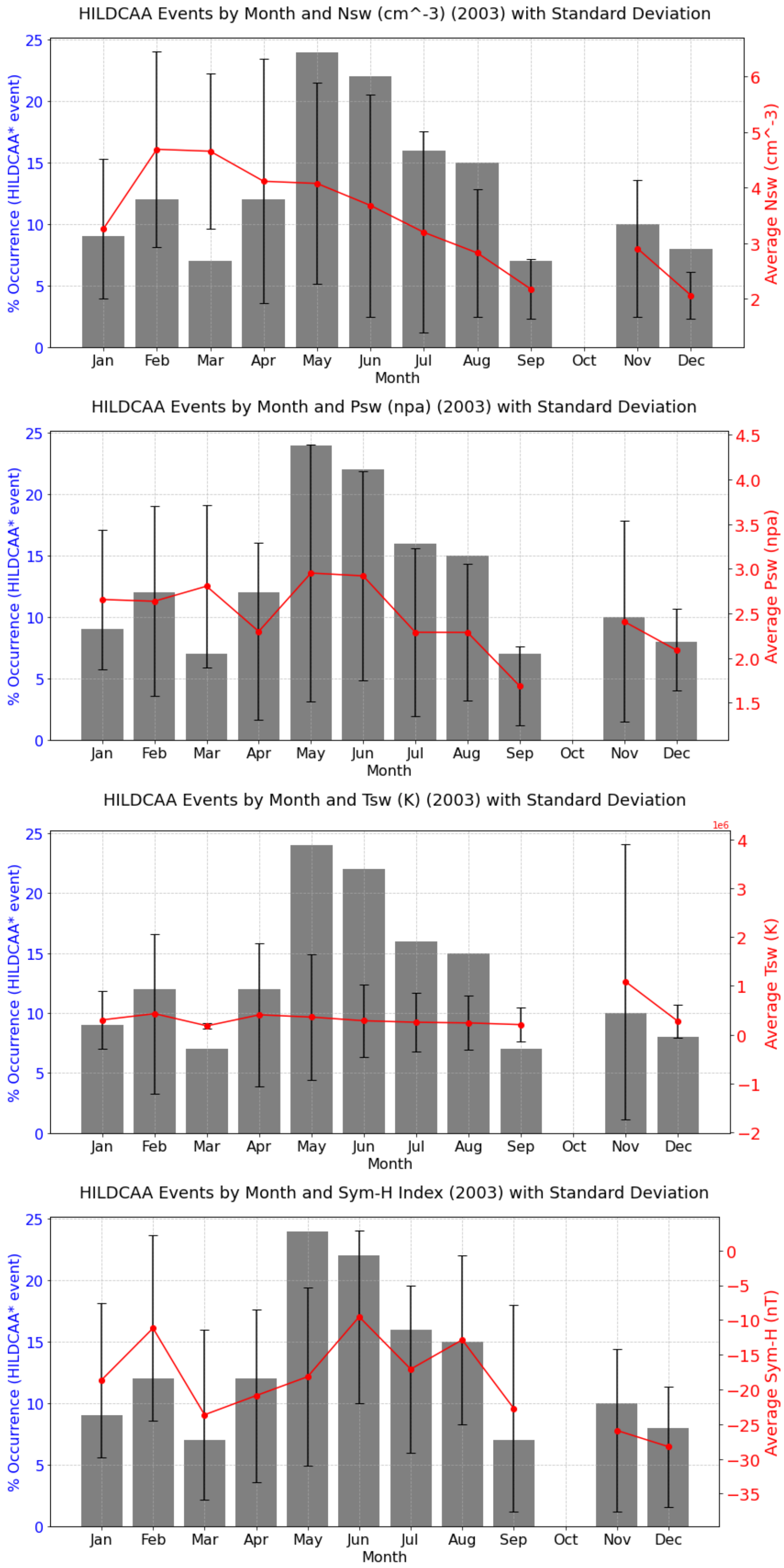

Figure 46 – Histograms of proton density (N_{sw} in cm^{-3}), flow pressure (Psw, in nPa), temperature (Tsw, in K) and the Sym-H index in nT are shown for disturbed days (HILDCAA* events) conditions in 2003.

The monthly relationship between the IMF magnitude and HILDCAA event occurrences reveals a moderately positive correlation, particularly during the high-frequency HILDCAA months of May and June. During these months, the average IMF strength hovers around 6.8–7.0 nT, suggesting that a moderately strong IMF supports the sustained solar wind–magnetosphere coupling characteristic of HILDCAA conditions. Although the IMF is strongest in March ($\approx$ 7.8 nT), HILDCAA activity is relatively low, possibly indicating that strong IMF alone is insufficient without accompanying high-speed solar wind or fluctuating Bz components. In contrast, during April, despite a slightly weaker IMF ($\approx$ 6.5 nT), HILDCAA frequency rises, likely due to the presence of other contributing solar wind conditions. the analysis suggests that IMF strength contributes to but does not solely govern HILDCAA onset; rather, it acts in conjunction with parameters like solar wind speed, density, and magnetic fluctuations to sustain substorm activity in the recovery phase of geomagnetic storms. The variation of the average IMF-Bz indicate the influence of sustained Bz orientation on substorm activity. During months with high HILDCAA frequency (May and June), the average Bz values are either weakly southward or fluctuating near zero, supporting the theory that HILDCAAs are driven by prolonged intervals of weakly southward or fluctuating Bz under high-speed stream conditions.

Interestingly, in April despite a strongly southward Bz average ($\approx$ -1.0 nT), HILDCAA activity is comparatively low, likely due to transient storm conditions rather than steady-state HSS influences. Meanwhile, positive or northward Bz values in January and June do not inhibit HILDCAA events, reinforcing that strongly southward Bz is not a strict requirement; instead, moderate and sustained conditions often suffice. This underscores the role of Alfvénic fluctuations in solar wind-magnetosphere coupling during HILDCAA intervals, even under relatively weak Bz magnitudes.

With respect to Vsw, strong seasonal variation is observed in HILDCAA* activity. The most significant occurrences are seen in May (24%) and June (22%), coinciding with the late-autumn to early-winter period in the Southern Hemisphere. These months also exhibit relatively high average solar wind speeds (Vsw > 600 km/s), suggesting a connection between elevated solar wind speed and enhanced HILDCAA activity. July and August also show moderate levels of activity (16% each), maintaining above-average Vsw levels ($\approx$ 640 km/s). Interestingly, February, a summer month shows relatively low HILDCAA occurrence ($\approx$ 12%) despite having one of the lowest Vsw values ($\approx$ 540 km/s). December, however, has a low event percentage ($\approx$ 8%) but the highest average Vsw ($\approx$ 715 km/s). This decoupling suggests that while elevated Vsw is a key driver for HILDCAA* events, other interplanetary conditions (e.g., prolonged southward IMF Bz, low geomagnetic activity) are necessary for their development. The low activity in March and September ($\approx 7\%$), traditionally equinoctial months known for geomagnetic disturbances, might indicate that HILDCAA events favor sustained HSS during solstices over transient CME-driven events common during equinoxes. Generally, the alignment between Vsw peaks and HILDCAA event frequency is partial—highlighting that persistent HSS from coronal holes are not the sole triggers, and internal magnetospheric processes and preconditioning from preceding storms could modulate event onset and persistence.

The distribution of HILDCAA* events in relation to the Nsw reveals key insights into the plasma environment conducive to sustained substorm activity. The HILDCAA peak in May and June occurs during a period when Nsw steadily declines from its earlier maximum in February ($\approx$ 4.6 cm^{-3}) to below $\approx$ 4.0 cm^{-3}. This suggests that while elevated densities may coincide with some events, HILDCAA intervals are more likely associated with moderate to low-density, high-speed solar wind streams originating from coronal holes. The sharp density decrease observed from July to September, alongside diminishing HILDCAA occurrence, supports this trend. Interestingly, the months with the highest solar wind density—February and March, do not correspond to the highest HILDCAA activity, indicating that high density alone is not a primary driver. Instead, moderate densities may facilitate the formation of Alfvénic fluctuations, which help sustain magnetospheric convection during HILDCAA events.

Similar behavior of HILDCAA event occurrence, alongside the average Tsw, highlights a complex relationship between solar wind thermal conditions and extended auroral activity. The most active months for HILDCAA events May and June coincide with moderately elevated Tsw values ($\approx$ 400,000–500,000 K), suggesting that warm, high-speed streams from coronal holes might be a contributing factor. Notably, November exhibits an anomalously high Tsw (>1,000,000 K) despite a relatively low HILDCAA occurrence ($\approx 10\%$), indicating a transient event such as an interplanetary shock or the tail end of a ICME, rather than typical HSS. The generally lower Tsw values during March, July, and September align with reduced HILDCAA activity, reinforcing the idea that moderate to high solar wind temperatures, often associated with HSS regions, help sustain the magnetospheric conditions needed for HILDCAA development. However, the non-linear correlation suggests that Tsw alone is not the sole driver; rather, it acts in concert with solar wind speed, dynamic pressure, and IMF orientation to create conducive conditions for prolonged substorm activity.

Psw reveals a prominent mid-year peak in HILDCAA occurrences, with May (24%) and June (22%) showing the highest rates. These peaks coincide with elevated Psw values, reaching $\approx$ 2.95 nPa during these months. The results suggest a seasonal modulation in

HILDCAA activity, likely influenced by the interaction between HSS and the Earth's magnetosphere. periods of increased Psw, notably from April through June, appear to enhance the likelihood of sustaining long-duration substorm activity characteristic of HILDCAAs. Conversely, months with reduced Psw (e.g., September at ≈ 1.75 nPa and December at ≈ 2.05 nPa correspond with diminished HILDCAA occurrences. This relationship supports the hypothesis that elevated solar wind dynamic pressure, often associated with the trailing edges of CIRs or embedded HSS, contributes to the magnetospheric conditions favorable for HILDCAA development. These findings are consistent with the known geoeffectiveness of solar wind structures during the declining phase of the solar cycle and provide further insight into the solar wind–magnetosphere coupling during such events.

As shown in Figure 47, the AE index used as a proxy for auroral activity further supports the observed pattern. May (24%) and June (22%) once again exhibit the highest occurrences of HILDCAA events, aligning with the earlier analysis of Vsw. These months are also associated with elevated AE index values (≈ 420 nT and 390 nT, respectively), reinforcing the notion that HILDCAA intervals are marked by sustained, moderate geomagnetic activity rather than intense geomagnetic storms.

March and September show the lowest HILDCAA* occurrence (7%) and also the lowest AE index (≈ 270 nT), which supports the association between auroral activity and HILDCAA generation. Interestingly, November, which shows a modest HILDCAA occurrence ($\approx 10\%$), has the highest AE index (≈ 450 nT). This could be due to a strong but isolated geomagnetic disturbance that did not meet the sustained conditions for HILDCAA classification highlighting that not all high AE conditions correspond to HILDCAA intervals. March, April, and August show moderate AE levels ($\approx 375--390$ nT) but relatively low HILDCAA* occurrence, further supporting the idea that both intensity and duration of substorm activity (AE) must be considered. The highest HILDCAA* occurrence occur in May (24%) and June (22%), which correspond to moderate AL values (≈ -240 to -220 nT). Notably, February, which shows low HILDCAA* activity (12%), registers the least negative AL value (≈ -160 nT) indicating weaker substorm activity that month.

In November, despite a relatively high AL magnitude (≈ -300 nT), only shows a modest HILDCAA* percentage ($\approx 10\%$). This suggests that intense substorm activity does not necessarily translate to HILDCAA* formation, likely because HILDCAA* intervals require persistent, moderate disturbances rather than short-lived bursts. The months of July to September reflect a gradual decline in both AL magnitude and HILDCAA* occurrence, maintaining the trend that sustained moderate geomagnetic activity, rather than extreme fluctuations, is more conducive to HILDCAA* development.

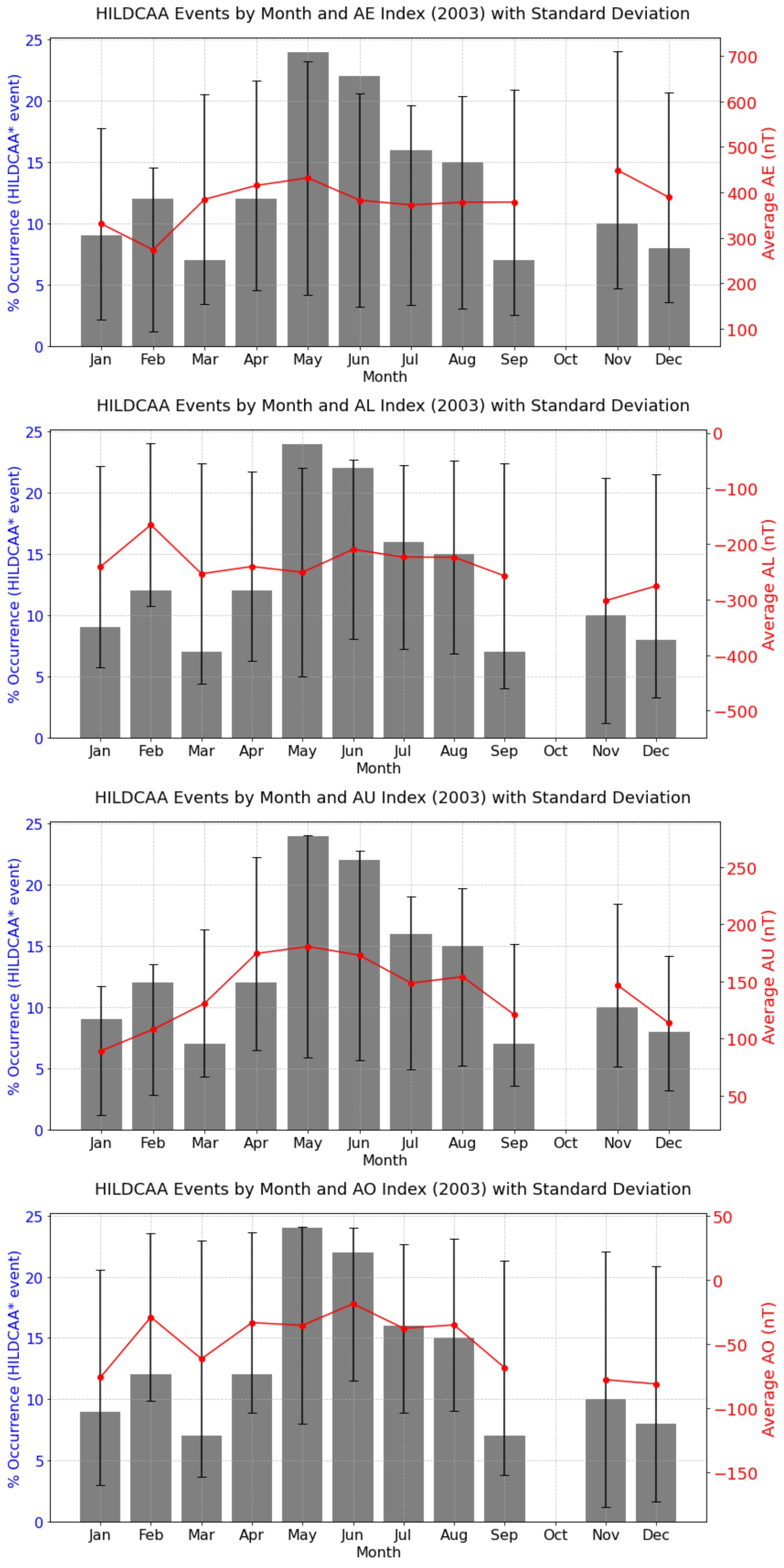

Figure 47 – Histograms of auroral electrojet indices in nT; AE, AU, AL, and AO are shown for disturbed days (HILDCAA* events) conditions in 2003.

Similarly, in 47 the most active months in terms of HILDCAA* occurrence was in May (24%) and June (22%)are associated with moderate substorm activity, as indicated by AL index values around -240 to -220. Conversely, February records the highest (least negative) AL value (≈ -160 nT), which aligns with a lower HILDCAA* frequency ($\approx$ 12%), suggesting subdued geomagnetic conditions.

Interestingly, despite the strong auroral activity in November (AL ≈ -300 nT), the HILDCAA* occurrence remains low ($\approx$ 10%), implying that the persistence and structure of the substorm activity, rather than its peak intensity, is crucial for HILDCAA formation. These findings reinforce the notion that HILDCAA intervals are more associated with continuous, moderate westward electrojet activity driven by recurrent HSS. A strong correspondence is observed between high HILDCAA* activity and elevated AU values, particularly during May and June when both parameters peak ($\approx$ 24% and $\approx$ 22% occurrence with AU values around 180 and 170 nT, respectively). This reinforces the notion that HILDCAA* intervals are characterized by enhanced and persistent eastward auroral electrojet activity. From January to May, the concurrent increase in both AU and HILDCAA* frequency suggests a progressive strengthening of solar wind-magnetosphere coupling, likely associated with recurring high-speed streams. Conversely, months like October and March, with relatively low AU values ($\approx$ 0 and $\approx$ 120 nT), show minimal to no HILDCAA* activity. These results support previous findings that HILDCAA periods are associated with continuous, moderate geomagnetic activity rather than isolated substorms or intense storms.

The monthly distribution of HILDCAA events, as shown in the histogram, highlights a significant temporal variability in occurrence rates, with the highest percentages observed in May (24.48%) and June (23.08%). These months correspond to the late autumn and early winter period in the Southern Hemisphere. Conversely, minimal activity is noted in March and September (6.29% and 4.90%, respectively). The overlay of the average AE-derived AO index indicates a general inverse relationship between HILDCAA occurrence and geomagnetic activity levels, with more negative AO values seen during months of reduced HILDCAA event rates. Notably, June—the month with the highest event percentage also recorded the highest AO value (least negative), suggesting enhanced auroral electrojet activity during sustained substorm-like conditions. Meanwhile, the lowest AO values (more negative) are observed in December and November, months with fewer HILDCAA occurrences. This result aligns with previous findings that HILDCAA events are predominantly driven by high-speed solar wind streams and CIRs, which tend to have seasonal dependencies, potentially modulated by Earth's heliographic latitude and the Russell-McPherron effect.

Similarly, the Sym-H index a high-resolution version of the Dst index that indicates the strength of the ring current and thus overall geomagnetic storm intensity as shown in in 45. The months of May and June stand out with the highest HILDCAA* occurrence (24% and 22%) and comparatively less negative Sym-H values (≈ –14 and –10 nT), indicating weak to moderate storm conditions, a typical feature of HILDCAA periods. Notably, March, November, and December show more negative Sym-H averages (approaching –27 to –28 nT), yet exhibit lower HILDCAA* occurrence (7–10%). This inverse behavior supports the idea that HILDCAA* events are not strongly associated with intense geomagnetic storms but are rather linked with sustained, moderate geomagnetic activity often driven by high-speed solar wind streams and CIRs. The results reaffirm the association of HILDCAA* events with weak to moderate geomagnetic activity. The highest occurrences in May and June (≈ 24% and –14 and –10 nT, respectively), typical of non-storm or weak storm conditions. In contrast, months like March, November, and December exhibit more negative Sym-H values (-25 to -28 nT), suggesting stronger ring current activity, yet they correspond to lower HILDCAA* occurrences (≈ 7–10%).

This emphasizes that intense geomagnetic storms are not a defining feature of HILDCAA intervals; rather, these episodes are predominantly associated with HSS and CIRs instead of CME-driven disturbances. Building on this distinction, the variability during HILDCAA intervals, as reflected in monthly standard deviations (SD), reveals systematic patterns across geomagnetic indices and solar-wind parameters.

For the auroral indices, the AE index exhibits SDs of ≈ ±60–100 nT, with pronounced variability in May, June, and November, while February and September show much smaller SDs, indicating steadier auroral electrojet conditions. Similarly, the AU index displays SDs of about ±40–80 nT, peaking in May–June and November, whereas January, March, and September reveal lower dispersion and more stable eastward electrojet activity. In contrast, the AL index maintains elevated SDs of roughly ±70–120 nT from February through August, reflecting strong westward electrojet variability during geomagnetically active periods. The AO index records SDs of ±40–80 nT, highest between September–December and again during May–July, signifying enhanced Alfvénic fluctuations and frequent HILDCAA episodes.

Turning to the interplanetary IMF, the total magnitude typically varies with SD ≈ ±1–2 nT, punctuated by larger SD episodes in January, February, and May that indicate stronger field variability. The IMF Bz component shows SDs of about ±2–3.5 nT, with March, April, and October revealing pronounced north–south swings, and April–June corresponding to the largest dispersion, consistent with elevated HILDCAA activity. Concurrently, the Sym-H index reaches SDs of roughly ±8–15 nT, maximized in May–June, signaling intensified and highly variable ring-current dynamics.

Solar-wind parameters display comparable contrasts. The proton Tsw remains low in March (±0.1×10^5 K) but rises markedly in November (±0.3–0.5×10^5 K), indicating irregular thermal input despite moderate HILDCAA frequency. The Psw registers SDs of ±0.4–0.6 nPa, largest in May–June and subdued in March, September, and December, implying steadier driving during quieter intervals. The Vsw fluctuates with SDs of ±40–60 km/s in May–July, exceeding ±70 km/s in December, paralleling the incidence of high-speed stream events typical of the declining solar cycle. Finally, the Nsw exhibits SDs of roughly ±1.5–2.5 cm^{-3}, peaking during April–June and closely following periods of enhanced HILDCAA activity. To contextualize their ionospheric impact. Table 7 synthesizes the key solar and geomagnetic parameters and outlines their contributions to disturbance-driven effects on the ionosphere.

Figure 48 presents an analysis of HILDCAA event occurrences alongside the monthly average values of F-region height parameters (hmF2, h′F) and the critical frequency foF2. The highest percentage of HILDCAA events was recorded in May ($\approx$ 24%), followed by June (around 22%) and July (about 16%). These months fall within the Southern Hemisphere winter season, a period often associated with increased geomagnetic activity, primarily driven by HSSs and CIRs. The clustering of events during this time frame suggests the recurring presence of solar wind structures, likely linked to the persistent nature of CIR/HSS-induced geomagnetic disturbances. Notably, h′F values showed a gradual increase during the months with peak HILDCAA activity, reaching a maximum average height of $\approx$ 293 km in July. This rise in h′F is indicative of intensified geomagnetic forcing, which involves enhanced electric fields, thermospheric heating, and ion drag mechanisms that promote upward plasma transport in the equatorial ionosphere. The elevated h′F in July likely reflects stronger upward E×B plasma drifts, characteristic of disturbed ionospheric conditions.

Table 7 – Summary observations of HILDCAA* Events vs solar and geomagnetic Parameters (2003)

Month	**% HILDCAA Days**	**Avg. Solar & Geomagnetic Parameters**	**Key Observations/ Remarks**
January	9%	IMF: 6.2 nT, Bz: +0.3 nT, Vsw: 570 km/s, Nsw: 4.2 cm^{-3}, Tsw: 370,000 K, Psw: 2.3 nPa, AE: 310 nT, AL: −190 nT, AU: 140 nT, Sym-H: −18 nT, AO: −67 nT	Low activity with weak southward Bz and moderate solar wind. Positive Bz may have limited coupling efficiency.
February	12%	IMF: 6.0 nT, Bz: −0.2 nT, Vsw: 540 km/s, Nsw: 4.6 cm^{-3}, Tsw: 330,000 K, Psw: 2.7 nPa, AE: 270 nT, AL: −160 nT, AU: 120 nT, Sym-H: −11 nT, AO: −25 nT	Lowest HILDCAA occurrence, coinciding with low Vsw and AE. High density but low energy transfer.
March	7%	IMF: 7.8 nT, Bz: −0.6 nT, Vsw: 580 km/s, Nsw: 4.3 cm^{-3}, Tsw: 360,000 K, Psw: 2.5 nPa, AE: 375 nT, AL: −210 nT, AU: 150 nT, Sym-H: −23 nT, AO: −62 nT	Strong IMF but low HILDCAA activity, possibly due to lack of sustained HSS. Equinox effects may favor CMEs.
April	12%	IMF: 6.5 nT, Bz: −1.0 nT, Vsw: 610 km/s, Nsw: 4.0 cm^{-3}, Tsw: 410,000 K, Psw: 2.8 nPa, AE: 385 nT, AL: −230 nT, AU: 160 nT, Sym-H: −20 nT, AO: −33 nT	Bz most southward, Vsw elevated; moderate HILDCAA. Other factors may modulate event formation.
May	24%	IMF: 6.8 nT, Bz: −0.2 nT, Vsw: 640 km/s, Nsw: 3.9 cm^{-3}, Tsw: 470,000 K, Psw: 2.95 nPa, AE: 420 nT, AL: −240 nT, AU: 180 nT, Sym-H: −17 nT, AO: −35 nT	Peak HILDCAA month. Sustained high-speed streams and high AE/AL/AU support ideal conditions.
June	22%	IMF: 7.0 nT, Bz: +0.2 nT, Vsw: 630 km/s, Nsw: 3.8 cm^{-3}, Tsw: 460,000 K, Psw: 2.9 nPa, AE: 390 nT, AL: −220 nT, AU: 170 nT, Sym-H: −10 nT, AO: −18 nT	Continued HSS influence with high AE. Despite weak northward Bz, Alfvénic fluctuations may support events.
July	16%	IMF: 6.4 nT, Bz: −0.4 nT, Vsw: 640 km/s, Nsw: 3.6 cm^{-3}, Tsw: 430,000 K, Psw: 2.7 nPa, AE: 370 nT, AL: −230 nT, AU: 160 nT, Sym-H: −17 nT, AO: −39 nT	HSS-driven activity persists; moderately active month with favorable solar wind parameters.
August	15%	IMF: 6.0 nT, Bz: −0.3 nT, Vsw: 620 km/s, Nsw: 3.5 cm^{-3}, Tsw: 410,000 K, Psw: 2.6 nPa, AE: 390 nT, AL: −220 nT, AU: 155 nT, Sym-H: −13 nT, AO: −36 nT	Sustained high-speed wind and moderate AE/AL conducive to prolonged auroral activity.
September	7%	IMF: 6.1 nT, Bz: −0.1 nT, Vsw: 580 km/s, Nsw: 3.3 cm^{-3}, Tsw: 390,000 K, Psw: 2.4 nPa, AE: 350 nT, AL: −200 nT, AU: 150 nT, Sym-H: −22 nT, AO: −65 nT	Decline in activity despite equinox. Moderate Vsw and IMF not sufficient to sustain events.
November	10%	IMF: 6.9 nT, Bz: −0.2 nT, Vsw: 590 km/s, Nsw: 3.5 cm^{-3}, Tsw: >1,000,000 K, Psw: 2.6 nPa, AE: 450 nT, AL: −300 nT, AU: 170 nT, Sym-H: −26 nT, AO: −75 nT	Despite high AE and AL, low HILDCAA suggests transient storms likely due to CMEs rather than HSS.
December	8%	IMF: 6.3 nT, Bz: +0.1 nT, Vsw: 715 km/s, Nsw: 3.2 cm^{-3}, Tsw: 520,000 K, Psw: 2.05 nPa, AE: 325 nT, AL: −200 nT, AU: 140 nT, Sym-H: −28 nT, AO: −80 nT	Highest Vsw month but low HILDCAA. Lack of AE and Psw support suggests non-sustained stream interaction.

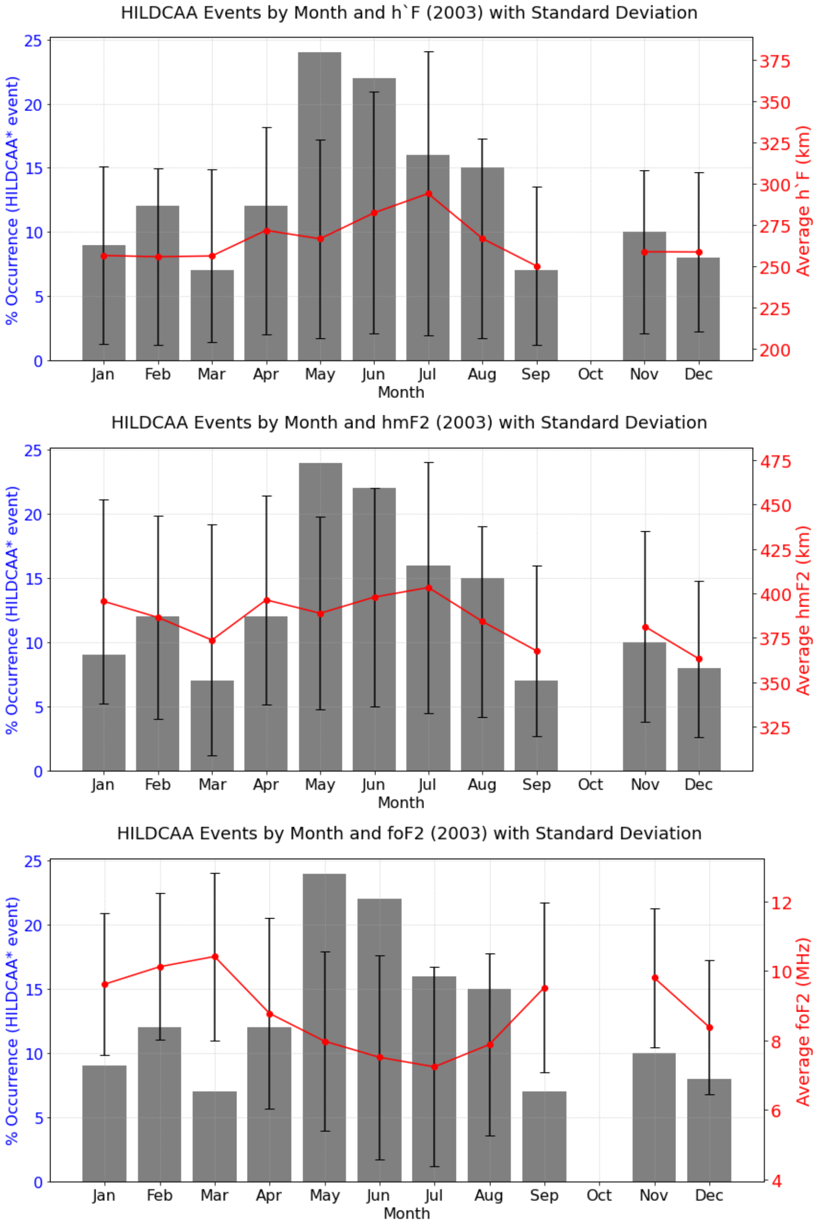
HILDCAA Events by Month and h`F (2003) with Standard Deviation

HILDCAA Events by Month and hmF2 (2003) with Standard Deviation

HILDCAA Events by Month and foF2 (2003) with Standard Deviation

Figure 48 – Histograms of h’F, hmF2 and foF2, are shown for both disturbed days (HILDCAA* events) conditions in 2003.

In contrast, the months of March and September each accounted for less than ≈ 7% of HILDCAA occurrences. This reduction likely corresponds to the absence of long-lived HSSs or the presence of solar wind flow discontinuities during these periods. Such conditions are consistent with solar wind sector structures dominated by low-speed streams, which are less favorable for the development of HILDCAA events. It is important to note that the variation in h′F does not always correlate directly with the frequency of HILDCAA occurrences.

For instance, April exhibited a moderate h′F (≈ 273 km) despite a relatively low event percentage (≈ 12%). Similarly, August, which had a higher event occurrence (≈ 15%), showed a lower average h′F (≈ 268 km) compared to July. This observation suggests that while h′F tends to peak during the Southern Hemisphere winter (particularly in June and July), its variability is modulated by additional factors beyond event frequency. A marked decrease in h′F is observed in September (≈ 250 km), even though some HILDCAA days were present. Such seasonal differences in h′F behavior may be attributed to variations in thermospheric density and ion-neutral coupling efficiency, which affect the vertical plasma dynamics in the F-region. During equinoxes and solstices, changes in background conductivity and thermospheric wind patterns can lead to differential impacts on F-region morphology.

Additionally, clear seasonal pattern was observed in the ionospheric response to HILDCAA* events in 2003, as reflected in the monthly mean values of the F2-layer peak height. The highest hmF2 (≈ 403 km) was recorded in July, indicating the most significant ionospheric uplift during this period. In contrast, December exhibited the lowest hmF2 (≈ 363 km), likely due to thermospheric contraction associated with the December solstice. The month of May registered the highest frequency of HILDCAA* events (34 events, ≈ 24% of the annual total), Notably, the solstice months particularly June and July were characterized by stronger ionospheric uplifts compared to the equinoctial and winter periods, suggesting a seasonal modulation of the ionospheric response. In January, ≈ 9% of the total HILDCAA* events occurred, with an average hmF2 of ≈ 395 km. This moderately elevated height reflects a relatively subdued thermospheric response, likely influenced by mild yet sustained energy input from HSSs. In February, the occurrence of HILDCAA* events increased to ≈ 12%; however, the average hmF2 decreased slightly to ≈ 388 km. This may imply that, despite increased geomagnetic activity, seasonal thermospheric cooling moderated the upward plasma transport. March recorded the lowest occurrence of HILDCAA* events (≈ 7%) and an average hmF2 of ≈ 376 km, indicating weak geomagnetic forcing and minimal ionospheric disturbance during the late equinox transition. In April, the frequency of events rose again (≈ 12%), accompanied by an increase in average hmF2 to ≈ 395 km. This suggests a reintensification of magnetospheric energy input, potentially aided by seasonal factors that favor thermospheric heating and vertical plasma motion. May, despite having the highest number of HILDCAA* events (≈ 24%), showed a mean hmF2 of ≈ 390 km. While still elevated, this value was not the highest for the year, possibly due to saturation effects in the ionosphere or enhanced recombination limiting further uplift. In June, which recorded a high event frequency (≈ 22%), the mean hmF2 increased to ≈ 397 km. This supports the hypothesis that prolonged energy input during HILDCAA* intervals in the June solstice period can significantly raise the F2-layer peak, with thermospheric expansion and neutral wind dynamics playing a contributory role.

Interestingly, July, with a slightly reduced event occurrence ($\approx 16\%$), displayed the highest average hmF2 (≈ 403 km) for the entire year. This peak suggests that the cumulative intensity of geomagnetic disturbances, rather than mere event count, may drive the strongest ionospheric responses. In August, the frequency of events declined ($\approx 15\%$) along with a corresponding decrease in hmF2 (≈ 383 km), indicating a reduced ionospheric response potentially linked to waning solar wind energy input or seasonal limitations in ionospheric-magnetospheric coupling. September also exhibited a low frequency of events ($\approx 7\%$) and a notably reduced hmF2 (≈ 368 km), indicative of limited geomagnetic forcing and a transition toward equinoctial ionospheric neutrality. October showed no HILDCAA* activity, marking a clear cessation in disturbances and underscoring the episodic nature of these intervals. In November, the frequency of events rebounded slightly ($\approx 10\%$), with the average hmF2 ($\approx$ 380 km) suggesting a moderate level of ionospheric uplift. December, however, recorded both a low event frequency ($\approx 8\%$) and the lowest mean hmF2 (≈ 363 km), emphasizing the reduced solar-terrestrial coupling efficiency during the December solstice. This is likely due to diminished thermospheric temperatures and reduced solar EUV radiation.

Overall, the most pronounced ionospheric uplifts occurred during the solstice months particularly June and July underscoring the combined influence of seasonal thermospheric dynamics and sustained geomagnetic activity in modulating the vertical structure of the ionosphere during HILDCAA events. Moreover, this monthly modulation is accompanied by marked variability, as evidenced by the standard deviations. Months with enhanced HILDCAA activity (April–August) exhibit the largest deviations, reaching ±7–9%, thereby indicating strong fluctuations in ionospheric responses during active intervals, whereas months with lower activity (March, September, and December) show reduced variability of ±3–4%, reflecting comparatively stable ionospheric conditions.

We observed a clear inverse relationship between prolonged geomagnetic activity and ionospheric electron density, as indicated by foF2 values. The period from May to July, marked by the highest HILDCAA* event occurrence (peaking in May at $\approx 24\%$ of total events), consistently exhibits the lowest monthly average values of the F2-layer foF2. This pattern highlights the suppressive impact of HILDCAA* events on ionospheric plasma density in the equatorial region. Correlation analysis further supports this conclusion, with a moderate negative Pearson correlation coefficient ($R = -0.44$) indicating that increased HILDCAA* events is statistically associated with a decrease in foF2. This anti-correlation is not only statistically significant but also physically meaningful, reflecting the dynamic interplay between solar wind magnetosphere coupling and ionospheric structure. The months with minimal HILDCAA* activity, such as March and September, show comparatively elevated foF2 values. These months, corresponding to the equinoxes, benefit from favorable solar illumination and enhanced EIA development, which promote greater electron density despite the low geomagnetic forcing. In contrast, solstice months especially June and December demonstrate lower foF2 values, coinciding with higher HILDCAA* occurrence and increased vulnerability to storm-time thermospheric alterations.

The ionospheric depletion observed during HILDCAA* intervals is likely driven by multiple mechanisms. HSS and CIRs, commonly associated with HILDCAA* events, inject sustained energy into the coupled magnetosphere–ionosphere–thermosphere system. This energy input alters the thermospheric composition, most notably reducing the O/N_2 ratio, and intensifies equatorward neutral winds. Both effects act to suppress ion production in the F2 region and facilitate downward and equatorward plasma transport, resulting in decreased foF2 values. Interestingly, foF2 continues to decline even after the peak in HILDCAA* activity during May, reaching its lowest in July. This delayed response suggests cumulative effects or extended recovery dynamics within the ionosphere, consistent with previous findings on prolonged geomagnetic disturbances. Such extended suppression can be attributed to residual thermospheric cooling, slow restoration of the O/N_2 ratio, and lingering disruptions in electrodynamic processes.

As indicated in Fig 49, the highest HILDCAA* event occurrences are observed during May ($\approx$ 17%), June ($\approx$ 15.4%), and July ($\approx$ 11.9%). These months correspond to the transition from late southern-hemisphere autumn into early winter, a period marked by enhanced magnetosphere–ionosphere coupling driven by persistent HSS and their associated CIRs. Such conditions are characteristic of the declining phase of the solar cycle, as observed in 2003. Furthermore, the standard deviations reveal that months with elevated TEC also show larger variability—for example, August (±3 TECu) and March (±2.5 TECu) whereas months with low TEC, such as September, display minimal variability. This indicates that high-TEC months tend to experience greater fluctuations, likely reflecting equinoctial effects and/or geomagnetic modulation. In parallel, the HILDCAA standard deviation peaks between May and August (up to ±5%), signifying pronounced month-to-month variability in occurrence rates during this interval.

Despite the elevated geomagnetic activity in May and June, TEC values during these months are notably low, indicating ionospheric depletion. This phenomenon is consistent with the negative phase of ionospheric storms, where enhanced thermospheric heating drives upwelling of molecular-rich air (e.g., increased N_2), reducing the O/N_2 ratio. This results in suppressed ion production and elevated recombination rates at F-region altitudes, thereby lowering the electron content. This pattern illustrates the classic signature of negative ionospheric storm effects during extended geomagnetic activity.

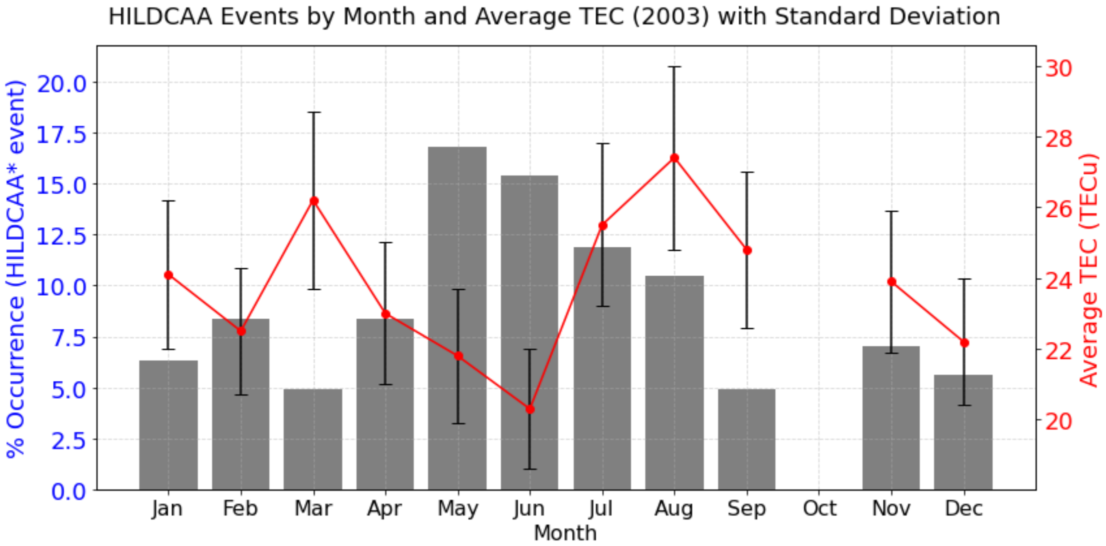

Figure 49 – Histograms of TEC are shown for both disturbed days (HILDCAA* events).

Conversely, months like August, March, and July exhibit relatively high TEC values. The peak in August, despite fewer HILDCAA* days, suggests residual thermospheric energy input, possibly coupled with favorable background conditions such as enhanced solar EUV radiation and equatorial plasma fountain activity promoting electron density recovery or buildup. March and September, aligned with the equinoxes, also demonstrate elevated TEC values with low HILDCAA* activity, underscoring the role of equinoctial solar conditions, the EIA, and mechanisms such as the Russell–McPherron effect that enhance solar wind–magnetosphere coupling during equinoxes, particularly in March. These observations highlight a temporal and physical decoupling between storm-time geomagnetic forcing and TEC variability. While HILDCAA* events peak during May to July, the ionospheric response, in terms of TEC, does not always align directly with these disturbances. This decoupling arises due to competing factors: solar EUV variability, local time effects, thermospheric composition changes, and electrodynamic responses such as the upward drift.

Statistically, the analysis indicates an inverse correlation between monthly HILDCAA* occurrence and average TEC values. This supports the hypothesis that prolonged geomagnetic activity, even at moderate levels such as those during HILDCAA* intervals, can significantly modulate equatorial ionospheric plasma content. The observed inverse relationship between foF2/TEC and HILDCAA occurrences highlights the critical need to account for these prolonged geomagnetic disturbances in ionospheric prediction models and space weather monitoring systems. The equatorial ionosphere's sensitivity to such long-duration, substorm like events reaffirms the importance of including HILDCAA* impacts in regional TEC forecasting models and ionospheric correction algorithms for satellite-based communication and navigation systems. The ionospheric monthly responses to geomagnetic disturbances due to HILDCAAs are described in the Table 8.

Table 8 – Summary observations of HILDCAA* Events vs Ionospheric Parameters (2003)

Month	**% HILDCAA* events [TEC / h'F, hmF2 &foF2]**	**Avg TEC (TECU)**	**Avg hmF2 (km)**	**Avg h'F (km)**	**Avg foF2 (MHz)**	**Key Observation/ Remarks**
January	6.25 / 9	24.0	395	259	9.6	Low HILDCAA* occurrence, high TEC and foF2
February	8.33 / 12	22.5	388	258	10.0	HILDCAA* rising, TEC and foF2 high
March	4.86 / 7	26.3	376	259	10.3	peak TEC and foF2, lowest HILDCAA* occurrence
April	8.33 / 12	23.0	388	270	8.6	Rising HILDCAA* occurrence, foF2 decreases
May	16.67 / 24	21.5	392	267	7.9	Peak HILDCAA* occurrence, drop in TEC and foF2.
June	15.28 / 22	20.4	398	283	7.5	High HILDCAA* occurrence, low TEC/foF2, h'F increases.
July	11.11 / 16	25.7	403	293	7.2	High HILDCAA* occurrence declined, peak hmF2/h'F, lowest foF2
August	10.42 / 15	27.3	384	267	7.9	Stable HILDCAA* occurrence, foF2 and TEC improve
September	4.86 / 7	24.5	373	251	9.6	Low HILDCAA* occurrence, TEC and foF2 recover
November	6.94 / 10	23.8	381	259	9.8	Balanced HILDCAA* occurrence and ionospheric values
December	5.56 / 8	22.5	364	259	8.7	Declining trends in all the parameters

5.6 Statistical Analysis on Relative Differential TEC (ΔTEC)

The latitudinal analysis of TEC must incorporate the site-specific geophysical context—most notably the large magnetic declination and steep ionospheric gradients—which together modulate plasma behavior during episodes of heightened disturbance. TEC variations are quantified here as departures of the VTEC from a climatological reference level (MUKHTAROV; ANDONOV; PANCHEVA, 2018). A straightforward comparison of mean VTEC on geomagnetically quiet versus disturbed (HILDCAA) days fails to expose statistically significant differences (MANNUCCI et al., 2014; BAGIYA et al., 2009; MENDILLO, 2006). To enhance sensitivity, we therefore adopt the relative differential metric $\Delta\mathrm{TEC}$, which isolates perturbations attributable to HILDCAA activity. Positive and negative excursions of $\Delta\mathrm{TEC}$ capture the recurring enhancements and depletions that characterize these events. Figures A.16–A.21 depict the month-to-month evolution of vertical $\Delta\mathrm{TEC}$ along the magnetic equator and the southern crest of the EIA; complementary details are given in Appendix A.

During the first disturbed January interval (19–23 January 2003), an eastward PPEFs set in just after local sunset and forced an upward $\mathbf{E}\times\mathbf{B}$ drift. This uplift produced an immediate increase in total electron content: at 02:00 UT on 19 January $\Delta\mathrm{TEC}$ reached ≈ 18 TECU above Fortaleza (near the magnetic dip equator) and ≈ 20 TECU at the southern-crest stations BOMJ and BRAZ. Between 14:00 UT and 00:00 UT the surplus plasma was redistributed pole-ward by the equatorial fountain, so the enhancement persisted almost exclusively over the southern crest while equatorial values relaxed toward their quiet-time level. Beginning around 00:00 UT on 20–21 January, the electrodynamics reversed: a westward DDEF, generated by storm-time thermospheric winds and auroral Joule heating, drove downward drift and composition changes (a reduced $\mathrm{O/N\_2}$ ratio), yielding a depletion of ≈ -15 TECU at the crest and ≈ -9 TECU at the equator. The morning of 22 January remained quiescent, but a renewed dusk-sector PPEF elevated the southern crest to ≈ 25 TECU at 18:40 UT (GPS data were unavailable at FZ). The polarity flip at 00:00 UT depletion at BOMJ versus enhancement at VICOsa (VICO) confirms the competing influence of the DDEFs. On 23 January the system was again dominated by depletion, with the exception of VICO, which attained a local maximum of ≈ 30 TECU at 18:00 UT; elsewhere the crest remained near -12 TECU and the equatorial region near -9 TECU.

The second January HILDCAA episode (23–27 January) followed a similar sequence. TEC remained close to background on 24 January except for a brief pre-dawn surge of ≈ 15 TECU at BRAZ. Minimum values occurred at 12:00 UT on 25 January (≈ 8 TECU at FZ and ≈ 16 TECU at the crest), but a strong dusk PPEFs later the same day propelled the crest to ≈ 30 TECU at 21:00 UT. From $\approx 02{:}00$ UT to $\approx 17{:}00$ UT on 27 January the westward dynamo once more prevailed, driving a sustained depletion that marked the end of the disturbed interval. The alternation between crest focused enhancements during eastward PPEFs phases and widespread depletions during westward DDEFs phases is fully consistent with accepted low-latitude electrodynamics, and the reported magnitudes (up to ≈ 30 TECU) agree with previously documented responses to high-speed-stream–driven storms of comparable intensity.

During the second pair of HILDCAA episodes (06–11 February and 16–21 February 2003) the low-latitude ionosphere again alternated between storm-time uplift and dynamo-driven depletion in a manner fully consistent with established electrodynamics. On 06 February an eastward PPEF acting near local noon raised the F-region over Fortaleza to a peak of $\Delta\mathrm{TEC} \approx 9$ TECU at 11:00 UT, while the southern crest stations BOMJ, BRAZ and VICO registered ≈ 13 TECU. A second PPEFs related enhancement occurred near 18:00 UT, reaching ≈ 15 TECU at the equator and ≈ 18 TECU at the crest. After dusk, however, the westward DDEF became dominant; by 23:30 UT it had driven the crest into depletion while leaving the equatorial region slightly enhanced, a polarity pattern characteristic of a DDEFs reversal.

Beginning at 03:00 UT on 07 February the eastward field re-emerged, lifting $\Delta\mathrm{TEC}$ to ≈ 12 TECU at FZ and ≈ 16 TECU at the crest (RIOD and POAL were out of service). Daylight hours were largely uneventful except for modest surges at VICO and UEPP, underscoring the variable impact of geomagnetic forcing across longitude. A similar pre-dawn enhancement recurred on 08 February, but by 11:20 UT the DDEF again prevailed, producing depletions of ≈ -8 TECU at the equator and ≈ -10 TECU at the crest. This “negative phase” persisted until the next local sunset, when the evening PPEF restored positive values that peaked near 18:00 UT.

The pattern repeated on 09–10 February: a daytime uplift drove VICO to ≈ 20 TECU, followed by a sharp post-midnight depletion of ≈ -13 TECU across the crest at 02:00 UT on 10 February. Thereafter the system entered a recovery phase with $\Delta\mathrm{TEC}$ fluctuating close to zero.

The third February HILDCAA interval (16–21 February) opened with a strong pre-dawn uplift on 16 February: $\Delta\mathrm{TEC} \approx 24$ TECU at FZ and ≈ 15–12 TECU at BRAZ and UEPP, respectively. By sunrise the enhancement had dissipated, indicating that the penetration component was short-lived. Successive nights behaved similarly, with brief post-midnight depletions (e.g. ≈ -5 TECU at 03:00 UT on 17 February, except at BOMJ where the crest still showed +20 TECU) and renewed daytime growth. On 18 February the southern crest again exceeded the equator by ≈ 20 TECU during local afternoon and replicated this behaviour on the following days; from 19 to 21 February the largest deviations occurred between 12:00 UT and 19:00 UT, with smaller but still measurable changes around 23:00 UT and 00:00–02:00 UT. These observations confirm that daytime eastward PPEFs are the primary driver of TEC enhancements during HILDCAA conditions, while the westward DDEF and composition changes associated with auroral Joule heating are responsible for the intermittent depletions. The magnitude and timing of the reported $\Delta\mathrm{TEC}$ values agree with earlier case studies of high-speed-stream–driven storms at comparable geomagnetic latitudes, lending confidence to the physical interpretation presented here (see Fig. A.16).

FigureA.17 documents two further HILDCAA-driven disturbances—04–07 March and 14–16 March 2003 whose behaviour again alternates between uplift produced by eastward PPEFs and depletion driven by the westward DDEF.

On 04March a pre-dawn PPEF lifted the F-region to $\Delta\mathrm{TEC} \approx +8$ TECU at FZ and $\approx +12$ TECU at the southern-crest stations (05:00 UT); the subsequent dominance of the DDEF reversed the drift, and by 15:00–18:30 UT depletions of roughly -10 to -14 TECU were recorded at VICO, RIOD and POAL. After local sunset the eastward field re-appeared, restoring moderate enhancements at VICO and RIOD.

The early-morning PPEF on 05 March was stronger: at ∼06:00 UT $\Delta\mathrm{TEC}$ reached $\approx +30$ TECU at BRAZ and $\approx +15$ TECU at FZ, whereas the nighttime equatorial response remained weak and grew pole-ward in accord with the fountain effect. On 06 March the evening DDEF produced a broad depletion at 19:30 UT, but the field polarity flipped by 23:00 UT, returning all crest stations to positive values (GPS reception at FZ and UEPP was unavailable for this interval). A similar cycle occurred on 07 March, with a pronounced dawn-sector depletion of ~ -15 TECU at the equator and a mirror enhancement near 23:00 UT.

The next HILDCAA episode began quietly: from 00:00 UT to 17:00 UT on 14 March $\Delta\mathrm{TEC}$ hovered near zero. A dusk PPEF then lifted the southern crest above the equator, presaging the large pre-dawn enhancement of 15 March: at 05:00 UT $\Delta\mathrm{TEC}$ attained $\approx +24$ TECU at FZ, $\approx +30$ TECU at BOMJ and $\approx +26$ TECU at BRAZ. Values relaxed toward quiet-time levels during daylight, but a final uplift at about 19:00 UT on 16 March again intensified the crest.

The sequence of pre-dawn or dusk-sector enhancements, followed by post-sunset or post-midnight depletions, is exactly what is expected when alternating eastward PPEFs and westward DDEFs modulate the low-latitude ionosphere (FEJER; LARSEN; FARLEY, 1983; ABDU et al., 2009). Neutral-wind coupling plays only a secondary role here, because the small magnetic-dip angle near the equator limits wind-driven dynamo efficiency (BUONSANTO; FOSTER, 1993). The recorded magnitudes—ranging from about -15 TECU during depletion phases to $+30$ TECU at the height of uplift—are within the climatological limits for high-speed-stream events at these latitudes, confirming the physical consistency of the present interpretation.

Figure A.17 shows that the April 2003 HILDCAA activity forced the ionosphere through a clear sequence of post-midnight depletions and dusk-sector uplifts. On 15 April the westward DDEF dominated: $\Delta\mathrm{TEC} \approx -8$ TECU at FZ and down to ≈ -25 TECU at the southern EIA crest attest to strong storm-time depletion. A comparable pattern recurred on 16 April, yet by local dusk (19:00 UT) an eastward PPEF had reversed the drift, producing a crest enhancement of almost +20 TECU (BOMJ and POAL were off-line). The evening PPEFs on 17 April was still more effective, lifting the equator to $\approx +22$ TECU and the crest to $\approx +10$ TECU; the larger equatorial amplitude is consistent with equatorward neutral-wind convergence and upward $\mathbf{E} \times \mathbf{B}$ drift (LIU et al., 2008).

A second HILDCAA April episode began on 20 April, in the equinox season when daytime ion production and upward drifts can act simultaneously. Around 18:00 UT all low-latitude stations registered a broad enhancement of $\approx +20$ TECU that persisted into the post-midnight hours (to $\sim$02:00 UT on 21 April) at the crest while the equator relaxed toward zero. Daylight on 21 April was quiet, but the dusk PPEFs returned modest positive values at both latitudes. The following two days were markedly more disturbed: with no GPS data at FZ, the crest nevertheless climbed to $\approx +30$ TECU (22–23 April, 18:00–19:00 UT) while the equatorial region—where data were available—reached about +16 TECU. Such magnitudes exceed those of earlier April events and point to stronger high-latitude forcing. By 24 April the system had subsided to a marginal enhancement.

The interval 25–28 April opened with a pronounced depletion: at 00:00 UT $\Delta\mathrm{TEC}$ fell to ≈ -13 TECU at FZ, and by 19:00 UT UEPP recorded ≈ -30 TECU. As often occurs under DDEF control, the polarity inverted after midnight, leaving the crest mildly enhanced and the equator still depleted. TEC remained near its quiet value for most of 26 April, rising only slightly after local sunset, and repeated the familiar pattern on 27 April. On 28 April the midday crest again surged above the equator by $\approx +20$ TECU, but a rapid fall to ≈ -10 TECU (crest) at 19:30 UT closed the sequence, confirming the cyclical hand-off between eastward PPEF uplifts and westward DDEF-driven depletions that characterises HILDCAA conditions at low latitudes.

During the May HILDCAA episode examined (01–04 May 2003) the storm-time electrodynamic cycle again imposed opposite signatures at the magnetic equator and at the southern EIA crest. On 01 May a strong pre-dawn eastward PPEF lifted the F-region above FZ to a level well in excess of the low-latitude sites, while RIOD and neighbouring stations registered only modest post-midnight enhancements of $\Delta\mathrm{TEC} \approx 12$–$15$ TECU around 06:00 UT. Near local noon the polarity reversed: FZ entered a depletion of ≈ -9 TECU, whereas the crest stations began to climb, peaking at $\approx +30$ TECU around 19:00 UT. This dusk-sector uplift, produced by the combined action of the eastward PPEF and the equatorial fountain, conforms to the daytime "positive storm" effect frequently reported at geomagnetically low latitudes, while the simultaneous equatorial depletion reflects the reduced plasma density in the anomaly trough (WANG et al., 2010).

A comparable sequence followed on 02 May. The early-morning enhancement amounted to $\approx +9$ TECU at the equator and rose dramatically to $\approx +40$ TECU at the southern crest by 18:00 UT, confirming that the evening PPEF remained efficient. In contrast, 03 May was uneventful: TEC stayed near its quiet-time level at both latitudes, with a weak noon-time dip at the equator and no usable GPS data for FZ. Activity resumed on 04 May when a late-afternoon eastward field once more intensified the crest, yielding a peak of $\approx +25$ TECU between 17:00 UT and 18:00 UT. Throughout this interval the magnitude, local-time dependence and latitude contrast of the observed $\Delta\mathrm{TEC}$ are entirely consistent with the alternating dominance of eastward PPEFs which drive upward $\mathbf{E} \times \mathbf{B}$ drift and fountain type plasma redistribution—and westward disturbance-dynamo electric fields, which promote post-midnight depletions at both the equator and the crest.

From 05 May to 29 May 2003 the ionosphere continued to oscillate between post-midnight quiescence, midday depletions, and pronounced dusk-sector uplifts, as summarised in Fig. A.19. On 05 May no appreciable perturbation was detected before dawn, but by local noon the FZ receiver recorded a depletion of $\Delta\mathrm{TEC} \approx -10$ TECU. A few hours later (15:00–19:00 UT) an eastward PPEF raised the equatorial layer to $\approx +16$ TECU while the southern EIA crest reached $\approx +9$ TECU, illustrating the classic "positive storm" response at low latitudes. The following day (06 May) remained quiet at the equator, though a weak crest enhancement persisted; on 07 May the pattern inverted, yielding a noon-time trough of ≈ -10 TECU at FZ and a simultaneous crest surge approaching $+30$ TECU, again consistent with afternoon PPEF forcing.

A similar alternation appeared on 08 May, with midday depletion at the equator and a late-afternoon dip at the crest. The most severe depletion of the month occurred on 10–11 May, when high solar-wind dynamic pressure within the CIR compressed the magnetosphere and accelerated neutral-composition changes (BAKARE; CHUKWUMA, 2010), FZ fell to ≈ -13 TECU while the crest still reached about $+15$ TECU, before a brief post-midnight recovery at the equator on 11 May. Between 12 May and 14 May the two latitudinal bands again oscillated in antiphase, with daytime departures of roughly -10 to -12 TECU.

The dusk PPEF on 15 May drove the southern crest to $\approx +20$ TECU at 18:00 UT but left the equator depleted by about -12 TECU; 16 May showed the same polarity, though with smaller amplitudes. A quiet spell ensued until 22 May, when both latitudes exhibited mild depletions (≈ -8 TECU at FZ, ≈ -10 TECU at the crest), save for a localised $+8$ TECU surge at POAL. The crest rebounded to $\approx +16$ TECU on 24 May, whereas FZ data were unavailable. After another noon-time dip at FZ on 26 May (≈ -12 TECU) the month closed with two strong dusk enhancements: on 27 May the equator climbed to $\approx +15$ TECU and the crest to $\approx +25$ TECU, and nearly identical values were repeated on 29 May.

During the austral winter solstice the background F-region density is already reduced, so the June 2003 HILDCAA episodes (02–12 June, 13–16 June, and 24 June–06 July) exhibit smaller-amplitude TEC variations than those seen in equinox months; nonetheless the alternation between uplift by eastward PPEFs and depletion by the westward DDEF remains clear in Figs. A.19 and A.18.

From 02 to 04 June only the southern EIA crest was monitored. An incipient PPEF produced a weak enhancement of $\Delta\mathrm{TEC} \approx +8$ TECU, but the next evening (03 June, 19:00 UT) the DDEF drove a depletion of ≈ -12 TECU. On 04–05 June the same polarity pattern was recorded at both latitudes when data were available: near 18:00 UT the equatorial site reached ≈ -9 TECU while the crest fell to about ≈ -12 TECU. Enhancements were again limited to the crest on 06 June and were negligible on 07 June; a modest depletion of ≈ -10 TECU recurred at 18:00 UT on 08 June.

A stronger eastward field penetrated just after midnight on 09 June, lifting the crest to $\approx +20$ TECU at 00:00 UT, but subsequent gaps in equatorial GPS data preclude a conjugate comparison for 09–10 June. The remainder of the first interval (11–12 June) was characterised by small daytime deviations: on 11 June the equator dipped to ≈ -5 TECU while the crest reached ≈ -11 TECU; on 12 June a brief dusk enhancement raised the crest to $\approx +8$ TECU while the equator remained depleted at ≈ -23 TECU around 18:45 UT.

The second June HILDCAA episode (13–16 June) opened with an unusual noon-time enhancement on 13 June ($\approx +8$ TECU at the equator, $\approx +12$ TECU at the crest) that flipped to depletion by 18:00 UT (about -7 TECU and -15 TECU, respectively). A classic PPEF signature returned on 14 June, producing positive values at both latitudes; the DDEF then dominated 15 June before an evening uplift on 16 June carried the crest to $\approx +20$ TECU (19:00 UT) while the equator reached only $\approx +10$ TECU—consistent with the reduced fountain efficiency during the solstice season.

Throughout 24–30 June the equatorial receiver registered small noon-time troughs (minimum $\Delta\mathrm{TEC} \approx -9$ TECU) while the crest alternated between a depletion of ≈ -14 TECU at 15:00 UT and an enhancement of $\approx +13$ TECU at 19:00 UT. Finally, during 01–06 July the equatorial ionosphere displayed a repeatable "day–night" pattern: a midday depletion of ≈ -15 TECU followed by an evening uplift of roughly the same magnitude, mirrored—where data exist—by comparable oscillations at the crest.

Figure A.18 shows that the mid-winter HILDCAA sequences of 12–15 July, 18–21 July, and 29 July–04 August 2003 follow the same electrodynamic template seen earlier in the year, although the amplitudes are muted by the low solar EUV flux typical of July.

During 12–15 July a pre-dawn eastward PPEF lifted the southern EIA crest to $\Delta\mathrm{TEC} \approx +16$ TECU at 02:00 UT on 12 July, while the equatorial receiver registered little change. The enhancement persisted through local noon and decayed only after 14:00 UT on 13 July, when both latitudes still showed moderate uplifts of $\approx +11$ TECU (equator) and $\approx +13$ TECU (crest). On 14 July the DDEF became dominant after sunset, driving nearly symmetric depletions of ≈ -11 TECU (equator) and ≈ -12 TECU (crest) between 18:00 UT and 20:00 UT. The pattern repeated on 15 July but with reduced amplitudes: the evening PPEFs produced enhancements of only $\approx +8$ TECU and $\approx +10$ TECU at the two latitude belts.

The second July HILDCAA, 18–21 July, began with a mild dusk enhancement on 18 July (about $+9$ TECU at the equator and $+11$ TECU at the crest). A post-midnight DDEF quickly followed: at 02:00 UT on 19 July $\Delta\mathrm{TEC}$ fell to ≈ -5 TECU (equator) and ≈ -8 TECU (crest). The dusk PPEF on 20 July was stronger, pushing the crest to $\approx +18$ TECU while the equator reached $\approx +11$ TECU; by the next evening (21 July) the system had relaxed to near-zero values, indicating only a weak geomagnetic influence (see also Appendix A).

According to Fig. A.20, 29 July–04 August period was characterised by persistent depletions. Between 29 and 31 July the equator remained negative, reaching a minimum of ≈ -8 TECU on 30 July. The crest was likewise depleted at local noon (≈ -9 TECU) but briefly reversed sign around 14:00 UT, attaining $\approx +12$ TECU before returning to quiet levels on 31 July. From 01–04 August, the westward DDEF dominated almost continuously: post-midnight depletions of ≈ -8, -15, -6, and -8 TECU were logged at the equator on

1–4 August, respectively, while concurrent dusk-sector troughs of roughly -13 to -12 TECU were observed at the crest. The absence of any appreciable evening PPEF during these days suggests that magnetospheric forcing was confined to high latitudes and never penetrated effectively to the dusk terminator.

During the winter HILDCAA of 7-14 August 2003, the ionosphere remained under the persistent influence of the westward DDEF. Each day the midday F-region was driven downward, yielding depletions of $\Delta\mathrm{TEC} \approx -10$ TECU at Fortaleza (magnetic equator) and ≈ -15 TECU at the southern EIA crest around 14:00 UT. Only when an eastward PPEF briefly reached low latitudes near dusk (≈19:00 UT) did the crest recover, peaking at $\approx +18$ TECU on 07 August. The same polarity pattern persisted on 08–09 August: an afternoon trough of ≈ -12 TECU (equator) and ≈ -20 TECU (crest) on 08 August, followed by a slightly weaker depletion on 09 August (≈ -6 and -14 TECU, respectively). Activity subsided on 10 August—apart from a small negative excursion at POAL—and remained subdued through 12 August, when the noon-time DDEF again produced depletions of roughly ≈ -8 TECU (equator) and ≈ -12 TECU (crest). On 13 August the equatorial ionosphere was near its quiet level, yet the crest still showed a -15 TECU trough at 18:00 UT, confirming that the westward field retained some strength. Conditions on 14 August mirrored those of the preceding day.

A shorter HILDCAA event on 23–25 August repeated the sequence. From local noon until 19:00 UT the DDEF lowered the F-region, driving the equator to a minimum of ≈ -9 TECU and the crest to about ≈ -13 TECU on 25 August—the deepest depletion of the interval. A weak dusk PPEF then lifted the equator by ≈+8 TECU while the crest remained marginally negative, illustrating the familiar dusk-sector polarity reversal produced when a transient eastward field penetrates an otherwise westward-dominated ionosphere.

During the equinox-season HILDCAA intervals of 10–12 September 2003 and 19–22 September 2003 (Fig. A.21), the daytime ionosphere was dominated by the westward DDEF, whereas brief eastward PPEFs appeared after dusk. On 10 September a noon-to-dusk depletion reached $\Delta\mathrm{TEC} \approx -13$ TECU at Fortaleza (FZ, magnetic equator) and ≈ -17 TECU at the southern EIA crest except at Brasília (BRAZ), where a local uplift was recorded. By 23:30 UT an evening PPEF had lifted the crest markedly, while the equator remained near its quiet value. A similar noon-time trough re-emerged on 11 September (≈ -14 TECU at the crest); on 12 September the depletion persisted, but RIOD, POAL and UEPP showed isolated noon uplifts of ≈ +10 TECU, consistent with longitude-dependent PPEF penetration.

The next episode, 19–22 September, began with a strong dusk enhancement on 19

September: the equator rose to ≈ +14 TECU and the crest to ≈ +18 TECU at 18:00 UT. The following day the DDEF regained control, producing a noon depletion (≈ -12 TECU at FZ) and a deeper night-time trough of ≈ -22 TECU at UEPP, before a sunset uplift of ≈ +18 TECU. Both 21 and 22 September were comparatively quiet, exhibiting only small positive deviations.

The 1–4 November and 14–19 November 2003 intervals again illustrates the alternation of drivers. In the early-November case, a mild post-midnight PPEF on 1 November raised the equator by ≈ +15 TECU and the crest by ≈ +18 TECU at 02:00 UT. Daytime solar production combined with an eastward field then amplified the crest to ≈ +30 TECU, while the equator levelled near +15 TECU. Subsequent days in each sequence showed the now-familiar cycle: westward DDEFs induced depletions at local noon, followed by eastward PPEF uplifts in the dusk or post-midnight sectors, with magnitudes nowhere exceeding ±30 TECU—well within the expected range for Brazilian low latitudes during HILDCAA conditions.

During the continuation of the November HILDCAA interval, 2 November 2003 showed a pronounced depletion: $\Delta\mathrm{TEC}$ decreased steadily from 01:00 UT to approximately 14:00 UT at both latitudes, indicative of a dominant westward DDEF. By dusk (18:00 UT) the eastward PPEF briefly re-established itself, yielding a positive crest enhancement. On 3 November the ionosphere remained quiescent and $\Delta\mathrm{TEC}$ values hovered near zero. The following day (4 November) a modest daytime uplift of $\approx +14$ TECU at the equator and $\approx +17$ TECU at the southern crest was observed, but significant gaps in GPS coverage (particularly at POAL) complicate interpretation.

The mid-November interval opened on 14 November with a broad negative phase at both latitudes, again consistent with DDEFs forcing. On 15 November the equatorial and crest regions diverged: while the equator remained flat, the crest reached a brief +15 TECU enhancement near 19:00 UT following a pre-dawn depletion of ≈ -13 TECU at 01:00 UT. Between 16 and 19 November the equator displayed little daytime sensitivity to geomagnetic activity (values near zero) but registered a nocturnal depletion of ≈ -15 TECU around 23:00 UT. Crest stations showed a similar negative phase at local noon, punctuated on 17 November by a peak of $\approx +12$ TECU at 19:00 UT—the same polarity sequence noted on 15 November. The closing days (18–19 November) repeated this pattern, with positive PPEF-driven enhancements in the post-midnight (≈ 02:00 UT) and dusk (≈ 18:00 UT) sectors and negative depletions overnight. This latitudinally consistent behaviour illustrates how enhanced electric fields can lift plasma to higher altitudes, intensifying the EIA toward the crest, as shown in Fig. A.21.

The final HILDCAA interval of the year, 12–17 December 2003, was dominated by negative-storm signatures. Beginning on 10 December, noon-time depletions of ≈ -13 TECU at the equator and ≈ -15 TECU at the crest persisted until 18:00 UT, after which an evening PPEF briefly raised the crest by $\approx +13$ TECU at 19:30 UT and into the post-midnight hours (01:00 UT). By 11 December the latitudinal response had inverted, with the equator mildly enhanced and the crest depleted by up to -12 TECU. From 12 December onward the negative phase again prevailed at both latitudes ($\approx$ -15 TECU), underscoring the strength of the westward electric field. The diurnal pattern remained largely unchanged through 13–17 December, although the UEPP receiver documented an isolated daytime uplift of $\approx$ +20 TECU, highlighting the local-time and longitudinal variability of eastward PPEFs penetration (Fig. A.21).

TEC enhancements and suppressions are associated with the effects of positive and negative storms or associated disturbance such as HILDCAA phenomena as observed at equatorial and low latitudes during the daytime and near the geomagnetic equator. As mentioned affore in the equatorial region's, TEC is influenced by the EIA, which results in TEC accumulation at specific latitudes due to the formation of crests. The effects of storms at equatorial latitudes stem from modifications to the EIA caused by electric fields, winds, changes in neutral composition, and wind-induced transport (BLANC; RICHMOND, 1980; PRÖLSS, 1997; BUONSANTO, 1999). TEC dynamics are influenced by atmospheric heating, which increases the recombination rate, and downward vertical winds enriched with atomic oxygen, which elevate electron density. The variations in ΔTEC can be attributed to the increase in the dawn-to-dusk electric field across the magnetosphere during geomagnetic disturbances. This is because the solar wind electric field becomes superimposed on the magnetosphere during geomagnetic storm periods when the interplanetary magnetic field turns southward, as stated by Kelley (2009). The findings suggest that enhanced convection from geomagnetic storms, combined with photoionization of plasma at altitudes below the F-region peak, may be a key mechanism for enhancing TEC in this region during storms. An eastward electric field perturbation on the dayside raises the F-region to higher altitudes due to the ExB force in sunlit conditions. Plasma below the elevated F-region is quickly replenished by photoionization, while the simultaneous reduction in recombination rates at higher altitudes leaves the raised F-peak and topside plasma relatively undisturbed. These combined effects lead to a rapid and significant enhancement of VTEC, indicating a positive ionospheric response.

In equinotial months, the amplitude of positive ΔTEC in the southern crest of EIA is higher compared to the equatorial region. Variations in VTEC during the recovery phase of the storms were found to be linked to the PPEFs arising from under-shielding and over-shielding conditions for nearly all geomagnetic storms discussed in earlier sections. In most cases, VTEC shows significant ΔTEC during post-midnight, noon, and nighttime, while negative deviations are primarily observed around sunset. This phenomenon is largely due to thermospheric composition changes resulting from Joule heating effects at auroral latitudes, which generate electric field disturbances at low latitudes.

Generally, during HILDCAA events, the equatorial region demonstrated moderate TEC deviations, largely governed by intensified electric fields and the resulting fountain effect. This mechanism generated TEC peaks near $\pm 15^\circ$ magnetic latitude, corresponding to the EIA, with positive and negative deviations of $\approx$ +25 and -15 TECU, respectively. Notably, the Brazilian low-latitude region exhibited more pronounced TEC deviations (around ±35 TECU) relative to quiet-time baselines and exceeded the deviations observed in the equatorial region during these events. This behavior contrasts with the findings of (GUARNIERI et al., 2006; TSURUTANI et al., 2004; ABDU et al., 2009), which reported distinct TEC responses to geomagnetic storms during the same period. The largest TEC deviations were observed during nighttime, driven by enhanced penetration electric fields. In contrast, daytime TEC deviations were predominantly influenced by disturbed thermospheric conditions. The largest TEC deviations were observed during nighttime, driven by enhanced penetration electric fields. In contrast, daytime TEC deviations were predominantly associated to disturbed thermospheric conditions and strongly influenced by the combined effects of DDEFs and PPEFs.

5.6.1 A comprehensive analysis of TEC across the equatorial region and the southern crest of EIA

This overview study presents a comprehensive statistical analysis of HILDCAA* events in 2003, focusing on ionospheric TEC variations observed at two key regions: the FZ (equatorial station) and the southern crest of EIA. The relationships between parameters such as average TEC, positive and negative TEC variations, and storm-induced drifts were analyzed across different months, as illustrated in Figure A.22 and referenced in A. The analysis began with intra-station assessments before expanding to inter-station comparisons, highlighting the differences between the equatorial and low-latitude regions.

At the equatorial region as indicated in Figure A.22, TEC patterns reveal monthly and geomagnetic influences. The highest average TEC values occurred in March (66 TECU) and January (61 TECU), signifying heightened geomagnetic activity and increased ionospheric density during these months. Conversely, the lowest average TEC was recorded in June (30

TECU), indicating reduced ionospheric activity. These trends align with solar-ionization patterns, where equinox (March) and summer (January) bring enhanced solar energy, while geomagnetic energy loss mechanisms dominate during winter months like June. Positive TEC changes (ΔTEC increases) peaked in April (19 TECU) and March (16 TECU), highlighting periods of significant ionospheric electron density enhancements. These changes are attributed to solar wind-magnetosphere coupling during HILDCAA events, which facilitate plasma uplift and production through electric fields generated by geomagnetic storms. In contrast, the largest negative TEC changes (ΔTEC decreases) occurred in March (-15 TECU) and November (-15 TECU), with smaller reductions in June (-8 TECU) and July (-9 TECU). These reductions are linked to electron recombination, downward plasma motion, and energy dissipation processes during geomagnetic disturbances. Storm drift values followed a similar monthly trend, with peaks in November (27 m/s) and June (23 m/s), reflecting intense ionospheric plasma motion during these periods. The lowest drift (13 m/s) was also observed in June, corresponding to the month's reduced TEC average. This correlation suggests that diminished storm-driven ionospheric effects contribute to lower ionospheric activity in June.

As shown in Figure A.22, the ionospheric TEC at the southern crest of EIA is strongly affected by monthly changes and geomagnetic activity. The highest average TEC values were recorded in April (95 TECU) and January (91 TECU), indicating robust ionospheric activity during these months. By contrast, the lowest TEC values occurred in August (45 TECU) and July (53 TECU), reflecting reduced ionospheric density, likely due to seasonal changes and decreased solar ionization. These observations underscore the role of seasonal variability and geomagnetic activity in shaping ionospheric dynamics. Positive TEC changes (ΔTEC increases) peaked in March (26 TECU) and April (25 TECU), signaling pronounced electron density enhancements during these HILDCAA events. In contrast, lower positive TEC changes were recorded in July (13 TECU) and June (15 TECU), consistent with a period of reduced ionospheric activity. These enhancements are driven by energy input from geomagnetic storms, which stimulate plasma uplift and ion production.

The largest negative TEC changes (ΔTEC decreases) were observed in April (-28 TECU), indicating significant ionospheric electron depletion during geomagnetic disturbances. Moderate reductions occurred in September (-18 TECU) and August (-15 TECU), illustrating variability in electron loss processes across different months. Mechanisms such as electron recombination, downward plasma drift, and energy dissipation during geomagnetic activity drive these TEC reductions.Monthly and geomagnetic factors strongly modulate TEC variations and their associated changes. periods such as April and January, characterized by equinox conditions and higher solar ionization, exhibit elevated TEC activity due to the equatorial anomaly's double-crest structure. HILDCAA events inject substantial energy into the magnetosphere and ionosphere, leading to pronounced TEC perturbations. These events amplify ionospheric density (positive TEC changes) and accelerate electron depletion (negative TEC changes), depending on the interplay between energy input and loss processes, as detailed in Table 9.

Table 9 – Summary Comparison of Equatorial region and South Crest of EIA on TEC during HILDCAA* Events

Feature	**Equatorial Region**	**South Crest of EIA**	**Comparison and Insights**
Average TEC (TEC_AVG)	Peaks in **March (66 TECU)** and **January (61 TECU)**, lowest in **June (30 TECU)**.	Peaks in **April (95 TECU)** and **January (91 TECU)**, lowest in **August (45 TECU)**.	Both regions show higher TEC during **equinoctial months** (March and April). FZ exhibits a much lower TEC minimum in September.
Positive ΔTEC (TEC Increases)	Highest in **April (19 TECU)** and **March (16 TECU)**, lowest in **August (8 TECU)**.	Highest in **May (27 TECU)** and **March (26 TECU)**, lowest in **July (13 TECU)** and **June (15 TECU)**.	Both regions have significant TEC enhancements in **March-April**. South Crest of EIA experiences stronger positive TEC spikes, likely due to the **EIA's intensification mechanisms**.
Negative ΔTEC (TEC Decreases)	Largest reductions in **March (-15 TECU)** and **November (-15 TECU)**, smallest in **june (-8 TECU)** and **July (-9 TECU)**.	Largest reductions in **April (-28 TECU)** and **September (-18 TECU)**, smallest in **June (-15 TECU)** and **July (-11 TECU)**.	South Crest of EIA exhibits more pronounced TEC depletions, particularly in **April**, due to **geomagnetic energy dissipation** in the EIA.
Storm Drift (FZ only)	Peaks in **November (27 m/s)** and lowest in **June (13 m/s)**.	Not explicitly considered.	Storm Drift infers the properties of electric field for FZ, showing stronger plasma dynamics in **November**.
Monthly Influence	Strong monthly dependency, with lower activity in **mid-year months (June-August)**.	Similar monthly pattern, but with higher TEC values overall in equinoctial months.	Monthly trends are consistent, but South Crest of EIA generally exhibits **higher ionospheric activity**.
HILDCAA Effects	Causes moderate TEC increases and decreases, with localized effects.	Causes larger TEC increases and more dramatic depletions, particularly during geomagnetic storms.	The South Crest of EIA is more sensitive to HILDCAA events, reflecting its role in ionospheric dynamics and plasma transport.

5.7 Occurrence of Ionospheric irregularities During HILDCAA Events*

A quantitative analysis of ionospheric irregularities over the Brazilian equatorial and low-latitude regions during HILDCAA events in 2003, focusing on their occurrence and intensity through the ROTI, was performed. These irregularities, such as EPBs and TEC fluctuations, are governed by solar, geomagnetic, and electrodynamic processes, exhibiting complex variations over monthly, seasonal, and spatial scales.

Recent studies (JAKOWSKI et al., 2012; CHERNIAK; ZAKHARENKOVA, 2017; JACOBSEN; ANDALSVIK, 2016; PRIKRYL et al., 2016) indicate that ROTI is an effective indicator of TEC phase fluctuations and amplitude scintillations associated with ionospheric irregularities. These fluctuations in GNSS signals, caused by rapid changes in TEC, are primarily linked to ionospheric irregularities, which can degrade signals and adversely affect precise positioning due to fading electron density gradients. This, in turn, reduces the operational performance of navigation systems. To identify ionospheric irregularities, we first calculated the time derivative of TEC along a continuous GNSS satellite arc, referred to as ROT, as defined by Pi et al. (1997). The ROTI was then computed as the standard deviation of ROT values, serving as an effective measure of plasma density irregularities in the ionosphere. For this analysis, we calculated ROTI using a 5-minute running window of ROT observations during HILDCAA events and applied a 45^o elevation angle cutoff mask to minimize multipath distortion.

RINEX data with a standard 30-second resolution were collected from GNSS stations located in the equatorial region and low latitudes to monitor ionospheric irregularities. While several studies (AARONS; LIN, 1999; PHELPS; SAGALYN, 1976; WERNIK; SECAN; FREMOUW, 2003) have explored the effects of geomagnetic storms on equatorial and low-latitude ionospheric irregularities, research specifically addressing HILDCAA phenomena remains limited. Souza et al. (2018), highlighted the differences between irregularities caused by HILDCAA events and those induced by geomagnetic storms, based on their comparative study. Irregularities during HILDCAA events tend to be persistent and moderate, while storm-induced irregularities are characterized by their sudden and intense nature. In this context, we aimed to correlate ROTI with spread-F irregularities, which typically develop during the PRE period. Additionally, we conducted a comparative analysis of the monthly occurrence of ionospheric irregularities over the Brazilian equatorial and low-latitude ionosphere during Twenty-six HILDCAA events.

Significant ROTI intensity levels were classified as follows: ROTI $\leq$ 0.4 TECU/min corresponds to weak irregularities, 0.4 TECU/min < ROTI < 1.0 TECU/min indicates moderate irregularities, and ROTI > 1.0 denotes strong irregularities, similar to the classification outlined by Kotulak et al. (2020). The variations in the ROTI index across the Brazilian equatorial region (first panel) and low-latitude regions (second to sixth panels) during HILDCAA events from January to December 2003 are detailed below and illustrated in A.23, A.24, A.25, A.26, A.27, A.28, as references provided in A.

In reference to Figure A.23, during January, moderate irregularities were observed around post-midnight (02:00 UT) and nighttime (21:00 UT) on January 19. From January 20 to 23, the irregularities intensified to strong amplitudes during the same periods, with ROTI exceeding 1.0 TECU/min over the equatorial region and the southern crest of the EIA. On January 24 and 25, similar characteristics persisted over the southern crest (BOMJ and BRAZ), while on January 26, both the equatorial region and the southern crest experienced strong irregularities (ROTI > 1.0 TECU/min). POAL, however, showed only weak irregularity signatures.

Between February 6 and 11, significant moderate-to-strong irregularities were detected over the equatorial region and the southern crest of the EIA around 03:00 UT and 22:00 UT, respectively. Weak irregularities were observed on some days over lower latitudes. From February 16 to 21, the equatorial region consistently exhibited strong irregularities during post-midnight and nighttime hours. The southern crest showed similar behavior, particularly on February 17 and 18, except at RIOD and POAL, which had weak irregularities, and VICO, where activity was infrequent.

On March 4, strong irregularities were observed with high ROTI amplitudes across all latitudes during the post-midnight hours (01:00 UT/10:00 LT). However, weaker irregularities were noted during the nighttime. From March 5 to 7, weak irregularities were observed over the equatorial region and moderate ones at south crest of EIA during the nighttime ($\approx$ 22:00 UT/19:00 LT), with negligible irregularities during the post-midnight hours. During March 14–16, strong amplitude of irregularities was recorded during the post-midnight hours (01:00–05:00 UT) across all latitudes, except at VICO (March 14–15) and RIOD (March 15–16). While the equatorial region exhibited intense irregularities during the nighttime, weaker signatures were observed at south crest of EIA as indicated in A.24.

On April 15 and 16, strong irregularities developed over the equatorial region during post-midnight (03:00 UT) and nighttime (23:00 UT) hours. Over the southern crest of the EIA, strong signatures were limited to BOMJ, BRAZ, and UEPP, and these occurred only during post-midnight. Other stations displayed weak irregularities. The equatorial region maintained strong irregularities on April 21 and 23, persisting until April 24 during nighttime (22:00 UT) and post-midnight (02:00 UT). Meanwhile, the southern crest exhibited weak irregularities, except for UEPP, where moderate irregularities occurred on April 21 and 24. From April 25 to 28, the equatorial region continued to show strong irregularities. Stations such as BOMJ, BRAZ, RIOD, and UEPP on the southern crest displayed significant activity on April 25 and 26, while the following days showed weaker irregularities.

For the May cases, from May 1 to 4, as illustrated in Figure A.24, weak irregularities were observed at south crest of EIA during the post-midnight hours (02:00 UT/11:00 LT), while the equatorial region showed relatively stronger signatures. Conversely, from May 5 to 9, irregularities remained weak, particularly during the nighttime ($\approx$ 21:00 UT/18:00 LT) as presented in Figure A.25. However, significant intensity was observed over the equatorial region during the post-midnight hours on May 5 and 9. On May 8 at 16:00 UT, notable intensification was recorded at south crest of EIA (BOMJ, BRAZ, and VICO) with a ROTI threshold of 0.5 TECU/min, likely driven by eastward PPEF. From May 10 to 16, irregularities remained weak (ROTI below 0.5 TECU/min) across most stations, except for strong signatures over the equatorial region on May 10, 13, and 16 during the post-midnight hours. Finally, from May 22 to 29, strong irregularities were detected during the post-midnight hours (≈ 05:00 UT) on May 22, 27, 28, and 29, with a data gap (No data) from May 23–25. Low-latitude stations generally displayed weak signatures during this period, except on May 29, when significant intensity was observed at 23:00 UT/20:00 LT. Overall, during the May events, irregularities were predominantly suppressed at low latitudes. Previous studies (TROSHICHEV et al., 2000; DANILOV; LASTOVICKA, 2001) suggest that increased auroral heating, caused by energy input from polar cap potentials during geomagnetic disturbances, plays a critical role by driving DDEF, especially during storm recovery phases (RICHMOND; PEYMIRAT; ROBLE, 2003).

During June 2–12, weak irregularities were observed across all latitudes, with ROTI values below the 0.5 TECU/min threshold. However, on June 12, significant amplitudes were noted over the equatorial region at ≈ 05:00 UT. Similar characteristics were observed from June 13–16, with strong irregularities over the equatorial region during both nighttime (≈ 21:00 UT) and post-midnight hours (≈ 02:00 UT). From June 24 to July 6, weak irregularities persisted at south crest of EIA, while significant intensifications were observed during the post-midnight and nighttime hours from June 24–27 and July 1–6. On July 12, irregularities were strong over the equatorial region and moderate at south crest of EIA. Tsurutani et al. (2004) highlighted that irregularities were prominent over the equatorial region and moderate at the southern crest of EIA, reflecting consistent increases in TEC variability and more frequent irregularities over Brazil. Weak signatures persisted until July 15 as noted in Figure A.26.

As noted in A.27, from July 18–21, weak irregularities were observed on July 18, but strong amplitudes were detected over the equatorial region and moderate signatures at low latitudes (except at RIOD) during the post-midnight hours (≈ 02:00 UT). similarly, in the case of July 29–31, weak irregularities were observed across all stations in this sector. A notable latitudinal variation in irregularities was evident from August 1–4. Over the equatorial region, intense irregularities were recorded on August 1 and 3 around ≈ 03:00 UT. At low latitudes (BOMJ, BRAZ, and UEPP), moderate irregularities were observed during the nighttime (≈ 21:00 UT) and intensified during the post-midnight hours (02:00 UT) on August 1–2. For the remaining days, weak signatures persisted. Weak irregularities (ROTI 0.3) were first detected at 21:00 UT (18:00 LT) and persisted until 02:00 UT (11:00 LT) over Brazil's equatorial regions to south crest of EIA, observed from August 7 to 14. During this period, strong irregularities were observed at 02:00 UT (11:00 LT) over the equatorial region, while weaker irregularities were detected at south crest of EIA. This pattern continued from August 23 to 25. However, in September, irregularities appeared very weak at low latitudes, with the reverse occurring at the equatorial region during the post-midnight and nighttime hours from September 10 to 12. Around 02:00 UT, strong irregularities were observed over both the equatorial and low-latitude regions (BOMJ).

This pattern persisted over the equatorial region, with moderate signatures observed at south crest of EIA stations (BOMJ, BRAZ, VICO, UEPP) on September 21. Moderate irregularities were also detected in the equatorial region during the nighttime (22:00 UT) from September 19 to 22. Irregularities began to continue to dominate from November 1, with strong amplitudes observed around 03:00 UT over the equatorial region and moderate signatures at south crest of EIA. Moderate irregularities were observed at both latitudes on November 3 at around 22:00 UT, and these irregularities reappeared in the post-midnight hours (01:00 UT), with strong amplitudes observed on November 4. The nighttime characteristics remained intense over both latitudes on the same day. From November 14 to 19, irregularities were generally intense over the equatorial region and moderate at low-latitude stations, except for POAL. An intense irregularity signature was observed from November 17 to 19 at these latitudes. Overall, irregularities in November were more dominant over the equatorial region, with strong amplitudes during the post-midnight hours. On contrary from December 10 to 17, strong irregularities were observed during the post-midnight hours (01:00 UT) from December 10 to 17, except for December 12, where the irregularities were moderate. During the nighttime, the irregularities were generally moderate. At low latitudes, moderate to intense irregularities were observed on December 12, 13, 15, 16, and 17 during the post-midnight hours (02:00 UT). The nighttime irregularities at 21:00 UT over BOMJ and BRAZ were moderate, in contrast to the other stations as presented in A.28.

Irregularity signatures were observed during almost every month of HILDCAA events, with stronger amplitudes typically occurring in the equinoctial periods, followed by the summer months. This finding aligns with Abdu (2005), who noted that the Brazilian sector is characterized by a higher frequency of ionospheric irregularities during the equinoctial months (March–April and September–October), primarily due to the strong PRE of the zonal electric field, which fosters plasma instability. These monthly patterns are influenced by geomagnetic disturbances, showing variations in intensity depending on the phases of the storms. Additionally, Santos et al. (2022), provides similar conclusions in their studies. In the Brazilian longitudinal sector, irregularities are influenced by large negative magnetic declination and show high occurrence rates during local summer and equinoctial months (ABDU; BITTENCOURT; BATISTA, 1981). However, during winter, the poor alignment between the sunset terminator and magnetic field lines reduces post-sunset irregularities due to weak vertical plasma drifts.

According to Abdu (2001), post-midnight irregularities in summer result from the late Rayleigh-Taylor instability and strong upward drifts, which elevate the F-layer through the enhanced zonal (eastward) electric field, known as PRE. During geomagnetic disturbances, weak-to-moderate ionospheric irregularities were observed at south crest. Enhanced geomagnetic activity leads to intensified ROTI values in equatorial regions, caused by electric field penetration due to magnetic reconnection. During the recovery phase, the ionospheric disturbance dynamo, driven by prolonged auroral heating, dominates the regulation of ionospheric features at low latitudes and the equator. Daytime DDEF induces a westward electric field that inhibits ionospheric irregularities at low latitudes and the equator. However, after 21:00 LT, a reversal in electric field direction promotes irregularity formation and ROTI intensification. HSSWS events, linked with Alfvén waves, also contribute to significant ionospheric irregularities, as evident from enhanced ROTI values at both latitudes and increased AE index activity as highlighted by Liu et al. (2019).

Studies of ROTI during intense geomagnetic storms reveal that irregularity patterns respond directly to such disturbances, with maximum ROTI values observed in equatorial and low-latitude regions. DDEFs plays a key role in moderating irregularity signatures, while PPEFs exerts a contrasting influence during the main phase. The effects of electric fields, essential electrodynamic drivers of the equatorial ionosphere, depend on the local time of the southward turning of IMF Bz. These electric fields, displaying opposite polarities for PPEFs and DDEFs, lead to the formation of EIA and ionospheric irregularities.

As noted by Fejer et al. (1991a), the PRE-related electric field intensifies before sunset, raising the F-layer to higher altitudes where recombination is negligible. This creates favorable conditions for irregularity development, as described by Woodman e Hoz (1976). These irregularities result from Rayleigh-Taylor instability and gravity wave seed perturbations (KELLEY, 1989; TSUNODA, 2010). Their generation depends on variables like the electric field, neutral wind, Pedersen conductivity, F-region collision frequency, recombination rate, and F-layer height (SULTAN, 1996).

The equatorial ionosphere undergoes significant perturbations during geomagnetic storms and HILDCAA events due to electric fields affecting vertical plasma drifts. These disturbances enhance or suppress irregularity development, particularly during the main phase of a storm when the IMF Bz is southward (ABDU, 2012). During the recovery phase, the electric field's reversal in evening hours suppresses the PRE drift, inhibiting irregularity formation. DDEFs driven by auroral heating produces thermospheric circulation and equatorward winds, causing westward drift in the evening (BLANC; RICHMOND, 1980). This suppress or reverse the PRE, thus suppressing irregularity formation (ABDU, 1997). For example, during the main phase of the storm, PPEFs enhance the development of irregularities by raising the ionospheric F-region, whereas in the recovery phase, the effect is reversed, as noted by Abdu et al. (2009).

According to Tanaka (1981) and Basu et al. (1996), the rise in the F-layer under the influence of PRE, driven by $\vec{E} \times \vec{B}$ drift to higher altitudes, creates favorable conditions for RTI, leading to the occurrence of ionospheric irregularities. Additionally, Abdu (2012) emphasized the contribution of eastward electric fields in enhancing $\vec{E} \times \vec{B}$ drifts, which lead to the generation of irregularities during geomagnetic disturbance periods, similar to the findings of Fejer e Scherliess (1997), who demonstrated that under shielding conditions, electric fields modify the equatorial ionosphere behavior.

5.8 Empirical vertical-drift estimates during HILDCAA* events

To evaluate the penetration of storm-time electric fields into the equatorial ionosphere during HILDCAA* activity, we applied the empirical disturbance-drift formulation of Fejer e Scherliess (1997). In the HSS environment, large-amplitude southward IMF B_z fluctuations embedded in interplanetary Alfvén waves reconnect with the dayside magnetosphere, supplying Poynting flux to the polar upper atmosphere (TSURUTANI et al., 1995). The consequent Joule heating and particle precipitation intensify the auroral electrojets, driving the high-latitude current oscillations that define HILDCAA intervals (GONZALEZ; TSURUTANI, 1987; TSURUTANI et al., 2004). Through magnetosphere–ionosphere coupling, the associated PPEFs and longer-lived DDEFs modulate the low-latitude vertical plasma drift.

Figures A.29–A.34 (see Appendix A) summarise the 2003 HILDCAA* event: from top to bottom each panel displays the interplanetary magnetic field, the symmetric disturbance field index, the auroral electrojet index, and the empirical vertical-drift components—quiet-time mean ($V_{d\text{mean}}$), storm perturbation ($V_{d\text{storm}}$), and total ($V_{d\text{total}}$). The two electric-field contributions are separated into PPEF-driven and DDEF-driven drifts, which are then compared with the observed variations of the F-layer virtual height ($h'F$) at São Luís (dip latitude $\sim 1.5°$ S).

Referring to Figure A.29, the combined PPEF and DDEF drifts that accompanied the two consecutive HILDCAA intervals 19–23 January 2003 and 23–27 January 2003 produced clear electrodynamic signatures at low latitude. Throughout both events the AE index displayed large-amplitude, quasi-periodic oscillations, and each AE peak was mirrored by a negative excursion of the SYM-H index, signalling enhanced magnetospheric energy input.

During 19–23 January the storm-time vertical drift ($V_{d\text{storm}}$) fluctuated about $+15\ \mathrm{m\,s^{-1}}$

near the local pre-reversal enhancement (PRE) window ($\approx$ 07:00 UT); a maximum of $+23\ \mathrm{m\,s^{-1}}$ occurred at 00:42 UT on 21 January. At 01:11 UT on 23 January the model returned simultaneous eastward PPEF ($\approx 5\ \mathrm{mV\,m^{-1}}$) and westward DDEF ($\approx 11\ \mathrm{mV\,m^{-1}}$) components, implying a moderate net upward drift.

The second interval (23–27 January) was comparably active: $V_{d\mathrm{storm}}$ peaked at $+16\ \mathrm{m\,s^{-1}}$ at 01:55 UT on 24 January, while at 20:51 UT that same day the eastward PPEF and westward DDEF contributions were ≈ 8 and $\approx 6\ \mathrm{mV\,m^{-1}}$, respectively. Because DDEFs persist for several hours and oppose the prompt field, their superposition complicates the separation of the two drivers in data; together they shape the long-lasting "recovery-phase" response of the coupled ionosphere–thermosphere system during high-speed–stream forcing.

These contribution of the dynamo effect persisted, from February 6 to 11, 2003, and February 16 to 21, it was observed that the IMF Bz and AE indices fluctuated significantly for both events due to the associated Alfvénic waves, leading to high level of auroral auroral activities. For instance, the IMF Bz and AE indices fluctuated around zero, with average amplitudes of $\approx \pm 8$ nT and ≥ 1000 nT, respectively during the period. The minimum values of sym-H were $\approx$ -48 nT for the February 6-11 event and -10 nT for the Febraury 16-21 event. There was considerable geomagnetic activity in the high-latitude ionosphere, as indicated by the elevated AE index values, which were $\geq$1000 nT during both events. On the event days, the V_{dstorm} peaked at around 15 m/s at 16:18 UT on February 10. The combined effects of the PPEFs and DDEFs were estimated from the drift measurements, which showed null mV/m and 11 mV/m on February 8 at 00:54 UT during the PRE time for the February 6-11 event. In contrast, during the February 16-21 event, the V_{dstorm} peaked at around 11 m/s at 15:58 UT on February 19. The drift rates were measured as null mV/m and 6 mV/m for PPEFs and DDEFs around 00:22 UT on the same day. This plasma distribution caused an uplift of the F layer, leading to the observed spread F development in both cases throughout the period.

As noted in A.30, the auroral electrojet displayed pronounced oscillations in geomagnetic activity during 04–07 March. The V_{dmean} (mean drift) oscillated between 22 m/s at 07:16 UT and 26 m/s at 15:33 UT. V_{dstorm} (storm drift) peaked at $\approx$15 m/s around 23:43 UT (20:43 LT). Additionally, the V_d-total (total drift) including PPEF, was insignificant. However, the disturbance dynamo-driven drift during the HILDCAA event was $\approx$12 m/s at 23:56 UT (20:56 LT). On 05 March, the electric field remained insignificant throughout the day. Huang et al. (2005), predicted that the reversal of the disturbance zonal electric field occurs around 22:30 LT at Solar Local Time, associated with positive charge accumulation. Therefore, our findings indicate effective buildup of positive charges around pre-midnight during the HILDCAA period, leading to upward drifts.

Huang et al. (2005) and Huang et al. (2007) recently reported an intriguing model prediction regarding disturbance dynamo drifts following the main phase of geomagnetic storms at the magnetic equator, using TIEGCM numerical simulations. Their results suggest equatorward currents generated by disturbance winds result in positive charge accumulation at the equator, peaking around pre-midnight, with zonal disturbance winds persisting for several days after geomagnetic activity subsides. Disturbances in h'F and F-layer uplift are caused by DDEFs, as clearly observed in A.30. These upward drifts contribute to the generation of equatorial spread F.

However, with respect to March 14 to 16, we observed a series of fluctuations in the IMF-Bz and AE indices, despite the Sym-H dipping to a minimum of $\approx$ -50 nT. This level of geomagnetic disturbance is unlikely to have a significant impact on the ionosphere. The V_{dstorm} peaked at around 21 m/s at 14:33 UT on March 15, with an estimated drift of null mV/m and 18 mV/m on March 15 at 01:25 UT for the PPEFs and DDEFs, respectively. The uplift of the F layer resulted in spread F signatures as a consequence.

According to Liu et al. (2018) and Zhang et al. (2021), the transfer of energy from the solar wind to the magnetosphere-ionosphere system is influenced by temporary variations in IMF Bz, which control Joule heating, cross-polar cap potential, auroral peak electron flux, vertical plasma drift, and variations in the F2 peak density of the ionosphere globally, based on their Coupled Magnetosphere–Ionosphere–Thermosphere Model.

Between April 15 and 17, 2003, as indicated in Figure A.30, we observe a series of quasi-periodic variations in the IMF-Bz and AE indices. Joule heating and particle precipitation were prominent, as indicated by the AE index. The Sym-H dipped to a minimum of $\approx$ -35 nT on April 17. This level of geomagnetic disturbance is weak, suggesting that the ionospheric response may be attributed to HILDCAA phenomena. The V_{dstorm} peaked at around 18 m/s at 01:25 UT on April 17. We estimated a drift rate of 9 mV/m and 13 mV/m on April 15 at 15:00 UT for the PPEFs and DDEFs, respectively. Spread F development was observed each day during the PRE time.

For the period from April 20 to 24, we noted a similar level of fluctuations in the IMF-Bz and AE indices as in the previous event. A dip magnitude of about -60 nT in Sym-H was recorded on April 23. The V_{dstorm} drift peaked at around 29 m/s at 01:33 UT on April 24, with combined drift rates of 20 mV/m and 16 mV/m observed in the PPEFs and DDEFs, respectively, on the same day at 01:33 UT. A significant impact on the equatorial ionosphere was noted during the PRE time, and the development of spread F persisted throughout the period.

In addition, from April 25-28, the V_{dmean} (mean drift) exhibited upward trends during daytime hours and downward trends at night, ranging from 23 m/s at 07:16 UT to 25 m/s at 15:39 UT. On April 25, the V_{dstorm} peaks $\approx$ 12 m/s. Additionally, for PPEFs and DDEFs, drift rates of 9 mV/m and 14 m/s were observed around 23:43 UT, respectively. PPEFs effects were also evident during daytime hours.

Maruyama et al. (2005) noted that PPEFs dominates the equatorial disturbed electric field during the early stages of storms, while DDEFs becomes more pronounced later. At nighttime, PPEFs and DDEFs effects were comparable, indicating that DDEFs becomes the dominant disturbance electric field in the F-region when PPEFs is predominant during the daytime. Furthermore, on April 28, V_{dstorm} drift reached $\approx$ 28 m/s. The combined effect of PPEFs and DDEFs contributed to null results and $\approx$ 23 mV/m, respectively.

In reference to Figure A.31, multiple fluctuations were observed in the sustained IMF-Bz and high levels of oscillations due to the influence of Alfvén waves associated with solar wind and magnetospheric processes. These waves move charged particles, generating heat known as Joule heating at high latitudes, as reflected in the AE index. Throughout May, the level of geomagnetic disturbance was notably high.

As highlighted in Figure A.30, the V_{dstorm} during the period of May 1–4 reached a peak velocity of approximately 6 m/s at 01:05 UT on May 2, accompanied by a Sym-H magnitude of around -98 nT. The estimated drift rates for PPEFs and DDEFs were 4 mV/m and 11 mV/m, respectively, on the same day at around 21:58 UT.

As shown in Figure A.31, observations during the period of May 5–9 revealed that the V_{dstorm} reached a peak of around 21 m/s at 23:26 UT on May 6, with an estimated drift rate of null mV/m and 13 mV/m recorded at the same time. The magnitude of geomagnetic disturbances was $\approx$ -56 nT.

For the interval of May 10-16, the V_{dstorm} peaked at about 22 m/s at 01:17 UT on May 11, with a Sym-H value similar to that observed from May 1-4. The drift rates for PPEFs and DDEFs were measured at 4 mV/m and 13 mV/m, respectively, on May 12 at 01:17 UT.

In the case of May 22-29, the estimated maximum peak for the V_{dstorm} was around 65 mV/m at 00:00 UT, with drift rates of 25 mV/m and 48 mV/m recorded for PPEFs and DDEFs on May 28. It is noteworthy that during the period from May 22-29, the ionospheric response was elevated due to significant geomagnetic activity. Spread F development persisted throughout this period as a consequence of the F layer uplift associated with the HILDCAA days, exceeding the average observed during the five quiet days average.

A significant response was observed in the IMF-Bz and AE indices. Sym-H recorded magnitudes of around -85 nT, -40 nT, and -88 nT during the intervals of June 2–12 in Figure A.31, June 13–16, and June 24 to July 6 in Figure A.32, respectively. Throughout this month, both the IMF-Bz and AE indices displayed substantial fluctuations and intense auroral activity, significantly impacting the equatorial ionosphere.

During the period from June 2-12, the V_{dstorm} peaked at around 25 m/s at 00:42 UT on June 6. The drift rates for PPEFs and DDEFs were estimated to be 7 mV/m and 15 mV/m, respectively, on June 23 at 01:11 UT during the same time of day. For the interval of June 13-16, the V_{dstorm} reached a maximum of about 23 m/s at 01:42 UT on June 15, with combined electric effects of 18 mV/m and 30 mV/m on June 23 at 01:42 UT, corresponding to PPEFs and DDEFs.

As shown in Figure A.32, between June 24 and July 6, the V_{dstorm} peaked at $\approx$ 20 m/s at 00:40 UT on both June 26 and 27. During this time, the estimated drift rates for PPEFs and DDEFs were 8 mV/m on those same days. We observed F layer uplift associated with the HILDCAA events during nearly the entire period, along with the development of spread F signatures, which in other words, are attributed to the oscillations caused by the southward incursions of IMF Bz, which are associated with PPEFs and the solar wind energy transfer mechanism as noticed similarly in July.

This led to a high level of auroral activity related to Joule heating and particle precipitation, as reflected in the AE index during the periods of July 12-15, July 18-21, 2003. The estimated magnitudes of the disturbances were approximately -85 nT, -55 nT, and -45 nT for the intervals of July 12-15, July 18-21, and July 29 to August 4, respectively. However, from July 18-21, V_{dstorm} peaked at around 18 m/s at 02:30 UT, with drift rates of 8 mV/m and 13 mV/m for PPEFs and DDEFs during the same period on July 14. With respect to July 18-21 interval, V_{dstorm} reached a maximum of about 13 m/s at 01:00 UT, with drift rates of 5 mV/m and 9 mV/m for PPEFs and DDEFs observed on July 19 during that time.

As referenced in Figure A.33, between July 29 and August 4, the V_{dstorm} peaked at around 20 m/s at 01:25 UT, while the drift rates for PPEFs and DDEFs were 9 mV/m and 13 mV/m, respectively, on July 30. During the observation period, the F layer uplift associated with the HILDCAA days was above the five quiet days average, resulting in the generation of spread F.

From August 7 to 14, 2003, and from August 23 to 25, we observed significant fluctuations in the IMF-Bz and AE indices, although the level of auroral activity was moderate, the effectiveness of the electric field effect was evident. This quasi-periodic variation persisted throughout both periods.

The minimum Sym-H dip was $\approx$ -60 nT for the interval of August 7-14 and around -35 nT for August 23-25. We recorded a maximum V_{dstorm} peak of 18 m/s around 02:00 UT on August 10, with estimated drift rates of 10 mV/m and 8 mV/m for PPEFs and DDEFs, respectively, during the HILDCAA event of August 7-14. V_{dstorm} peaked at $\approx$ 20 m/s at 02:30 UT, with drift rates of 9 mV/m and 13 mV/m observed on August 24 for PPEFs and DDEFs, respectively.

The development of spread F was noted during the uplift of the F layer associated with the HILDCAA events over the average of five quiet days from August 23 to 25.

The influence of HSS during the HSS/CIR storm led to significant fluctuations observed in the IMF-Bz and AE indices during the HILDCAA events from September 10 to 12, 2003, and from September 19 to 22. The measure of geomagnetic disturbance, as indicated by the Sym-H index, was estimated to be $\approx$ -32 nT and -63 nT for September 10-12 and September 19-22, respectively. This magnitude was insufficient to cause severe ionospheric effects. In other words, auroral activities may have been the primary factor responsible for any adverse effects.

From September 10 to 12, V_{dstorm} was negligible during the PRE time, with estimated drift rates of $\approx$ -4 mV/m and 3 mV/m on May 6 at 01:26 UT for PPEFs and DDEFs, respectively. A negative storm impact attributed to the disturbance dynamo effect was evident.

As indicated in Figure A.34, a similar trend was observed during the PRE time for the period from September 19–22. However the V_{dstorm} peaked at around 10 m/s at 22:26 UT on September 22, while PPEFs and DDEFs recorded drift rates of $\approx$ -15 mV/m at 00:00 UT and 8 mV/m around 22:00 UT. The ionospheric F layer experienced uplift associated with the HILDCAA events over the average of five quiet days.

Subsequently, between November 1 to 4, 2003, and from November 14 to 19, we observe insignificant oscillations in the IMF-Bz and AE indices during the November 1-4 event. In contrast, from November 14 to 19, we observed a series of greater fluctuations. The magnitude of the geomagnetic disturbance was $\approx$ -65 nT and -60 nT for the November 1-4 and November 14-19 intervals, respectively, as obtained from the Sym-H index.

However, for the case of November 1-4 event, the V_{dstorm} peaked at around 21 m/s at 01:30 UT on November 2, with drift rates of 15 mV/m and 9 mV/m for PPEFs and DDEFs, respectively.

During the November 14-19 interval, notable plasma drift rates were observed only on November 18, when the V_{dstorm} peaked at around 32 m/s at 00:00 UT. On November 18, PPEFs and DDEFs recorded drift rates of 15 mV/m and 30 mV/m during the same period. The combined effect of these electric fields induced an uplift in the F layer associated with the HILDCAA events, averaging over five quiet days, resulting in the generation of spread F signatures observed during the PRE time in both cases.

During the interval from December 10 to 17, 2003, the magnitude of the geomagnetic disturbance was $\approx$ -58 nT. The V_{dstorm} peaked at around 12 m/s at 01:22 UT, with estimated drift rates of 9 mV/m and 11 mV/m for PPEFs and DDEFs, respectively, on December 12. It is important to note that from December 14 to 17, the electric field was insignificant; thus, the ionospheric response observed during this period can be attributed to the influence of auroral activities, as manifested in the AE index. The level of geomagnetic disturbance caused an uplift in the ionospheric F layer, averaged over five quiet days, except for December 11 and 12 during the PRE time. Spread F development was observed throughout the entire interval.

According to Rishbeth (1971) and Heelis et al. (1974), the evening rise of the equatorial F layer is attributed to an intensified eastward electric field originating from the F region dynamo, driven by thermospheric winds. (KOGA et al., 2011) investigated electrodynamic coupling processes between the magnetosphere and the equatorial ionosphere in São Luis, Brazil, during a 5-day-long HILDCAA event in 2003. They noted that while PPEFs drifts were unclear, they attributed observed effects to DDEFs drifts. The study established a strong correlation between disturbed ionospheric height and DDEFs drifts calculated using the model developed by Fejer e Scherliess (1997).

(SOBRAL et al., 2006) conducted a study across three equatorial and low-latitude stations in Brazil, revealing evidence of DDEFs and disturbed thermospheric winds, but not significant PPEFs effects. HSSs, as depicted in Figure 39, induce enhanced magnetic flux merging at the dayside magnetopause, resulting in significant ionospheric Joule heating indicated by high AE indices. Each group of HSSs is expected to generate equatorial DDEFs. This also suggests that strong geomagnetic storms (high AE) can lead to substantial thermospheric disturbances extending to middle and low latitudes (FEJER; SCHERLIESS, 1995). Generally, CIRs have a more pronounced impact on the ionosphere compared to HSS/HILDCAA events due to higher auroral energy input (indicated by intense AE and large southward Bz values). However, the Vsw can amplify these effects, especially when associated with large-amplitude southward Bz variations of Alfvén waves during HILDCAA events.

As highlighted by Yeeram (2019), intermittent magnetic reconnection between southward components of Alfvén wave fluctuations and magnetopause magnetic fields leads to the penetration of convection electric fields. These magnetospheric penetration electric fields originating from high latitudes swiftly propagate to the equatorial ionosphere. Meridional neutral winds, driven by Joule heating of the thermosphere in the auroral region, propagate towards the equatorial region, causing DDEFs. These disturbance electric fields manifest during CIRs and HSSs coinciding with auroral activities as indicated by the AE index. Regarding prolonged AE activities such as HILDCAA.

Santos et al. (2016) and Abdu et al. (1991) suggest that disturbance electric fields are weak but persistent. PPEFs typically oscillate with periods of 1-3 hours during HILDCAA events due to intermittent coupling by Alfvén waves in HSS, whereas the effects of Disturbance Dynamo can endure for more than a day (FEJER; SCHERLIESS, 1997).

6 Conclusion and Recommendation

This study has explored the ionospheric response to CIR/HSS-driven geomagnetic storms and associated HILDCAA events during the year 2003 over the Brazilian sector. Although these solar wind structures are generally moderate in intensity compared to ICME-driven storms, they exert prolonged and significant effects on the coupled magnetosphere-ionosphere-thermosphere (MIT) system. The persistence of HSSs, along with their embedded Alfvén waves characteristic of CIRs drives extended periods of geomagnetic activity, commonly manifested through HILDCAA events.

Our findings underscore the importance of systematic investigations into these moderate but long-duration storms, particularly during HILDCAA intervals, as they offer crucial insights into cumulative space weather impacts. While CIRs-driven disturbances may not trigger abrupt disruptions, their persistent nature can gradually degrade satellite-based technologies, including GPS navigation and communication systems (HAJRA et al., 2013; CHINGARANDI et al., 2023). Furthermore, their long-term influence on thermospheric heating and density variations contributes to increased satellite drag and orbital decay factors critical for satellite lifespan prediction and orbital maintenance.

The analysis combined multiple data sources and techniques, including thousands of digisonde ionograms from equatorial (São Luís) and low-latitude (Cachoeira Paulista) stations, GNSS-derived vertical TEC (VTEC) across a latitudinal transect in South America (from Fortaleza to Uruguaiana), thermospheric O/N_2 ratios from GUVI measurements, and empirical estimations of vertical plasma drift based on the model by Fejer e Scherliess (1997). Both case studies and statistical methods (including Gaussian fits) were employed to investigate ionospheric parameters such as TEC, foF2, h'F, and ROTI.

A notable example is the CIR-driven geomagnetic storm observed between 12–23 October 2003, preceding the well-known CME-driven Halloween storm. This case revealed substantial disturbances in ionospheric parameters, emphasizing the geoeffectiveness of CIR/HSS events in altering ionospheric structure and dynamics. The study further demonstrated that southward interplanetary Alfvén waves embedded within CIRs play a significant role in driving HILDCAA events and modulating the ionosphere.

In conclusion, this work affirms that in addition to ICMEs traditionally regarded as dominant drivers of intense geomagnetic storms CIR/HSS structures also represent a key component of space weather variability. Their contributions to long-duration ionospheric perturbations, thermospheric composition changes, and geomagnetic activity demand closer consideration in both forecasting models and ionospheric research. The main conclusions drawn from this investigation are as follows:

- **Ionospheric disturbances during CIR/HSS-driven geomagnetic storms were pronounced over Brazil**, characterized by strengthened $E \times B$ vertical plasma drifts during HILDCAA intervals. This was driven by sustained interplanetary electric fields associated with Alfvén wave activity, leading to prolonged TEC intensifications during the recovery phase of the storm.

- **F-layer uplift during the main phase** of the storm was triggered by PPEFs, which intensified equatorial vertical drifts and displaced the southern EIA crest poleward, beyond its typical latitudinal range.

- **Thermospheric composition changes**, represented by a decline in the [O]/[N_2] ratio, indicated enhanced Joule heating and plasma-neutral interactions during the storm. This altered the recombination rates in the F-region, particularly at low latitudes.

- **Periodic F-layer height variations during the recovery phase** were attributed to a combination of PPEFs and DDEFs. The interplay of these electric fields sustained the ionospheric uplift and prolonged storm-time ionospheric variability.

- **Enhanced fountain effect and TEC values** during the storm's main phase were a consequence of intensified vertical drifts, which redistributed plasma and extended the EIA to higher latitudes (up to $-20°$ dip latitude).

- **GNSS-derived ROTI revealed intense plasma irregularities** between $10°$ and $15°$ dip latitude, with equatorward and poleward expansion during the storm. These irregularities were driven by post-sunset plasma instabilities such as Rayleigh-Taylor instabilities amplified by storm-induced electric fields.

- **HILDCAA events facilitated equatorward-propagating disturbance winds**, which contributed to sustained electrodynamic coupling and prolonged ionospheric variability. These winds also supported the generation of DDEFs during storm recovery phases.

- **F2-layer uplift and occurrence of spread-F** during the nighttimes of HILDCAA days suggested enhanced PRE and irregularity growth, driven by modulated ionospheric electric fields and wave structures during HSS activity.

- **Nighttime uplift of the F-layer peaked around 23:30 UT**, while during winter months, this uplift extended from 00:00 to 07:00 UT, indicating seasonal dependence in the electrodynamic response of the ionosphere to storm activity.

- **Daytime foF2 enhancements** were dominated by solar photoionization, but further modulated by HILDCAA-induced electric fields, demonstrating solar wind-magnetosphere-ionosphere coupling effects even under sunlit conditions.

- **TEC enhancements were stronger at low latitudes than at the equator** during HILDCAA periods, due to the poleward displacement of EIA crests driven by vertical drifts and thermospheric dynamics.

- **Monthly variations showed higher TEC values during equinoxes and summer**, corresponding to enhanced PRE and favorable ionospheric conditions, whereas the lowest TEC and deviations occurred in winter, due to reduced ionization and altered thermospheric circulation.

- **TEC deviations at night** were largely controlled by PPEFs, while **daytime deviations** were influenced by disturbed thermospheric composition and wind variations caused by energy input from the solar wind.

- **No major changes in neutral composition** were observed during some HILDCAA periods, suggesting that electric field penetration, rather than thermospheric composition, was the dominant mechanism driving TEC enhancements during these times.

- **Monthly and regional irregularity patterns** showed that the equatorial region had the strongest ROTI amplitudes between March and April, while the low-latitude region was most affected between May and August, especially in July. These patterns aligned with the seasonal distribution of storm-time electrodynamic drivers.

- **HILDCAA events during equinoctial and summer months** resulted in widespread ionospheric irregularities with ROTI values exceeding 1.0 TECU/min. This was likely due to increased PRE and instability growth during periods of enhanced geomagnetic activity.

- **A total of 26 HILDCAA events** were recorded in 2003, driven by CIR/HSS interactions. These events were marked by sustained HSS ($\approx$ 619 km/s), enhanced IMF, elevated auroral indices (AE, AL, AU), and increased solar wind dynamic pressure and temperature, all of which contributed to extended geomagnetic and ionospheric activity.

- **Statistical Gaussian analysis revealed significant variability in ionospheric parameters during HILDCAA events**. TEC showed higher variability near the equator, while foF2 slightly decreased with increased variance, indicating enhanced electrodynamic fluctuations and irregularities in the equatorial ionosphere.
- This study has contributed to a better understanding of space weather dynamics during the declining phase of solar cycle 23. It highlights the geoeffectiveness of CIR/HSS and their role in modulating ionospheric behavior, offering valuable insights for space weather modeling, satellite operations, and communication system resilience.

Scientific Contribution

This thesis advances the understanding of space weather impacts during the declining phase of solar cycle 23, specifically the role of CIR/HSS structures and HILDCAA events in driving long-duration ionospheric perturbations. The findings provide novel insights into the physical processes governing ionospheric variability, the role of storm-time electrodynamics, and the monthly modulated response of the equatorial and low-latitude ionosphere.

This work adds significantly to the body of knowledge on the effects of CIR/HSS-driven geomagnetic storms and HILDCAA events on the equatorial and low-latitude ionosphere, with implications for both scientific understanding and technological applications in space weather.

Recommendation

Based on the findings of this study, the following recommendations are proposed:

- Further investigation into the coupling between Alfvénic wave energy and ionospheric electric field variability during HILDCAA events is necessary to refine predictive models of ionospheric disturbances.
- Operational space weather forecasting models should integrate both transient (ICME) and recurrent (CIR/HSS) drivers, especially considering the long-duration effects of HILDCAA events on GNSS-based systems and satellite orbits.
- Long-term observational campaigns involving coordinated ground-based and satellite measurements (e.g., ionosondes, GNSS receivers, GUVI, GOLD, Swarm) across multiple longitudinal sectors would enhance global understanding of HILDCAA-induced ionospheric dynamics.

- Future studies should consider comparative analysis across solar cycles to evaluate the changing nature of HILDCAA events and their impact under different solar activity regimes.
- Additional studies are required to explore and validate hypotheses, such as the one proposed by (HAJRA et al., 2013), which emphasizes the reduced HILDCAA activity during the ascending and maximum phases of the solar cycle compared to the declining phase. These efforts aim to improve our understanding of the phenomenon.

Bibliographic References

AARONS, J.; LIN, B. Development of high latitude phase fluctuationsduring the january 10, april 10–11, and may 15, 1997magnetic storms. *Journal of atmospheric and solar-terrestrial physics*, Elsevier, v. 61, n. 3-4, p. 309–327, 1999. Citado na página 167.

ABAIDOO, S. et al. Cir-driven geomagnetic storm and high-intensity long-duration continuous ae activity (hildcaa) event: Effects on brazilian equatorial and low-latitude ionosphere—observations and modeling. *Atmosphere*, MDPI AG, v. 16, n. 5, p. 499, abr. 2025. ISSN 2073-4433. Disponível em: <http://dx.doi.org/10.3390/atmos16050499>. Citado na página 79.

ABD, M. A.; MAJED, S. F.; ZHARKOVA, V. Automated classification of sunspot groups with support vector machines. In: SPRINGER. *Technological developments in networking, education and automation*. [S.l.], 2010. p. 321–325. Citado na página 9.

ABDU, M. Major phenomena of the equatorial ionosphere-thermosphere system under disturbed conditions. *Journal of Atmospheric and Solar-Terrestrial Physics*, Elsevier, v. 59, n. 13, p. 1505–1519, 1997. Citado 5 vezes nas páginas 1, 104, 118, 136, and 171.

ABDU, M. Outstanding problems in the equatorial ionosphere–thermosphere electrodynamics relevant to spread f. *Journal of Atmospheric and Solar-Terrestrial Physics*, Elsevier, v. 63, n. 9, p. 869–884, 2001. Citado na página 171.

ABDU, M. Equatorial spread f/plasma bubble irregularities under storm time disturbance electric fields. *Journal of atmospheric and solar-terrestrial physics*, Elsevier, v. 75, p. 44–56, 2012. Citado 4 vezes nas páginas 34, 62, 171, and 172.

ABDU, M. et al. Conjugate point equatorial experiment (copex) campaign in brazil: Electrodynamics highlights on spread f development conditions and day-to-day variability. *Journal of Geophysical Research: Space Physics*, Wiley Online Library, v. 114, n. A4, 2009. Citado 5 vezes nas páginas 10, 35, 157, 164, and 172.

ABDU, M.; BITTENCOURT, J.; BATISTA, I. Magnetic declination control of the equatorial f region dynamo electric field development and spread f. *Journal of Geophysical Research: Space Physics*, Wiley Online Library, v. 86, n. A13, p. 11443–11446, 1981. Citado na página 170.

ABDU, M. et al. Magnetospheric disturbance effects on the equatorial ionization anomaly (eia): An overview. *Journal of Atmospheric and Terrestrial Physics*, Elsevier, v. 53, n. 8, p. 757–771, 1991. Citado 5 vezes nas páginas 3, 38, 60, 87, and 179.

ABDU, M. A. Equatorial ionosphere–thermosphere system: Electrodynamics and irregularities. *Advances in Space Research*, Elsevier, v. 35, n. 5, p. 771–787, 2005. Citado na página 170.

ABDU, M. A. Day-to-day and short-term variabilities in the equatorial plasma bubble/spread f irregularity seeding and development. *Progress in Earth and Planetary Science*, SpringerOpen, v. 6, n. 1, p. 1–22, 2019. Citado na página 86.

ABDU, M. A. et al. Equatorial ionospheric electric fields during magnetospheric disturbances: local time/longitude dependences from recent eits campaigns. *Journal of Atmospheric and Terrestrial Physics*, Elsevier, v. 57, n. 10, p. 1065–1083, 1995. Citado 8 vezes nas páginas 10, 30, 31, 62, 86, 104, 135, and 136.

ABDU, M. A.; BRUM, C. G. M. Electrodynamics of the vertical coupling processes in the atmosphere-ionosphere system of the low latitude region. *Earth, planets and space*, Springer, v. 61, p. 385–395, 2009. Citado na página 3.

ABDU, M. A. et al. Ionospheric responses to the october 2003 superstorm: Longitude/local time effects over equatorial low and middle latitudes. *Journal of Geophysical Research: Space Physics*, Wiley Online Library, v. 112, n. A10, 2007. Citado 4 vezes nas páginas 35, 41, 54, and 59.

ABDU, M. A. et al. Abnormal evening vertical plasma drift and effects on esf and eia over brazil-south atlantic sector during the 30 october 2003 superstorm. *Journal of Geophysical Research: Space Physics*, Wiley Online Library, v. 113, n. A7, 2008. Citado na página 94.

ADEBIYI, S.; ADIMULA, I.; OLADIPO, O. Investigation on mid-latitude stations to storm-time variations of gps-tec. *Advances in Space Research*, Elsevier BV, v. 55, n. 5, p. 1339–1348, mar. 2015. ISSN 0273-1177. Disponível em: <http://dx.doi.org/10.1016/j.asr.2014.11.030>. Citado na página 76.

ADHIKARI, B. Hildcaa-related effects recorded in middle low latitude magnetometers. *InstitutoNacional de PesquisasEspaciais, Sao Jose dos Campos, Brasil*, 2015. Citado na página 30.

ADHIKARI, B. et al. Study of interplanetary parameters, polar cap potential, and polar cap index during quiet event and high intensity long duration continuous ae activities (hildcaas). *Russian Journal of Earth Sciences*, v. 18, n. 1, p. 1–10, 2018. Citado na página 36.

AHN, B.-H.; MOON, G.-H. Seasonal and universal time variations of the au, al and dst indices. *Journal of The Korean Astronomical Society, vol. 36, issue spc1, pp. 93-99*, v. 36, p. 93–99, 2003. Citado na página 130.

AKASOFU, S.-I. A historical review of the geomagnetic storm-producing plasma flows from the sun. *Space science reviews*, Springer, v. 164, p. 85–132, 2011. Citado na página 21.

AKASOFU, S.-I.; CHAPMAN, S. The development of the main phase of magnetic storms. *Journal of Geophysical Research*, Wiley Online Library, v. 68, n. 1, p. 125–129, 1963. Citado na página 25.

ALEXEEV, I. The penetration of interplanetary magnetic and electric fields into the magnetosphere. *Journal of geomagnetism and geoelectricity*, Society of Geomagnetism and

Earth, Planetary and Space Sciences, v. 38, n. 11, p. 1199–1221, 1986. Citado 2 vezes nas páginas 22 and 34.

ALFVÉN, H. Existence of electromagnetic-hydrodynamic waves. *Nature*, Nature Publishing Group UK London, v. 150, n. 3805, p. 405–406, 1942. Citado 3 vezes nas páginas 28, 29, and 30.

ALFVÉN, H. Electric currents in cosmic plasmas. *Reviews of Geophysics*, Wiley Online Library, v. 15, n. 3, p. 271–284, 1977. Citado 2 vezes nas páginas 28 and 29.

ALLEN, J. S. Gps. *GIS Methodologies for Developing Conservation Strategies: Tropical Forest Recovery and Willdlife Management in Costa Rica*, Columbia University Press, p. 61–80, 1998. Citado na página 73.

ALLIS, W. P. Motions of ions and electrons. Massachusetts Institute of Technology, Research Laboratory of Electronics, 1956. Citado na página 48.

ANTONOVA, E. et al. Structure of magnetospheric current systems and mapping of high latitude magnetospheric regions to the ionosphere. *Journal of Atmospheric and Solar-Terrestrial Physics*, Elsevier, v. 177, p. 103–114, 2018. Citado na página 21.

APPLETON, E. V. Two anomalies in the ionosphere. *Nature*, Nature Publishing Group UK London, v. 157, n. 3995, p. 691–691, 1946. Citado na página 39.

ASTAFYEVA, E. Effects of strong imf b z southward events on the equatorial and mid-latitude ionosphere. In: COPERNICUS GMBH. *Annales Geophysicae*. [S.l.], 2009. v. 27, n. 3, p. 1175–1187. Citado na página 136.

BAGIYA, M. S. et al. Tec variations during low solar activity period (2005–2007) near the equatorial ionospheric anomaly crest region in india. In: COPERNICUS GMBH. *Annales Geophysicae*. [S.l.], 2009. v. 27, n. 3, p. 1047–1057. Citado 2 vezes nas páginas 114 and 154.

BAKARE, N.; CHUKWUMA, V. Relationship between dst and solar wind conditions during intense geomagnetic storms. *94.30. Lr; 94.30. vf*, CSIR, 2010. Citado na página 159.

BAKER, D. N. et al. Disturbed space environment may have been related to pager satellite failure. *Eos, Transactions American Geophysical Union*, American Geophysical Union (AGU), v. 79, n. 40, p. 477–483, out. 1998. ISSN 2324-9250. Disponível em: <http://dx.doi.org/10.1029/98EO00359>. Citado na página 36.

BALAN, N.; LIU, L.; LE, H. A brief review of equatorial ionization anomaly and ionospheric irregularities. *Earth and Planetary Physics*, Wiley Online Library, v. 2, n. 4, p. 257–275, 2018. Citado na página 62.

BALOGH, A. et al. The solar origin of corotating interaction regions and their formation in the inner heliosphere. *Space Science Reviews*, Springer, v. 89, p. 141–178, 1999. Citado na página 12.

BANKS, P. M.; KOCKARTS, G. *Aeronomy*. [S.l.]: Elsevier, 2013. Citado 3 vezes nas páginas 39, 46, and 49.

BARGATZE, L.; MCPHERRON, R.; BAKER, D. Solar wind/magnetosphere energy input functions. *Solar wind magnetosphere coupling*, v. 126, p. 101, 1986. Citado 2 vezes nas páginas 11 and 99.

BASU, S. et al. Day-to-day variability of the equatorial ionization anomaly and scintillations at dusk observed by guvi and modeling by sami3. *Journal of Geophysical Research: Space Physics*, Wiley Online Library, v. 114, n. A4, 2009. Citado na página 59.

BASU, S. et al. Scintillations, plasma drifts, and neutral winds in the equatorial ionosphere after sunset. *Journal of Geophysical Research: Space Physics*, Wiley Online Library, v. 101, n. A12, p. 26795–26809, 1996. Citado na página 172.

BATISTA, I. S. et al. Unusual early morning development of the equatorial anomaly in the brazilian sector during the halloween magnetic storm. *Journal of Geophysical Research: Space Physics*, Wiley Online Library, v. 111, n. A5, 2006. Citado 8 vezes nas páginas 3, 10, 14, 84, 89, 94, 101, and 134.

BATISTA, I. S. et al. Ionospheric effects of the march 13, 1989, magnetic storm at low and equatorial latitudes. *Journal of Geophysical Research: Space Physics*, Wiley Online Library, v. 96, n. A8, p. 13943–13952, 1991. Citado na página 136.

BAUMJOHANN, W. et al. Current systems in planetary magnetospheres and ionospheres. *Space science reviews*, Springer, v. 152, p. 99–134, 2010. Citado na página 22.

BELCHER, J.; JR, L. D. Large-amplitude alfvén waves in the interplanetary medium, 2. *Journal of Geophysical Research*, Wiley Online Library, v. 76, n. 16, p. 3534–3563, 1971. Citado 2 vezes nas páginas 35 and 109.

BERTONI, F. *Derivas ionosféricas em latitudes equatoriais: observaçoes e modelagem*. Tese (Doutorado) — Ph. D. thesis, Instituto Nacional de Pesquisas Espaciais, 2004. Citado na página 68.

BERTONI, H. L. *Radio propagation for modern wireless systems*. [S.l.]: Pearson Education, 1999. Citado na página 54.

BHARGAVA, S.; BHARGAVA, S. K. *Textbook of color doppler imaging*. [S.l.]: Jaypee Brothers Medical Publishers, 2019. Citado na página 71.

BHATTACHARYYA, A. Equatorial plasma bubbles: A review. *Atmosphere*, MDPI, v. 13, n. 10, p. 1637, 2022. Citado na página 89.

BIESECKER, D. et al. Sungrazing comets discovered with the soho/lasco coronagraphs 1996–1998. *Icarus*, Elsevier, v. 157, n. 2, p. 323–348, 2002. Citado na página 16.

BLANC, M.; RICHMOND, A. The ionospheric disturbance dynamo. *Journal of Geophysical Research: Space Physics*, Wiley Online Library, v. 85, n. A4, p. 1669–1686, 1980. Citado 10 vezes nas páginas 3, 31, 33, 35, 38, 62, 135, 136, 163, and 171.

BOHM-VITENSE, E. Chromospheres, transition regions, and cornas. *Science*, American Association for the Advancement of Science, v. 223, p. 777–785, 1984. Citado na página 8.

BOOKER, H.; WELLS, H. Scattering of radio waves by the f-region of the ionosphere. *Terrestrial Magnetism and Atmospheric Electricity*, Wiley Online Library, v. 43, n. 3, p. 249–256, 1938. Citado na página 62.

BOROVSKY, J. E.; DENTON, M. H. Differences between cme-driven storms and cir-driven storms. *Journal of Geophysical Research: Space Physics*, Wiley Online Library, v. 111, n. A7, 2006. Citado 4 vezes nas páginas 11, 13, 15, and 36.

BOTHMER, V.; SCHWENN, R. The structure and origin of magnetic clouds in the solar wind. In: SPRINGER. *Annales Geophysicae*. [S.l.], 1997. v. 16, n. 1, p. 1–24. Citado na página 19.

BRANDT, J. C. On the study of comet tails and models of the interplanetary medium. *Astrophysical Journal, vol. 133, p. 1091-1092*, v. 133, p. 1091–1092, 1961. Citado na página 13.

BUDDEN, K. G. *The propagation of radio waves: the theory of radio waves of low power in the ionosphere and magnetosphere*. [S.l.]: Cambridge University Press, 1988. Citado 2 vezes nas páginas 55 and 56.

BUONSANTO, M.; WITASSE, O. An updated climatology of thermospheric neutral winds and f region ion drifts above millstone hill. *Journal of Geophysical Research: Space Physics*, Wiley Online Library, v. 104, n. A11, p. 24675–24687, 1999. Citado na página 89.

BUONSANTO, M. J. Ionospheric storms—a review. *Space Science Reviews*, Springer, v. 88, n. 3, p. 563–601, 1999. Citado 2 vezes nas páginas 38 and 163.

BUONSANTO, M. J.; FOSTER, J. C. Effects of magnetospheric electric fields and neutral winds on the low-middle latitude ionosphere during the march 20-21, 1990, storm. *Journal of Geophysical Research: Space Physics*, American Geophysical Union (AGU), v. 98, n. A11, p. 19133–19140, nov. 1993. ISSN 0148-0227. Disponível em: <http://dx.doi.org/10.1029/93JA01807>. Citado na página 157.

BURESOVA, D. et al. Ionospheric disturbances under low solar activity conditions. *Advances in Space Research*, Elsevier, v. 54, n. 2, p. 185–196, 2014. Citado na página 27.

BURLAGA, L. F. Magnetic clouds and force-free fields with constant alpha. *Journal of Geophysical Research: Space Physics*, American Geophysical Union (AGU), v. 93, n. A7, p. 7217–7224, jul. 1988. ISSN 0148-0227. Disponível em: <http://dx.doi.org/10.1029/JA093iA07p07217>. Citado na página 19.

BURNS, A. et al. The ionospheric and thermospheric response to cmes: Challenges and successes. *Journal of atmospheric and solar-terrestrial physics*, Elsevier, v. 69, n. 1-2, p. 77–85, 2007. Citado na página 38.

BURTON, R. K.; MCPHERRON, R.; RUSSELL, C. An empirical relationship between interplanetary conditions and dst. *Journal of geophysical research*, Wiley Online Library, v. 80, n. 31, p. 4204–4214, 1975. Citado na página 25.

CALAIS, E.; MINSTER, J. B. Gps detection of ionospheric perturbations following a space shuttle ascent. *Geophysical Research Letters*, Wiley Online Library, v. 23, n. 15, p. 1897–1900, 1996. Citado 2 vezes nas páginas 72 and 74.

CAMPOS, M. D. A.; WANNINGER, L.; SEEBER, G. Condiçoes ionosféricas pertubadas e os sinais gps. In: EUROPEAN ASSOCIATION OF GEOSCIENTISTS & ENGINEERS. *3rd International Congress of the Brazilian Geophysical Society*. [S.l.], 1993. p. cp–324. Citado na página 72.

CAROVILLANO, R. L.; SISCOE, G. L. Energy and momentum theorems in magnetospheric processes. *Reviews of Geophysics*, Wiley Online Library, v. 11, n. 2, p. 289–353, 1973. Citado na página 24.

CARTER, B. A. et al. On the occurrence of equatorial f-region irregularities during solar minimum using radio occultation measurements. *Journal of Geophysical Research: Space Physics*, Wiley Online Library, v. 118, n. 2, p. 892–904, 2013. Citado na página 3.

CHAPMAN, N. R.; CHAPMAN, D. M. A coherent ray model of plane-wave reflection from a thin sediment layer. *The Journal of the Acoustical Society of America*, Acoustical Society of America, v. 94, n. 5, p. 2731–2738, 1993. Citado na página 55.

CHAPMAN, S. An outline of a theory of magnetic storms. *Proceedings of the Royal Society of London. Series A, Containing Papers of a Mathematical and Physical Character*, The Royal Society London, v. 95, n. 666, p. 61–83, 1918. Citado na página 26.

CHAPMAN, S. The normality of geomagnetic disturbance at huancayo. *Geofisica pura e applicata*, Springer, v. 19, p. 151–158, 1951. Citado na página 99.

CHEN, P. Coronal mass ejections: models and their observational basis. *Living Reviews in Solar Physics*, Springer, v. 8, n. 1, p. 1–92, 2011. Citado na página 16.

CHERNIAK, I.; ZAKHARENKOVA, I. New advantages of the combined gps and glonass observations for high-latitude ionospheric irregularities monitoring: case study of june 2015 geomagnetic storm. *Earth, Planets and Space*, Springer, v. 69, p. 1–14, 2017. Citado na página 166.

CHINGARANDI, F. et al. Assessing the effects of a minor cir-hss geomagnetic storm on the brazilian low-latitude ionosphere: Ground and space-based observations. *Space Weather*, Wiley Online Library, v. 21, n. 9, p. e2023SW003500, 2023. Citado 3 vezes nas páginas 76, 77, and 181.

CHITTA, L.; SMITHA, H.; SOLANKI, S. K. Solar photosphere. In: *Oxford Research Encyclopedia of Physics*. [S.l.: s.n.], 2020. Citado 2 vezes nas páginas 8 and 9.

COWLEY, S. A qualitative study of the reconnection between the earth's magnetic field and an interplanetary field of arbitrary orientation. *Radio Science*, Wiley Online Library, v. 8, n. 11, p. 903–913, 1973. Citado na página 9.

CRANMER, S. R. Coronal holes. *Living Reviews in Solar Physics*, Springer, v. 6, p. 1–66, 2009. Citado na página 15.

CYR, O. S. et al. Properties of coronal mass ejections: Soho lasco observations from january 1996 to june 1998. *Journal of Geophysical Research: Space Physics*, Wiley Online Library, v. 105, n. A8, p. 18169–18185, 2000. Citado na página 16.

DAGLIS, I. A. Ring current dynamics. *Space science reviews*, Springer, v. 124, p. 183–202, 2006. Citado na página 22.

DAGLIS, I. A. et al. The terrestrial ring current: Origin, formation, and decay. *Reviews of Geophysics*, Wiley Online Library, v. 37, n. 4, p. 407–438, 1999. Citado 2 vezes nas páginas 20 and 22.

DANILOV, A.; LASTOVICKA, J. Effects of geomagnetic storms on the ionosphere and atmosphere. *International Journal of geomagnetism and aeronomy*, Citeseer, v. 2, n. 3, p. 209–224, 2001. Citado na página 169.

DAS, A. K. The solar cycle and the associated behaviours of sunspots and prominences. Government Observatory, Madras, 1958. Citado na página 9.

DAVIES, K. *Ionospheric radio*. [S.l.]: IET, 1990. Citado 3 vezes nas páginas 19, 20, and 67.

DAVIS, T. N.; SUGIURA, M. Auroral electrojet activity index ae and its universal time variations. *Journal of Geophysical Research*, Wiley Online Library, v. 71, n. 3, p. 785–801, 1966. Citado na página 30.

DENARDINI, C. M. et al. Ionospheric responses during hildcaa events in the brazilian sector. *Annales Geophysicae*, v. 42, p. 45–53, 2021. Citado na página 135.

DENG, Z.-X. et al. Study on the ionospheric tec storms over china. *Chinese journal of geophysics*, Chinese Journal of Geophysics, v. 55, n. 07, p. 2177–2184, 2012. Citado na página 118.

DESSLER, A.; PARKER, E. N. Hydromagnetic theory of geomagnetic storms. *Journal of Geophysical Research*, Wiley Online Library, v. 64, n. 12, p. 2239–2252, 1959. Citado na página 24.

DEVRIESE, S. *A model for the evolution of slow coronal mass ejections up to 1 AU*. Tese (Doutorado) — MSc thesis, KU Leuven, 2011 (66pp), 2011. Citado na página 11.

DUNGEY, J. W. Interplanetary magnetic field and the auroral zones. *Physical Review Letters*, APS, v. 6, n. 2, p. 47, 1961. Citado 3 vezes nas páginas 12, 36, and 130.

ECHER, E. et al. High speed stream properties and related geomagnetic activity during the whole heliosphere interval (whi): 20 march to 16 april 2008. *Solar Physics*, Springer, v. 274, p. 303–320, 2011. Citado 6 vezes nas páginas 1, 14, 15, 28, 29, and 110.

ESSIEN, P. et al. Long-term study on medium-scale traveling ionospheric disturbances observed over the south american equatorial region. *Atmosphere*, MDPI, v. 12, n. 11, p. 1409, 2021. Citado na página 76.

EZEKOYE, B.; OBODO, R. The effects of solar radiations on telecommunications. The Pacific Journal of Science and Technology, 2007. Citado na página 61.

FARLEY, D. et al. The prereversal enhancement of the zonal electric field in the equatorial ionosphere. *Journal of Geophysical Research: Space Physics*, Wiley Online Library, v. 91, n. A12, p. 13723–13728, 1986. Citado na página 60.

FEDDER, J.; LYON, J. The solar wind-magnetosphere-ionosphere current-voltage relationship. *Geophysical Research Letters*, Wiley Online Library, v. 14, n. 8, p. 880–883, 1987. Citado 2 vezes nas páginas 37 and 38.

FEJER, B. G. Low latitude ionospheric electrodynamics. *Space Science Reviews*, Springer, v. 158, p. 145–166, 2011. Citado na página 118.

FEJER, B. G. et al. Dependence of equatorial f region vertical drifts on season and solar cycle. *Journal of Geophysical Research: Space Physics*, Wiley Online Library, v. 84, n. A10, p. 5792–5796, 1979. Citado na página 89.

FEJER, B. G.; LARSEN, M.; FARLEY, D. Equatorial disturbance dynamo electric fields. *Geophysical Research Letters*, Wiley Online Library, v. 10, n. 7, p. 537–540, 1983. Citado 2 vezes nas páginas 38 and 157.

FEJER, B. G. et al. Average vertical and zonal f region plasma drifts over jicamarca. *Journal of Geophysical Research: Space Physics*, Wiley Online Library, v. 96, n. A8, p. 13901–13906, 1991. Citado 2 vezes nas páginas 89 and 171.

FEJER, B. G. et al. Average vertical and zonal f region plasma drifts over jicamarca. *Journal of Geophysical Research: Space Physics*, American Geophysical Union (AGU), v. 96, n. A8, p. 13901–13906, ago. 1991. ISSN 0148-0227. Disponível em: <http://dx.doi.org/10.1029/91JA01171>. Citado na página 118.

FEJER, B. G.; SCHERLIESS, L. Time dependent response of equatorial ionospheric electric fields to magnetospheric disturbances. *Geophysical Research Letters*, Wiley Online Library, v. 22, n. 7, p. 851–854, 1995. Citado 2 vezes nas páginas 97 and 178.

FEJER, B. G.; SCHERLIESS, L. Empirical models of storm time equatorial zonal electric fields. *Journal of Geophysical Research: Space Physics*, Wiley Online Library, v. 102, n. A11, p. 24047–24056, 1997. Citado 10 vezes nas páginas 3, 32, 33, 77, 79, 84, 172, 178, 179, and 181.

FEJER, B. G.; SCHERLIESS, L.; PAULA, E. D. Effects of the vertical plasma drift velocity on the generation and evolution of equatorial spread f. *Journal of Geophysical Research: Space Physics*, Wiley Online Library, v. 104, n. A9, p. 19859–19869, 1999. Citado 2 vezes nas páginas 61 and 62.

FERNÁNDEZ, J. A. *Comets: Nature, Dynamics, Origin, and their Cosmogonical Relevance*. [S.l.]: Springer Science & Business Media, 2005. v. 328. Citado na página 13.

FOSTER, J. C. Ionospheric signatures of magnetospheric convection. *Journal of Geophysical Research: Space Physics*, Wiley Online Library, v. 89, n. A2, p. 855–865, 1984. Citado na página 38.

FULLER-ROWELL, T. et al. *Ionospheric Space Weather: Longitude Dependence and Lower Atmosphere Forcing*. [S.l.]: John Wiley & Sons, 2016. v. 220. Citado na página 137.

GAGNEPAIN, J.; CROCHET, M.; RICHMOND, A. D. Comparison of equatorial electrojet models. *Journal of Atmospheric and Terrestrial Physics*, Elsevier, v. 39, n. 9-10, p. 1119–1124, 1977. Citado na página 47.

GANUSHKINA, N. Y.; LIEMOHN, M.; DUBYAGIN, S. Current systems in the earth's magnetosphere. *Reviews of Geophysics*, Wiley Online Library, v. 56, n. 2, p. 309–332, 2018. Citado na página 20.

GOMBOSI, T. I. *Physics of the space environment*. [S.l.]: Cambridge University Press, 1998. Citado na página 22.

GONÇALVES, E. M.; FERREIRA, R.; BATISTA, I. Estudo das tendências de longo termo dos parâmetros ionosféricos sobre a região brasileira: Cachoeira paulista. In: EAGE PUBLICATIONS BV. *10th International Congress of the Brazilian Geophysical Society*. [S.l.], 2007. p. cp–172. Citado na página 65.

GONZALEZ, W. et al. Extreme geomagnetic storms, recent gleissberg cycles and space era-superintense storms. *Journal of Atmospheric and Solar-Terrestrial Physics*, Elsevier, v. 73, n. 11-12, p. 1447–1453, 2011. Citado 4 vezes nas páginas 11, 12, 19, and 26.

GONZALEZ, W. et al. Magnetospheric energetics during hildcaas. *Recurrent magnetic storms: corotating solar wind*, v. 167, p. 175, 2006. Citado 5 vezes nas páginas 2, 21, 29, 45, and 110.

GONZALEZ, W. et al. What is a geomagnetic storm? *Journal of Geophysical Research: Space Physics*, Wiley Online Library, v. 99, n. A4, p. 5771–5792, 1994. Citado 13 vezes nas páginas 1, 2, 10, 12, 20, 23, 24, 25, 26, 34, 80, 84, and 110.

GONZALEZ, W.; MOZER, F. A quantitative model for the potential resulting from reconnection with an arbitrary interplanetary magnetic field. *Journal of Geophysical Research*, Wiley Online Library, v. 79, n. 28, p. 4186–4194, 1974. Citado 3 vezes nas páginas 28, 36, and 130.

GONZALEZ, W.; TSURUTANI, B.; GONZALEZ, A. C. de. Geomagnetic storms contrasted during solar maximum and near solar minimum. *Advances in Space Research*, Elsevier, v. 30, n. 10, p. 2301–2304, 2002. Citado 2 vezes nas páginas 11 and 25.

GONZALEZ, W. D.; TSURUTANI, B. T. Criteria of interplanetary parameters causing intense magnetic storms (dst<- 100 nt). *Planetary and Space Science*, Elsevier, v. 35, n. 9, p. 1101–1109, 1987. Citado 14 vezes nas páginas 1, 2, 14, 15, 25, 28, 29, 30, 32, 83, 85, 99, 110, and 172.

GONZALEZ, W. D.; TSURUTANI, B. T.; GONZALEZ, A. L. Clúa de. Interplanetary origin of geomagnetic storms. *Space Science Reviews*, Springer, v. 88, n. 3-4, p. 529–562, 1999. Citado 4 vezes nas páginas 1, 3, 11, and 12.

GOOD, S. et al. Turbulence properties of interplanetary coronal mass ejections in the inner heliosphere: Dependence on proton beta and flux rope structure. *The Astrophysical Journal Letters*, IOP Publishing, v. 956, n. 1, p. L30, 2023. Citado na página 18.

GOPALSWAMY, N. The cme link to geomagnetic storms. *Proceedings of the International Astronomical Union*, Cambridge University Press, v. 5, n. S264, p. 326–335, 2009. Citado 3 vezes nas páginas 14, 16, and 19.

GOPALSWAMY, N. et al. The relationship between the expansion speed and radial speed of cmes confirmed using quadrature observations of the 2011 february 15 cme. *arXiv preprint arXiv:1205.0744*, 2012. Citado na página 16.

GOPALSWAMY, N. et al. Variability of solar eruptions during cycle 23. *Advances in Space Research*, Elsevier, v. 34, n. 2, p. 391–396, 2004. Citado 2 vezes nas páginas 11 and 14.

GOSLING, J. et al. Geomagnetic activity associated with earth passage of interplanetary shock disturbances and coronal mass ejections. *Journal of Geophysical Research: Space Physics*, Wiley Online Library, v. 96, n. A5, p. 7831–7839, 1991. Citado 3 vezes nas páginas 12, 17, and 18.

GOSLING, J. T. et al. Geomagnetic activity associated with earth passage of interplanetary shock disturbances and coronal mass ejections. *Journal of Geophysical Research: Space Physics*, American Geophysical Union (AGU), v. 96, n. A5, p. 7831–7839, maio 1991. ISSN 0148-0227. Disponível em: <http://dx.doi.org/10.1029/91JA00316>. Citado na página 18.

GRECHNEV, V.; KUZMENKO, I. A geoeffective cme caused by the eruption of a quiescent prominence on 29 september 2013. *Solar Physics*, Springer, v. 295, n. 4, p. 55, 2020. Citado na página 16.

GREEN, L. M. et al. The origin, early evolution and predictability of solar eruptions. *Space Science Reviews*, Springer, v. 214, p. 1–52, 2018. Citado na página 17.

GUARNIERI, F. The nature of auroras during high-intensity long-duration continuous ae activity (hildcaa) events: 1998 to 2001. *Recurrent Magnetic Storms: Corotating Solar Wind*, v. 167, p. 235, 2006. Citado 2 vezes nas páginas 29 and 30.

GUARNIERI, F. L. et al. Icme and cir storms with particular emphasis on hildcaa events. In: *ILWS Workshop*. [S.l.: s.n.], 2006. p. 19–20. Citado 5 vezes nas páginas 101, 102, 103, 111, and 164.

GUO, J. et al. Alfvén waves as a solar-interplanetary driver of the thermospheric disturbances. *Scientific reports*, Nature Publishing Group UK London, v. 6, n. 1, p. 18895, 2016. Citado na página 28.

HAJRA, R. et al. Solar cycle dependence of high-intensity long-duration continuous ae activity (hildcaa) events, relativistic electron predictors? *Journal of Geophysical Research: Space Physics*, Wiley Online Library, v. 118, n. 9, p. 5626–5638, 2013. Citado 8 vezes nas páginas 28, 29, 30, 102, 115, 117, 181, and 185.

HAJRA, R. et al. Solar wind-magnetosphere energy coupling efficiency and partitioning: Hildcaas and preceding cir storms during solar cycle 23. *Journal of Geophysical Research: Space Physics*, Wiley Online Library, v. 119, n. 4, p. 2675–2690, 2014. Citado 3 vezes nas páginas 14, 129, and 130.

HALE, G. E. The law of sun-spot polarity. *Proceedings of the National Academy of Sciences*, National Acad Sciences, v. 10, n. 1, p. 53–55, 1924. Citado na página 9.

HARIDAS, M. M.; MANJU, G.; ARUNAMANI, T. Solar activity variations of equatorial spread f occurrence and sustenance during different seasons over indian longitudes: Empirical model and causative mechanisms. *Advances in Space Research*, Elsevier, v. 61, n. 10, p. 2585–2592, 2018. Citado na página 62.

HARRISON, R. et al. Coronal mass ejections in the heliosphere. *Advances in Space Research*, Elsevier BV, v. 45, n. 1, p. 1–9, jan. 2010. ISSN 0273-1177. Disponível em: <http://dx.doi.org/10.1016/j.asr.2009.09.013>. Citado na página 18.

HARTREE, D. The propagation of electromagnetic waves in a refracting medium in a magnetic field. In: CAMBRIDGE UNIVERSITY PRESS. *Mathematical Proceedings of the Cambridge Philosophical Society*. [S.l.], 1931. v. 27, n. 1, p. 143–162. Citado 2 vezes nas páginas 57 and 58.

HARVEY, J. W.; JR, N. R. S. Coronal holes and solar magnetic fields. *Space Science Reviews*, Springer, v. 23, n. 2, p. 139–158, 1979. Citado na página 15.

HASTINGS, D. A review of plasma interactions with spacecraft in low earth orbit. *Journal of Geophysical Research: Space Physics*, Wiley Online Library, v. 100, n. A8, p. 14457–14483, 1995. Citado na página 3.

HATHAWAY, D. H. The solar cycle. *Living reviews in solar physics*, Springer, v. 12, n. 1, p. 4, 2015. Citado 2 vezes nas páginas 9 and 10.

HEELIS, R. Electrodynamics in the low and middle latitude ionosphere: A tutorial. *Journal of Atmospheric and Solar-Terrestrial Physics*, Elsevier, v. 66, n. 10, p. 825–838, 2004. Citado 3 vezes nas páginas 43, 50, and 54.

HEELIS, R. et al. Electrical coupling of the e-and f-regions and its effect on f-region drifts and winds. *Planetary and Space Science*, Elsevier, v. 22, n. 5, p. 743–756, 1974. Citado 3 vezes nas páginas 52, 89, and 178.

HEELIS, R.; MAUTE, A. Challenges to understanding the earth's ionosphere and thermosphere. *Journal of Geophysical Research: Space Physics*, Wiley Online Library, v. 125, n. 7, p. e2019JA027497, 2020. Citado 2 vezes nas páginas 54 and 110.

HERMAN, J. R. Spread f and ionospheric f-region irregularities. *Reviews of Geophysics*, Wiley Online Library, v. 4, n. 2, p. 255–299, 1966. Citado na página 62.

HEWINS, I. M. et al. The evolution of coronal holes over three solar cycles using the mcintosh archive. *Solar Physics*, Springer, v. 295, p. 1–15, 2020. Citado na página 15.

HILL, R.; BOWHILL, S. Collision frequencies for use in the continuum momentum equations applied to the lower ionosphere. *Journal of Atmospheric and Terrestrial Physics*, Elsevier, v. 39, n. 7, p. 803–811, 1977. Citado na página 47.

HOLLING, C. S. Cross-scale morphology, geometry, and dynamics of ecosystems. *Ecological monographs*, Wiley Online Library, v. 62, n. 4, p. 447–502, 1992. Citado na página 61.

HUANG, C. Disturbance dynamo electric fields in response to geomagnetic storms occurring at different universal times. *Journal of Geophysical Research: Space Physics*, Wiley Online Library, v. 118, n. 1, p. 496–501, 2013. Citado na página 35.

HUANG, C. et al. *Storm-time penetration electric fields and their effects*. [S.l.]: Wiley Online Library, 2006. Citado 2 vezes nas páginas 111 and 118.

HUANG, C.-S. et al. A strong positive phase of ionospheric storms observed by the millstone hill incoherent scatter radar and global gps network. *Journal of Geophysical Research: Space Physics*, Wiley Online Library, v. 110, n. A6, 2005. Citado 3 vezes nas páginas 134, 173, and 174.

HUANG, C.-S.; FOSTER, J. C.; KELLEY, M. C. Long-duration penetration of the interplanetary electric field to the low-latitude ionosphere during the main phase of magnetic storms. *Journal of Geophysical Research: Space Physics*, Wiley Online Library, v. 110, n. A11, 2005. Citado 3 vezes nas páginas 32, 34, and 134.

HUANG, C.-S. et al. Penetration electric fields: Efficiency and characteristic time scale. *Journal of Atmospheric and Solar-Terrestrial Physics*, Elsevier, v. 69, n. 10-11, p. 1135–1146, 2007. Citado 2 vezes nas páginas 34 and 174.

HUNDHAUSEN, A. Composition and dynamics of the solar wind plasma. *Reviews of Geophysics*, Wiley Online Library, v. 8, n. 4, p. 729–811, 1970. Citado na página 14.

III, J. M. R.; MLYNCZAK, M. G.; GORDLEY, L. L. Overview of the sounding of the atmosphere using broadband emission radiometry (saber) experiment for the thermosphere-ionsphere-mesosphere energetics and dynamics (timed) mission. *Optical* *spectroscopic techniques and instrumentation for atmospheric and space research*, SPIE, v. 2266, p. 406–415, 1994. Citado 2 vezes nas páginas 112 and 129.

IUCCI, N. et al. A compilation of geomagnetic sudden commencements (sscs)-their origin and the associated interplanetary disturbances and cosmic ray variations (1966/1974). *Astronomy and Astrophysics Supplement Series*, v. 72, p. 369–371, 1988. Citado na página 11.

IWAI, K. et al. Pressure change accompanying alfvén waves in a liquid metal. *Magnetohydrodynamics*, v. 39, n. 3, p. 245–250, 2003. Citado na página 30.

IYEMORI, T. Storm-time magnetospheric currents inferred from mid-latitude geomagnetic field variations. *Journal of geomagnetism and geoelectricity*, Society of Geomagnetism and Earth, Planetary and Space Sciences, v. 42, n. 11, p. 1249–1265, 1990. Citado na página 24.

JACKSON, B. et al. A heliospheric imager for deep space: lessons learned from helios, smei, and stereo. *Solar Physics*, Springer, v. 265, p. 257–275, 2010. Citado na página 18.

JACOBS, J. A. *Geomagnetism: Volume 4*. [S.l.]: Elsevier, 2016. v. 4. Citado na página 23.

JACOBSEN, K. S.; ANDALSVIK, Y. L. Overview of the 2015 st. patrick's day storm and its consequences for rtk and ppp positioning in norway. *Journal of Space Weather and Space Climate*, EDP Sciences, v. 6, p. A9, 2016. Citado na página 166.

JAGGI, R. K.; WOLF, R. Self-consistent calculation of the motion of a sheet of ions in the magnetosphere. *Journal of Geophysical Research*, Wiley Online Library, v. 78, n. 16, p. 2852–2866, 1973. Citado 2 vezes nas páginas 31 and 86.

JAKOWSKI, N. et al. Monitoring, tracking and forecasting ionospheric perturbations using gnss techniques. *Journal of Space Weather and Space Climate*, EDP Sciences, v. 2, p. A22, 2012. Citado na página 166.

JAKOWSKI, N. et al. Space weather effects detected by gps based tec monitoring. In: *Workshop on Space Weather, WPP-155, ESTEC, Noordwijk*. [S.l.: s.n.], 1999. p. 241–244. Citado na página 116.

JANKOVIČOVÁ, D. et al. Neural network-based nonlinear prediction of magnetic storms. *Journal of Atmospheric and Solar-Terrestrial Physics*, Elsevier, v. 64, n. 5-6, p. 651–656, 2002. Citado 2 vezes nas páginas 105 and 110.

JAYACHANDRAN, P. et al. Effect of equatorial ionization anomaly on the occurrence of spread-f. In: SPRINGER. *Annales Geophysicae*. [S.l.], 1997. v. 15, p. 255–262. Citado na página 136.

JIAN, L. et al. Properties of interplanetary coronal mass ejections at one au during 1995–2004. *Solar Physics*, Springer, v. 239, p. 393–436, 2006. Citado na página 12.

JR, G. N. Structure of the solar corona. *Annual Review of Astronomy and Astrophysics*, Annual Reviews 4139 El Camino Way, PO Box 10139, Palo Alto, CA 94303-0139, USA, v. 5, n. 1, p. 213–266, 1967. Citado na página 8.

KAMIDE, Y.; CHIAN, A. *Handbook of the solar-terrestrial environment*. [S.l.]: Springer, 2007. Citado na página 20.

KAMIDE, Y. et al. Two-step development of geomagnetic storms. *Journal of Geophysical Research: Space Physics*, Wiley Online Library, v. 103, n. A4, p. 6917–6921, 1998. Citado 4 vezes nas páginas 18, 105, 109, and 110.

KAN, J.; LEE, L. Energy coupling function and solar wind-magnetosphere dynamo. *Geophysical Research Letters*, Wiley Online Library, v. 6, n. 7, p. 577–580, 1979. Citado na página 136.

KANE, R. Longitudinal spread of equatorial sq variability. *Journal of Atmospheric and Terrestrial Physics*, Elsevier, v. 34, n. 8, p. 1425–1430, 1972. Citado na página 27.

KELLEY, M. Ionospheric radio. *Peter Peregrinus Ltd., London*, 1989. Citado na página 171.

KELLEY, M.; FEJER, B. G.; GONZALES, C. An explanation for anomalous equatorial ionospheric electric fields associated with a northward turning of the interplanetary magnetic field. *Geophysical Research Letters*, Wiley Online Library, v. 6, n. 4, p. 301–304, 1979. Citado 2 vezes nas páginas 32 and 62.

KELLEY, M. C. *The Earth's ionosphere: Plasma physics and electrodynamics*. [S.l.]: Academic press, 2009. Citado 15 vezes nas páginas 10, 21, 31, 32, 41, 44, 45, 48, 51, 54, 55, 86, 87, 135, and 163.

KELLEY, M. C. et al. Penetration of the solar wind electric field into the magnetosphere/ionosphere system. *Geophysical Research Letters*, Wiley Online Library, v. 30, n. 4, 2003. Citado 3 vezes nas páginas 3, 34, and 134.

KELLY, M. *The Earth's ionosphere: Plasma physics and electrodynamics*. [S.l.]: Elsevier, 2012. v. 43. Citado 3 vezes nas páginas 39, 41, and 60.

KIL, H. et al. O and n2 disturbances in the f region during the 20 november 2003 storm seen from timed/guvi. *Journal of Geophysical Research: Space Physics*, Wiley Online Library, v. 116, n. A2, 2011. Citado na página 9.

KILPUA, E. et al. Geoeffective properties of solar transients and stream interaction regions. *Space Science Reviews*, Springer, v. 212, n. 3-4, p. 1271–1314, 2017. Citado 2 vezes nas páginas 12 and 18.

KIVELSON, M. G.; RUSSELL, C. T. *Introduction to space physics*. [S.l.]: Cambridge university press, 1995. Citado na página 129.

KLAUSNER, V. et al. Principal component analysis in the modeling of hildcaas during the solar minimum of cycle 23/24. *Journal of Atmospheric and Solar-Terrestrial Physics*, Elsevier BV, v. 213, p. 105516, fev. 2021. ISSN 1364-6826. Disponível em: <http://dx.doi.org/10.1016/j.jastp.2020.105516>. Citado 5 vezes nas páginas 2, 14, 15, 28, and 29.

KLAUSNER, V. et al. An alternative way to identify local geomagnetically quiet days: a case study using wavelet analysis. In: COPERNICUS PUBLICATIONS GÖTTINGEN, GERMANY. *Annales Geophysicae*. [S.l.], 2016. v. 34, n. 4, p. 451–462. Citado na página 129.

KOGA, D. et al. Electrodynamic coupling processes between the magnetosphere and the equatorial ionosphere during a 5-day hildcaa event. *Journal of atmospheric and solar-terrestrial physics*, Elsevier, v. 73, n. 1, p. 148–155, 2011. Citado 5 vezes nas páginas 29, 77, 83, 85, and 178.

KOSTER, J. Some measurements of the irregularities giving rise to radio-star scintillations at the equator. *Journal of Geophysical Research*, Wiley Online Library, v. 68, n. 9, p. 2579–2590, 1963. Citado na página 61.

KOSUGI, T.; ISHIGURO, M.; SHIBASAKI, K. Polar-cap and coronal-hole-associated brightenings of the sun at millimeter wavelengths. *Astronomical Society of Japan, Publications (ISSN 0004-6264), vol. 38, no. 1, 1986, p. 1-11.*, v. 38, p. 1–11, 1986. Citado na página 15.

KOTADIA, K. Variations in critical frequency of the f2-layer of the ionosphere associated with geomagnetic storms at equatorial stations. *Journal of Atmospheric and Terrestrial Physics*, Elsevier, v. 27, n. 6, p. 723–733, 1965. Citado na página 136.

KOTULAK, K. et al. Climatology characteristics of ionospheric irregularities described with gnss roti. *Remote Sensing*, MDPI, v. 12, n. 16, p. 2634, 2020. Citado na página 167.

KOUBA, D.; KNÍŽOVÁ, P. K. Analysis of digisonde drift measurements quality. *Journal of atmospheric and solar-terrestrial physics*, Elsevier, v. 90, p. 212–221, 2012. Citado na página 67.

KOZYRA, J. et al. Response of the upper/middle atmosphere to coronal holes and powerful high-speed solar wind streams in 2003. *Recurrent Magnetic Storms: Corotating Solar Wind*, v. 167, p. 319, 2006. Citado na página 29.

KOZYRA, J. U.; LIEMOHN, M. W. Ring current energy input and decay. *Magnetospheric Imaging—the Image Prime Mission*, Springer, p. 105–131, 2003. Citado 2 vezes nas páginas 3 and 22.

KRIEGER, A.; TIMOTHY, A.; ROELOF, E. A coronal hole and its identification as the source of a high velocity solar wind stream. *Solar Physics*, Springer, v. 29, p. 505–525, 1973. Citado na página 17.

KUMAR, A.; RUST, D. M. Interplanetary magnetic clouds, helicity conservation, and current-core flux-ropes. *Journal of Geophysical Research: Space Physics*, American Geophysical Union (AGU), v. 101, n. A7, p. 15667–15684, jul. 1996. ISSN 0148-0227. Disponível em: <http://dx.doi.org/10.1029/96JA00544>. Citado na página 19.

LAKHINA, G. et al. Supermagnetic storms: Hazard to society. *Extreme events and natural hazards: The complexity perspective*, American Geophysical Union Washington, DC, v. 196, p. 267–278, 2012. Citado na página 23.

LAKHINA, G. S.; TSURUTANI, B. T. Geomagnetic storms: historical perspective to modern view. *Geoscience Letters*, Springer, v. 3, p. 1–11, 2016. Citado 2 vezes nas páginas 23 and 25.

LAMONT, J. von. *Handbuch des Magnetismus*. [S.l.]: Voss, 1866. v. 15. Citado na página 23.

LANG, K. R. *The Cambridge encyclopedia of the sun*. [S.l.: s.n.], 2001. Citado 2 vezes nas páginas 7 and 8.

LARIO, D.; ROELOF, E. Energetic particles during the first and third ulysses southern high-latitude excursions: Probing global corotating interaction region structure beyond 5 au. *Journal of Geophysical Research: Space Physics*, Wiley Online Library, v. 112, n. A9, 2007. Citado na página 12.

LEAN, J. L. Cycles and trends in solar irradiance and climate. *Wiley interdisciplinary reviews: climate change*, Wiley Online Library, v. 1, n. 1, p. 111–122, 2010. Citado na página 9.

LEE, W. K. et al. The effect of geomagnetic-storm-induced enhancements to ionospheric emissions on the interpretation of the timed/guvi o/n2 ratio. *Journal of Geophysical Research: Space Physics*, Wiley Online Library, v. 118, n. 12, p. 7834–7840, 2013. Citado na página 137.

LI, K.-F. et al. The 11 year solar cycle response of the equatorial ionization anomaly observed by gps radio occultation. *Journal of Geophysical Research: Space Physics*, Wiley Online Library, v. 123, n. 1, p. 848–861, 2018. Citado na página 39.

LIDDLE, A. R.; LYTH, D. H. *Cosmological inflation and large-scale structure*. [S.l.]: Cambridge university press, 2000. Citado na página 61.

LIU, J. et al. Temporal variation of solar wind in controlling solar wind-magnetosphere-ionosphere energy budget. *Journal of Geophysical Research: Space Physics*, American Geophysical Union (AGU), v. 123, n. 7, p. 5862–5869, jul. 2018. ISSN 2169-9402. Disponível em: <http://dx.doi.org/10.1029/2017JA025154>. Citado na página 174.

LIU, J. et al. A statistical study on the characteristics of ionospheric storms in the equatorial ionization anomaly region: Gps-tec observed over taiwan. *Journal of Geophysical Research: Space Physics*, Wiley Online Library, v. 118, n. 6, p. 3856–3865, 2013. Citado na página 77.

LIU, J.; ZHAO, B.; LIU, L. Time delay and duration of ionospheric total electron content responses to geomagnetic disturbances. In: COPERNICUS GMBH. *Annales Geophysicae*. [S.l.], 2010. v. 28, n. 3, p. 795–805. Citado na página 114.

LIU, L. et al. Solar activity effects of the ionosphere: A brief review. *Chinese Science Bulletin*, Springer, v. 56, p. 1202–1211, 2011. Citado 2 vezes nas páginas 33 and 59.

LIU, L. et al. Case study on total electron content enhancements at low latitudes during low geomagnetic activities before the storms. In: COPERNICUS GMBH. *Annales Geophysicae*. [S.l.], 2008. v. 26, n. 4, p. 893–903. Citado na página 157.

LIU, Y. et al. Analyzing ionosphere tec and roti responses on 2010 august high speed solar winds. *IEEE Access*, IEEE, v. 7, p. 29788–29804, 2019. Citado 3 vezes nas páginas 36, 39, and 171.

LOW, B. Coronal mass ejections, magnetic flux ropes, and solar magnetism. *Journal of Geophysical Research: Space Physics*, Wiley Online Library, v. 106, n. A11, p. 25141–25163, 2001. Citado na página 16.

LUGAZ, N. Eruptive prominences and their impact on the earth and our life. *Solar prominences*, Springer, p. 433–453, 2015. Citado na página 16.

LYON, J. G. The solar wind-magnetosphere-ionosphere system. *Science*, American Association for the Advancement of Science, v. 288, n. 5473, p. 1987–1991, 2000. Citado 3 vezes nas páginas 36, 38, and 74.

MA, J. et al. Nonlinear wave–wave coupling related to whistler-mode and electron bernstein waves observed by the parker solar probe. *The Astrophysical Journal*, IOP Publishing, v. 918, n. 1, p. 26, 2021. Citado na página 109.

MAKAROV, V.; SIVARAMAN, K. New results concerning the global solar cycle. *Solar physics*, Springer, v. 123, p. 367–380, 1989. Citado na página 9.

MANN, I.; O'BRIEN, T.; MILLING, D. Correlations between ulf wave power, solar wind speed, and relativistic electron flux in the magnetosphere: Solar cycle dependence. *Journal of Atmospheric and Solar-Terrestrial Physics*, Elsevier, v. 66, n. 2, p. 187–198, 2004. Citado na página 11.

MANNUCCI, A. et al. Interplanetary magnetic field by control of prompt total electron content increases during superstorms. *Journal of Atmospheric and Solar-Terrestrial Physics*, Elsevier, v. 115, p. 7–16, 2014. Citado na página 154.

MANNUCCI, A. et al. Superposed epoch analysis of the dayside ionospheric response to four intense geomagnetic storms: Large geomagnetic storms. *Journal of geophysical research*, v. 114, n. A3, 2009. Citado 2 vezes nas páginas 123 and 134.

MANOJ, C. et al. Penetration characteristics of the interplanetary electric field to the daytime equatorial ionosphere. *Journal of Geophysical Research: Space Physics*, Wiley Online Library, v. 113, n. A12, 2008. Citado na página 111.

MARIČIĆ, D. et al. Sun-to-earth observations and characteristics of isolated earth-impacting interplanetary coronal mass ejections during 2008–2014. *Solar physics*, Springer, v. 295, n. 7, p. 91, 2020. Citado na página 10.

MAROV, M. Y.; MAROV, M. Y. The sun and heliosphere. *The Fundamentals of Modern Astrophysics: A Survey of the Cosmos from the Home Planet to Space Frontiers*, Springer, p. 157–175, 2015. Citado na página 8.

MARTINIS, C.; MENDILLO, M.; AARONS, J. Toward a synthesis of equatorial spread f onset and suppression during geomagnetic storms. *Journal of Geophysical Research: Space Physics*, Wiley Online Library, v. 110, n. A7, 2005. Citado na página 61.

MARUYAMA, N. et al. Interaction between direct penetration and disturbance dynamo electric fields in the storm-time equatorial ionosphere. *Geophysical Research Letters*, Wiley Online Library, v. 32, n. 17, 2005. Citado na página 175.

MENDILLO, M. Storms in the ionosphere: Patterns and processes for total electron content. *Reviews of Geophysics*, Wiley Online Library, v. 44, n. 4, 2006. Citado 3 vezes nas páginas 116, 136, and 154.

MENVIELLE, M.; BERTHELIER, A. The k-derived planetary indices: Description and availability. *Reviews of Geophysics*, Wiley Online Library, v. 29, n. 3, p. 415–432, 1991. Citado na página 23.

MIKIĆ, Z.; LEE, M. An introduction to theory and models of cmes, shocks, and solar energetic particles. *Space Science Reviews*, Springer, v. 123, n. 1, p. 57–80, 2006. Citado na página 16.

MOORE, R.; RABIN, D. Sunspots. *IN: Annual review of astronomy and astrophysics. Volume 23 (A86-14507 04-90). Palo Alto, CA, Annual Reviews, Inc., 1985, p. 239-266. Research supported by the US National Research Council and NASA.*, v. 23, p. 239–266, 1985. Citado na página 9.

MOUIKIS, C. G. et al. The storm-time ring current response to icmes and cirs using van allen probe observations. *Journal of Geophysical Research: Space Physics*, Wiley Online Library, v. 124, n. 11, p. 9017–9039, 2019. Citado na página 11.

MUKHTAROV, P.; ANDONOV, B.; PANCHEVA, D. Empirical model of tec response to geomagnetic and solar forcing over balkan peninsula. *Journal of Atmospheric and Solar-Terrestrial Physics*, Elsevier, v. 167, p. 80–95, 2018. Citado na página 154.

NANDY, D. et al. Causality in heliophysics: magnetic fields as a bridge between the sun's interior and the earth's space environment. *Journal of Atmospheric and Solar-Terrestrial Physics*, Elsevier, p. 106081, 2023. Citado na página 8.

NEGRETI, P. M. de S.; PAULA, E. R. de; CANDIDO, C. M. N. Total electron content responses to hildcaas and geomagnetic storms over south america. In: COPERNICUS GMBH. *Annales Geophysicae*. [S.l.], 2017. v. 35, n. 6, p. 1309–1326. Citado 3 vezes nas páginas 32, 111, and 135.

NEWELL, P.; SOTIRELIS, T.; WING, S. Diffuse, monoenergetic, and broadband aurora: The global precipitation budget. *Journal of Geophysical Research: Space Physics*, Wiley Online Library, v. 114, n. A9, 2009. Citado na página 46.

NIEVES-CHINCHILLA, T. et al. Understanding the internal magnetic field configurations of icmes using more than 20 years of wind observations. *Solar Physics*, Springer, v. 293, p. 1–31, 2018. Citado na página 18.

NISHIDA, A. Coherence of geomagnetic dp 2 fluctuations with interplanetary magnetic variations. *Journal of Geophysical Research*, Wiley Online Library, v. 73, n. 17, p. 5549–5559, 1968. Citado na página 31.

NěMEčEK, Z. et al. (non)radial solar wind propagation through the heliosphere. *The Astrophysical Journal Letters*, American Astronomical Society, v. 897, n. 2, p. L39, jul. 2020. ISSN 2041-8213. Disponível em: <http://dx.doi.org/10.3847/2041-8213/ab9ff7>. Citado na página 35.

PANDA, S. K.; GEDAM, S. S.; JIN, S. Ionospheric tec variations at low latitude indian region. *Satellite Positioning-Methods, Models and Applications. Tech-Publisher, Rijeka, Croatia*, p. 149–174, 2015. Citado na página 59.

PARKER, E. Interaction of the solar wind with the geomagnetic field. *The Physics of Fluids*, AIP Publishing, v. 1, n. 3, p. 171–187, 1958. Citado na página 13.

PARKS, G. K. *Physics of space plasmas: an introduction*. [S.l.]: CRC Press, 2019. Citado 2 vezes nas páginas 28 and 29.

PEDATELLA, N.; FORBES, J. Electrodynamic response of the ionosphere to high-speed solar wind streams. *Journal of Geophysical Research: Space Physics*, Wiley Online Library, v. 116, n. A12, 2011. Citado na página 38.

PHELPS, A.; SAGALYN, R. Plasma density irregularities in the high-latitude top side ionosphere. *Journal of Geophysical Research*, Wiley Online Library, v. 81, n. 4, p. 515–523, 1976. Citado na página 167.

PI, X. et al. Monitoring of global ionospheric irregularities using the worldwide gps network. *Geophysical Research Letters*, Wiley Online Library, v. 24, n. 18, p. 2283–2286, 1997. Citado 2 vezes nas páginas 77 and 167.

PRESTES, A. et al. Statistical analysis of solar wind parameters and geomagnetic indices during hildcaa/hildcaa occurrences between 1998 and 2007. *Advances in Space Research*, Elsevier, v. 60, n. 8, p. 1850–1865, 2017. Citado 8 vezes nas páginas 1, 3, 15, 28, 29, 78, 100, and 110.

PRESTES, A. et al. Hildcaa* events between 1998 and 2007 and their related interplanetary magnetic field and plasma values. *arXiv preprint arXiv:1612.03887*, 2016. Citado 3 vezes nas páginas 29, 83, and 85.

PRIKRYL, P. et al. Gps phase scintillation at high latitudes during the geomagnetic storm of 17–18 march 2015. *Journal of Geophysical Research: Space Physics*, Wiley Online Library, v. 121, n. 10, p. 10–448, 2016. Citado na página 166.

PRÖLSS, G.; ROEMER, M.; SLOWEY, J. Dissipation of solar wind energy in the earth's upper atmosphere: The geomagnetic activity effect. *Advances in space research*, Elsevier, v. 8, n. 5-6, p. 215–261, 1988. Citado 2 vezes nas páginas 135 and 137.

PRÖLSS, G. W. Magnetic storm associated perturbations of the upper atmosphere. *Geophysical Monograph Series*, v. 98, p. 227–241, 1997. Citado 2 vezes nas páginas 137 and 163.

RAM, S. T. et al. Duskside enhancement of equatorial zonal electric field response to convection electric fields during the st. patrick's day storm on 17 march 2015. *Journal of Geophysical Research: Space Physics*, Wiley Online Library, v. 121, n. 1, p. 538–548, 2016. Citado na página 62.

RASTOGI, R.; IYER, K.; SHARMA, R. Ionospheric total electron content and slab-thickness at low latitudes in indian zone. In: SPRINGER. *Proceedings of the Indian Academy of Sciences-Section A*. [S.l.], 1977. v. 85, p. 415–428. Citado na página 116.

REINISCH, B. Tenth international digisonde training seminar at umass lowell reviews state of real-time mapping of the ionosphere. *IEEE Antennas and Propagation Magazine*, IEEE, v. 46, n. 5, p. 110–117, 2004. Citado 4 vezes nas páginas 54, 65, 66, and 67.

REINISCH, B. et al. Recent advances in real-time analysis of ionograms and ionospheric drift measurements with digisondes. *Journal of Atmospheric and Solar-Terrestrial Physics*, Elsevier, v. 67, n. 12, p. 1054–1062, 2005. Citado 3 vezes nas páginas 65, 67, and 68.

REINISCH, B. W.; XUEQIN, H. Automatic calculation of electron density profiles from digital ionograms: 3. processing of bottomside ionograms. *Radio Science*, Wiley Online Library, v. 18, n. 3, p. 477–492, 1983. Citado na página 69.

REN, Z. et al. A theoretical model for mid-and low-latitude ionospheric electric fields in realistic geomagnetic fields. *Chinese Science Bulletin*, Springer, v. 53, n. 24, p. 3883–3890, 2008. Citado na página 33.

REZENDE, L. F. C. d. et al. Study of ionospheric irregularities during intense magnetic storms. *Revista Brasileira de Geofísica*, SciELO Brasil, v. 25, p. 151–158, 2007. Citado 2 vezes nas páginas 2 and 3.

RICHARDSON, I.; CANE, H.; CLIVER, E. Sources of geomagnetic activity during nearly three solar cycles (1972–2000). *Journal of Geophysical Research: Space Physics*, Wiley Online Library, v. 107, n. A8, p. SSH–8, 2002. Citado na página 12.

RICHARDSON, I.; CLIVER, E.; CANE, H. Sources of geomagnetic storms for solar minimum and maximum conditions during 1972–2000. *Geophysical Research Letters*, Wiley Online Library, v. 28, n. 13, p. 2569–2572, 2001. Citado na página 12.

RICHMOND, A. Ionospheric wind dynamo theory: A review. *Journal of geomagnetism and geoelectricity*, Society of Geomagnetism and Earth, Planetary and Space Sciences, v. 31, n. 3, p. 287–310, 1979. Citado 3 vezes nas páginas 31, 51, and 53.

RICHMOND, A.; PEYMIRAT, C.; ROBLE, R. Long-lasting disturbances in the equatorial ionospheric electric field simulated with a coupled magnetosphere-ionosphere-thermosphere model. *Journal of Geophysical Research: Space Physics*, Wiley Online Library, v. 108, n. A3, 2003. Citado 2 vezes nas páginas 86 and 169.

RICHMOND, A. D. Ionospheric electrodynamics. In: *Handbook of atmospheric electrodynamics (1995)*. [S.l.]: CRC press, 2017. p. 249–290. Citado 4 vezes nas páginas 27, 46, 49, and 50.

RILEY, P.; LINKER, J.; MIKIĆ, Z. An empirically-driven global mhd model of the solar corona and inner heliosphere. *Journal of Geophysical Research: Space Physics*, Wiley Online Library, v. 106, n. A8, p. 15889–15901, 2001. Citado na página 12.

RISHBETH, H. Polarization fields produced by winds in the equatorial f-region. *Planetary and Space Science*, Elsevier, v. 19, n. 3, p. 357–369, 1971. Citado 2 vezes nas páginas 89 and 178.

RISHBETH, H. F-region storms and thermospheric circulation. *Journal of Atmospheric and Terrestrial Physics*, Elsevier, v. 37, n. 6-7, p. 1055–1064, 1975. Citado na página 135.

RISHBETH, H. Dynamics of the equatorial f-region. *Journal of atmospheric and terrestrial physics*, Elsevier, v. 39, n. 9-10, p. 1159–1168, 1977. Citado na página 53.

RISHBETH, H.; GARRIOTT, O. K. Introduction to ionospheric physics. *Introduction to ionospheric physics*, 1969. Citado na página 42.

ROSTOKER, G.; LAM, H.-L.; HUME, W. D. Response time of the magnetosphere to the interplanetary electric field. *Canadian Journal of Physics*, NRC Research Press Ottawa, Canada, v. 50, n. 6, p. 544–547, 1972. Citado na página 23.

RUSSELL, C. et al. The effect of solar wind dynamic pressure changes on low and mid-latitude magnetic records. *Geophysical Research Letters*, Wiley Online Library, v. 19, n. 12, p. 1227–1230, 1992. Citado na página 11.

RUSSELL, C. T. The configuration of the magnetosphere. In: *Critical problems of magnetospheric physics*. [S.l.: s.n.], 1972. p. 1. Citado na página 21.

SABINE, E. V. on periodical laws discoverable in the mean effects of the larger magnetic disturbances. *Philosophical transactions of the Royal Society of London*, The Royal Society London, n. 141, p. 123–139, 1851. Citado na página 23.

SABINE, E. Viii. on periodical laws discoverable in the mean effects of the larger magnetic disturbance.—no. ii. *Philosophical Transactions of the Royal Society of London*, The Royal Society London, n. 142, p. 103–124, 1852. Citado na página 23.

SAHAI, Y. et al. Observations of the f-region ionospheric irregularities in the south american sector during the october 2003" halloween storms". In: COPERNICUS GMBH. *Annales Geophysicae*. [S.l.], 2009. v. 27, n. 12, p. 4463–4477. Citado 2 vezes nas páginas 94 and 121.

SANDANGER, M. et al. Proton injections into the ring current associated with b˜ z variations during hildcaa events. *GEOPHYSICAL MONOGRAPH-AMERICAN GEOPHYSICAL UNION*, AGU AMERICAN GEOPHYSICAL UNION, v. 155, p. 249, 2005. Citado na página 110.

SANTOS, A. M. et al. F region electric field effects on the intermediate layer dynamics during the evening prereversal enhancement at the equatorial region over brazil. *Authorea Preprints*, Authorea, 2022. Citado na página 170.

SANTOS, A. M. d. et al. Disturbance zonal and vertical plasma drifts in the peruvian sector during solar minimum phases. *Journal of Geophysical Research: Space Physics*, Wiley Online Library, v. 121, n. 3, p. 2503–2521, 2016. Citado na página 179.

SCHRÖDER, W. Some aspects of the earlier history of solar-terrestrial physics. *Planetary and space science*, Elsevier, v. 45, n. 3, p. 395–400, 1997. Citado na página 23.

SCHULZ, M. The magnetosphere. *Geomagnetism*, 1991. Citado na página 21.

SCHWENN, R. Relationship of coronal transients to interplanetary shocks: 3d aspects. *Space Science Reviews*, Springer, v. 44, n. 1, p. 139–168, 1986. Citado na página 16.

SCHWENN, R. Large-scale structure of the interplanetary medium. *Physics of the inner heliosphere I: large-scale phenomena*, Springer, p. 99–181, 1990. Citado na página 14.

SCKOPKE, N. A general relation between the energy of trapped particles and the disturbance field near the earth. *Journal of Geophysical Research*, Wiley Online Library, v. 71, n. 13, p. 3125–3130, 1966. Citado na página 24.

SEEMALA, G. K. *GPS-TEC Analysis Software*. 2009. <https://www.researchgate.net/publication/255978205_GPS-TEC_analysis_software>. Institute for Scientific Research, Boston College, USA. Accessed August 27, 2025. Citado na página 76.

SETHIA, G. et al. A numerical model for low-latitude ionospheric tec. *Indian Journal of Radio and Space Physics*, v. 7, p. 149–151, 1978. Citado na página 116.

SHKAROFSKY, I.; JOHNSTON, T.; BACHYNSKI, M. *The Particle Kinetics of Plasmas (Addision*. [S.l.]: Wesley Publishing Company, Montreal, Canada, 1966. Citado na página 47.

SILVA, R. P. et al. Latitudinal responses of the ionosphere over south america during hildcaa intervals: Case studies. *Advances in Space Research*, Elsevier, v. 71, n. 12, p. 5185–5195, 2023. Citado na página 111.

SIQUEIRA, P. D. et al. Storm-time total electron content and its response to penetration electric fields over south america. In: COPERNICUS PUBLICATIONS GÖTTINGEN, GERMANY. *Annales Geophysicae*. [S.l.], 2011. v. 29, n. 10, p. 1765–1778. Citado na página 33.

SOBRAL, J. H. A. et al. Equatorial ionospheric responses to high-intensity long-duration auroral electrojet activity (hildcaa). *Journal of Geophysical Research: Space Physics*, Wiley Online Library, v. 111, n. A7, 2006. Citado 10 vezes nas páginas 30, 31, 32, 99, 102, 104, 110, 113, 118, and 178.

SOBRAL, J. H. A. et al. Responses of the low-latitude ionosphere to very intense geomagnetic storms. *Journal of Atmospheric and Solar-Terrestrial Physics*, Elsevier, v. 63, n. 9, p. 965–974, 2001. Citado 2 vezes nas páginas 30 and 104.

SOMAYAJULU, Y. Changes in the f region during magnetic storms. *Journal of Geophysical Research*, Wiley Online Library, v. 68, n. 7, p. 1899–1922, 1963. Citado na página 136.

SØRAAS, F. et al. Evidence for particle injection as the cause of dst reduction during hildcaa events. *Journal of atmospheric and solar-terrestrial physics*, Elsevier, v. 66, n. 2, p. 177–186, 2004. Citado 3 vezes nas páginas 28, 29, and 110.

SOUZA, J. R. et al. Comparative study of ionospheric irregularities during storms and hildcaa events over the brazilian region. *Space Weather*, v. 16, n. 6, p. 741–754, 2018. Citado na página 167.

STERN, D. P. Large-scale electric fields in the earth's magnetosphere. *Reviews of Geophysics*, Wiley Online Library, v. 15, n. 2, p. 156–194, 1977. Citado na página 42.

STIX, M. *The sun: an introduction*. [S.l.]: Springer Science & Business Media, 2004. Citado 2 vezes nas páginas 8 and 14.

SUBEDI, A.; ADHIKARI, B.; MISHRA, R. K. Variation of solar wind parameters during intense geomagnetic storms. *Himalayan physics*, p. 80–85, 2017. Citado na página 9.

SULTAN, P. Linear theory and modeling of the rayleigh-taylor instability leading to the occurrence of equatorial spread f. *Journal of Geophysical Research: Space Physics*, Wiley Online Library, v. 101, n. A12, p. 26875–26891, 1996. Citado 3 vezes nas páginas 61, 62, and 171.

SUN, W. et al. A comparison of the observed mid-latitude magnetic disturbance fields with those reproduced from the high-latitude modeling current system. *Journal of Geophysical Research: Space Physics*, Wiley Online Library, v. 89, n. A12, p. 10881–10889, 1984. Citado na página 33.

SUN, W.-J. et al. Analysis of ionospheric features in middle and low latitude region of china during the geomagnetic storm in march 2015. *Chinese Journal of Geophysics*, Chinese Journal of Geophysics, v. 60, n. 1, p. 1–10, 2017. Citado na página 114.

TANAKA, T. Severe ionospheric disturbances caused by the sudden response of evening subequatorial ionospheres to geomagnetic storms. *Journal of Geophysical Research: Space Physics*, Wiley Online Library, v. 86, n. A13, p. 11335–11349, 1981. Citado na página 172.

TITHERIDGE, J.; BUONSANTO, M. A comparison of northern and southern hemisphere tec storm behaviour. *Journal of atmospheric and terrestrial physics*, Elsevier, v. 50, n. 9, p. 763–780, 1988. Citado na página 116.

TROSHICHEV, O. et al. Polar cap index (pc) as a proxy for ionospheric electric field in the near-pole region. *Geophysical research letters*, Wiley Online Library, v. 27, n. 23, p. 3809–3812, 2000. Citado na página 169.

TSUNODA, R. T. On equatorial spread f: Establishing a seeding hypothesis. *Journal of Geophysical Research: Space Physics*, Wiley Online Library, v. 115, n. A12, 2010. Citado na página 171.

TSURUTANI, B. et al. The interplanetary causes of magnetic storms, hildcaas and viscous interaction. *Physics and Chemistry of the Earth, Part C: Solar, Terrestrial & Planetary Science*, Elsevier, v. 24, n. 1-3, p. 93–99, 1999. Citado 4 vezes nas páginas 1, 14, 28, and 83.

TSURUTANI, B. et al. Nonlinear alfvén waves, discontinuities, proton perpendicular acceleration, and magnetic holes/decreases in interplanetary space and the magnetosphere: Intermediate shocks? *Nonlinear Processes in Geophysics*, Copernicus Publications Göttingen, Germany, v. 12, n. 3, p. 321–336, 2005. Citado 2 vezes nas páginas 12 and 134.

TSURUTANI, B. et al. Global dayside ionospheric uplift and enhancement associated with interplanetary electric fields. *Journal of Geophysical Research: Space Physics*, Wiley Online Library, v. 109, n. A8, 2004. Citado 9 vezes nas páginas 1, 30, 32, 34, 110, 134, 164, 169, and 172.

TSURUTANI, B. et al. Prompt penetration electric fields (ppefs) and their ionospheric effects during the great magnetic storm of 30–31 october 2003. *Journal of Geophysical Research: Space Physics*, Wiley Online Library, v. 113, n. A5, 2008. Citado 4 vezes nas páginas 32, 34, 109, and 134.

TSURUTANI, B. T.; GONZALEZ, W. D. The cause of high-intensity long-duration continuous ae activity (hildcaas): Interplanetary alfvén wave trains. *Planetary and Space Science*, Elsevier, v. 35, n. 4, p. 405–412, 1987. Citado 7 vezes nas páginas 38, 80, 82, 84, 102, 109, and 110.

TSURUTANI, B. T. et al. Interplanetary origin of geomagnetic activity in the declining phase of the solar cycle. *Journal of Geophysical Research: Space Physics*, Wiley Online Library, v. 100, n. A11, p. 21717–21733, 1995. Citado 12 vezes nas páginas 1, 13, 15, 28, 29, 30, 35, 36, 38, 86, 103, and 172.

TSURUTANI, B. T. et al. Corotating solar wind streams and recurrent geomagnetic activity: A review. *Journal of Geophysical Research: Space Physics*, Wiley Online Library, v. 111, n. A7, 2006. Citado 7 vezes nas páginas 14, 15, 17, 27, 30, 36, and 108.

TSURUTANI, B. T. et al. Origin of interplanetary southward magnetic fields responsible for major magnetic storms near solar maximum (1978–1979). *Journal of Geophysical Research: Space Physics*, Wiley Online Library, v. 93, n. A8, p. 8519–8531, 1988. Citado na página 19.

TSURUTANI, B. T. et al. Auroral zone dayside precipitation during magnetic storm initial phases. *Journal of Atmospheric and Solar-Terrestrial Physics*, Elsevier, v. 63, n. 5, p. 513–522, 2001. Citado 4 vezes nas páginas 2, 26, 28, and 89.

TUCKER-HOOD, K. et al. Validation of a priori cme arrival predictions made using real-time heliospheric imager observations. *Space Weather*, American Geophysical Union (AGU), v. 13, n. 1, p. 35–48, jan. 2015. ISSN 1542-7390. Disponível em: <http://dx.doi.org/10.1002/2014SW001106>. Citado na página 18.

UWAMAHORO, J. *An analysis of sources and predictability of geomagnetic storms*. Tese (Doutorado) — Rhodes University, 2011. Citado na página 16.

VALIO, A. et al. Correlations of sunspot physical characteristics during solar cycle 23. *Solar Physics*, Springer, v. 295, n. 9, p. 120, 2020. Citado na página 9.

VANDAS, M. et al. Evidence for a spheroidal structure of magnetic clouds. *Journal of Geophysical Research: Space Physics*, American Geophysical Union (AGU), v. 98, n. A12, p. 21061–21069, dez. 1993. ISSN 0148-0227. Disponível em: <http://dx.doi.org/10.1029/93JA01749>. Citado na página 19.

VASYLIUNAS, V. M. Mathematical models of magnetospheric convection and its coupling to the ionosphere. In: SPRINGER. *Particles and Fields in the Magnetosphere: Proceedings of a Symposium Organized by the Summer Advanced Study Institute, Held at the University of California, Santa Barbara, Calif., August 4–15, 1969*. [S.l.], 1970. p. 60–71. Citado na página 111.

VASYLIUNAS, V. M. The interrelationship of magnetospheric processes. In: SPRINGER. *Earth's Magnetospheric Processes: Proceedings of a Symposium Organized by the Summer Advanced Study Institute and Ninth ESRO Summer School, Held in Cortina, Italy, August 30-September 10, 1971*. [S.l.], 1972. p. 29–38. Citado na página 111.

VENKATESAN, D.; ZHU, B. On the high-speed plasma streams, stormtime sudden commencements and cosmic-ray intensity: Relation amongst them during epoch 1978 to 1982. *Solar physics*, Springer, v. 131, p. 385–393, 1991. Citado na página 12.

VERKHOGLYADOVA, O. et al. Variability of ionospheric tec during solar and geomagnetic minima (2008 and 2009): external high speed stream drivers. In: COPERNICUS PUBLICATIONS GÖTTINGEN, GERMANY. *Annales Geophysicae*. [S.l.], 2013. v. 31, n. 2, p. 263–276. Citado 3 vezes nas páginas 32, 111, and 135.

VERKHOGLYADOVA, O. P. et al. Simulation of ppef effects in dayside low-latitude ionosphere for the october 30, 2003, superstorm. *Washington DC American Geophysical Union Geophysical Monograph Series*, v. 181, p. 169–177, 2008. Citado 2 vezes nas páginas 32 and 134.

VLASOV, M.; KELLEY, M.; KIL, H. Analysis of ground-based and satellite observations of f-region behavior during the great magnetic storm of july 15, 2000. *Journal of atmospheric and solar-terrestrial physics*, Elsevier, v. 65, n. 11-13, p. 1223–1234, 2003. Citado na página 34.

VOLLAND, H. *Handbook of atmospheric electrodynamics*. [S.l.]: CRC Press, 1995. v. 2. Citado na página 135.

WANG, Q. et al. Characteristic analysis of the differences between tec values in gim grids. *Annales Geophysicae*, v. 42, p. 45–53, 2024. Citado na página 135.

WANG, W. et al. Ionospheric response to the initial phase of geomagnetic storms: Common features. *Journal of Geophysical Research: Space Physics*, American Geophysical Union (AGU), v. 115, n. A7, jul. 2010. ISSN 0148-0227. Disponível em: <http://dx.doi.org/10.1029/2009JA014461>. Citado na página 158.

WANG, Y.-M. et al. The solar eclipse of 2006 and the origin of raylike features in the white-light corona. *The Astrophysical Journal*, IOP Publishing, v. 660, n. 1, p. 882, 2007. Citado na página 8.

WEBB, D.; DAVIS, J.; MCINTOSH, P. Observations of the reappearance of polar coronal holes and the reversal of the polar magnetic field. *Solar physics*, Springer, v. 92, p. 109–132, 1984. Citado na página 15.

WEBB, D. F.; HOWARD, R. A. The solar cycle variation of coronal mass ejections and the solar wind mass flux. *Journal of Geophysical Research: Space Physics*, Wiley Online Library, v. 99, n. A3, p. 4201–4220, 1994. Citado na página 11.

WEBB, D. F. et al. Studying geoeffective interplanetary coronal mass ejections between the sun and earth: Space weather implications of solar mass ejection imager observations. *Space Weather*, American Geophysical Union (AGU), v. 7, n. 5, maio 2009. ISSN 1542-7390. Disponível em: <http://dx.doi.org/10.1029/2008SW000409>. Citado na página 19.

WEI, Y. et al. Unusually long lasting multiple penetration of interplanetary electric field to equatorial ionosphere under oscillating imf bz. *Geophysical Research Letters*, Wiley Online Library, v. 35, n. 2, 2008. Citado 5 vezes nas páginas 30, 32, 34, 111, and 119.

WEI, Y. et al. Electric field penetration into earth's ionosphere: A brief review for 2000–2013. *Science Bulletin*, Elsevier, v. 60, n. 8, p. 748–761, 2015. Citado 4 vezes nas páginas 3, 31, 33, and 135.

WERNER, S.; PRÖLSS, G. The position of the ionospheric trough as a function of local time and magnetic activity. *Advances in Space Research*, Elsevier, v. 20, n. 9, p. 1717–1722, 1997. Citado na página 137.

WERNIK, A.; SECAN, J.; FREMOUW, E. Ionospheric irregularities and scintillation. *Advances in Space Research*, Elsevier, v. 31, n. 4, p. 971–981, 2003. Citado na página 167.

WOODMAN, R. Spread f–an old equatorial aeronomy problem finally resolved? In: COPERNICUS PUBLICATIONS GÖTTINGEN, GERMANY. *Annales geophysicae*. [S.l.], 2009. v. 27, n. 5, p. 1915–1934. Citado na página 62.

WOODMAN, R. F.; HOZ, C. L. Radar observations of f region equatorial irregularities. *Journal of Geophysical Research*, Wiley Online Library, v. 81, n. 31, p. 5447–5466, 1976. Citado na página 171.

WRIGHT, J.; ARGO, P.; PITTEWAY, M. On the radiophysics and geophysics of ionogram spread f. *Radio Science*, Wiley Online Library, v. 31, n. 2, p. 349–366, 1996. Citado na página 67.

XIAO, Z. et al. Deep-learning for ionogram automatic scaling. *Advances in Space Research*, Elsevier, v. 66, n. 4, p. 942–950, 2020. Citado na página 69.

XIONG, B. et al. Constructing a regional ionospheric tec model in china with empirical orthogonal function and dense gnss observation. *Remote Sensing*, MDPI, v. 15, n. 21, p. 5207, 2023. Citado na página 118.

YAMAZAKI, Y.; KOSCH, M. J. The equatorial electrojet during geomagnetic storms and substorms. *Journal of Geophysical Research: Space Physics*, Wiley Online Library, v. 120, n. 3, p. 2276–2287, 2015. Citado na página 27.

YASHIRO, S. et al. A catalog of white light coronal mass ejections observed by the soho spacecraft. *Journal of Geophysical Research: Space Physics*, Wiley Online Library, v. 109, n. A7, 2004. Citado na página 16.

YASYUKEVICH, Y. et al. Ionospheric global and regional electron contents in solar cycles 23–25. *Symmetry*, MDPI, v. 15, n. 10, p. 1940, 2023. Citado na página 136.

YA'ACOB, N.; ABDULLAH, M.; ISMAIL, M. *GPS total electron content (TEC) prediction at ionosphere layer over the equatorial region*. [S.l.]: IntechOpen, 2010. Citado na página 72.

YEERAM, T. Interplanetary drivers of daytime penetration electric field into equatorial ionosphere during cir-induced geomagnetic storms. *Journal of Atmospheric and Solar-Terrestrial Physics*, Elsevier, v. 157, p. 6–15, 2017. Citado na página 32.

YEERAM, T. The solar wind-magnetosphere coupling and daytime disturbance electric fields in equatorial ionosphere during consecutive recurrent geomagnetic storms. *Journal of Atmospheric and Solar-Terrestrial Physics*, Elsevier, v. 187, p. 40–52, 2019. Citado 4 vezes nas páginas 30, 32, 111, and 178.

YEH, K. C.; LIU, C.-H. Radio wave scintillations in the ionosphere. *Proceedings of the IEEE*, IEEE, v. 70, n. 4, p. 324–360, 1982. Citado na página 55.

YERMOLAEV, Y. I.; YERMOLAEV, M. Y. Statistical relationships between solar, interplanetary, and geomagnetospheric disturbances, 1976–2000. *Cosmic Research*, Springer, v. 40, p. 1–14, 2002. Citado na página 12.

YEŞIL, A.; ÜNAL, İ. Electromagnetic wave propagation in ionospheric plasma. *Behaviour of electromagnetic waves in different media and structures*, BoD–Books on Demand, v. 189, 2011. Citado na página 54.

YOKOYAMA, T.; STOLLE, C. Low and midlatitude ionospheric plasma density irregularities and their effects on geomagnetic field. *Space Science Reviews*, Springer, v. 206, n. 1-4, p. 495–519, 2017. Citado na página 61.

YUAN, Z.; DENG, X. Effects of continuous solar wind pressure variations on the long-lasting penetration of the interplanetary electric field during southward interplanetary magnetic field. *Advances in Space Research*, Elsevier, v. 39, n. 8, p. 1342–1346, 2007. Citado na página 34.

YUE, X. et al. Development of a middle and low latitude theoretical ionospheric model and an observation system data assimilation experiment. *Chinese Science Bulletin*, Springer, v. 53, n. 1, p. 94–101, 2008. Citado na página 33.

ZAGAINOVA, Y. S. et al. Study of the magnetic properties of sunspot umbrae. *Astronomy Reports*, Springer, v. 66, n. 2, p. 116–164, 2022. Citado na página 9.

ZHANG, Q. et al. Plasma transport between the ionosphere and plasmasphere in response to solar wind dynamic pressure pulsation. *Chinese Science Bulletin*, Springer, v. 58, p. 4126–4132, 2013. Citado na página 34.

ZHANG, Y. et al. Periodic variations in solar wind and responses of the magnetosphere and thermosphere in march 2017. *Journal of Geophysical Research: Space Physics*, American Geophysical Union (AGU), v. 126, n. 8, ago. 2021. ISSN 2169-9402. Disponível em: <http://dx.doi.org/10.1029/2021JA029387>. Citado na página 174.

ZHAO, B.; WAN, W.; LIU, L. Responses of equatorial anomaly to the october-november 2003 superstorms. In: COPERNICUS PUBLICATIONS GÖTTINGEN, GERMANY. *Annales Geophysicae*. [S.l.], 2005. v. 23, n. 3, p. 693–706. Citado na página 34.

ZHAO, B. et al. Features of annual and semiannual variations derived from the global ionospheric maps of total electron content. In: COPERNICUS PUBLICATIONS GÖTTINGEN, GERMANY. *Annales Geophysicae*. [S.l.], 2007. v. 25, n. 12, p. 2513–2527. Citado 2 vezes nas páginas 114 and 116.

ZONG, Q.-G. et al. Dayside ionospheric response to the intense interplanetary shocks–solar wind discontinuities: Observations from the digisonde global ionospheric radio observatory. *Journal of Geophysical Research: Space Physics*, Wiley Online Library, v. 115, n. A6, 2010. Citado na página 34.

ĎUROVCOVá, T.; ŠAFRáNKOVá, J.; NěMEčEK, Z. Proton beam abundance variations and their relation to alpha particle properties. *The Astrophysical Journal*, American Astronomical Society, v. 923, n. 2, p. 170, dez. 2021. ISSN 1538-4357. Disponível em: <http://dx.doi.org/10.3847/1538-4357/ac2c03>. Citado na página 35.

A Chapter 5: Additional figures

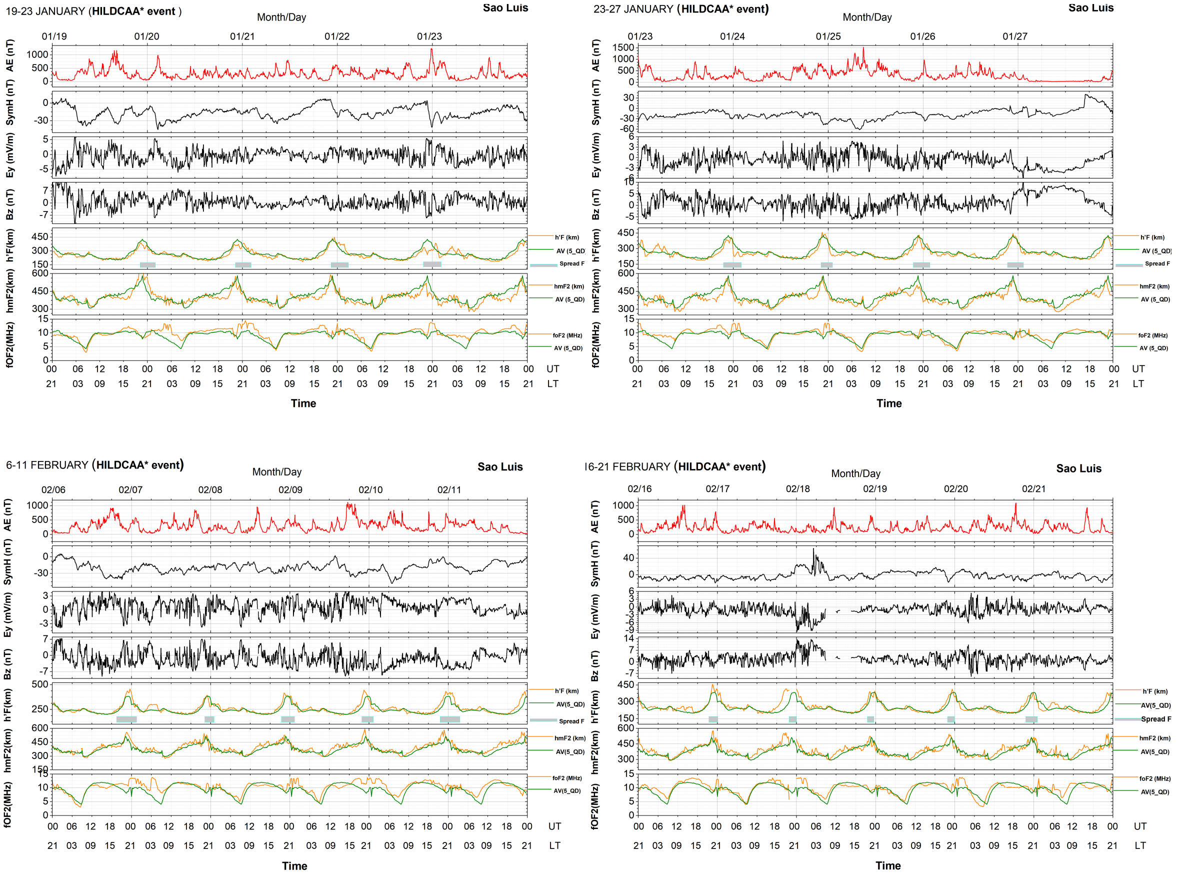

19-23 JANUARY (**HILDCAA* event**)

23-27 JANUARY (**HILDCAA* event)**

6-11 FEBRUARY (**HILDCAA* event)**

I6-21 FEBRUARY (**HILDCAA* event)**

Figure A.1 – Variation of Sym-H, Ey, and Bz, and Ionospheric Parameters (h’F, hmF2, foF2) during the HILDCAA events on 19-23 January, 23-27 January, 6-11 February and 18-21 February. The gold and solid olive lines represent the current days (HILDCAA) and average quiet-days (5QD) variations of h’F, hmF2, and foF2, while the horizontal bar indicates spread F.

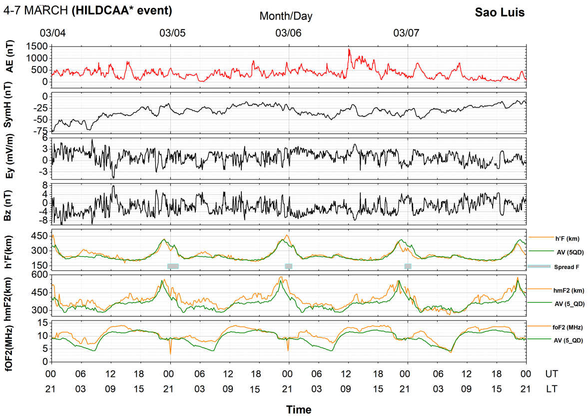

4-7 MARCH **(HILDCAA* event)**

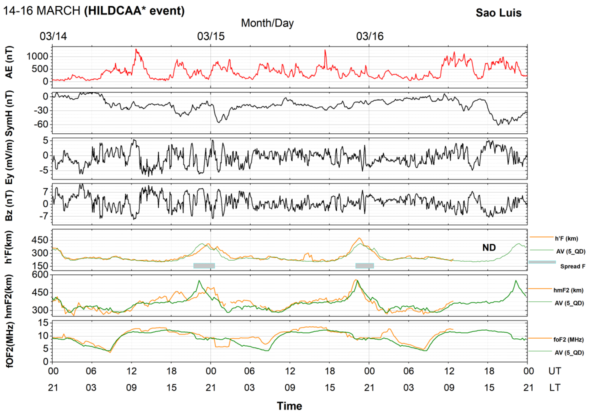

14-16 MARCH **(HILDCAA* event)**

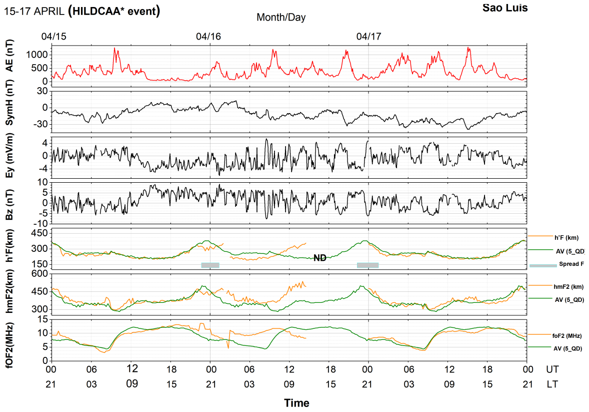

15-17 APRIL **(HILDCAA* event)**

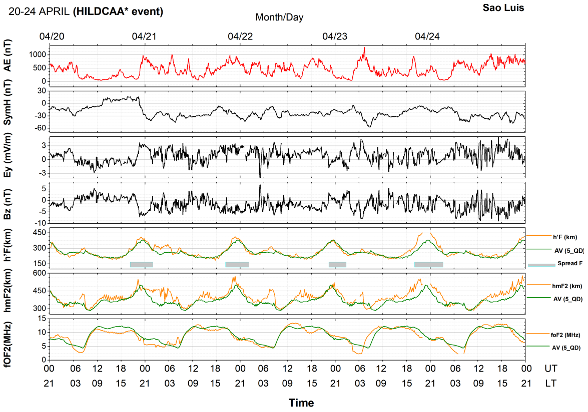

20-24 APRIL **(HILDCAA* event)**

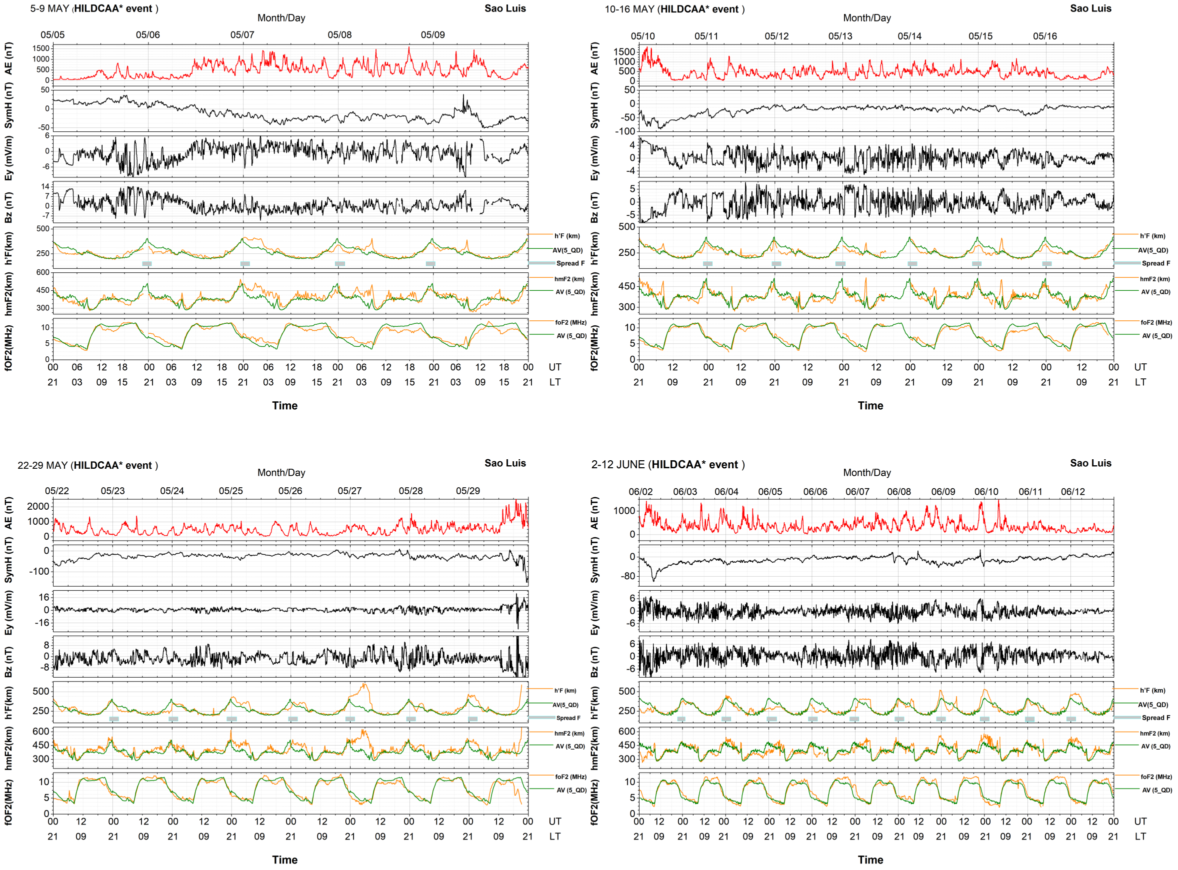

Figure A.2 – Variation of Sym-H, Ey, and Bz, and Ionospheric Parameters (h’F, hmF2, foF2) during the HILDCAA events on 5-9 May, 10-16 May, 22-29 May and 2-12 June in 2003. The gold and solid olive lines represent the current days (HILDCAA) and average quiet-days (5QD) variations of h’F, hmF2, and foF2, while the horizontal bar indicates spread F.

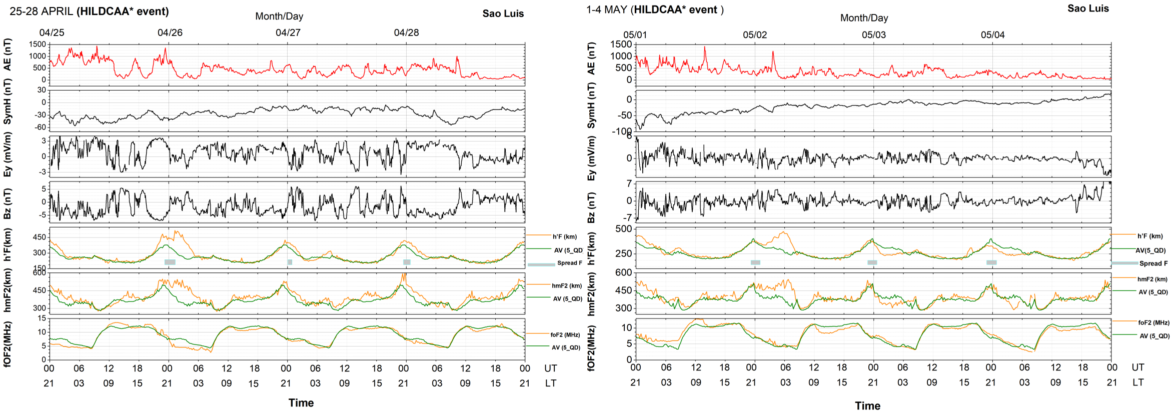

Figure A.3 – Variation of Sym-H, Ey, and Bz, and Ionospheric Parameters (h’F, hmF2, foF2) during the HILDCAA events on 04-07 March, 14-16 March, 15-17 Apirl, 20-24 April, 25-28 April in 2003 and 01-04 May. The gold and solid olive lines represent the current days (HILDCAA) and average quiet-days (5QD) variations of h’F, hmF2, and foF2, while the horizontal bar indicates spread F.

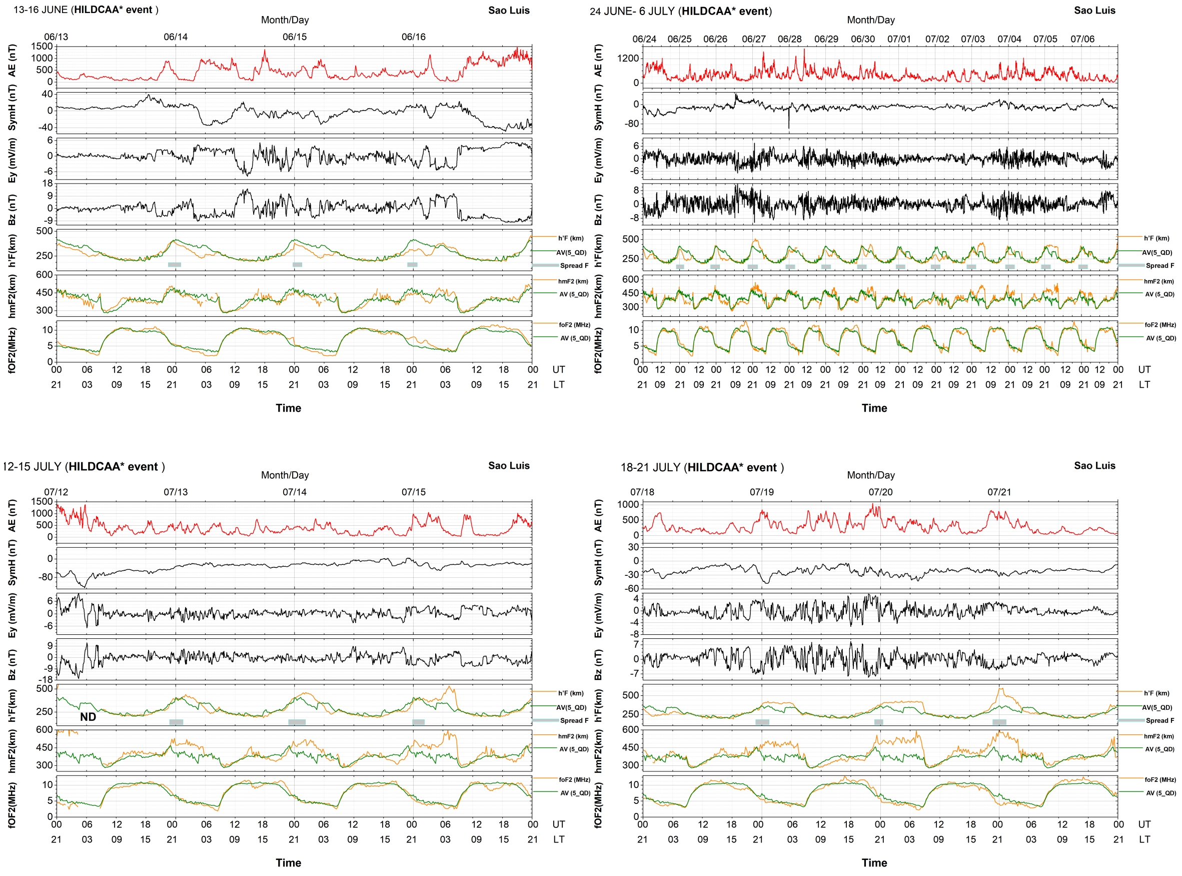

Figure A.4 – Variation of Sym-H, Ey, and Bz, and Ionospheric Parameters (h'F, hmF2, foF2) during the HILDCAA events on 13-16 June, 24 June-6 July, 12-15 July and 18-21 July in 2003. The gold and solid olive lines represent the current days (HILDCAA) and average quiet-days (5QD) variations of h'F, hmF2, and foF2, while the horizontal bar indicates spread F.

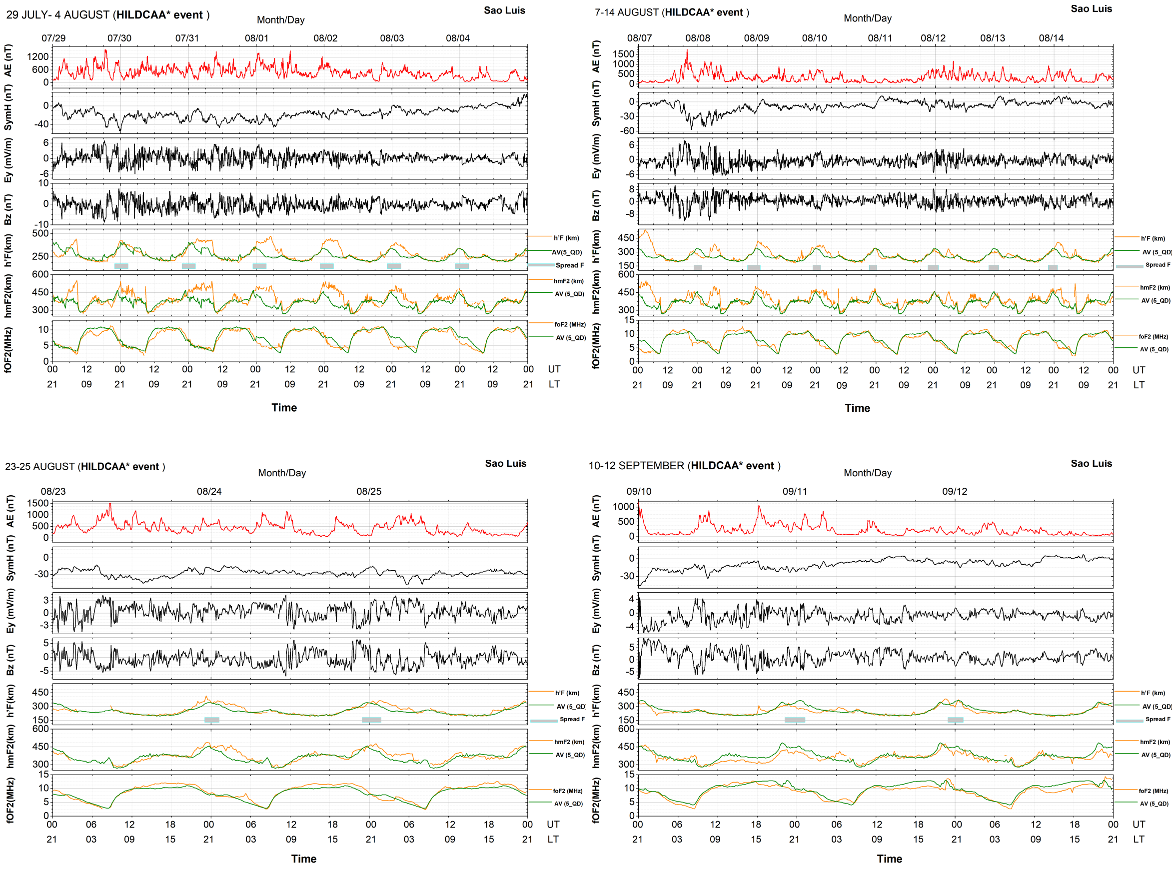

Figure A.5 – Variation of Sym-H, Ey, and Bz, and Ionospheric Parameters (h’F, hmF2, foF2) during the HILDCAA events on 29 July-4 August, 7-14 August, 23-25 August and 10-12 September in 2003. The gold and solid olive lines represent the current days (HILDCAA) and average quiet-days (5QD) variations of h’F, hmF2, and foF2, while the horizontal bar indicates spread F.

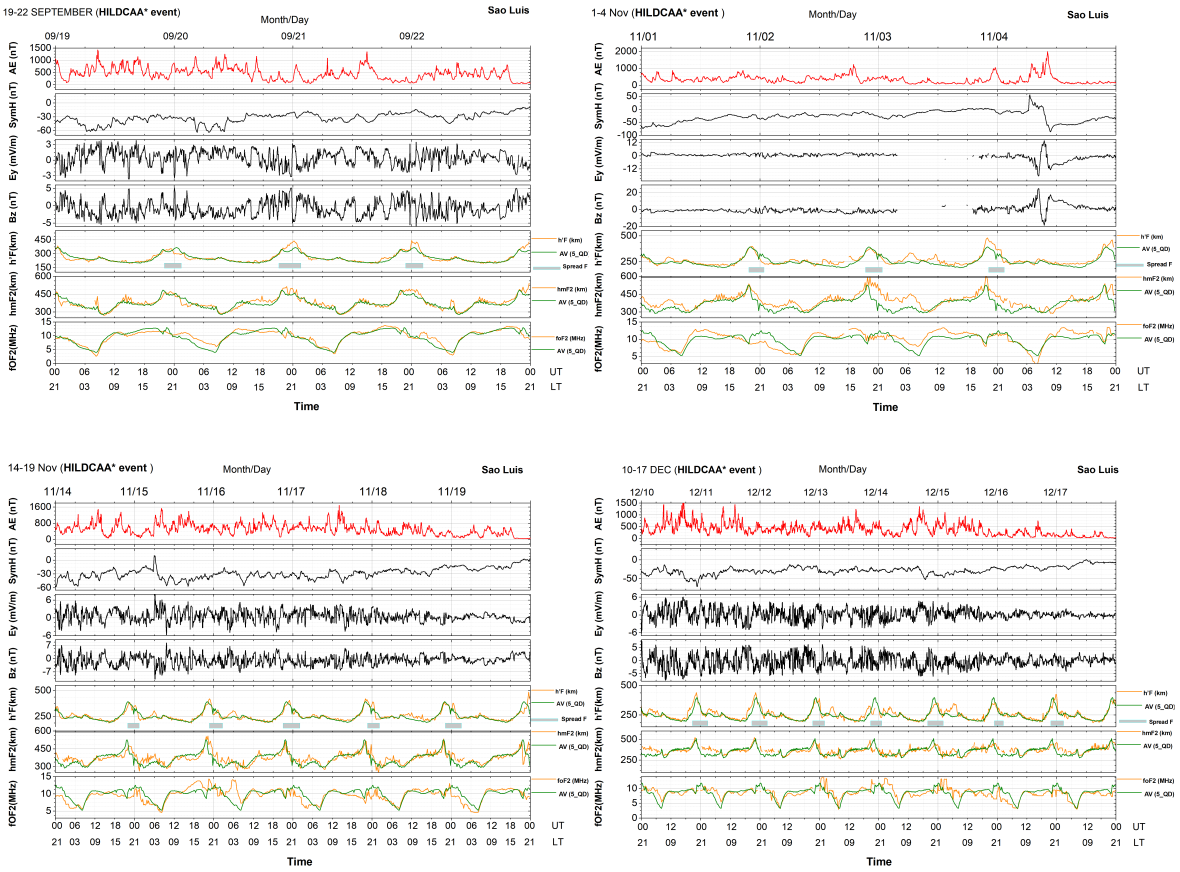

Figure A.6 – Variation of Sym-H, Ey, and Bz, and Ionospheric Parameters (h'F, hmF2, foF2) during the HILDCAA events on 19-22 September, 1-4 November, 14-19 November and 10-17 December in 2003. The gold and solid olive lines represent the current days (HILDCAA) and average quiet-days (5QD) variations of h'F, hmF2, and foF2, while the horizontal bar indicates spread F.

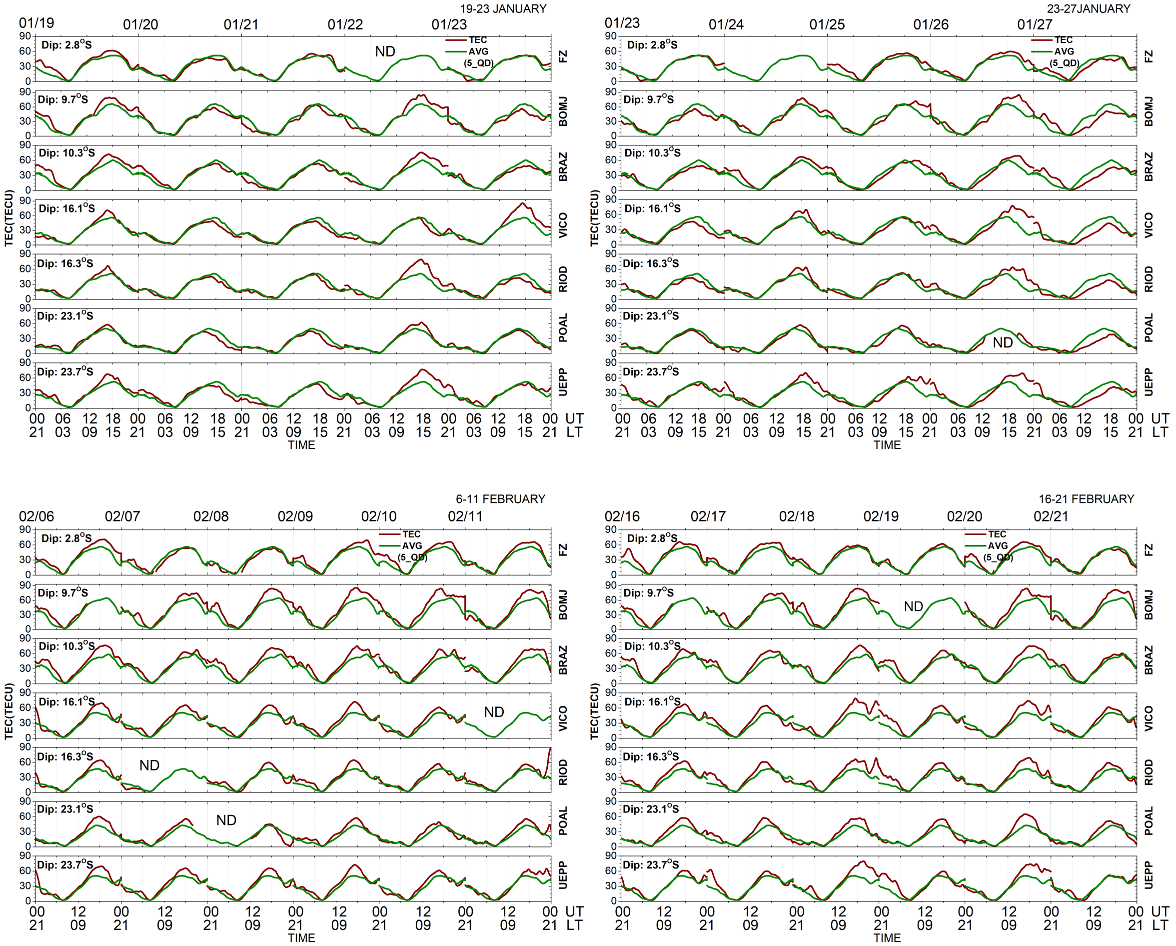

Figure A.7 – VTEC variation during the HILDCAA events, on 19-23 January, 23-27 January, 6-11 February and 18-21 February, over equatorial region and the south crest of EIA. The wine color line represents the HILDCAA days, the olive line represents the average quiet-days (5QD) variations and ND represent No data

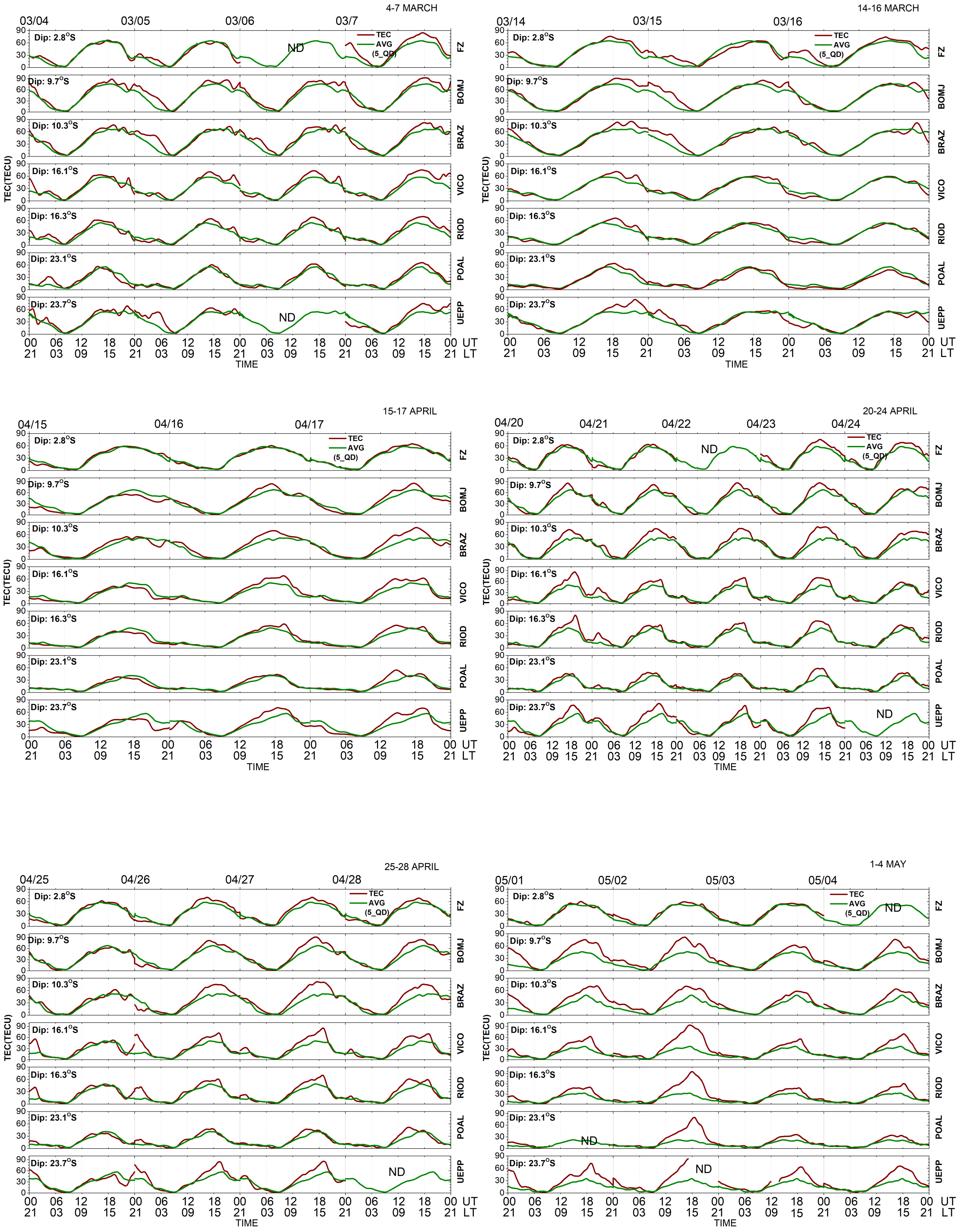

Figure A.8 – VTEC variation during the HILDCAA events, on 04-07 March, 14-16 March, 15-17 Apirl, 20-24 April, 25-28 April in 2003 and 01-04 May, over equatorial region and the south crest of EIA. The wine color line represents the HILDCAA days, the olive line represents the average quiet-days (5QD) variations and ND represent No data

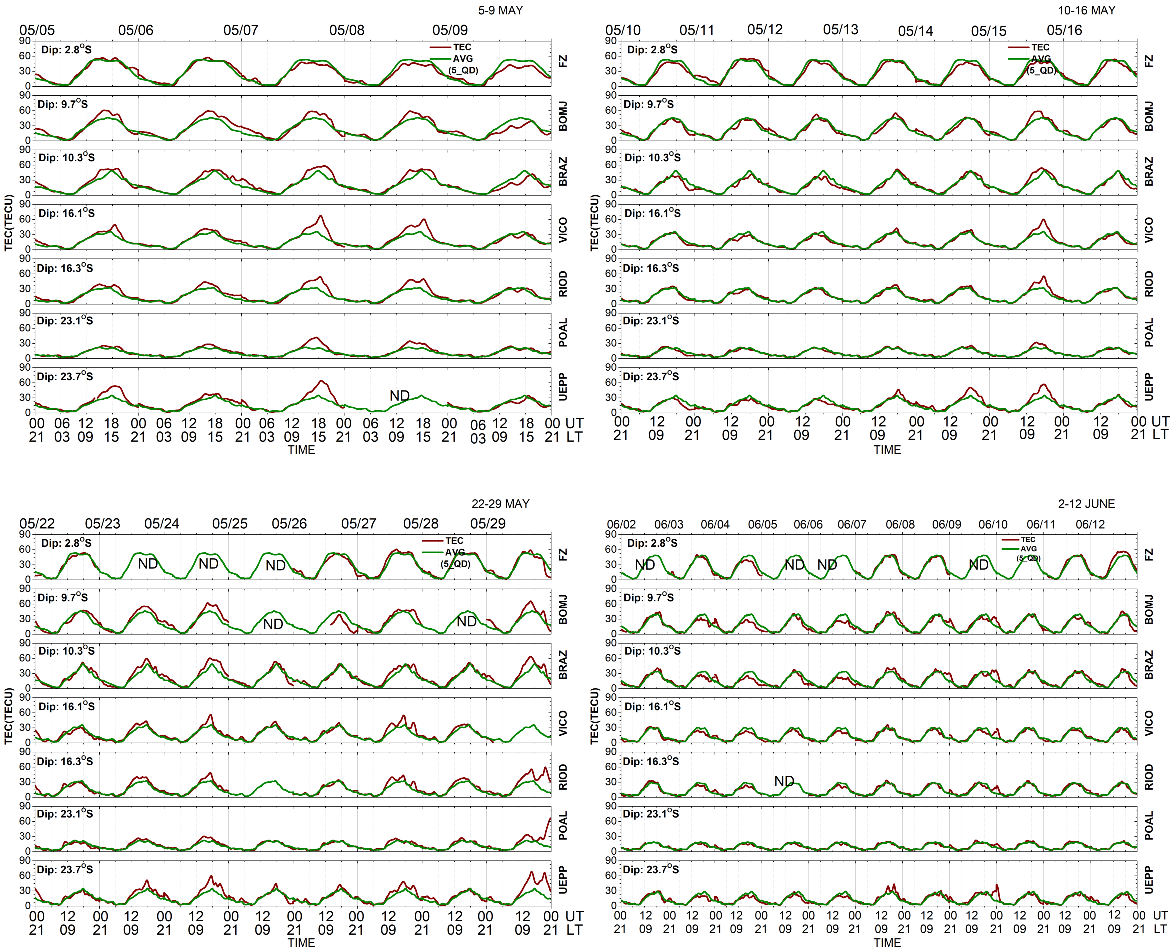

Figure A.9 – VTEC variation during the HILDCAA events on 5-9 May, 10-16 May, 22-29 May and 02-12 June in 2003, over euatorial region and the south crest of EIA. The wine color line represents the HILDCAA days, the olive line represents the average quiet-days (5QD) variations and ND represent No data

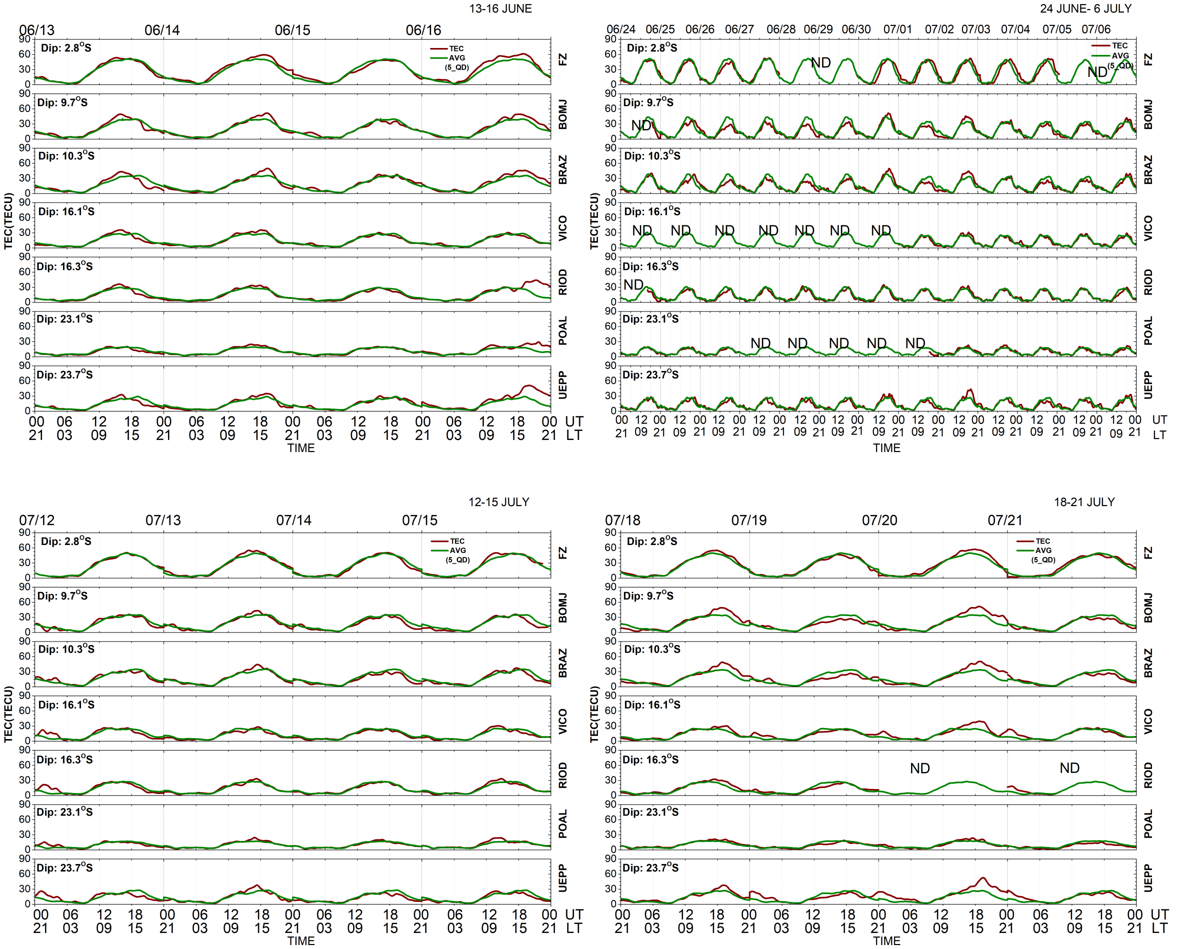

Figure A.10 – VTEC variation during the HILDCAA events on 13-16 June, 24 June-6 July, 12-15 July and 18-21 July in 2003, over equatorial region and the south crest of EIA. The wine color line represents the HILDCAA days, the olive line represents the average quiet-days (5QD) variations and ND represent No data

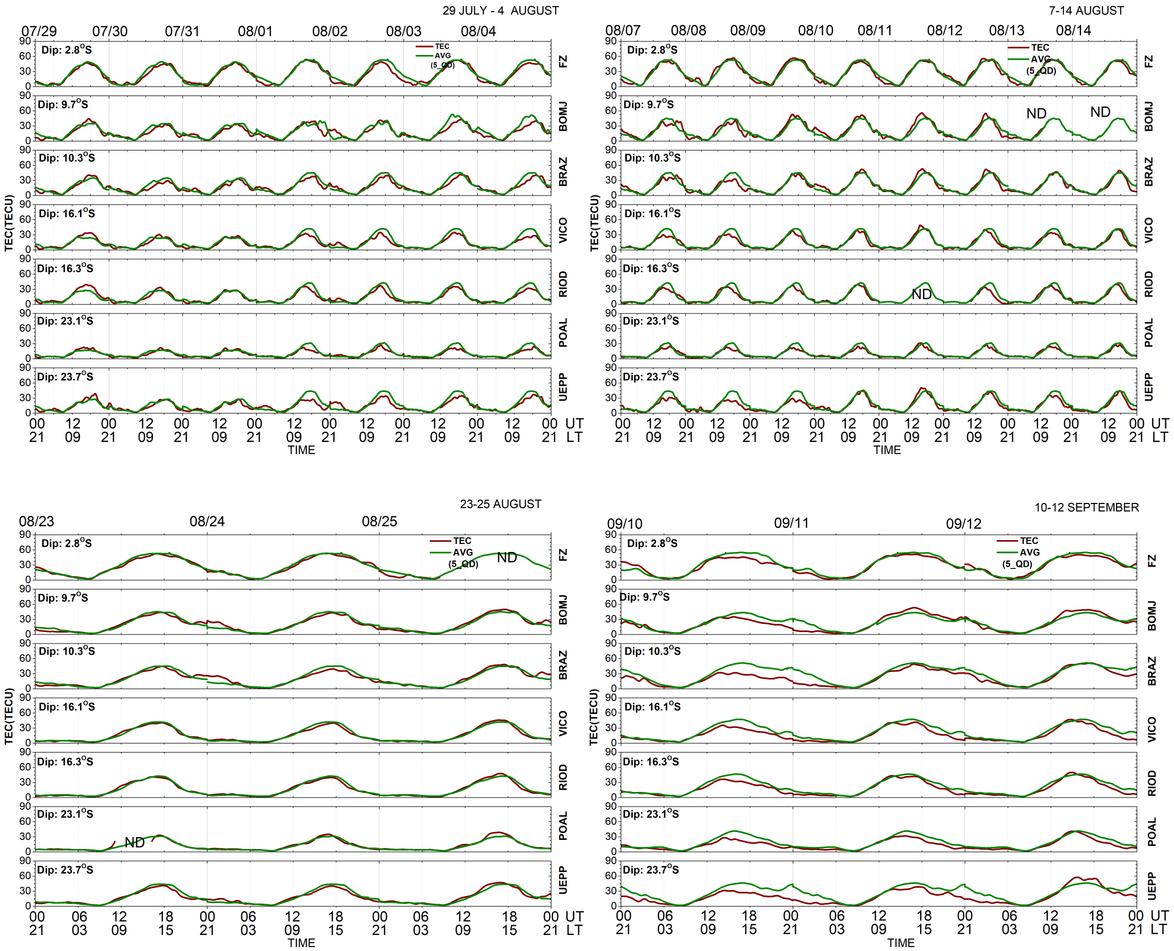

Figure A.11 – VTEC variation during the HILDCAA events, on 29 July-4 August, 7-14 August, 23-25 August and 10-12 September in 2003, over euatorial region and the south crest of EIA. The wine color line represents the HILDCAA days, the olive line represents the average quiet-days (5QD) variations and ND represent No data

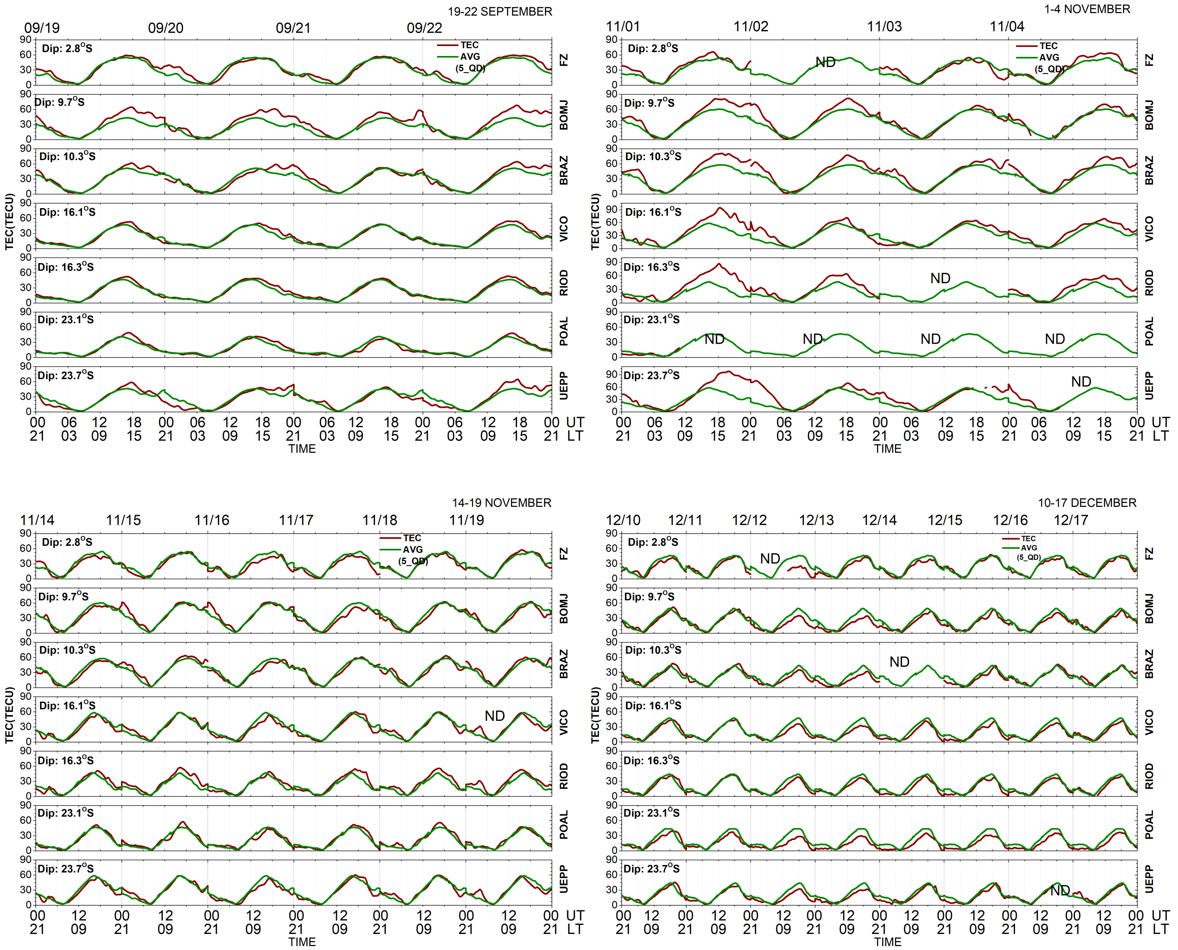

Figure A.12 – VTEC variation during the HILDCAA events, on 19-22 September, 1-4 November, 14-19 November and 10-17 December in 2003, over equatorial region and the south crest of EIA. The wine color line represents the HILDCAA days, the olive line represents the average quiet-days (5QD) variations and ND represent No data

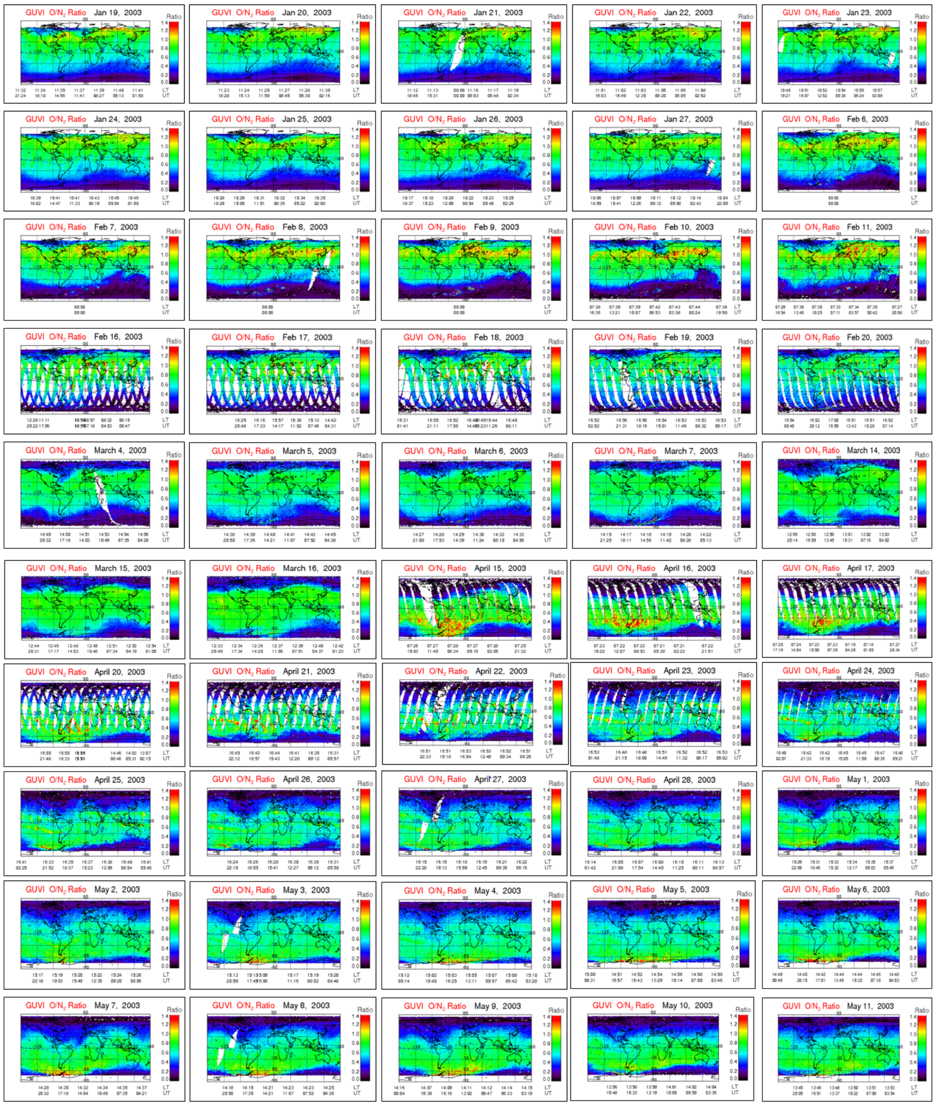

Figure A.13 – World map showing GUVI O/N_2 ratio during the HILDCAA events on 19-23 January, 23-27 January, 6-11 February and 18-21 February and 04–07 March.

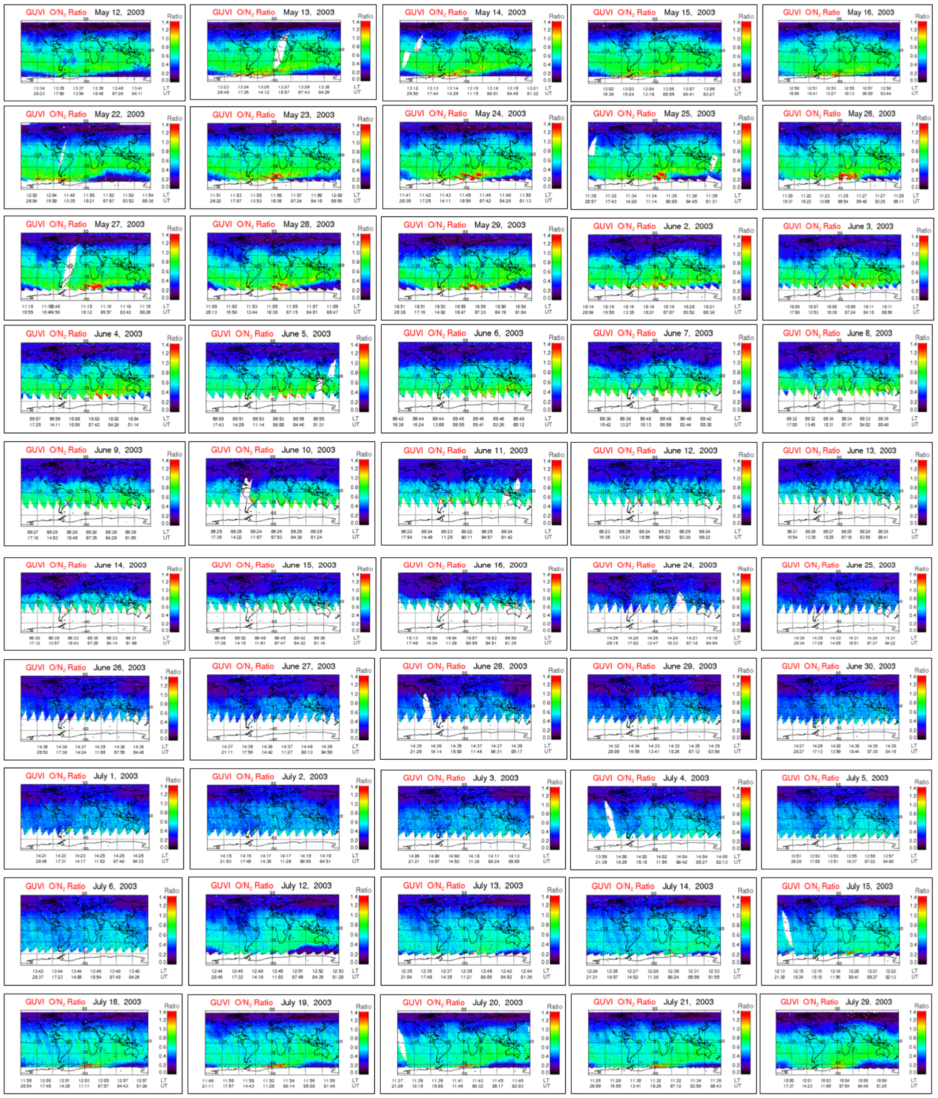

Figure A.14 – World map showing GUVI O/N_2 ratio during the HILDCAA events on 11-16 May, 22-29 May, 02-13 June, 14-16 June, 24 June- 06 July, 12-15 July, 18-21 July.

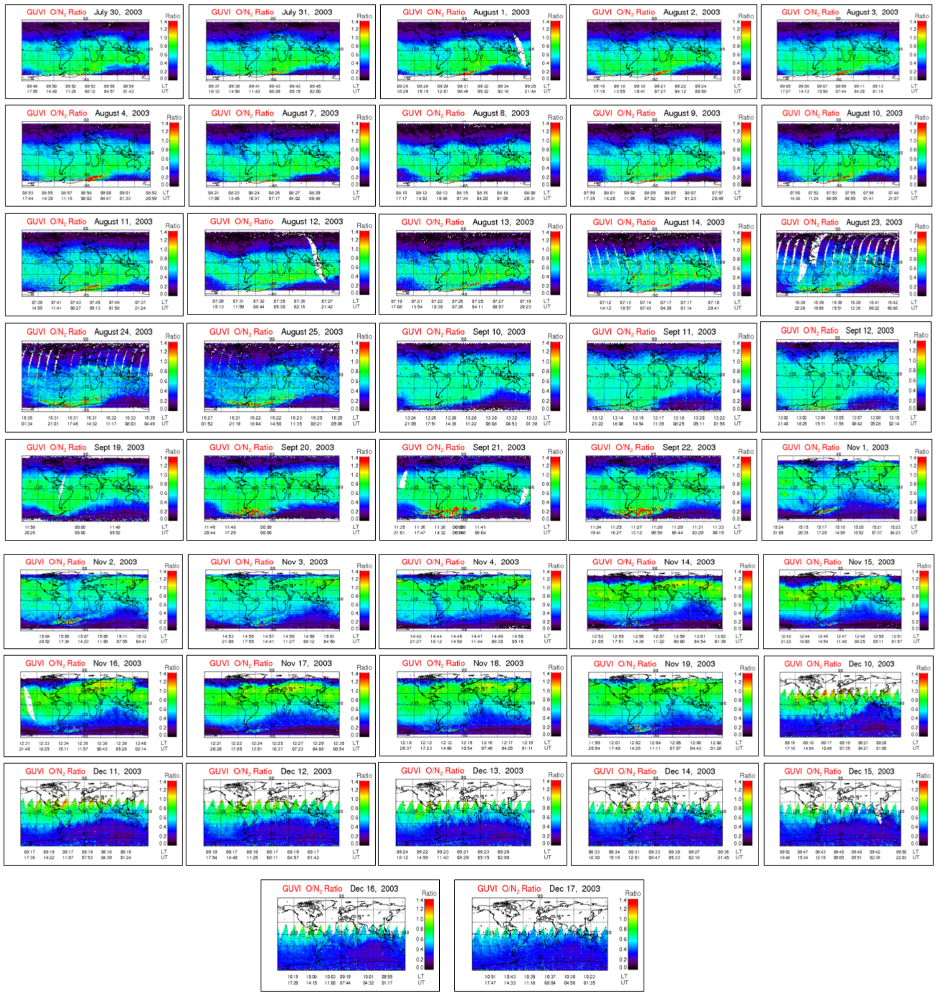
GUVI O/N$_2$ Ratio July 30, 2003
GUVI O/N$_2$ Ratio July 31, 2003
GUVI O/N$_2$ Ratio August 1, 2003
GUVI O/N$_2$ Ratio August 2, 2003
GUVI O/N$_2$ Ratio August 3, 2003
GUVI O/N$_2$ Ratio August 4, 2003
GUVI O/N$_2$ Ratio August 7, 2003
GUVI O/N$_2$ Ratio August 8, 2003
GUVI O/N$_2$ Ratio August 9, 2003
GUVI O/N$_2$ Ratio August 10, 2003
GUVI O/N$_2$ Ratio August 11, 2003
GUVI O/N$_2$ Ratio August 12, 2003
GUVI O/N$_2$ Ratio August 13, 2003
GUVI O/N$_2$ Ratio August 14, 2003
GUVI O/N$_2$ Ratio August 23, 2003
GUVI O/N$_2$ Ratio August 24, 2003
GUVI O/N$_2$ Ratio August 25, 2003
GUVI O/N$_2$ Ratio Sept 10, 2003
GUVI O/N$_2$ Ratio Sept 11, 2003
GUVI O/N$_2$ Ratio Sept 12, 2003
GUVI O/N$_2$ Ratio Sept 19, 2003
GUVI O/N$_2$ Ratio Sept 20, 2003
GUVI O/N$_2$ Ratio Sept 21, 2003
GUVI O/N$_2$ Ratio Sept 22, 2003
GUVI O/N$_2$ Ratio Nov 1, 2003
GUVI O/N$_2$ Ratio Nov 2, 2003
GUVI O/N$_2$ Ratio Nov 3, 2003
GUVI O/N$_2$ Ratio Nov 4, 2003
GUVI O/N$_2$ Ratio Nov 14, 2003
GUVI O/N$_2$ Ratio Nov 15, 2003
GUVI O/N$_2$ Ratio Nov 16, 2003
GUVI O/N$_2$ Ratio Nov 17, 2003
GUVI O/N$_2$ Ratio Nov 18, 2003
GUVI O/N$_2$ Ratio Nov 19, 2003
GUVI O/N$_2$ Ratio Dec 10, 2003
GUVI O/N$_2$ Ratio Dec 11, 2003
GUVI O/N$_2$ Ratio Dec 12, 2003
GUVI O/N$_2$ Ratio Dec 13, 2003
GUVI O/N$_2$ Ratio Dec 14, 2003
GUVI O/N$_2$ Ratio Dec 15, 2003
GUVI O/N$_2$ Ratio Dec 16, 2003
GUVI O/N$_2$ Ratio Dec 17, 2003

Figure A.15 – World map showing GUVI O/N_2 ratio during the HILDCAA events on 29 July-04 August, 07-14 August, 23-25 August, 10-12 September, 19-22 September, 01-04 November, 14-19 November, 10-17 December.

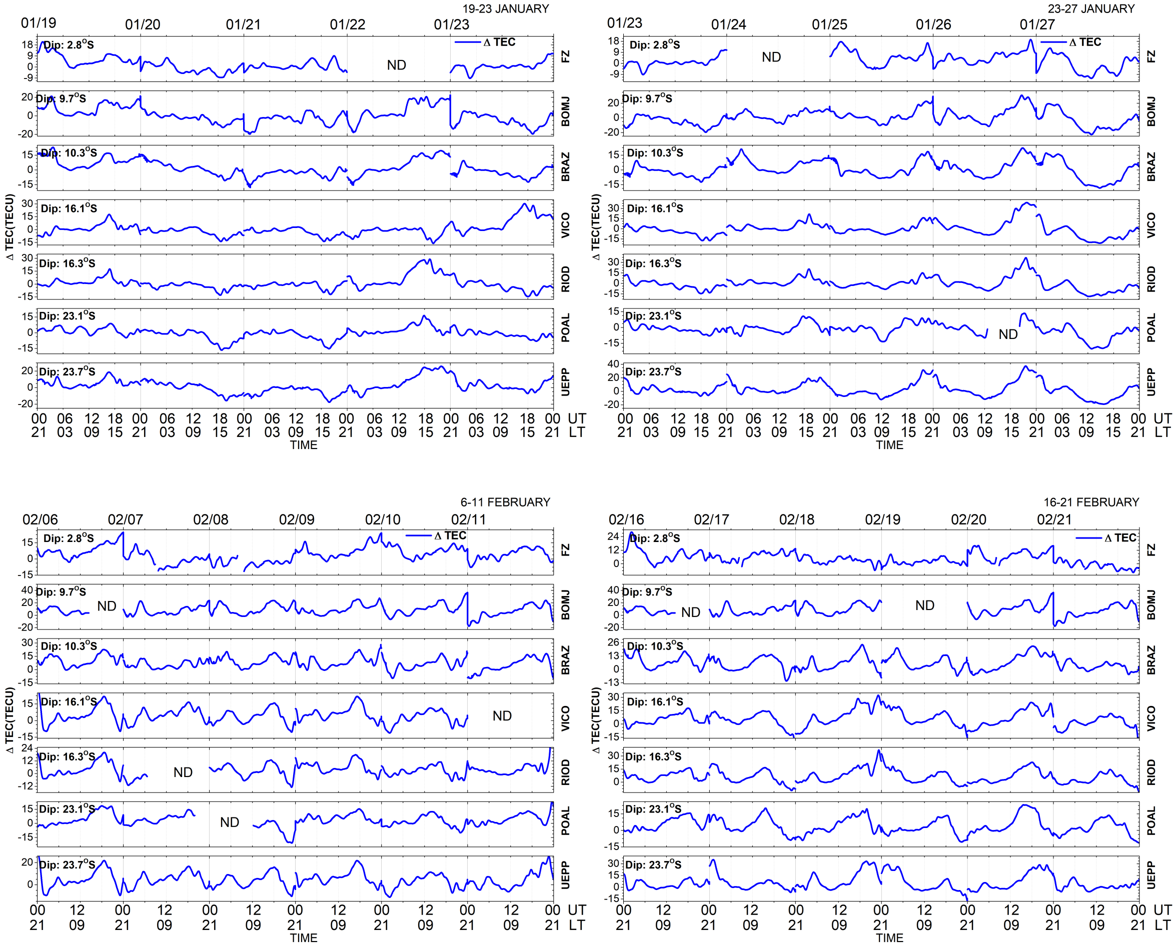

Figure A.16 – Relative differential variation in TEC during the HILDCAA events on 19-23 January, 23-27 January, 6-11 February, 18-21 February in 2003, over euatorial region and the south crest of EIA. The blue color line represents the ΔTEC and ND represent No data

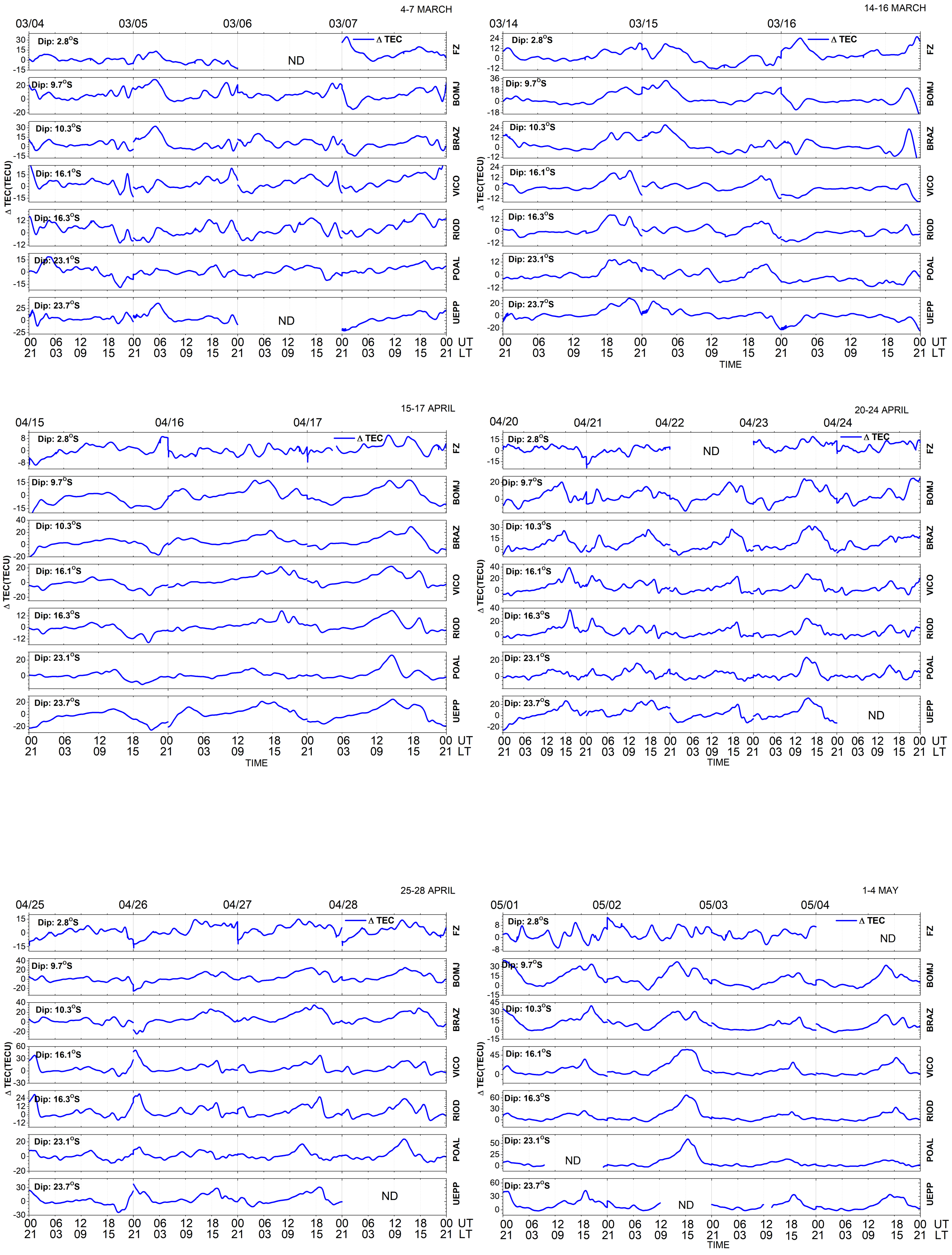

Figure A.17 – Relative differential variation in TEC during the HILDCAA events on 04-07 March, 14-16 March, 15-17 Apirl, 20-24 April, 25-28 April and 1-4 May in 2003, over equatorial region and the south crest of EIA. The blue color line represents the ΔTEC and ND represent No data

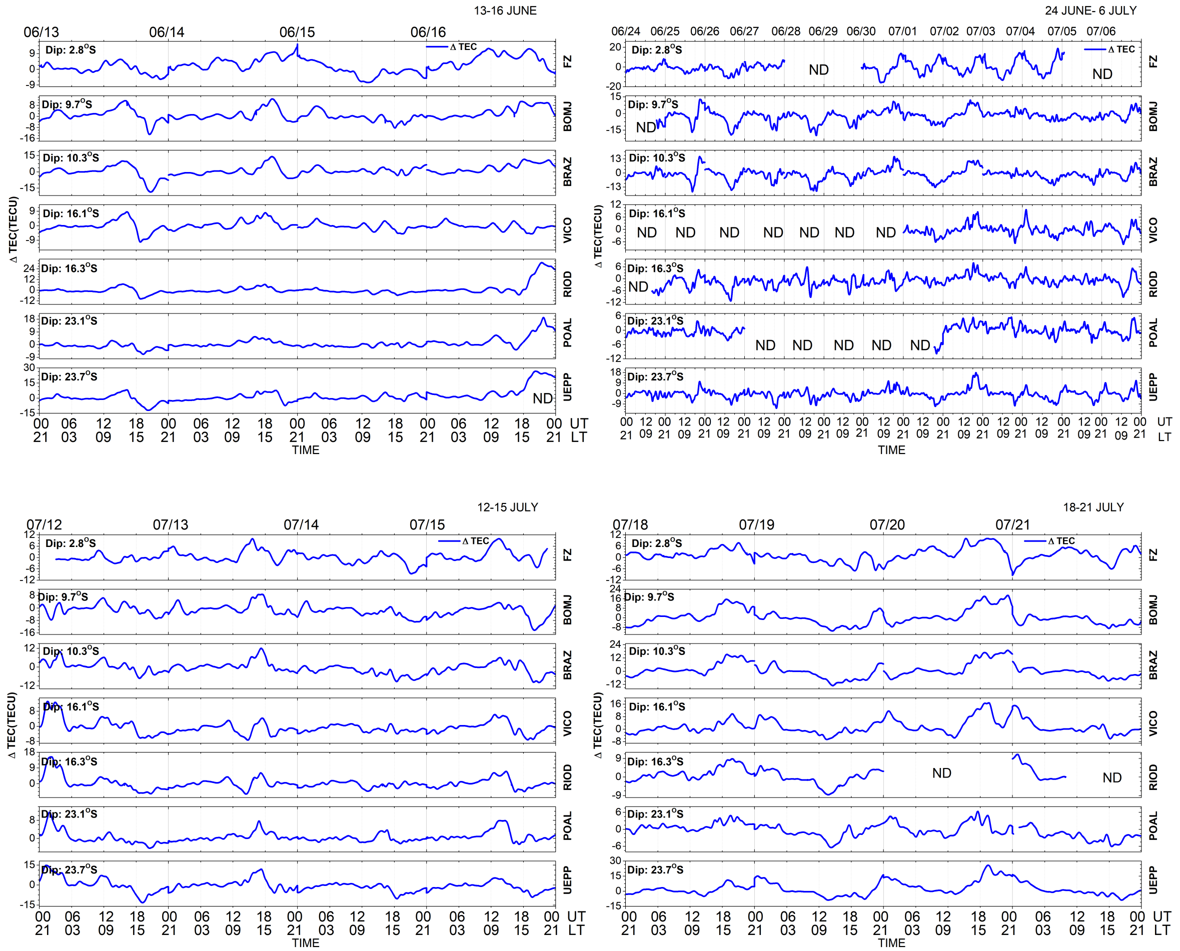

Figure A.18 – Relative differential variation in TEC during the HILDCAA events, on 13-16 June, 24 June-6 July, 12-15 July and 18-21 July in 2003, over equatorial region and the south crest of EIA. The blue color line represents the ΔTEC and ND represent No data

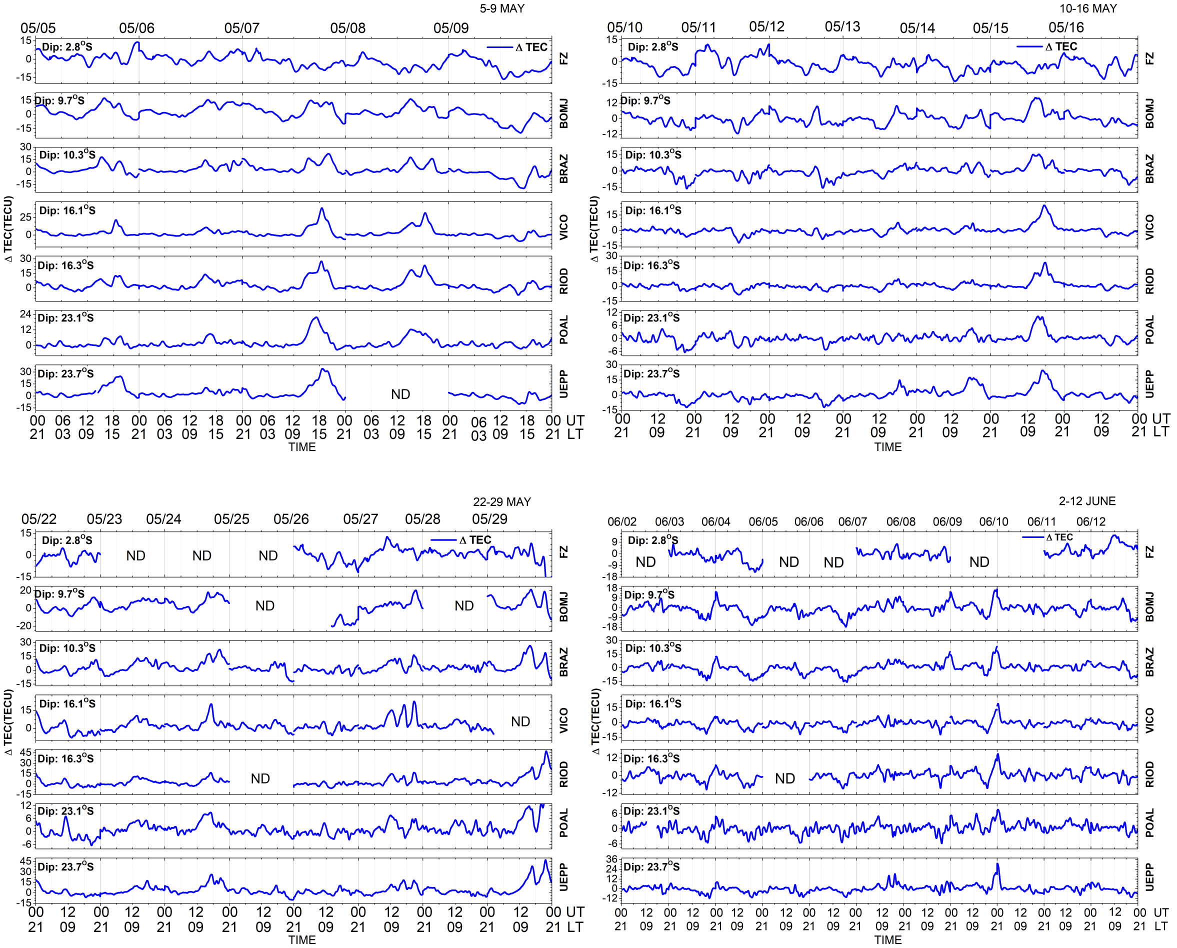

Figure A.19 – Relative differential variation in TEC during the HILDCAA events on 5-9 May, 10-16 May, 22-29 May and 2-12 June in 2003, over euatorial region and the south crest of EIA. The blue color line represents the ΔTEC and ND represent No data

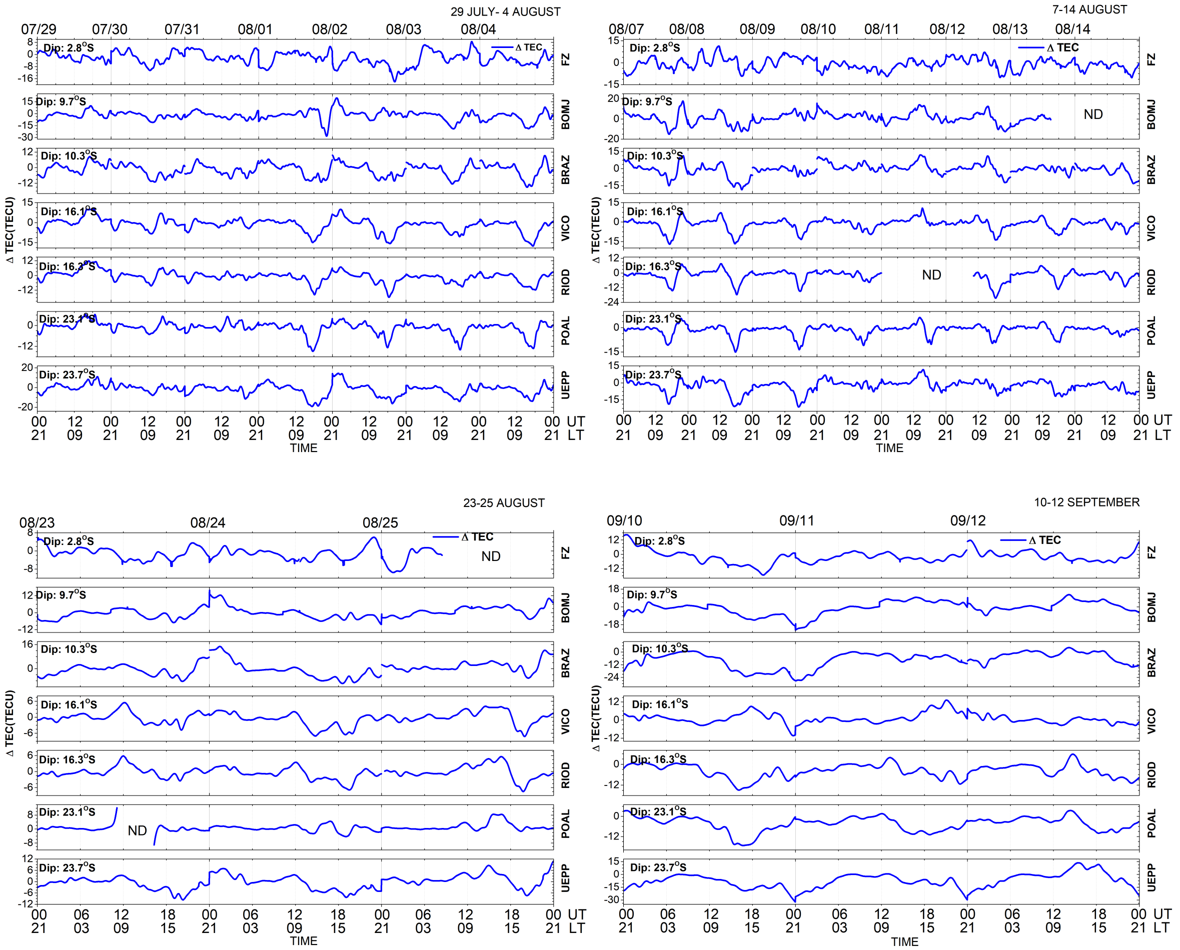

Figure A.20 – Relative differential variation in TEC during the HILDCAA events, on 29 July-4 August, 7-14 August, 23-25 August and 10-12 September in 2003, over euatorial region and the south crest of EIA. The blue color line represents the ΔTEC and ND represent No data

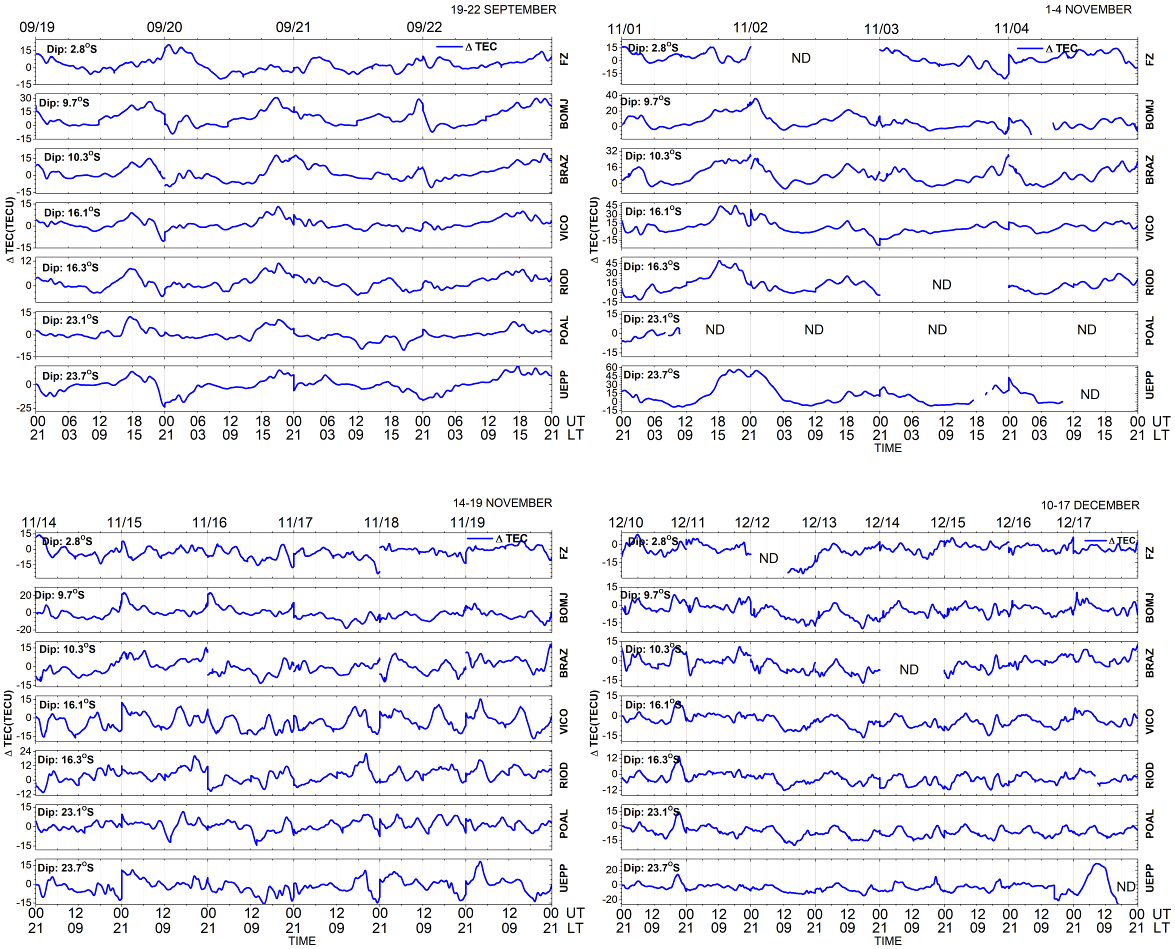

Figure A.21 – Relative differential variation in TEC during the HILDCAA events, on 19-22 September, 1-4 November, 14-19 November and 10-17 December in 2003, over euatorial region and the south crest of EIA. The blue color line represents the ΔTEC and ND represent No data

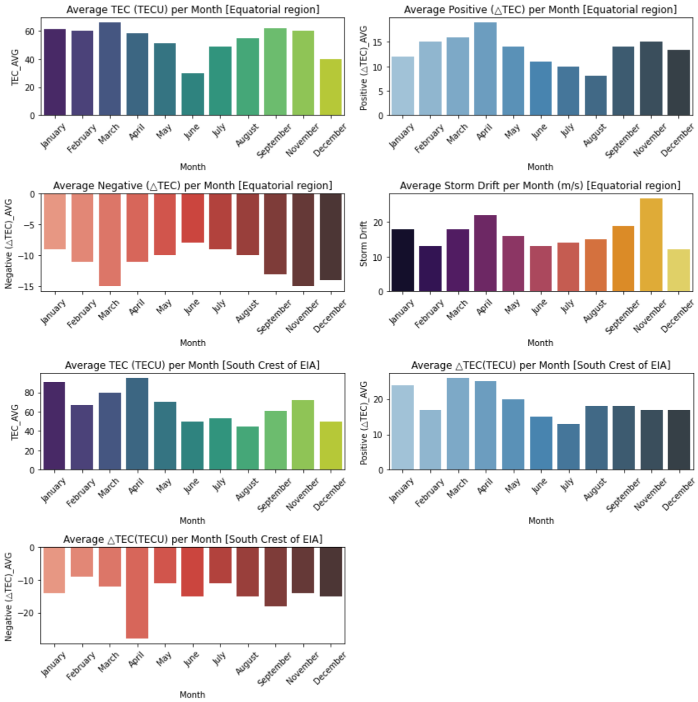

Figure A.22 – Monthly variations in the statistical differences of TEC over the Equatorial region and southern crest of EIA.

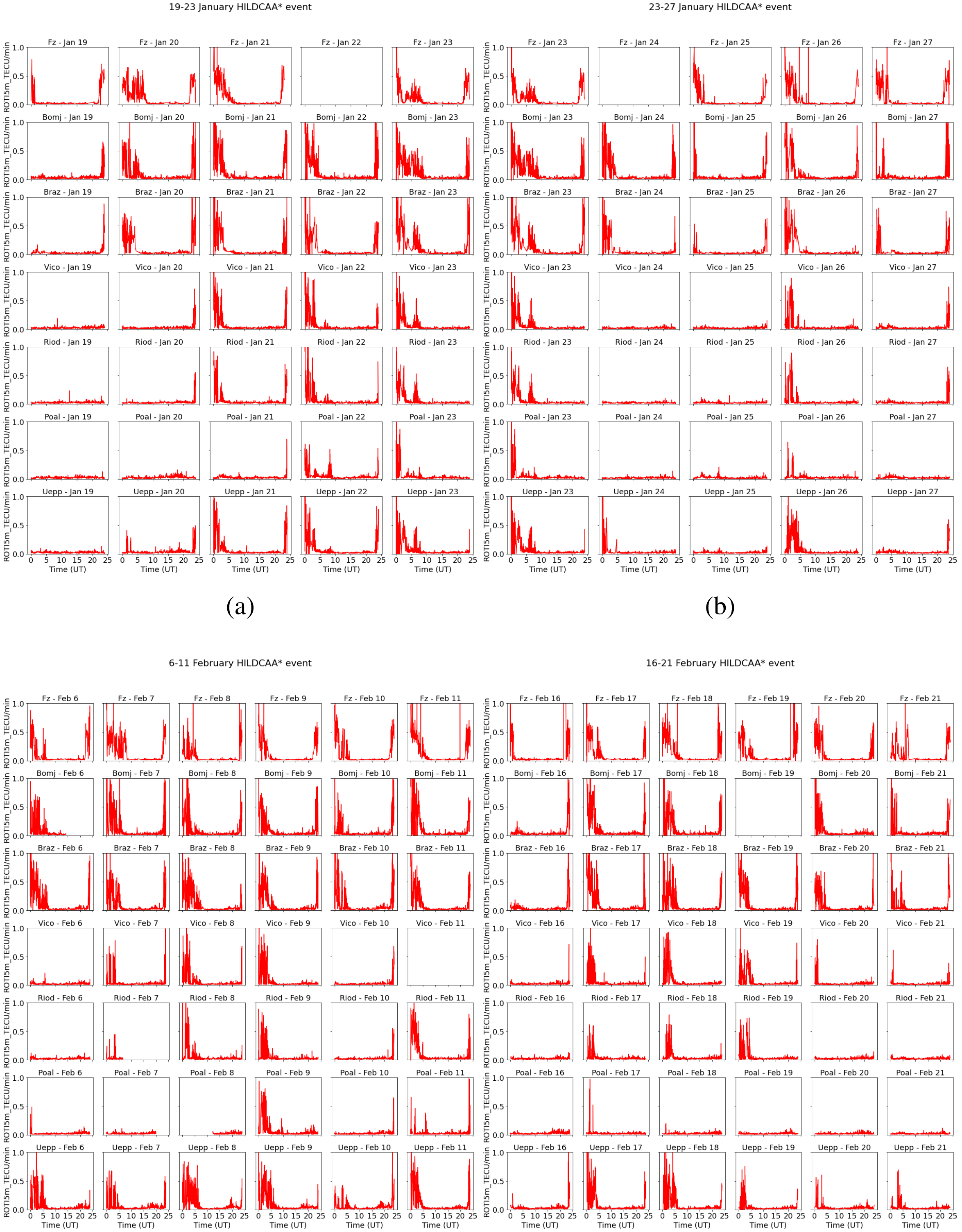

(a) (b)

(c) (d)

Figure A.23 – Temporal variations of ROTI during the HILDCAA events: (a) 19-23 January, (b) 23-27 January, (c) 6-11 February, and (d) 16-21 February in 2003, over the equatorial region and the south crest of EIA. The red line represents the distribution of ROTI values.

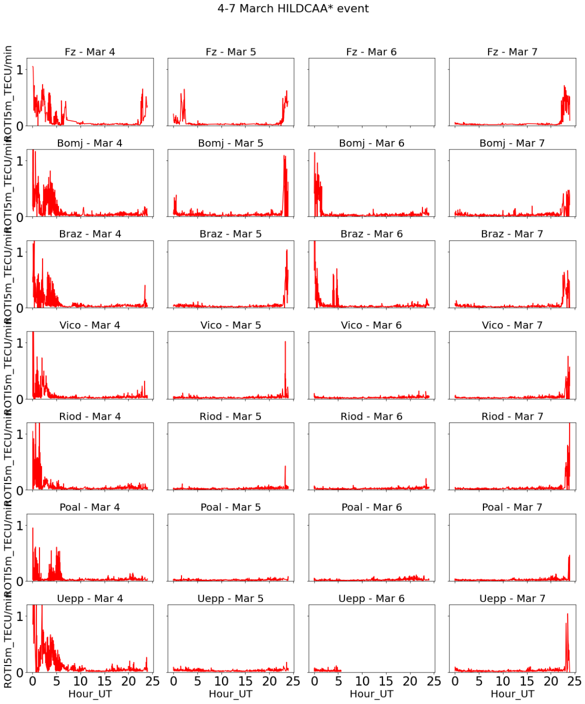
4-7 March HILDCAA* event
Fz - Mar 4
Fz - Mar 5
Fz - Mar 6
Fz - Mar 7
Bomj - Mar 4
Bomj - Mar 5
Bomj - Mar 6
Bomj - Mar 7
Braz - Mar 4
Braz - Mar 5
Braz - Mar 6
Braz - Mar 7
Vico - Mar 4
Vico - Mar 5
Vico - Mar 6
Vico - Mar 7
Riod - Mar 4
Riod - Mar 5
Riod - Mar 6
Riod - Mar 7
Poal - Mar 4
Poal - Mar 5
Poal - Mar 6
Poal - Mar 7
Uepp - Mar 4
Uepp - Mar 5
Uepp - Mar 6
Uepp - Mar 7
ROTI5m_TECU/min
Hour_UT

(m)

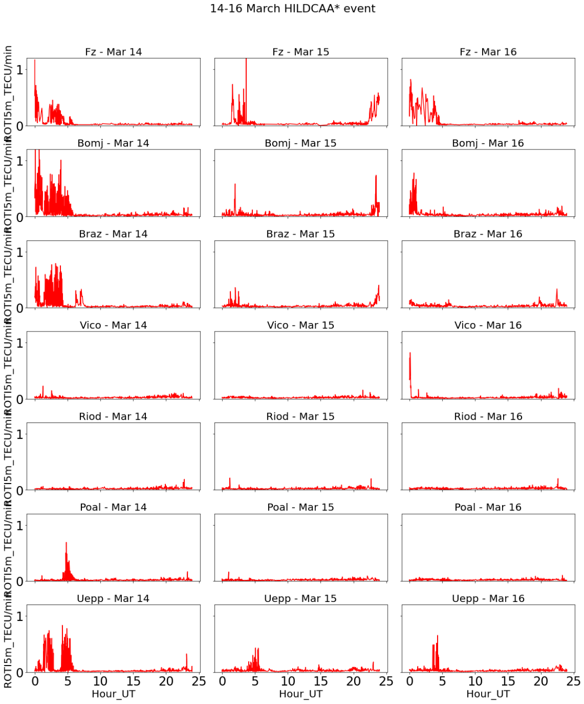
14-16 March HILDCAA* event
Fz - Mar 14
Fz - Mar 15
Fz - Mar 16
Bomj - Mar 14
Bomj - Mar 15
Bomj - Mar 16
Braz - Mar 14
Braz - Mar 15
Braz - Mar 16
Vico - Mar 14
Vico - Mar 15
Vico - Mar 16
Riod - Mar 14
Riod - Mar 15
Riod - Mar 16
Poal - Mar 14
Poal - Mar 15
Poal - Mar 16
Uepp - Mar 14
Uepp - Mar 15
Uepp - Mar 16
ROTI5m_TECU/min
Hour_UT

(n)

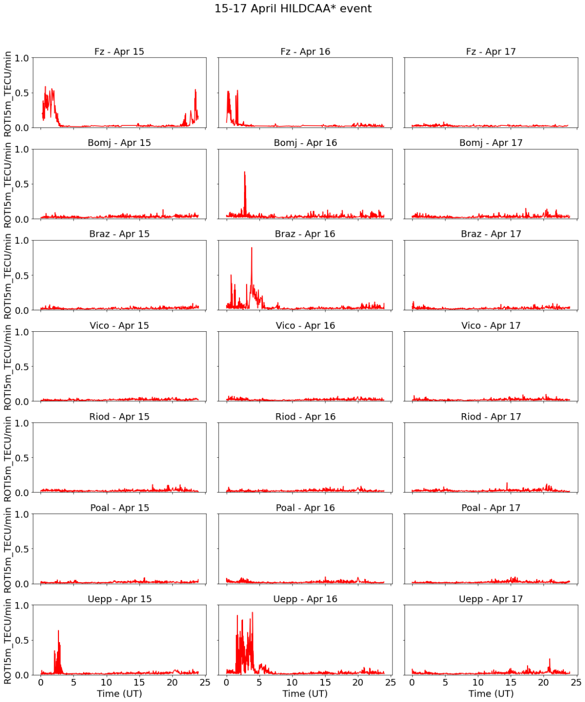
15-17 April HILDCAA* event
Fz - Apr 15
Fz - Apr 16
Fz - Apr 17
Bomj - Apr 15
Bomj - Apr 16
Bomj - Apr 17
Braz - Apr 15
Braz - Apr 16
Braz - Apr 17
Vico - Apr 15
Vico - Apr 16
Vico - Apr 17
Riod - Apr 15
Riod - Apr 16
Riod - Apr 17
Poal - Apr 15
Poal - Apr 16
Poal - Apr 17
Uepp - Apr 15
Uepp - Apr 16
Uepp - Apr 17
ROTI5m_TECU/min
Time (UT)

(o)

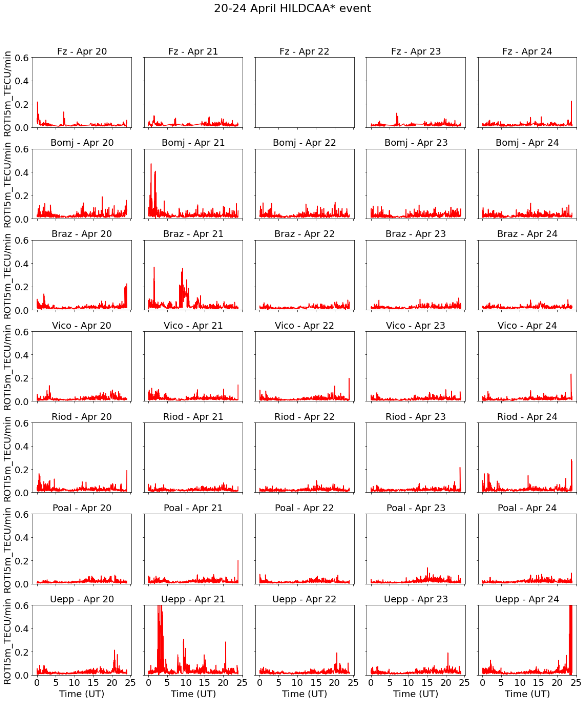
20-24 April HILDCAA* event
Fz - Apr 20
Fz - Apr 21
Fz - Apr 22
Fz - Apr 23
Fz - Apr 24
Bomj - Apr 20
Bomj - Apr 21
Bomj - Apr 22
Bomj - Apr 23
Bomj - Apr 24
Braz - Apr 20
Braz - Apr 21
Braz - Apr 22
Braz - Apr 23
Braz - Apr 24
Vico - Apr 20
Vico - Apr 21
Vico - Apr 22
Vico - Apr 23
Vico - Apr 24
Riod - Apr 20
Riod - Apr 21
Riod - Apr 22
Riod - Apr 23
Riod - Apr 24
Poal - Apr 20
Poal - Apr 21
Poal - Apr 22
Poal - Apr 23
Poal - Apr 24
Uepp - Apr 20
Uepp - Apr 21
Uepp - Apr 22
Uepp - Apr 23
Uepp - Apr 24
ROTI5m_TECU/min
Time (UT)

(p)

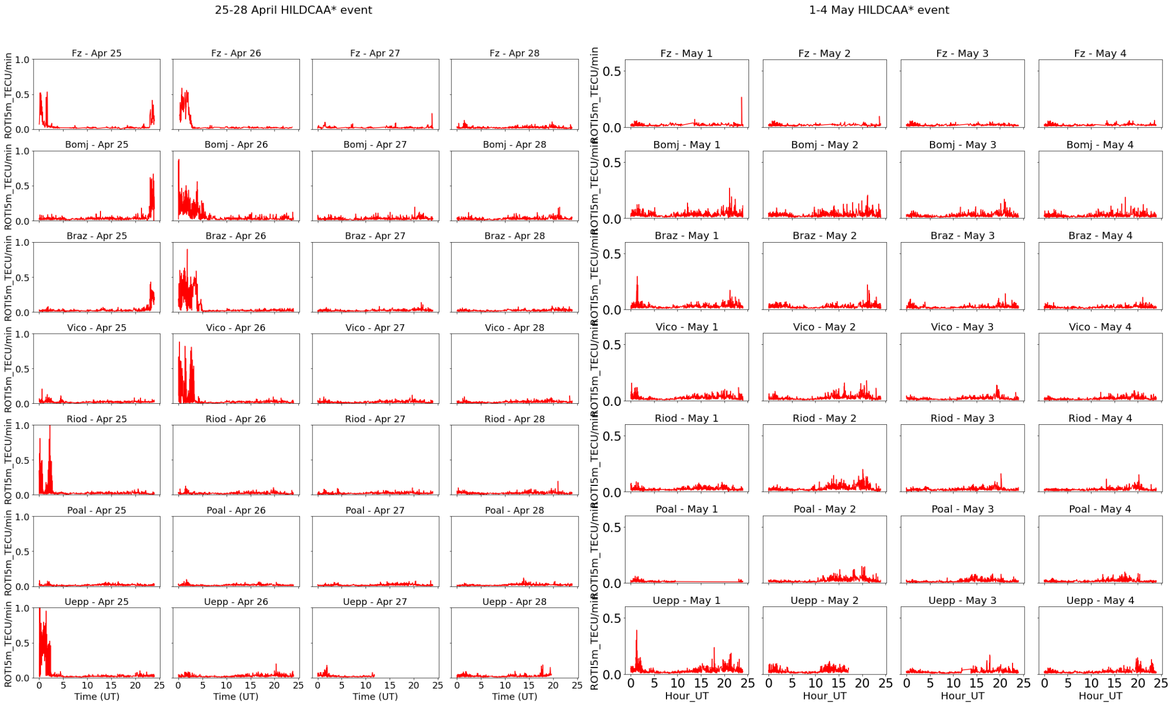

(q)

(r)

Figure A.24 – Temporal variations of ROTI during the HILDCAA events in 2003: (m) 4-7 March, (n) 14-16 March, (o) 15-17 April, (p) 20-24 April, (q) 25-28 April, and (r) 1-4 May, over the equatorial region and the south crest of EIA. The red line represents the distribution of ROTI values.

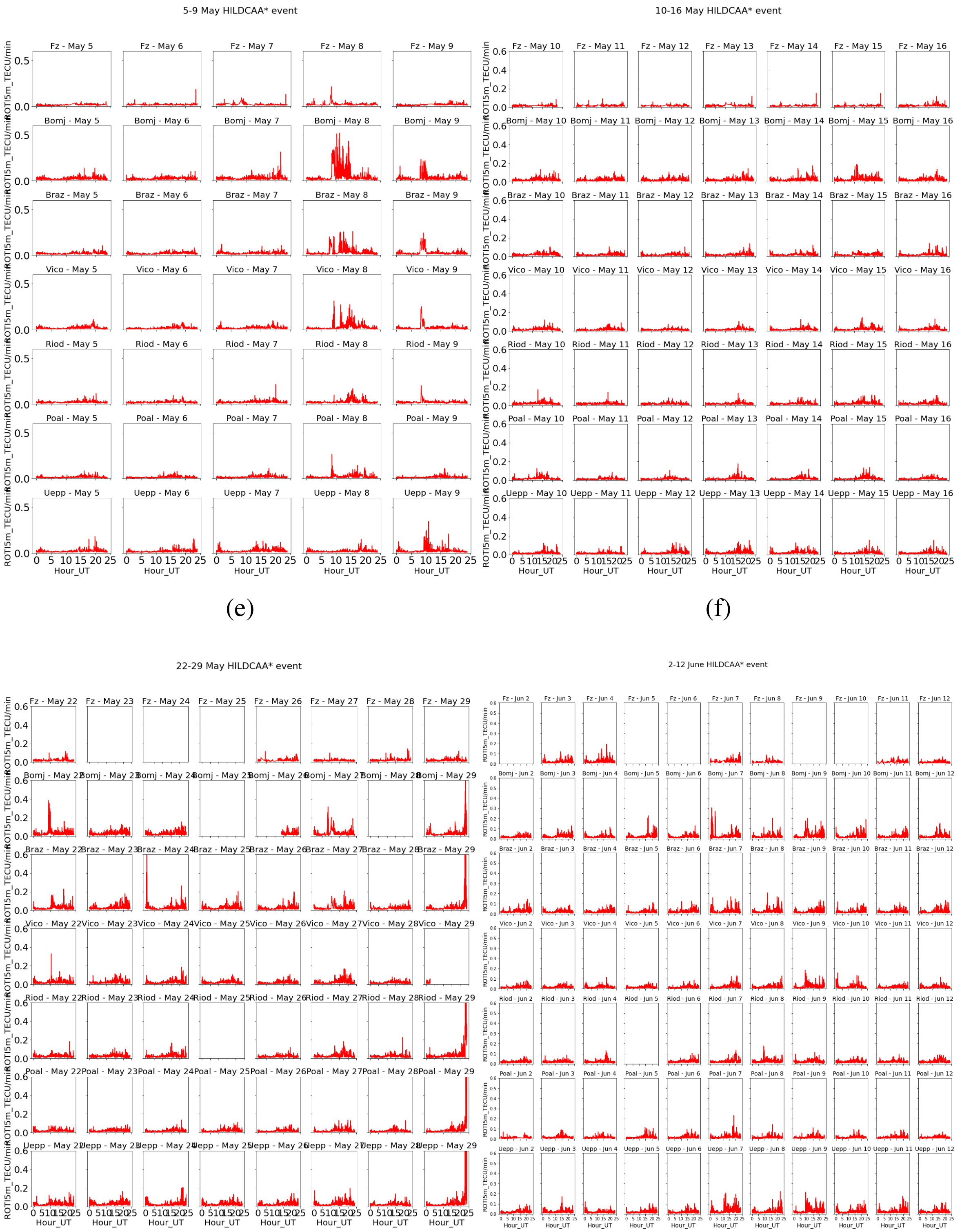

(e) (f)

(g) (h)

Figure A.25 – Temporal variations of ROTI during the HILDCAA events: (e) 5-9 May, (f) 10-16 May, (g) 22-29 May, and (h) 2-12 June in 2003, over the equatorial region and the south crest of EIA. The red line represents the distribution of ROTI values.

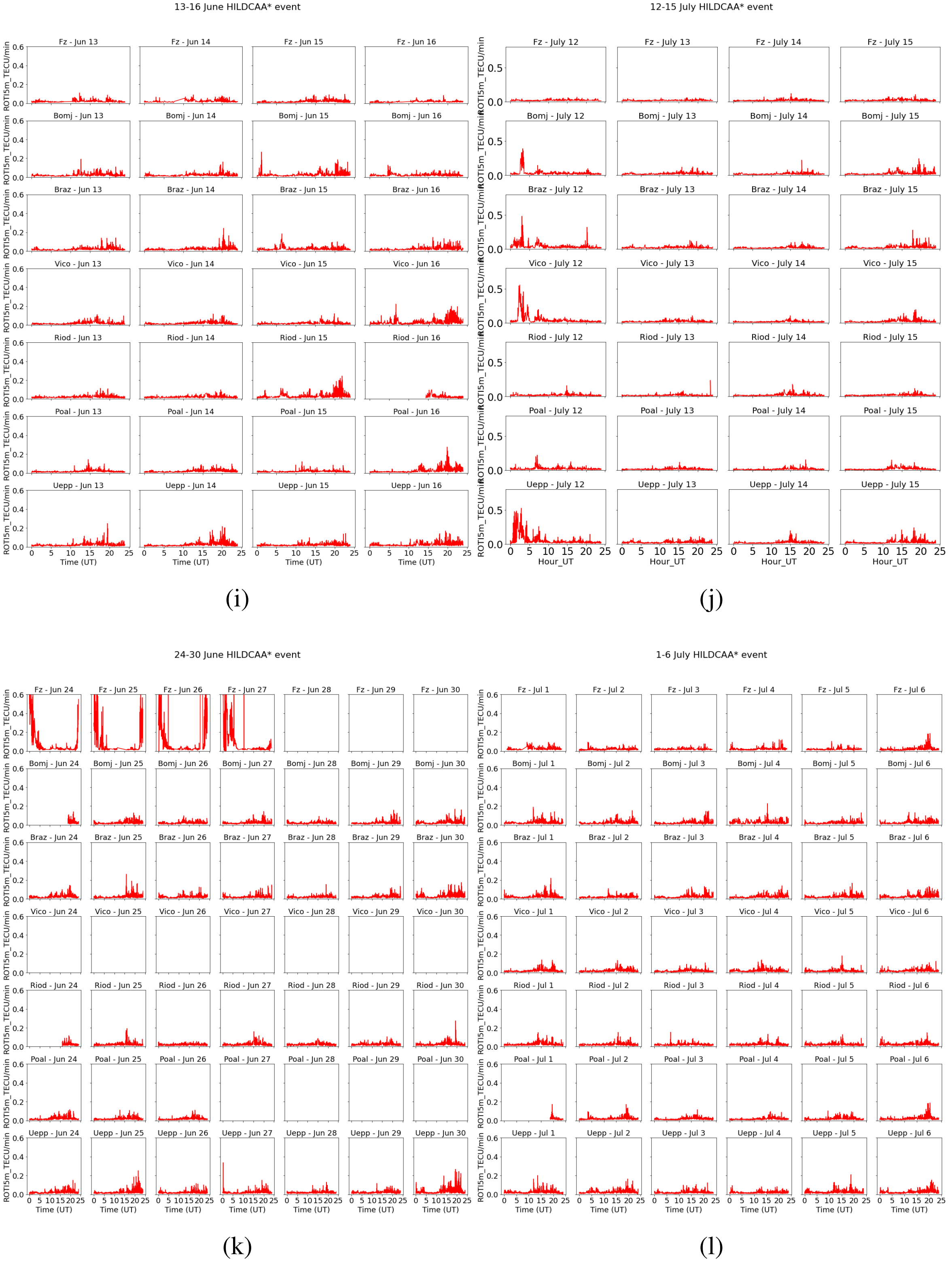

(i)

(j)

(k)

(l)

Figure A.26 – Temporal variations of ROTI during the HILDCAA events: (i) 13-16 June, (j) 12-15 July, (k) 24-30 June, and (l) 1-6 July in 2003, over the equatorial region and the south crest of EIA. The red line represents the distribution of ROTI values.

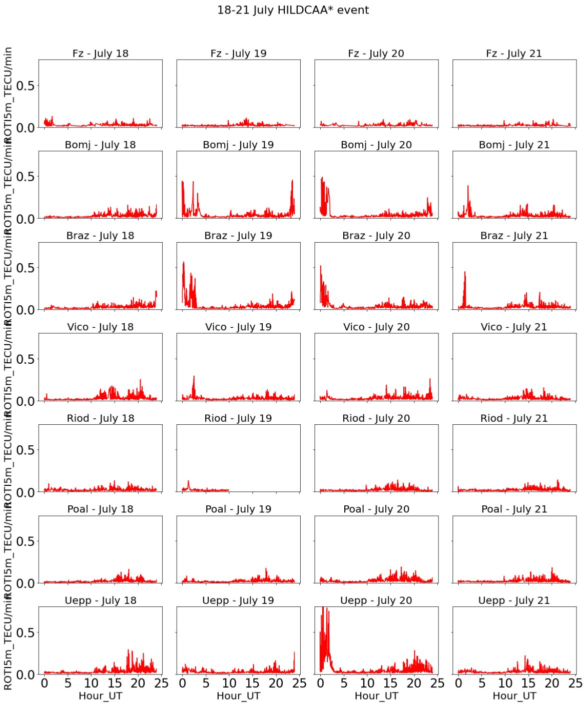
18-21 July HILDCAA* event
Fz - July 18
Fz - July 19
Fz - July 20
Fz - July 21
Bomj - July 18
Bomj - July 19
Bomj - July 20
Bomj - July 21
Braz - July 18
Braz - July 19
Braz - July 20
Braz - July 21
Vico - July 18
Vico - July 19
Vico - July 20
Vico - July 21
Riod - July 18
Riod - July 19
Riod - July 20
Riod - July 21
Poal - July 18
Poal - July 19
Poal - July 20
Poal - July 21
Uepp - July 18
Uepp - July 19
Uepp - July 20
Uepp - July 21
ROTI5m_TECU/min
Hour_UT
0.0
0.5
0 5 10 15 20 25

(s)

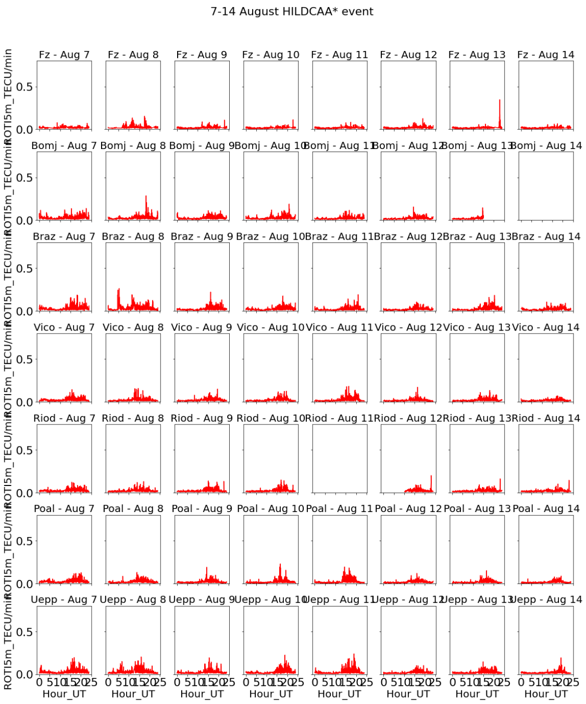
7-14 August HILDCAA* event
Fz - Aug 7
Fz - Aug 8
Fz - Aug 9
Fz - Aug 10
Fz - Aug 11
Fz - Aug 12
Fz - Aug 13
Fz - Aug 14
Bomj - Aug 7
Bomj - Aug 8
Bomj - Aug 9
Bomj - Aug 10
Bomj - Aug 11
Bomj - Aug 12
Bomj - Aug 13
Bomj - Aug 14
Braz - Aug 7
Braz - Aug 8
Braz - Aug 9
Braz - Aug 10
Braz - Aug 11
Braz - Aug 12
Braz - Aug 13
Braz - Aug 14
Vico - Aug 7
Vico - Aug 8
Vico - Aug 9
Vico - Aug 10
Vico - Aug 11
Vico - Aug 12
Vico - Aug 13
Vico - Aug 14
Riod - Aug 7
Riod - Aug 8
Riod - Aug 9
Riod - Aug 10
Riod - Aug 11
Riod - Aug 12
Riod - Aug 13
Riod - Aug 14
Poal - Aug 7
Poal - Aug 8
Poal - Aug 9
Poal - Aug 10
Poal - Aug 11
Poal - Aug 12
Poal - Aug 13
Poal - Aug 14
Uepp - Aug 7
Uepp - Aug 8
Uepp - Aug 9
Uepp - Aug 10
Uepp - Aug 11
Uepp - Aug 12
Uepp - Aug 13
Uepp - Aug 14
ROTI5m_TECU/min
Hour_UT
0.0
0.5
0 510152025

(t)

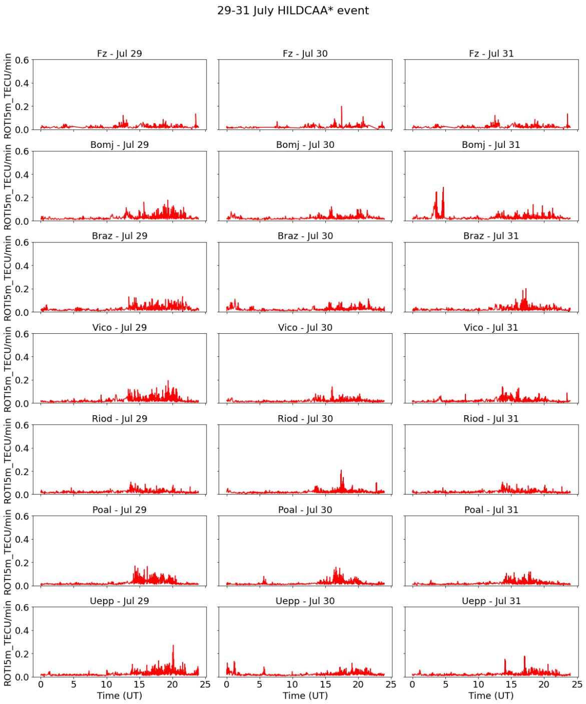
29-31 July HILDCAA* event
Fz - Jul 29
Fz - Jul 30
Fz - Jul 31
Bomj - Jul 29
Bomj - Jul 30
Bomj - Jul 31
Braz - Jul 29
Braz - Jul 30
Braz - Jul 31
Vico - Jul 29
Vico - Jul 30
Vico - Jul 31
Riod - Jul 29
Riod - Jul 30
Riod - Jul 31
Poal - Jul 29
Poal - Jul 30
Poal - Jul 31
Uepp - Jul 29
Uepp - Jul 30
Uepp - Jul 31
ROTI5m_TECU/min
Time (UT)
0.0
0.2
0.4
0.6
0 5 10 15 20 25

(u)

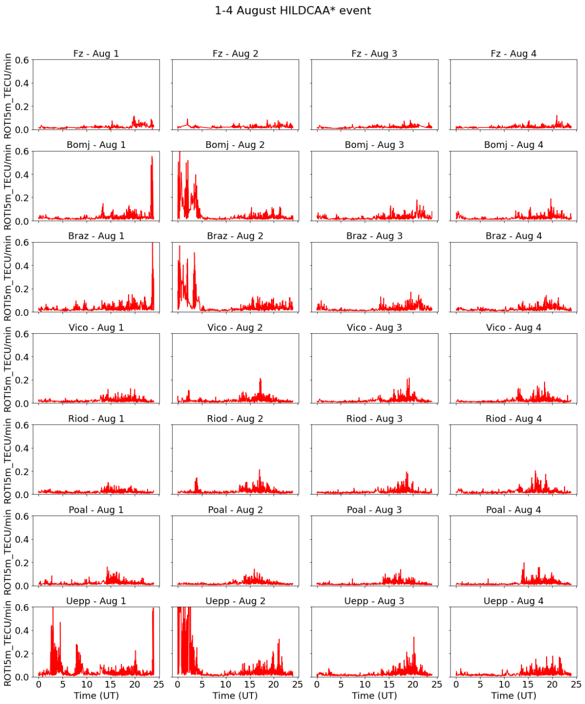
1-4 August HILDCAA* event
Fz - Aug 1
Fz - Aug 2
Fz - Aug 3
Fz - Aug 4
Bomj - Aug 1
Bomj - Aug 2
Bomj - Aug 3
Bomj - Aug 4
Braz - Aug 1
Braz - Aug 2
Braz - Aug 3
Braz - Aug 4
Vico - Aug 1
Vico - Aug 2
Vico - Aug 3
Vico - Aug 4
Riod - Aug 1
Riod - Aug 2
Riod - Aug 3
Riod - Aug 4
Poal - Aug 1
Poal - Aug 2
Poal - Aug 3
Poal - Aug 4
Uepp - Aug 1
Uepp - Aug 2
Uepp - Aug 3
Uepp - Aug 4
ROTI5m_TECU/min
Time (UT)
0.0
0.2
0.4
0.6
0 5 10 15 20 25

(v)

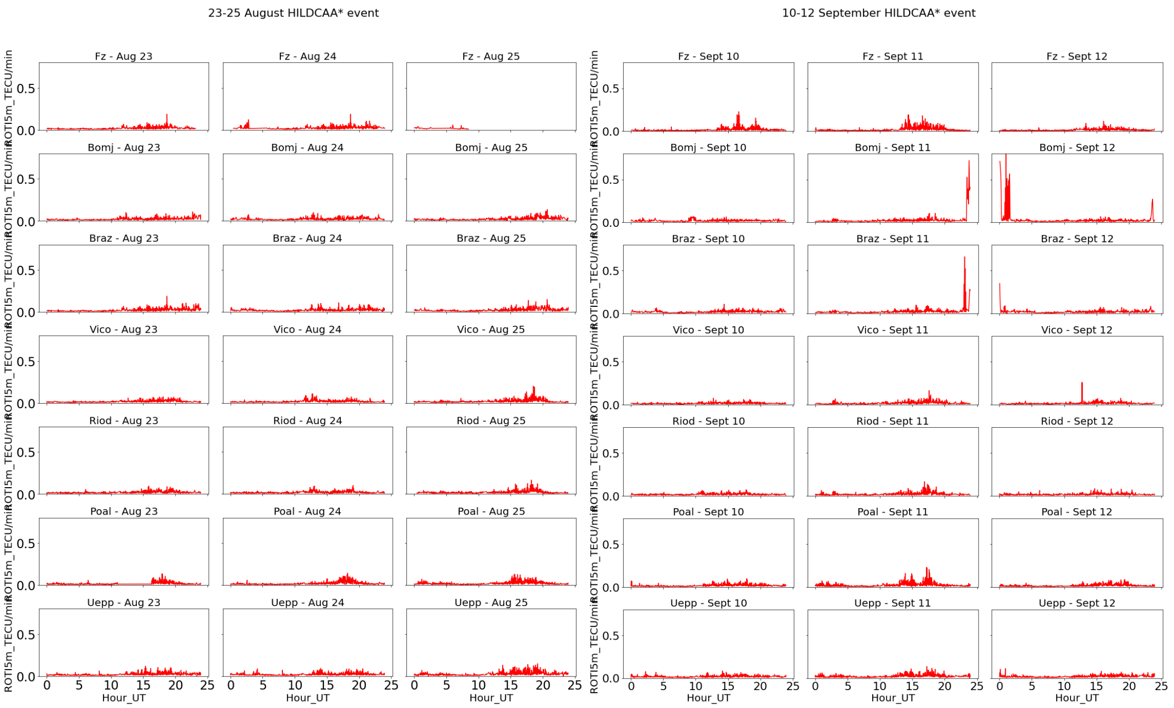

(w) (x)

Figure A.27 – Temporal variations of ROTI during the HILDCAA events in 2003: (s) 18-21 July, (t) 7-14 August, (u) 29-31 July, (v) 1-4 August, (w) 23-25 August, and (x) 10-12 September, over the equatorial region and the south crest of EIA. The red line represents the distribution of ROTI values.

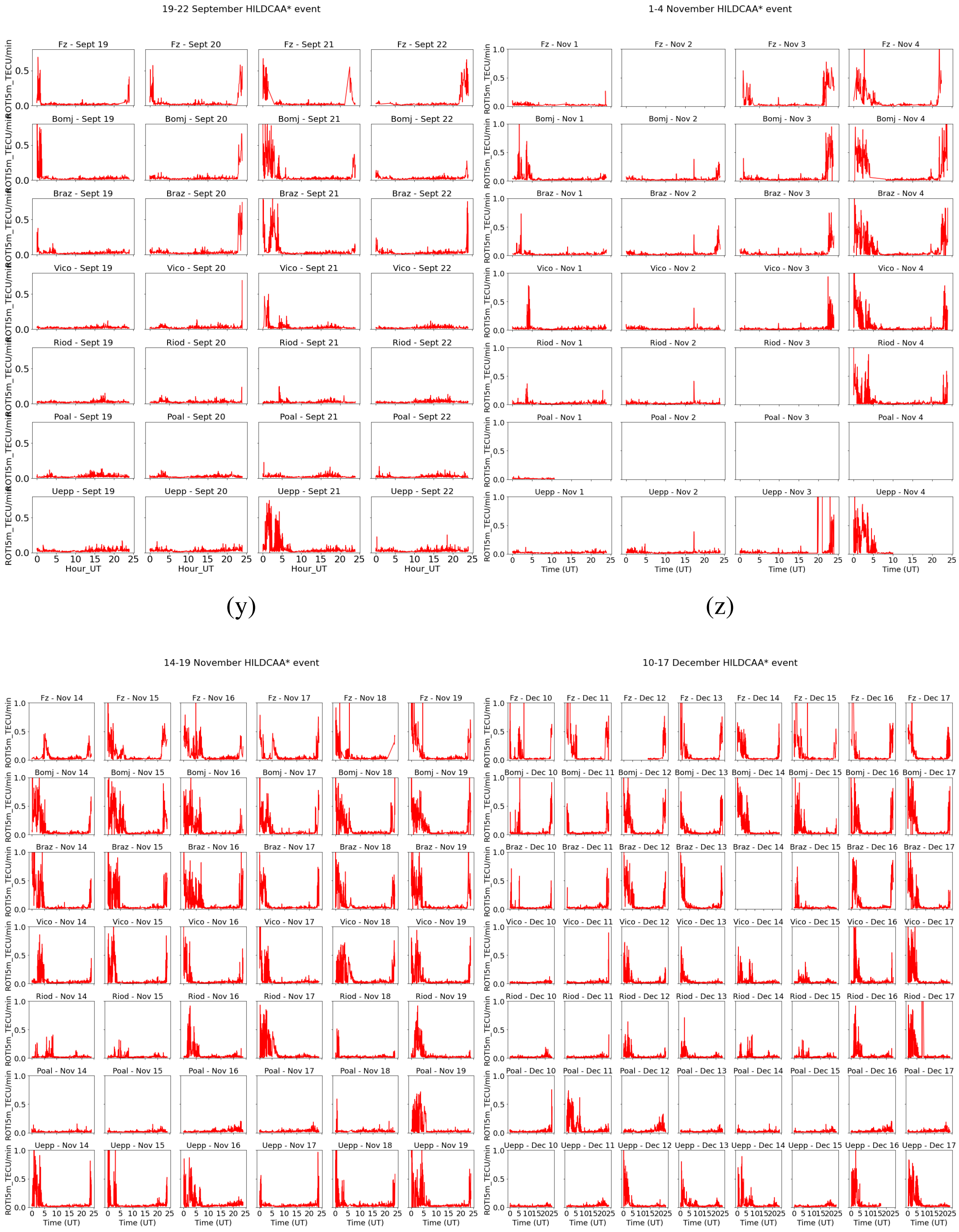

(y)

(z)

(i)

(ii)

Figure A.28 – Temporal variations of ROTI during the HILDCAA events: (y) 19-22 September, (z) 1-4 November, (i) 14-19 November, (ii) 10-17 December in 2003, over the equatorial region and the south crest of EIA. The red line represents the distribution of ROTI values.

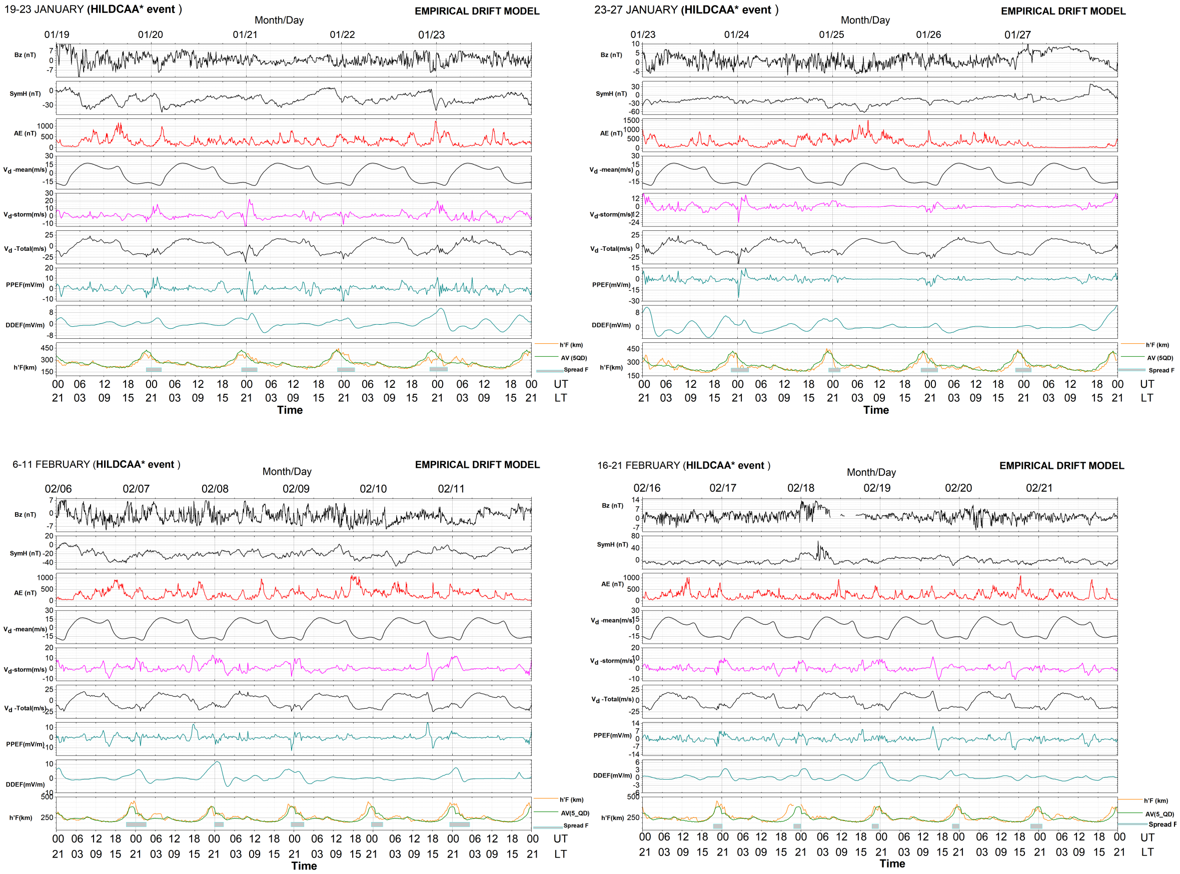

Figure A.29 – Variations of interplanetary magnetic field (Bz) in (nT), symmetric disturbance index (Sym-H) in (nT), auroral electrojet index (AE), empirical calculation of V_d-mean, V_d-storm, V_d-total, Prompt penetration (PPEF) and Disturbance dynamo drifts (DDEF) drifts components derived from our high time resolution model and ionospheric parameters, h'F (F layer virtual height) including the five quiet days average during the HILDCAA events on 19-23 January, 23-27 January, 6-11 February and 18-21 February in 2003

Figure A.30 – Variations of interplanetary magnetic field (Bz) in (nT), symmetric disturbance index (Sym-H) in (nT), auroral electrojet index (AE), empirical calculation of V_d-mean, V_d-storm, V_d-total, Prompt penetration (PPEF) and Disturbance dynamo drifts (DDEF) drifts components derived from our high time resolution model and ionospheric parameters, h'F (F layer virtual height) including the five quiet days average during the HILDCAA events on 04-07 March, 14-16 March, 15-17 Apirl, 20-24 April, 25-28 April and 1-4 May in 2003

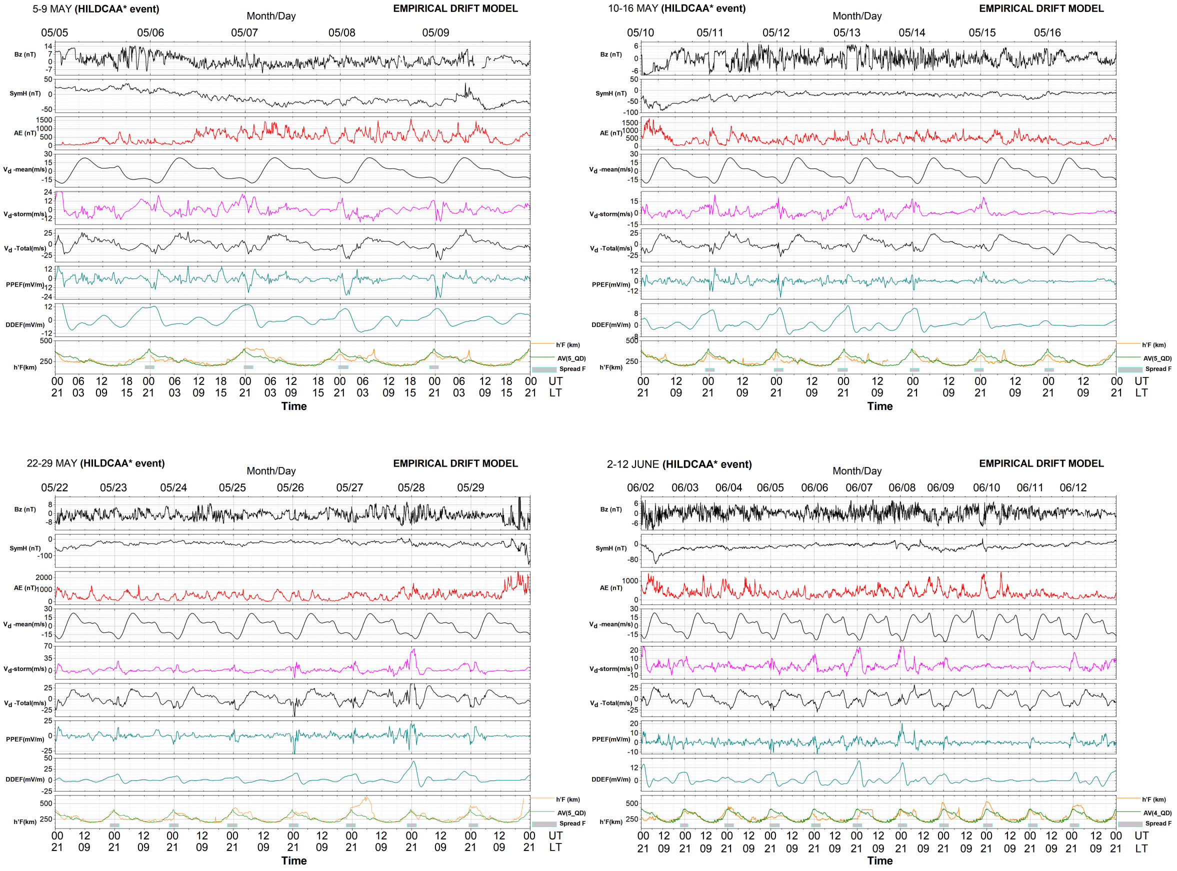

Figure A.31 – Variations of interplanetary magnetic field (Bz) in (nT), symmetric disturbance index (Sym-H) in (nT), auroral electrojet index (AE), empirical calculation of V_d-mean, V_d-storm, V_d-total, Prompt penetration (PPEF) and Disturbance dynamo drifts (DDEF) drifts components derived from our high time resolution model and ionospheric parameters, h'F (F layer virtual height) including the five quiet days average during the HILDCAA events on 5-9 May, 10-16 May, 22-29 May, 2-12 June in 2003

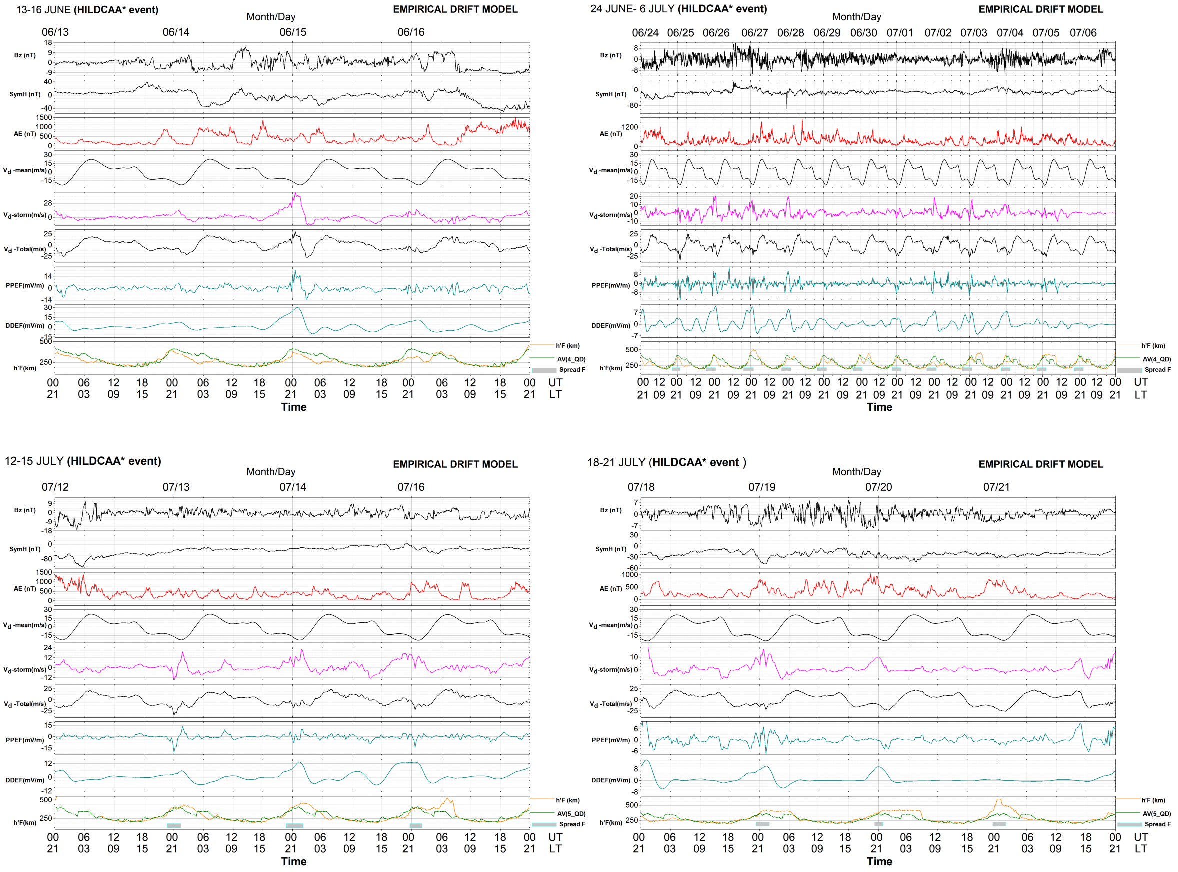

Figure A.32 – Variations of interplanetary magnetic field (Bz) in (nT), symmetric disturbance index (Sym-H) in (nT), auroral electrojet index (AE), empirical calculation of V_d-mean, V_d-storm, V_d-total, Prompt penetration (PPEF) and Disturbance dynamo drifts (DDEF) drifts components derived from our high time resolution model and ionospheric parameters, h'F (F layer virtual height) including the five quiet days average during the HILDCAA events on 13-16 June, 24 June-6 July, 12-15 July and 18-21 July in 2003

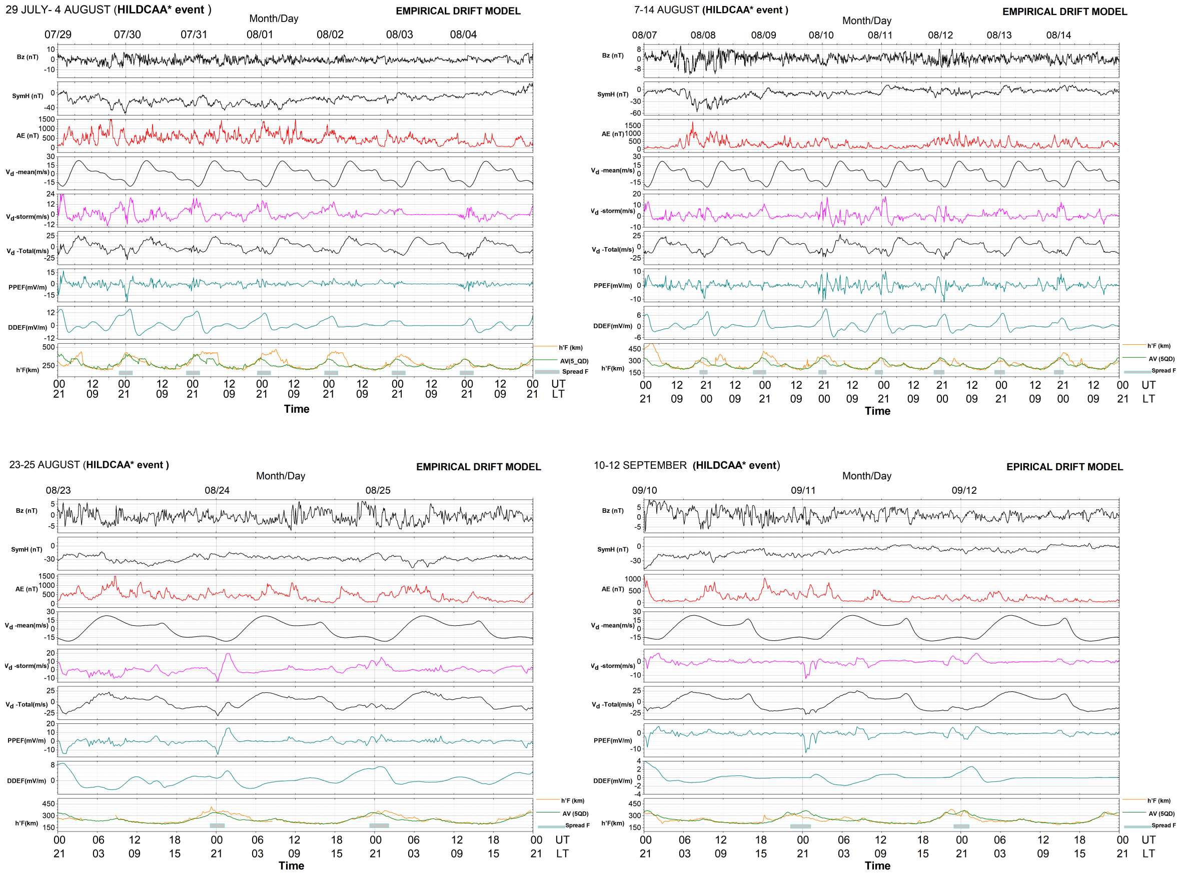

Figure A.33 – Variations of interplanetary magnetic field (Bz) in (nT), symmetric disturbance index (Sym-H) in (nT), auroral electrojet index (AE), empirical calculation of V_d-mean, V_d-storm, V_d-total, Prompt penetration (PPEF) and Disturbance dynamo drifts (DDEF) drifts components derived from our high time resolution model and ionospheric parameters, h'F (F layer virtual height) including the five quiet days average during the HILDCAA events on on 29 July-4 August, 7-14 August, 23-25 August and 10-12 September in 2003

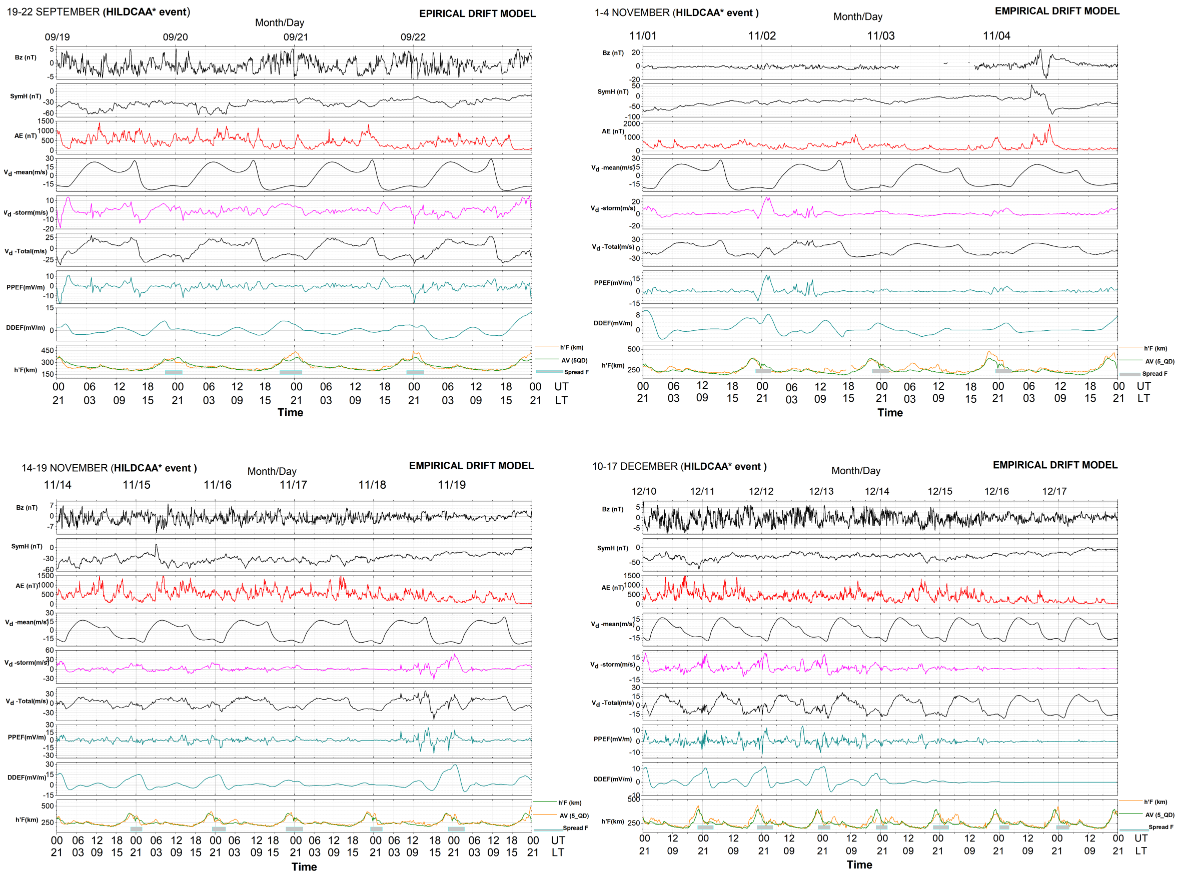

Figure A.34 – Variations of interplanetary magnetic field (Bz) in (nT), symmetric disturbance index (Sym-H) in (nT), auroral electrojet index (AE), empirical calculation of V_d-mean, V_d-storm, V_d-total, Prompt penetration (PPEF) and Disturbance dynamo drifts (DDEF) drifts components derived from our high time resolution model and ionospheric parameters, h'F (F layer virtual height) including the five quiet days average during the HILDCAA events on 19-22 September, 1-4 November, 14-19 November and 10-17 December in 2003